Dissertations (2009 -)   Dissertations, Theses, and Professional Projects

Synthesis and Characterization of Biologically Relevant Fe(II) Complexes Containing Redox-Active (Hydro)quinone Ligands

Amanda Elizabeth Baum
Marquette University

SYNTHESIS AND CHARACTERIZATION OF BIOLOGICALLY RELEVANT
FE(II) COMPLEXES CONTAINING REDOX-ACTIVE
(HYDRO)QUINONE LIGANDS

by

Amanda E. Baum, B.S.

A Dissertation submitted to the Faculty of the Graduate School,
Marquette University,
in Partial Fulfillment of the Requirements for
the Degree of Doctor of Philosophy

Milwaukee, Wisconsin

May 2016

ABSTRACT

SYNTHESIS AND CHARACTERIZATION OF BIOLOGICALLY RELEVANT
FE(II) COMPLEXES CONTAINING REDOX-ACTIVE
(HYDRO)QUINONE LIGANDS

Amanda E. Baum, B.S.

Marquette University, 2016

Redox-active p-(hydro)quinones work in concert with transition-metal centers to facilitate electron transfers in numerous biological contexts. While p-(hydro)quinones are known to interact with both heme and nonheme iron cofactors, the nonheme systems are particularly relevant to photosynthetic and bioremediation processes. In photosynthesis, two p-quinones facilitate an electron transfer away from the photoexcited P_{680} cofactor via a non-heme Fe(II) center. Based on EPR results, this interaction results in formation of transient Fe(II)/p-semiquinone (pSQ) species. In addition, a superoxo-iron(II)-pSQ species has been proposed as an intermediate of the oxidative cleavage mechanism of hydroquinone dioxygenases (HQDOs), which play a central role in the catabolism of aromatic pollutants. Despite the prevalence of iron-(hydro)quinone interactions observed in nature, there is a dearth of reported synthetic analogs.

We therefore aimed to synthesize five-coordinate monoiron(II) complexes featuring a variety of substituted p-quinone ligand or p-hydroquinone ligands. These complexes contain a tris(3,5-diphenylpyrazolyl)borate (^{Ph2}Tp) or tris(4,5-diphenyl-1-methylimidazol-2-yl)phosphine (^{Ph2}TIP) supporting ligand scaffold to mimic the different types of facial triads found in nonheme iron dioxygenases. The corresponding Fe(II)-pSQ intermediates were generated via two methods: (i) proton-coupled electron transfer from an iron-hydroquinonate precursor and (ii) chemical reduction of the mononuclear Fe(II)-p-quinone complexes. The presence of a pSQ radical coupled to a high-spin Fe(II) center was confirmed by spectroscopic (UV-vis, EPR, resonance Raman) and computational (DFT) methods. Recent O_2 reactivity studies have examined the ability of these complexes to serve as functional HQDO models.

Additionally, we synthesized a diiron(II) species that, upon treatment with a chemical oxidant, yields a stable complex in which two Fe(II) centers are bridged by a p-semiquinone radical. The unique $S=7/2$ electronic structure of this complex was studied extensively by spectroscopic and computational methods and represents the first complex to feature Fe(II) centers bound to a semiquinonate radical. Further studies were focused on the development of additional dimetal(II) species bridged by varying hydroquinonate ligands to explore their potential of generating novel species that display a high degree of electronic coupling upon one-electron oxidation.

ACKNOWLEDGEMENTS

Amanda E. Baum, B.S.

TABLE OF CONTENTS

LIST OF TABLES

LIST OF FIGURES

LIST OF COMPLEXES

Chapter 1

Introduction: Investigation of Metal-(Hydro)quinone Interactions Observed in Nature – Toward Elucidation of the Catalytic Mechanism of the Hydroquinone Dioxygenases
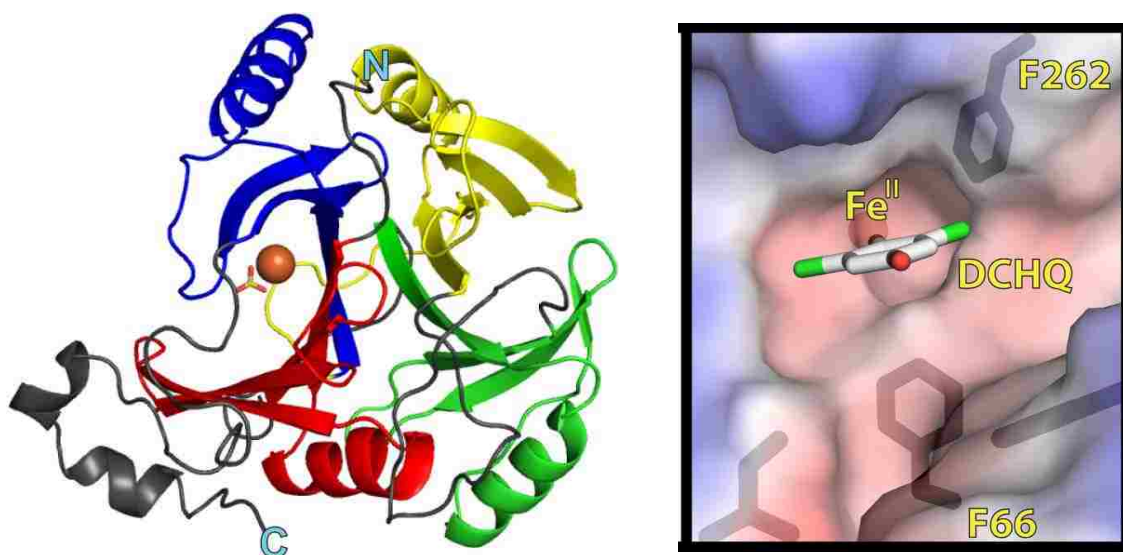
(Hayes, R. P.; Green, A. R.; Nissen, M. S.; Lewis, K. M.; Xun, L.; Kang, C., *Molecular Microbiology* **2013**, *88*, 523-536.)

Abstract: Redox-active molecules, such as *para*-(hydro)quinones, have the ability to participate in reversible one and two-electron reactions that are often coupled to proton transfers. In nature, these cofactors often operate in conjunction with protein-bound metal centers to carry out critical electron transfers. Furthermore, the ability of hydroquinones to act in a redox non-innocent manner suggests that these substrates have the ability to directly participate in the redox reactions encountered during their catabolism as facilitated by a class of non-heme iron dioxygenases known as the hydroquinone dioxygenases (HQDOs), to form a reactive intermediate that incorporates a substrate-based radical, however, this putative intermediate has yet to be observed experimentally. By employing a biomimetic approach, we hope to gain a better understanding of the geometric, electronic and catalytic properties of the HQDOs and, ultimately, gain insight into the cooperativity of these redox-active cofactors associated with metal centers as demonstrated in nature.

1.A. Non-heme Iron Dioxygenases

Due to the grave environmental concern of the presence of contaminants in groundwater and soil, recently, researchers have focused interest on the use of bioremedial technologies to eliminate toxic aromatic pollutants from our environment. This process can be carried out naturally by a variety of aerobic bacteria proficient in the catabolism and assimilation of single and multi-ring aromatic hydrocarbons.[1,2] In order to catalyze pollutant breakdown, these microorganisms utilize metalloenzymes classified as non-heme iron dioxygenases. These metalloenzymes contain an active site capable of aerobic degradation via oxidative ring cleavage in which both atoms of O_2 are incorporated into the final environmentally-benign product. In order to facilitate the breakdown of intrinsically stable aromatic hydrocarbons, the first step in many pathways is the oxidation of the substrate to the corresponding cis-1,2-diol. As demonstrated in Figure 1.1, the first step of the degradation of benzene involves oxidation to *cis*-1,2-dihydrobenzene-1,2-diol, a reaction that is catalyzed by the metalloenzyme benzene 1,2-dioxygenase.[3,4] The newly formed 1,2-diol then undergoes aromatization to catechol followed by oxidative ring cleavage aided by either an intra- or extradiol catechol dioxygenase.[5,6] The final ring-cleaved product can then be broken down further into intermediates for the citric acid cycle, ultimately allowing the microorganism to harness the pollutant in question as a source of energy as this overall process lends itself to the perpetuation of the global carbon cycle.[1]
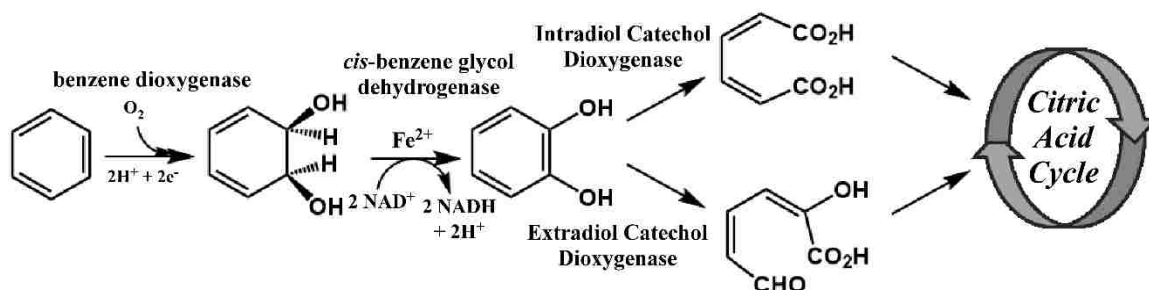
Figure 1.1. Catabolism of benzene via oxidation to catechol followed by oxidative ring cleavage.[5]

In order to overcome the intrinsic stability of aromatic compounds and the high activation barrier associated with reaction with triplet dioxygen, most ring-cleaving dioxygenases have been observed to simultaneously bind both O_2 and substrate to an Fe(II) site. Most ring-cleaving dioxygenases employ a recurring, anionic binding motif known as the 2-His-1-carboxylate facial triad (2H1C). Crystallographic studies of the resting state of ring-cleaving dioxygenases (Figure 1.2) have indicated the presence of a high spin Fe(II) center bound facially by two histidines and one glutamate (or aspartate) as well as 2-3 bound H_2O molecules.[6-12] Therefore, unlike heme-based systems, which leave a single coordination site open for a cofactor to bind, the 2H1C motif allows three additional coordination sites to remain vacant upon displacement of all solvent-derived ligands. This permits both dioxygen and substrate to bind directly to the ferrous center to facilitate the C-C bond cleavage reaction.
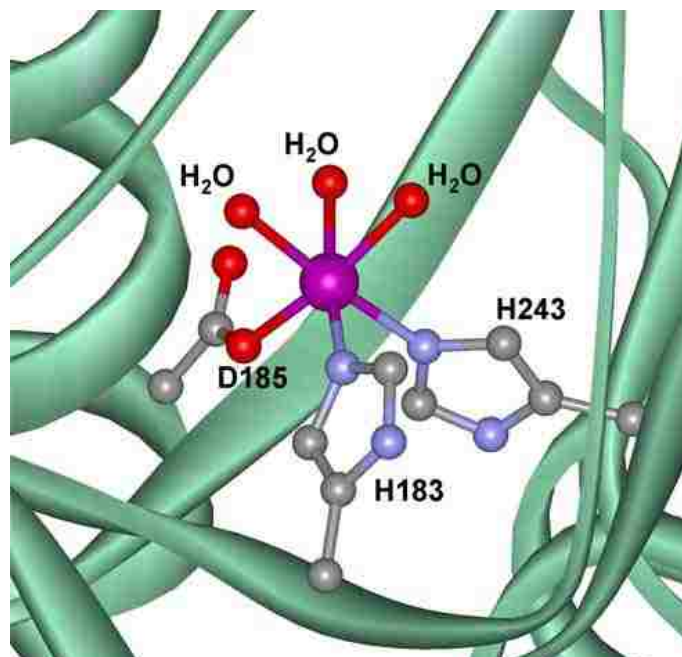
Figure 1.2. Resting state active site structure of deacetoxycephalosporin C synthase (DAOCS)—an α-ketoglutarate dependent mononuclear non-heme iron enzyme bound by the 2H1C facial triad.[7]

Non-heme iron dioxygenases are capable of oxidizing a variety of substrates (Figure 1.3) including catechols, protocatechuates,[13] hydroquinones,[14-16] *o*-aminophenols[17,18] and salicylates.[19-21] The most extensively and well-studied of these enzymes include a class referred to as the extradiol catechol dioxygenases (ECDOs). This class of enzymes is known for its ability to cleave aromatic substrates at a site adjacent to the hydroxyl groups, leading to formation of a ring-opened product.[9,11,22]
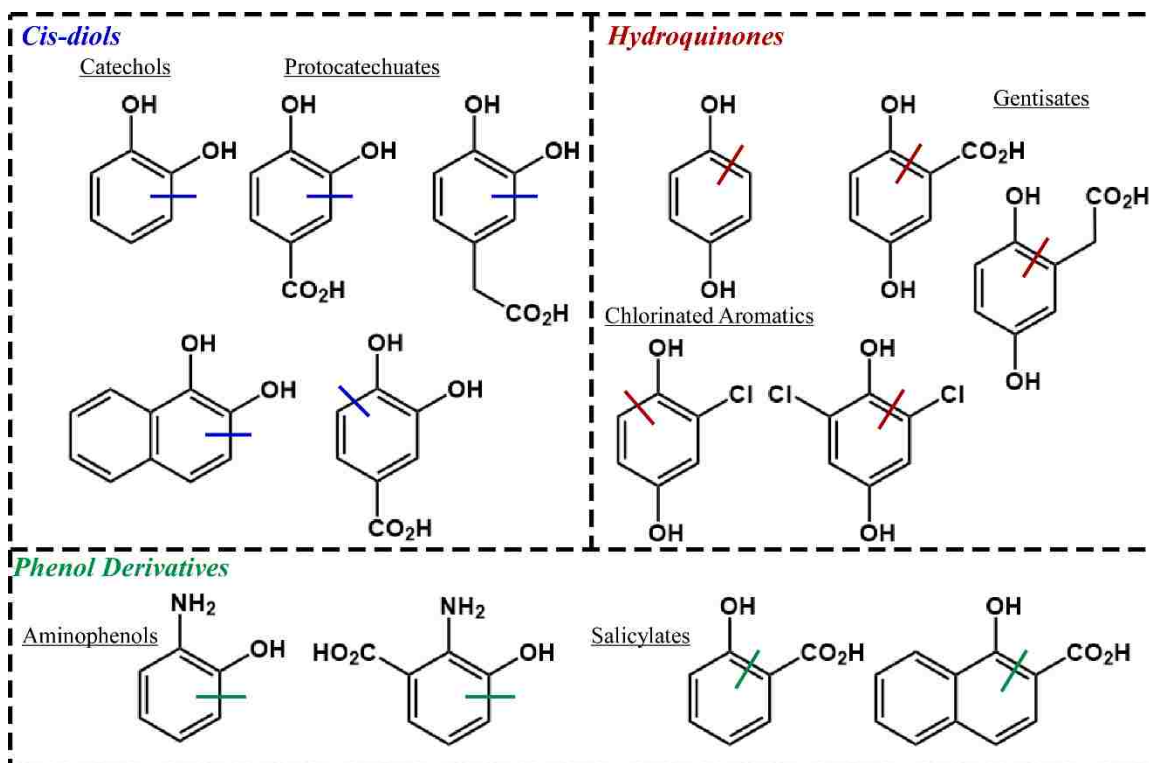
Figure 1.3. Various substrates that can undergo oxidative ring cleavage as facilitated by non-heme Fe dioxygenases. The solid lines indicate the site of C-C bond cleavage in each substrate.

1.B. Mechanism of Oxidative Ring Cleavage by Non-heme Iron Dioxygenases

The overall catalytic mechanism of extradiol catechol dioxygenases (ECDOs) has been studied extensively via experimental and computational means. It has been determined that upon loss of a proton, the first step of the mechanism involves coordination of the substrate to the metal center of the active site in its monoanionic form. The binding of a catechol in a bidentate manner causes the displacement of all bound solvent ligands, ultimately facilitating the binding of dioxygen in the vacant, sixth coordination site.[6,11,21,23] Upon binding of dioxygen, the Fe(II) center transfers an electron to the O_2 ligand, suggested to result in a short-lived Fe(III)-superoxo intermediate.

Formation of this fleeting species has been proposed to trigger a further electron transfer from bound catechol to the metal center. This step is proposed to generate an Fe(II)-bound o-semiquinone radical intermediate which would demonstrate the ability of the ferric center in coordinating a net electron transfer from the bound catechol to dioxygen, leading to activation of the O_2 radical.[11] The existence of this putative $SQ^{\cdot}$-Fe(II)-$O_2^{\cdot-}$ intermediate would require the deprotonation of the distal hydroxyl group by a second sphere residue. However, it is currently unknown if these catalytic events would occur in a stepwise or concerted manner. Regardless of the exact electronic identity of the activated intermediate, there is confidence that an Fe(II)-alkylperoxo intermediate is generated during the next step of the mechanism. This species would then undergo a Criegee rearrangement, followed by hydrolysis, to yield the final ring-opened product (Figure 1.4).[24] This proposed catalytic mechanism differs greatly from those of the cytochrome P450s,[25] methane monooxygenase[26] and α-ketoglutarate dependent oxygenases[27] which are proposed to generate a high-valent Fe(IV)-oxo intermediate in order to perform the energetically-demanding hydroxylation of an aliphatic substrate. Both previous experimental and computational work on the ECDOs has revealed that a high-valent iron-oxo intermediate is not generated during the catalytic process.[21,28-30]
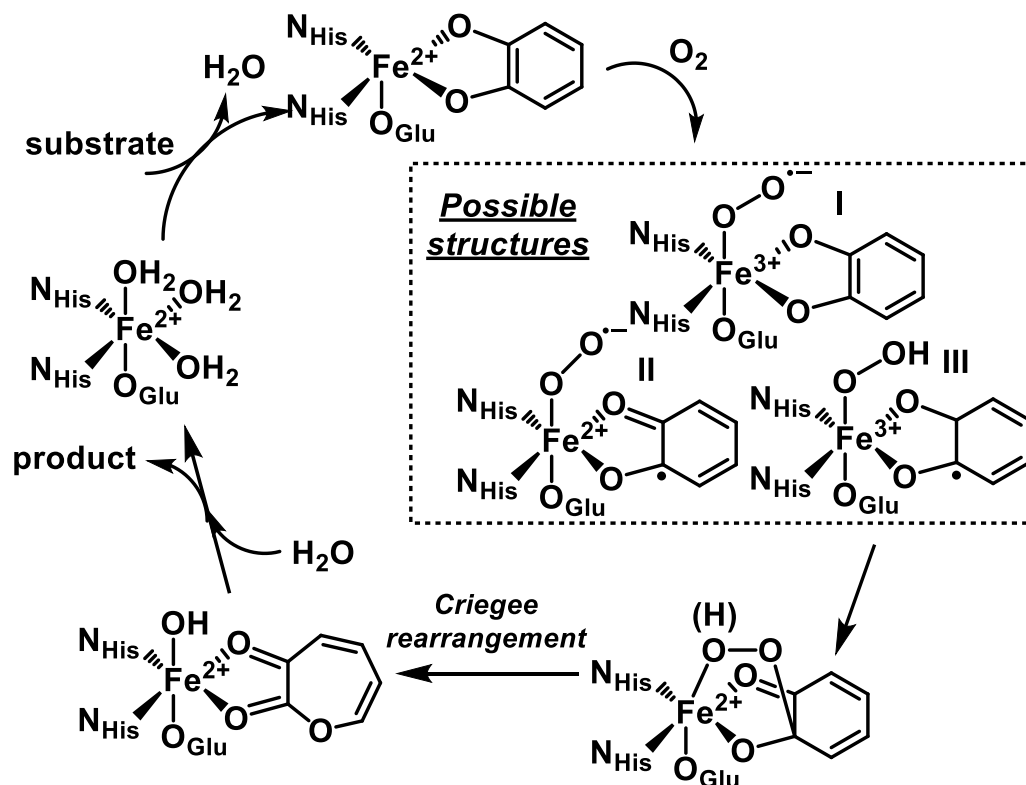
Figure 1.4. Proposed catalytic cycle of extradiol catechol dioxygenase.[24]

Despite the extensive work done toward the elucidation of the catalytic mechanism of the ECDOs, the exact electronic structure of the Fe-O_2-substrate adduct is still disputed in the literature. Work previously completed by Lipscomb[31] and Bugg[32] suggested that the catalytic mechanism proceeds through the putative semiquinone-iron(II)-superoxo species. This proposal was centered around the premise that the substrate in its semiquinone form could undergo facile radical coupling with the bound superoxo ligand, ultimately overcoming the kinetic barrier toward formation of a peroxy intermediate. Numerous studies confirmed the ability of catecholates to act in a "non-innocent" manner when bound to redox active metal centers, lending support for the proposed formation a bound semiquinone species.[33-35] Additionally, the catalytic cycle of the ECDO (2,3-dihydroxyphenyl)propionate 1,2-dioxygenase (MhpB) was investigated

using a cyclopropyl-based radical trap incorporated into a substrate analogue. These studies indicated the generation of a semiquinone-Fe(II)-superoxo species (**II**; <u>Figure 1.3</u>) during the progression of the catalytic cycle.[36] Further support for the generation of this species was provided by computational work completed by Siegbahn, who employed density functional theory (DFT) calculations.[37-39] The formation of this putative intermediate was further examined through a comparative study of two ECDOs, Fe-HPCD and Mn-MndD that incorporate iron and manganese, respectively.[40] Que, et al. examined the reactivity of both the native and the opposite metal-substituted states of HPCD and MndD, determining that both ECDOs remained equally catalytically active, despite the intrinsic difference in redox potentials between iron and manganese. These results lead to the proposal that the creation of a semiquinone-Fe(II)-superoxo intermediate would occur upon reduction of dioxygen via the donation of an electron from the bound catechol ligand, implying that the iron center acts strictly as a conduit for electron transfer between the ligands rather than directly undergoing a change in oxidation state.

Despite the wealth of evidence suggesting that the catalytic cycle of extradiol catechol dioxygenases proceeds through a $SQ^{\bullet-}$-Fe(II)-superoxo intermediate, recent studies have questioned the formation of this substrate-based radical during the mechanism of ring-cleavage. Until recently, studies detailing the isolation of Fe/O_2 adducts of ECDOs were nonexistent due to rapid reaction rates and the transient nature of catalytic intermediates. Lipscomb et al were successful in the isolation and spectroscopic characterization of an $Fe-O_2$ adduct of an HPCD (H200N) mutant.[41] H200 is proposed to be an important second sphere residue that participates in necessary acid/base reactions

during the catalytic cycle. Therefore, the H200N mutation was suggested to slow

catalytic activity to allow the observation of intermediates. This study was further

enhanced by the use of the "slow" substrate, 4-nitrocatechol, whose electron-withdrawing

nitro-group effectively reduces the amount of electron density localized on the aromatic

ring, further decreasing the rate of catalysis. The combination of these experimental

conditions allowed for the isolation of an intermediate with S=2, described as a Fe^{3+},

S=5/2 center antiferromagenetically coupled to a bound superoxide ($O_2^{\cdot-}$) radical, S=1/2

(**I**; Figure 1.3). Further experimental work involving the incorporation of the native

substrate into the H200N-HPCD mutant resulted in the observation of a novel

hydroperoxo-Fe(III)-semiquinone adduct (**III**; Figure 1.3) upon exposure to dioxygen.[42]

Despite the significant stability of a hydroperoxo-Fe(III)-semiquinone

intermediate, computational analysis by Ye and Neese concluded that this species

represents a thermodynamic sink that is not catalytically viable in the process of oxidative

ring-cleavage.[43] Additionally, this study found no evidence for the formation of a subsrate-

based radical during the ECDO catalytic mechanism. Instead, Ye and Neese favor a

mechanism in which a ferric-superoxo intermediate undergoes a direct conversion to a

bridged hydroperoxo-Fe(II) species. They suggest the kinetic barrier towards formation of

the hydroperoxo species is lowered by coupling with a concurrent proton transfer from a

second-sphere histidine residue to the proximal oxygen of the bound peroxo ligand.

In response to the doubt cast on the formation of a substrate-based radical, Dong

et al. conducted a QM/MM study focused on the O_2 activation step in the mechanism of

homoprotocatechuate 2,3-dioxygenase.[44] While they determined the presence of an

catechol-Fe(III)-$O_2^{\cdot-}$ species (Fe: S=5/2 antiferromagnetically coupled to $O_2^{\cdot-}$: S=1/2)

within the protein environment, they concluded that another semiquinone-Fe(II)-$O_2^{\cdot-}$ species (Fe(II)-SQ$^{\cdot}$ unit: S=5/2 antiferromagnetically coupled to $O_2^{\cdot-}$: S=1/2) was present as well. Interestingly, they suggested that the reactive oxygen species in the cycle could not be accurately represented solely by either of these electronic configurations. Instead they proposed the reactive species to be a hybrid state described as containing mixed character of Cat-Fe(III)-$O_2^{\cdot-}$/SQ$^{\cdot}$-Fe(II)-$O_2^{\cdot-}$ with a hydrogen bond shared between the proximal oxygen of O_2 and the H200 donor (Figure 1.5).
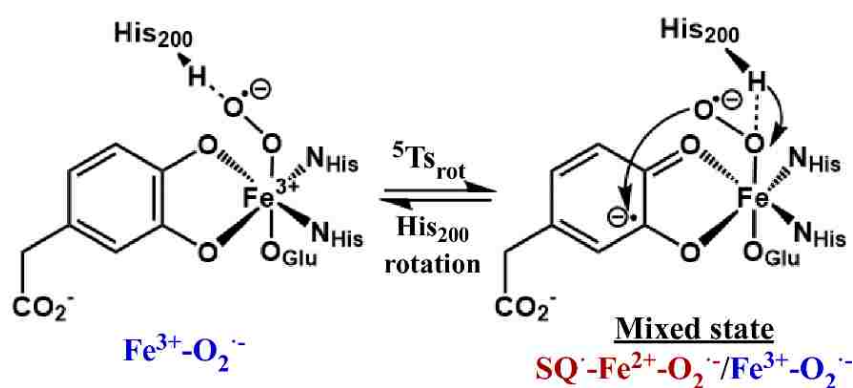
Figure 1.5. Proposed mixed state suggested to act as the reactive Fe-dioxygen adduct of HPCD, an EDCO, by Dong et al.[44]

As previously mentioned, the H200 residue of HPCD has been demonstrated to be essential for catalytic turnover. Dong et al. stress the importance of H200 in their study and suggest that a simple reorientation of the hydrogen bond initially donated to the substrate oxygen shifts to interact with the proximal oxygen atom of the Cat-Fe(III)-$O_2^{\cdot-}$ moiety, facilitating electronic rearrangement to the hybrid state.[44] They propose stabilization of the Fe(III)-$O_2^{\cdot-}$ species by H200 allows for the partial electron transfer

from the substrate to the O_2 ligand via the metal center, resulting in the catalytically-active species.

1.C. Hydroquinone Dioxygenases: A novel class of ring cleaving dioxygenases

Despite the numerous studies that have been conducted toward the elucidation of the catalytic mechanism of ECDOs, little work has been done in relevance to non-heme Fe-dioxygenases that oxidatively cleave substrates other than catechols, in particular, *p*-hydroquinones. Of the work that has been done, it is currently proposed that the oxidative mechanism of hydroquinone dioxygenases (HQDOs) closely follows the catalytic cycle previously proposed for the ECDOs (*vide supra*). However, it is clear that the native substrates for ECDOs and HQDOs are intrinsically different due to the positioning of their hydroxyl groups relative to one another. This observation leads to interesting mechanistic considerations. For example, the ortho substitution pattern of catechols allows for facile bidentate ligation of substrate to a Fe(II) center. Conversely, hydroquinones lacking a carboxylate functional group in an ortho position would be expected to bind in a monodentate manner through a phenolate donor, allowing an open coordination site to remain unoccupied. This significant difference in the mode of substrate binding could lead to differences in the overall mechanism of ring cleavage. Another important contrast between ECDOs and HQDOs is the difference in substrate specificity and enzyme inactivation. For example, the HQDO 2,6-dichlorohydroquinone 1,2-dioxygenase (PcpA) is involved in the degradation pathway of the toxic pollutant pentachlorophenol, by ultimately cleaving the pathway intermediate, 2,6-

dichlorohydroquinone (Figure 1.6). While the substrate does not contain an ortho –OH

group to allow bidentate chelation of the active site, it contains two chlorine substituents

in both positions ortho to the proximal hydroxyl group. Previous studies have determined

that chlorinated substrates tend to inactivate ECDOS,[45-49] yet this chlorinated molecule

acts as the native substrate for PcpA.[15]
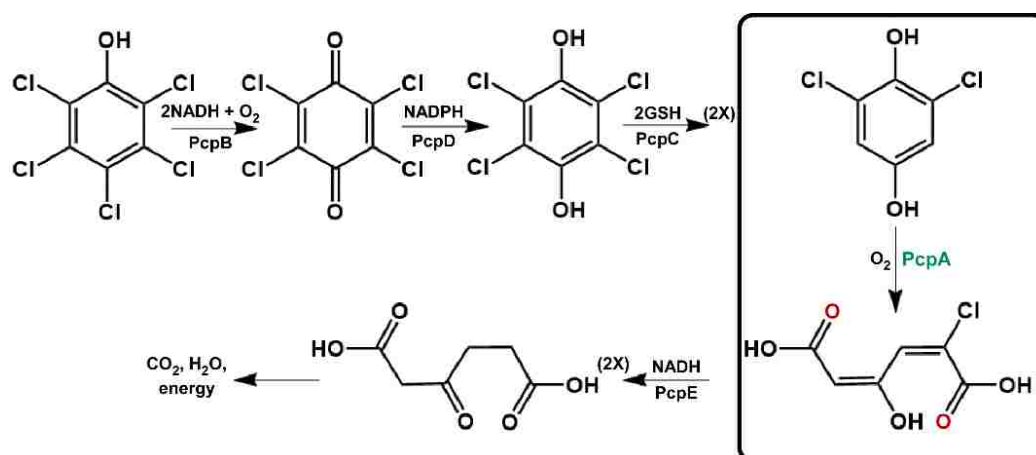
Figure 1.6. Pathway of catabolism for degradation of pentachlorophenol by 2.6-
dichlorohydroquinone 1,2-dioxygenase (PcpA).[15]

Despite a potential importance to bioremedial technologies, few studies of

hydroquinone dioxygenases have been conducted and only a few HQDOs have been

reported in literature.[14,50] These enzymes can be categorized into two classes based on the

types of substrates they incorporate into their active sites. The first class is characterized

by the ability of the enzyme to degrade hydroquinones with carboxylate donors *ortho* to

the phenolate donor, such as gentisate[14,50] and homogentisate[16,51] suggesting bidentate

coordination to an Fe(II) center.   The second class includes HQDOs that incorporate

halogenated or unsubstituted hydroquinone substrates, which coordinate in a monodentate fashion due to the absence of a metal-binding moiety at the ortho position. Some examples of these HQDOs include 2,6-dichlorohydroquinone 1,2-dioxygenase (PcpA),[15,52-54] chlorohydroquinone 1,2-dioxygenase (LinE)[55,56] and hydroquinone 1,2-dioxygenase (MnpC).[57]

As mentioned previously, the mechanism of hydroquinone dioxygenases has been proposed to mirror that of the ECDOs. Jeoung, et al. sought to corroborate this assertion in their study of trapped reaction intermediates of the enzyme homogentisate 1,2-dioxygenase (HGDO) *in crystallo*.[58] Crystallographic studies of the resting state of HGDO revealed an Fe(II) center bound by a 2H1C motif, with the carboxylate donor bound as a bidentate ligand, the six-coordinate site being completed by two water molecules. Upon substrate binding in anaerobic conditions, the phenolate donor of the singly deprotonated homogentisate (HG) binds in a monodentate fashion upon displacement of one molecule of H_2O. This observation is interesting to note as it is surprising carboxylate moiety of the substrate does not participate in a binding interaction with the metal center as previously predicted. X-ray analysis indicates that the distal hydroxyl group shares a H-bond with a second sphere histidine residue, H288, which is likely to be involved in acid/base reactions during the catalytic cycle (Figure 1.7).
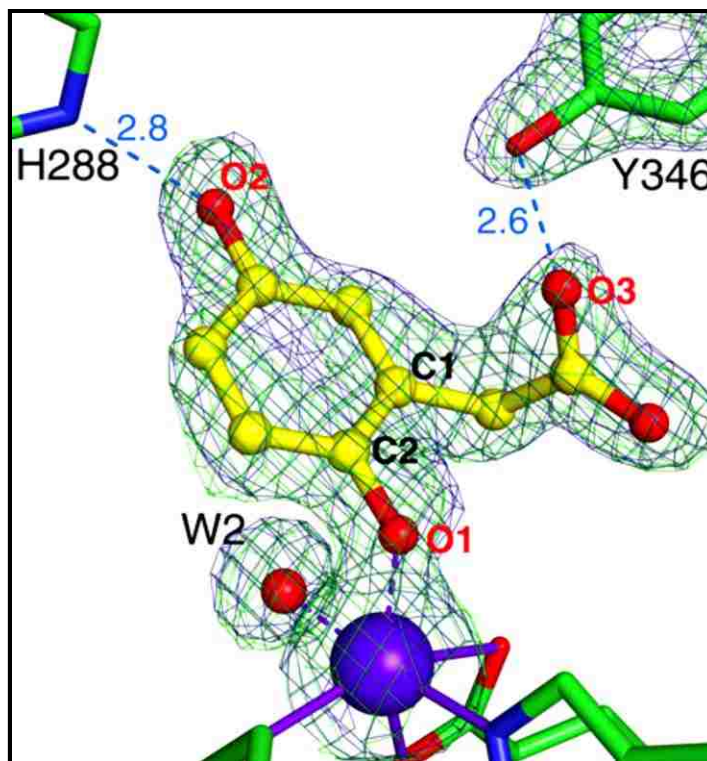
Figure 1.7. Active site structure of substrate-bound HGDO. Possible hydrogen–bonding interactions are shown as dashed lines with distances given in angstroms.[58]

In order to study reaction intermediates of the process, Jeoung, et al. grew crystals of HGDO in an anaerobic environment, exposed them to air and rapidly cooled them in liquid nitrogen to trap three distinct species in one crystal. The first observed intermediate represents the species formed immediately upon O_2 binding. Further investigation of this species revealed asymmetric, side-on binding of dioxygen to an Fe(II) center bound to a semiquinone ring. The radical state of the substrate was determined by a distinct puckering of the ligand at $C2_{HG}$, compared to its initial planar conformation. This putative species would require the deprotonation of the distal –OH group by H288, allowing formation of a semiquinone radical. This proposed $SQ^{\cdot}\text{-}Fe(II)\text{-}O_2^{\cdot\text{-}}$ intermediate, as visualized by x-ray crystallography, is strikingly similar to reaction intermediates

proposed for the ECDOs and lends additional support for the formation of a substrate-based radical in the mechanism of a ring-cleaving dioxygenase (Figure 1.8).
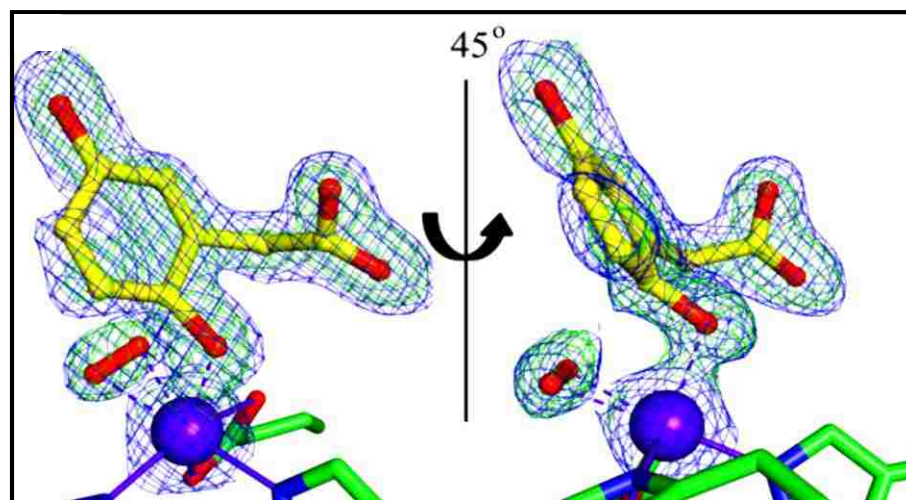
Figure 1.8. Reaction intermediate of HGDO trapped and characterized by Jeoung et al. This structure represents the semiquinone state of HG, visualized by puckering of ring at C2, upon side-on binding of dioxygen.[58]

The second observed intermediate is described as an alkylperoxo species, based on the short distance observed between $O1_{O2}$ and $C2_{HG}$, indicating a formation of a new bond to generate the bridged species. The final trapped intermediate displays a break in electron density between $C1_{HG}$ and $C2_{HG}$, signifying cleavage of the C-C bond to give the final maleylacetoacetate product. The complete proposed catalytic mechanism for the oxidative ring cleavage of HGDO as elucidated by Jeong et al. is presented in Figure 1.9.
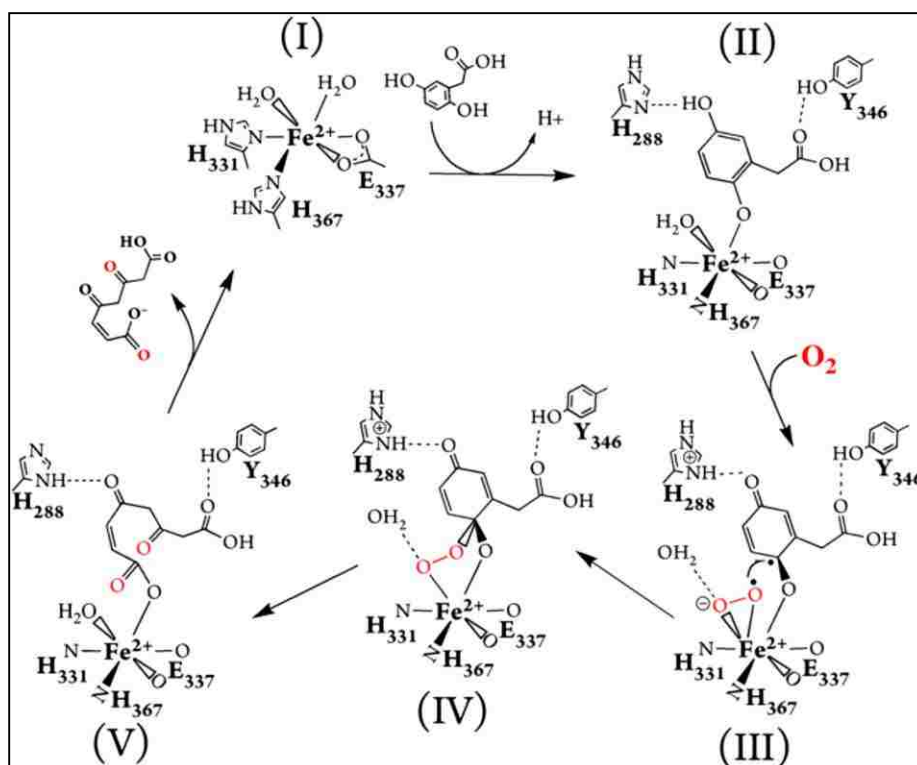
Figure 1.9. Overall mechanism of homogentisate 1,2-dioxygenase (HGDO) proposed by Jeong et al.[58]

Previous to the aforementioned study, computational work utilizing hybrid DFT methods was employed to study the mechanism of HGDOs; however, crystal structure data of the enzyme with bound substrate was not yet available.[59] In the absence of this data, Lipscomb, et al. operated under the assumption that homogentisate would bind in a bidentate fashion. Because the starting geometry of the enzyme is not a faithful model of the enzyme-substrate complex of HGDO, the study predicted end-on binding of dioxygen as well as the formation of the alkylperoxo species at $C1_{HG}$, bearing the 1-acetate group, rather than at $C2_{HG}$. As mentioned previously, it is interesting to note that *in vivo* HG binds in a monodentate fashion versus the bidentate mode predicted by Lipscomb.

Despite the lack of additional computational work to support the experimentally assigned intermediates of HGDO, the current results do not agree with recent studies of HPCD with 4-nitrocatechol (*vide supra*). This could be due to the fact that HGDO and HPCD bear little sequence and structural similarity to one another. For example, HGDO was been shown to bind its para- substituted HQ substrate in a monodentate fashion, whereas HPCD binds ortho substituted catechols in a bidentate manner. Another interesting difference manifests itself in the stabilization of superoxo intermediates by hydrogen bonds within the active enzyme. The proposed $Fe(II)-O_2^{\cdot-}$ intermediate of HPCD is shown to be stabilized by a network of H-bonds donated from second sphere residues, however this same occurrence is not observed in the formation of the Fe(II)-superoxo intermediate of HGDO. Instead, the only candidates for donation of stabilizing H-bonds are the residual water molecules present in the active site, which were previously displaced upon substrate and dioxygen binding. However, despite structural differences in these nonhomologous Fe(II)-dependent dioxygenases, the ability of these enzymes to catalyze cleavage of aromatic rings is suggested to be an intrinsic characteristic of the 2H1C facial triad.

Despite the widespread utilization of the canonical 2H1C motif by metalloenzymes to facilitate dioxygenases chemistry, it is interesting to note that two crystal structures of cysteine dioxygenase were reported in 2006 which indicated the presence of a mononuclear iron site supported by a neutral 3His facial triad.[60,61] Subsequently, several additional metalloenzymes incorporating this 3His motif were structurally characterized and reported including, β-diketone dioxygenase (Dke1),[62,63] salicylate dioxygenase (SDO)[19] and most interestingly, gentisate 1,2-dioxygenase

(GDO),[50,64] a member of the hydroquinone dioxygenases. While it is apparent that GDO catalyzes a similar C-C bond cleavage reaction as demonstrated by the HQDOs incorporating the 2H1C triad, the catalytic implications of this difference in charge remains unclear.

1.D. Biomimetic Models of Non-heme Iron Dioxygenases

The study of metalloenzymes has been greatly augmented by the development of synthetic models that aim to mimic the important structural and functional characteristics displayed by enzymatic active sites in nature. While many biomimetic models of the catechol dioxygenases exist, there is a lack of modeling studies in relevance to the hydroquinone dioxygenases. It has been suggested that the scarcity of characterized Fe(II)-hydroquinonate complexes in literature is due to the intrinsic ability of hydroquinones to bridge two metal centers and form dimeric species. This has been demonstrated previously in the synthesis of ferric complexes supported by salen and porphyrin ligands that are bridged by dianionic hydroquinonate ligands (Figure 1.10).[65-67]
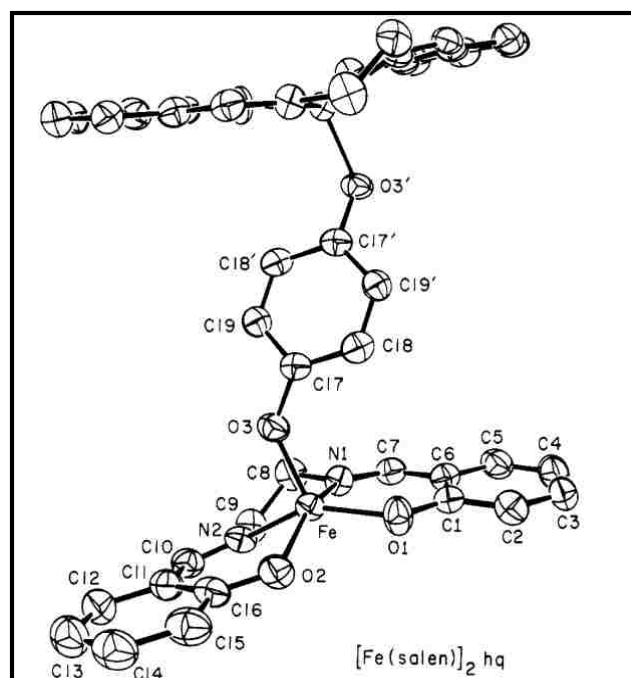
Figure 1.10. Crystal structure obtained by Que et al of a diferric–salen complex bridged by a hydroquinone ligand.[65]

In order to avoid the formation of a dimeric species, Holland and Machonkin recently developed a series of Fe(II)-phenolate complexes using the 1,3,5-tris-(tolylideneimino)cyclohexane (TACN-*o*-tolyl) ligand.[68] While these models lack a hydroxyl group at the para position and are therefore poor functional models, they were relatively effective structural models, used to study the substrate specificity of HQDOs by varying phenolate ligands. Characterization by ^{1}H-NMR determined that only phenolate ligands halogenated at the ortho position(s), such as 2-chlorophenol and 2,6-dichlorohydroquinone, were able to form a 1:1:1 (TACN-*o*-tolyl)-Fe(II)-phenolate complex with complete binding of the respective phenolate to the ferrous center. The authors attribute this observation to a proposed secondary binding interaction between

Fe(II) and the halogen substituent (X) by analyzing the experimentally-determined Fe-X

bond lengths by X-ray crystallography (<u>Figure 1.11</u>).
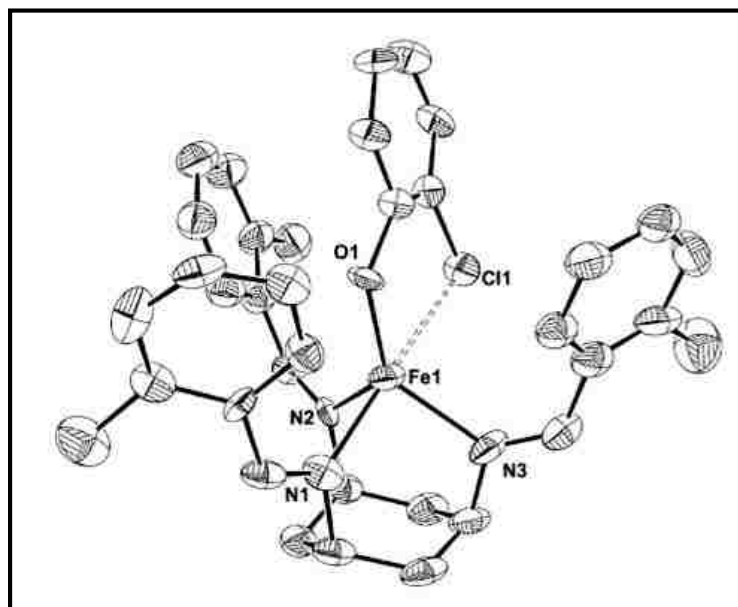
Figure 1.11. Solid state structure of [Fe(TACH-*o*-tolyl)(2-chlorophenolate)]OTf. The dashed line indicates the secondary Fe-Cl interaction, stabilizing the bound ligand. Hydrogen atoms and triflate anions have been omitted for clarity.[68]

Although this particular series of experiments did not lend itself to a better

understanding of the catalytic mechanism of HQDOs, it did allow for the rationalization

of substrate specificity of hydroquinone dioxygenases versus other ring cleaving

dioxygenases. In addition to the series of phenolate complexes described above, Holland

and Machonkin also synthesized a mononuclear Fe(II)-2-methylhydroquinone complex

supported by the TACN-o-tolyl ligand. Its formation was confirmed by ^{1}H-NMR

analysis, however, due to the great instability of the complex, crystals of the (TACN-*o*-

tolyl) were not obtained.

1.E. Use of bridging dioxolene ligands to facilitate magnetic superexchange

In addition to the biological relevance of the rich redox behavior of benzoquinoid ligands, particularly di- and tetraoxolene moieties, recent interest has been focused on exploiting this characteristic in the development of novel magnetic materials. The integration of radical ligand bridges between paramagnetic metal centers has been observed to increase not only the observed molecular spin state, but also the magnitude of magnetic exchange coupling between metals leading to the observation of single molecule magnet (SMM) behavior.[69-71] SMMs are compounds that exhibit magnetic hysteresis at low temperatures derived purely from the molecule itself, and not from long-range magnetic ordering. The inherent slow relaxation of magnetization of a small molecule magnet makes this novel class of materials perfect candidates for future applications in molecular spintronics and quantum information storage and processing.[72-75]

SMM behavior was first reported by Sessoli, et al. upon generation of a high spin [$Mn_{12}O_{12}(O_2CMe)_{16}(H_2O)_4$] cluster compound that displays a high degree of magnetic coupling and an overall spin state of $S = 10$.[76] Because of the success of this cage compound in mediating significant magnetic exchange, much of the effort devoted to the development of SMMs has been focused on the preparation of polynuclear complexes with large predicted spin states. Due to the synthetic challenges in preparing species high in nuclearity and the widespread use of diamagnetic bridging ligands in SMM targets, despite their inability to facilitate strong magnetic exchange, developments in the

generation of species incorporating radical ligands linking paramagnetic centers in low nuclearity complexes is of great recent interest.[77-79]

1.F. Project Objectives

Prior to our efforts, there was no report of a crystallographically characterized Fe(II) complex bound by a *p*-hydroquinonate ligand. The lack of synthetic prospects was due not only to the tendency of HQates to bridge metal centers, but also to the expectation that a faithful HQDO mimic would be 4C prior to binding of dioxygen. This would leave Fe(II) coordinatively unsaturated in the absence of a coordinating solvent ligand.

Due to the difficulty faced in generation of stable Fe(II)-HQate complexes, up to this point, functional HQDO models have not yet been developed. The main focus of this project involved the development of these models in order to gain a better understanding of the electronic nature of catalytic intermediates to further elucidate the mechanism of ring cleavage carried out by hydroquinone dioxygenases. We opted to use biomimetic models in order to gain insight into the catalytic mechanism of the hydroquinone dioxygenases as it is possible to modify the properties of our model complexes in a straightforward and systematic manner. By employing this methodical approach, we are able to gain a better understanding of factors affecting the electronic structure and reactivity of catalytic intermediates. Although similar changes can be made through point mutations made to protein active sites, such alterations can lead to significant changes in the enzyme, ultimately leading to inactivation. Instead, biomimetic studies allow for the

flexibility of studying a series of complexes with an extensive variety of geometric and electronic properties. In addition, while it is difficult to isolate and characterize catalytic intermediates within metalloenzymes, the creation of synthetic analogues allows for control over ligand properties and reaction conditions to trap and examine these elusive species.

In order to further our understanding of the catalytic mechanism of oxidative ring cleavage carried out by hydroquinone dioxygenases, we employed an integrated approach through a combination of synthetic methods, structural and spectroscopic characterization and computational analysis. Through use of this systematic process, we have laid the basis for further mechanistic studies of hydroquinone dioxygenases and the exploration of electronic communication between metal centers and paramagnetic (radical) ligands, similar to those observed in nature. The remaining chapters of this report will discuss the following results:

- Chapter 2: Herein, we report the preparation of mono- and dinuclear Fe(II) complexes with the (3,5-diphenylpyrazol-1-yl)borate(1-) supporting ligand (^{Ph2}Tp) and the investigation of the O_2 reactivity of several Fe(II)-HQate complexes. Notably, we were successful in the generation of the first crystallographically-characterized mononuclear Fe(II) complex featuring an untethered hydroquinonate ligand.

- Chapter 3: In order to gain insight into the variance of neutral and anionic binding motifs observed in the HQDOs, we developed a biomimetic model of the ES-complex of gentisate dioxygenase (GDO) which features a neutral scorpionate ligand and the monoanion of 2-(1-methylbenzimidazol-2-yl)hydroquinone. The

reactivity of this complex was compared to a previously synthesized HQDO model (as reported in <u>Chapter 2</u>). Oxidation of each species yielded the corresponding Fe(III) complexes that can undergo deprotonation, triggering a (de)protonation-induced valence tautomerization to yield two Fe(II)-*p*SQ species as proven by detailed spectroscopic and computational analysis.

- <u>Chapter 4</u>: The dioxygen reactivity of several Fe(II)-hydroquinonate complexes was studied in order to evaluate their viability as functional models of the enzyme-substrate complex of the hydroquinone dioxygenases.

- <u>Chapter 5</u>: The structure and reactivity of a new series of Fe(II) complexes featuring substituted 1,4-naphthoquinone ligands is reported. Two metastable mononuclear iron (II) *p*-semiquinonate complexes were generated upon treatment with an appropriate chemical reductant. Existence of a coordinated *p*SQ$^{\cdot-}$ radical in each complex was confirmed via detailed spectroscopic and computational analysis. To the best of our knowledge, these species represent the first reported examples of mononuclear Fe(II) complexes featuring *p*SQ$^{\cdot-}$ ligands.

- <u>Chapter 6</u>: The synthesis of a dinuclear Fe(II)-HQate bridged complex that incorporates a bound semiquinone radical upon one electron oxidation is reported. The complex was structurally characterized via X-ray crystallography and its electronic structure was probed via spectroscopic (absorption, EPR and resonance Raman) and computational methods. To the best of our knowledge, this complex represents the first crystallographically-characterized complex to feature ferrous centers bound to a semiquinone radical.

- Chapter 7: The syntheses of a variety of (hydro)quinonate-bridged dimetal(II) complexes are reported. The structure and reactivity of a dimanganese(II) analog is compared to that of the complex reported in Chapter 5. Additional species containing varying (hydro)quinonate ligands are explored.

Chapter 2

Structural, Spectroscopic and Electrochemical Properties of Non-heme Fe(II)—Hydroquinonate Complexes: Synthetic Models of Hydroquinone Dioxygenases
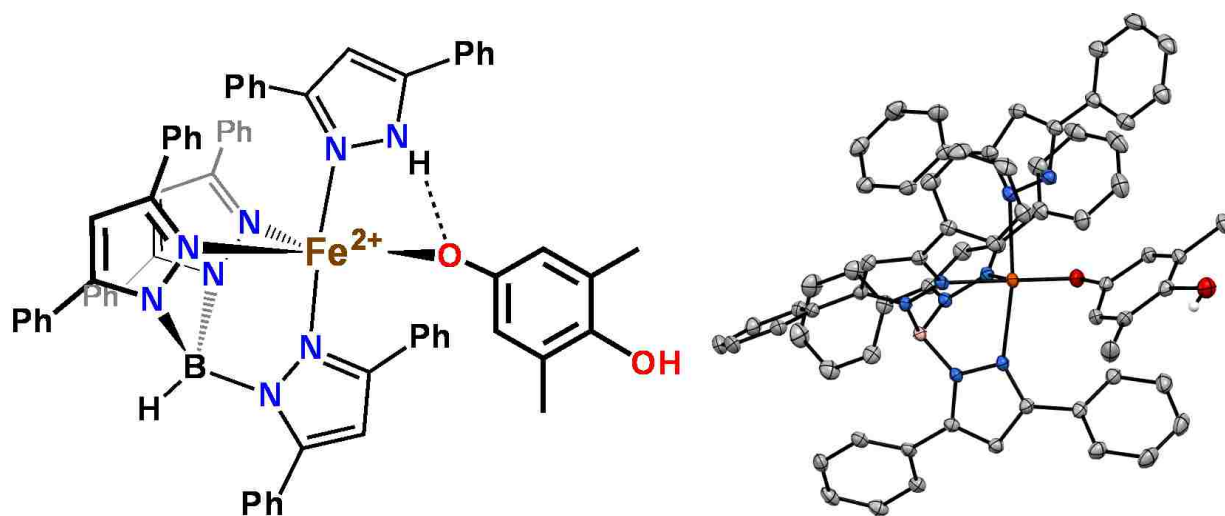
Abstract: Using the tris(3,5-diphenylpyrazol-1-yl)borate (^{Ph2}Tp) supporting ligand, a series of mono- and dinuclear ferrous complexes containing hydroquinonate (HQate) ligands have been prepared and structurally characterized. The monoiron(II) complexes serve as faithful mimics of the substrate-bound form of hydroquinone dioxygenases (HQDOs). Additionally, the formation of the first crystallographically-characterized example of a monoiron complex bound to an untethered HQate ligand is reported. The geometric and electronic structures of the Fe/HQate complexes were further probed with spectroscopic (UV-vis absorption, ^{1}H NMR) and electrochemical methods.

2.A. Introduction

The degradation and assimilation of single ring and polycyclic aromatic hydrocarbons by bacteria represents a key component of the global carbon cycle and the basis of bioremediation technologies. In aerobic environments, the catabolism of aromatic compounds is dependent on non-heme iron dioxygenases that cleave aromatic rings with incorporation of both atoms of O_2 into the product.[80-82] Such transformations are challenging due to the intrinsic stability of aromatic systems and the high activation barrier to reaction with triplet dioxygen. With the notable exception of the intradiol catechol dioxygenases, the active sites of ring-cleaving dioxygenases overcome these obstacles by coordinating both substrate and O_2 to a single Fe(II) site.[6,83] The iron center is typically supported by a facial array of one carboxylate (Asp or Glu) and two His residues (Figure 2.1),[7] although variants of this 2-His-1-carboxylate motif (e.g. the 3 His facial triad exhibited by gentisate 1,2-dioxygenase) have recently been reported.[63,84]
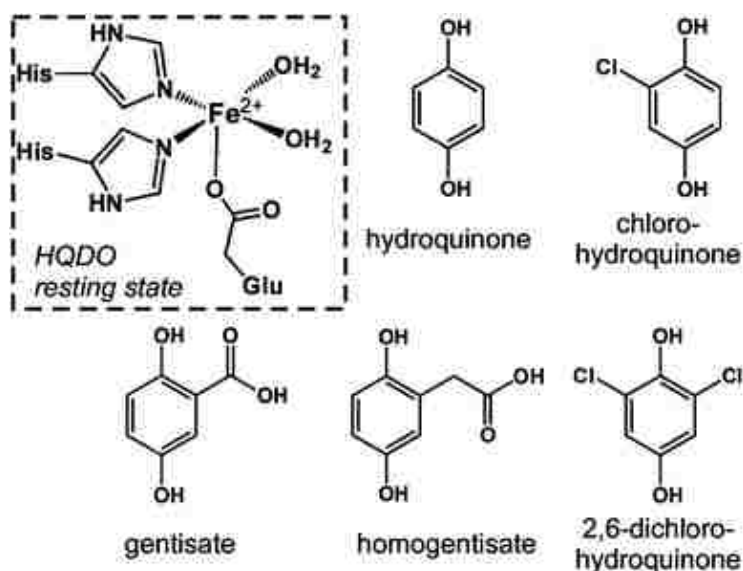
Figure 2.1. Schematic of the resting state of the hydroquinone dioxygenases pictured with various substrates degraded by hydroquinone dioxygenases.

While the well-studied extradiol catechol dioxygenases (ECDOs) are the prototypical ring-cleaving dioxygenases,[6,22,30,38,83,85-86] members of this enzymatic family employ a remarkable variety of substrates, including protocatechuates,[13] 2-aminophenols,[17,18,28] and salicylates.[19-21] Of particular relevance to this document are dioxygenases that cleave hydroquinones (HQs = 1,4-dihydroxybenzene and its derivatives). The HQ-cleaving dioxygenases (HQDOs) can be grouped into two categories. The first class oxidizes substrates with carboxylate groups at the 2-position of the aromatic ring, namely, gentisate[14,50] and homogentisate[16,51] (2,5-dihydroxybenzoate and 2,5-dihydroxyphenylacetate, respectively; Figure 2.1). In these enzymes, the substrate likely binds to iron in a bidentate manner via the phenolate and carboxylate donors.[87] In the second class, the substrate coordinates in a monodentate fashion, due to the lack of a metal binding moiety at the ortho position of the substrate. Examples include

2,6-dichlorohydroquinone 1,2-dioxygenase (PcpA),[52-54,88] chlorohydroquinone dioxygenase (LinE),[55,56] and hydroquinone 1,2-dioxygenase (MnpC).[57]

While there have been few mechanistic studies of the hydroquinone 1,2-dioxygenases, the proposed catalytic cycles largely follow the pattern derived from extensive studies of the ECDOs.[52] Coordination of the monoanionic HQ substrate to the Fe(II) center displaces some or all of the H_2O ligands present in the resting state (Figure 2.1), thereby facilitating O_2 binding to the iron center. Upon activation of dioxygen, the generation of a transient ferric-superoxo intermediate is thought to trigger the transfer of one electron from the substrate ligand to the iron center, resulting in a bound *p*-benzosemiquinone radical. The existence of this putative intermediate would likely require deprotonation of the distal –OH group by a second-sphere residue, although at this time it is unknown if these events (O_2 coordination, electron transfer and proton transfer) would occur in a stepwise or concerted manner. The degree of semiquinone character on the substrate ligand in the O_2-bound form of the enzyme is also uncertain; for instance, a recent computational study by Ye and Neese[43] has cast doubt on the existence of a superoxo-Fe(II)-semiquinone intermediate in the ECDO (and, by extension, the HQDO) mechanism. While the nature of this intermediate remains disputed, it is well-established that the next step of the catalytic cycle involves generation of an Fe(II)-alkylperoxo species, which undergoes a Criegee rearrangement and hydrolysis to eventually yield the ring-opened product.[12,43,89]

Unanswered questions regarding the HQDOs can be answered, in part, through the development of synthetic complexes that replicate the structure and/or function of the enzyme-substrate complex. Remarkably, a survey of the literature found only a single

example of a crystallographically-characterized monoiron(II)–hydroquinonate complex: Fe(L)$_2$, where is L is a deprotonated Schiff base of 2,5-dihydroxybenzaldehyde.[90] The lack of reported Fe/HQ complexes is partly due to the ability of hydroquinonate (HQate) ligands to adopt a bridging position between metal centers, as demonstrated by structures of diiron(III)–porphyrin and –salen complexes with bridging HQate dianions.[65-67] Recently, Machonkin and Holland described the formation and ^{1}H NMR characterization of a mononuclear iron(II)–2-methylhydroquinonate complex supported by the 1,3,5-tris(tolylideneimino)cyclohexane ligand;[68] however, this species is unstable and it was not possible to obtain crystals suitable for crystallographic analysis.

In this chapter, we report the synthesis and X-ray structural characterization of several monoiron(II) complexes containing HQate ligands. Each complex features the tris(3,5-diphenylpyrazol-1-yl)borate(1-) supporting ligand (^{Ph2}Tp), as substituted Tp ligands are well-known to faithfully mimic the coordination environment of the 2-His-1-carboxylate facial triad.[91,92] We found that inclusion of bulky phenyl groups at the 3-positions of the pyrazole rings generally discourages formation of the diiron(II) μ-hydroquinonate(2-) complexes, although dinuclear species were generated with certain HQs. As shown in Figure 2.2, two types of HQ ligands were employed in this study: (i) bidentate (or "tethered") ligands that feature an ortho substituent capable of metal coordination (H$_2$L$^{1-5}$), and (ii) the monodentate (or "untethered") ligand 2,6-dimethylhydroquinone (H$_2$L^6). These HQs were selected because they reflect the range of substrates oxidized by HQDOs, with the monodentate and bidentate ligands resembling (homo)gentisates and (chloro)hydroquinones, respectively. The ligand series also includes 2-hydroxyacetophenone (H$_2$L^3) as a control to properly evaluate the role of the

distal –OH group in tuning the structural and electronic properties of our HQDO models. Each of the resulting complexes was characterized with crystallographic, spectroscopic (UV-vis absorption, ^{1}H NMR), and electrochemical techniques. Indeed, we report here the first X-ray structure of a mononuclear Fe complex featuring an untethered hydroquinonate ligand. We also employed spectroscopic methods, including electron paramagnetic resonance (EPR), to examine the ferric species generated upon one-electron oxidation of the monoiron(II) complexes. These results lay the foundation for future studies that will explore the O_2 reactivity of complexes that mimic the enzyme-substrate intermediates of HQDOs.

Complexes 1-4 and 6 = [Fe(^{Ph2}Tp)(HL$^{1-4,6}$)]
Complexes 5 and 7 = [Fe$_2$(^{Ph2}Tp)$_2$(μ-L^{5,7})]
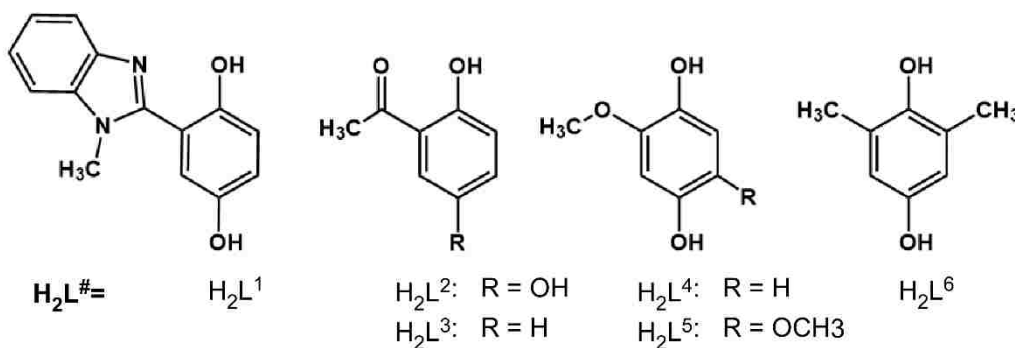
Figure 2.2. Hydroquinonate ligands utilized in this study. The use of both bidentate and monodentate ligands is intended to model the two substrate binding modes as observed in nature.

2.B. Results and Discussion

2.B.i. Fe(II) complexes with tethered hydroquinonate ligands

The mononuclear iron(II) complexes **1-4** (Figure 2.2) were prepared by mixing equimolar amounts of K(^{Ph2}Tp) and FeX$_2$ (X = Cl or OTf) with the corresponding singly-deprotonated ligands, in MeCN (or MeCN–CH$_2$Cl$_2$ solvent mixture). The resulting air-sensitive complexes dissolve easily in CH$_2$Cl$_2$, but are largely insoluble in more polar solvents like MeCN and MeOH. With the exception of **3**, which contains a 2-acetylphenolate ligand, the FTIR spectrum of each complex exhibits a ν(O–H) feature arising from the distal hydroxyl group, indicating that the HQ ligands are monoanionic and coordinated to a single Fe center.

Crystals of **1-4** suitable for X-ray structure determination were obtained by layering concentrated CH$_2$Cl$_2$ solutions with either MeCN or pentane. Details concerning data collection and analysis are provided in Table 2.4, and selected bond distances and angles for **1-4** are shown in Table 2.1. As illustrated in Figure 2.3, each complex features a five-coordinate (5C) Fe(II) center bound to a facially coordinating ^{Ph2}Tp ligand and bidentate HQate ligand. The Fe–N$_{Tp}$ bonds exhibit an average distance of 2.14 Å across the series, characteristic of high-spin (S = 2) ferrous complexes.[93-95] The Fe1–O1 distances, which range between 1.927(1) and 1.961(1) Å, are also typical for iron(II)–phenolate units in 5C complexes.[96,97]
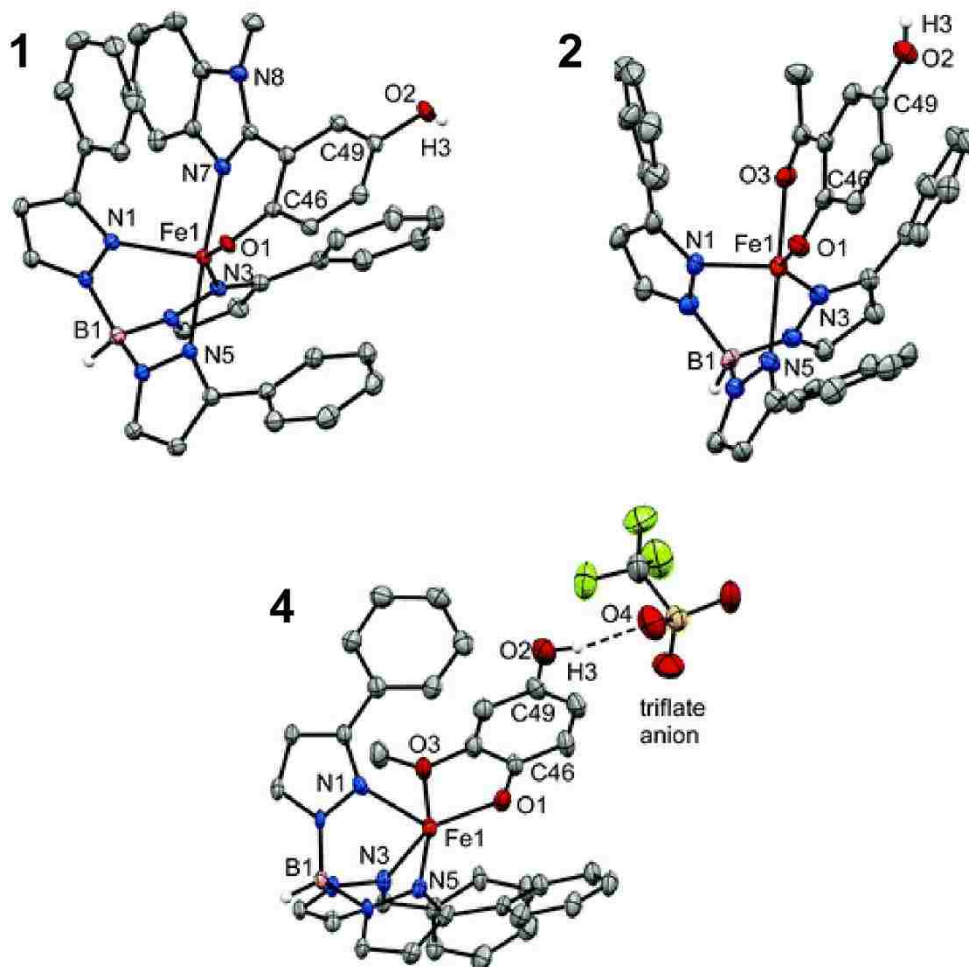
Figure 2.3. Thermal ellipsoid plots (50% probability) derived from the X-ray structures of **1**·CH$_2$Cl$_2$ (top), **2**·2CH$_2$Cl$_2$ (middle), and **4**·[HNEt$_3$]OTf (bottom). Non-coordinating solvent molecules and most hydrogen atoms have been omitted for clarity, as well as the Ph-rings at the 5-positions of the ^{Ph2}Tp ligand. The HNEt$_3^+$ counter cation in the **4**·[HNEt$_3$]OTf structure is not shown.

Table 2.1. Selected bond distances (Å) and bond angles (°) from the X-ray structures of monoiron(II) hydroquinonate complexes **1-4** and **6**.

	1·CH₂Cl₂	**2·2CH₂Cl₂**	**3**	**4·[HNEt₃]OTf**	**6**
Fe–O1	1.961(1)	1.937(4)	1.927(1)	1.931(3)	1.893(1)
Fe–N1	2.122(1)	2.131(5)	2.108(1)	2.130(4)	2.085(1)
Fe–N3	2.148(2)	2.089(5)	2.093(1)	2.129(4)	2.085(1)
Fe–N5	2.147(2)	2.185(5)	2.228(1)	2.186(4)	2.285(1)
Fe–L[a]	2.139(2)	2.079(4)	2.103(1)	2.317(3)	2.341(2)
O1–C46	1.341(2)	1.303(7)	1.304(2)	1.337(6)	1.338(2)
O2–C49	1.370(2)	1.370(7)		1.371(6)	1.390(2)
O1–Fe–N1	110.64(5)	129.5(2)	128.04(5)	128.5(2)	134.21(6)
O1–Fe–N3	153.34(5)	139.9(2)	140.01(5)	130.0(2)	131.98(6)
O1–Fe–N5	94.78(5)	97.9(2)	100.61(4)	115.6(1)	101.45(5)
O1–Fe–Lₓ	88.90(5)	86.4(2)	85.28(4)	75.7(1)	89.04(5)
N1–Fe–N3	95.65(6)	90.6(2)	91.50(4)	94.2(1)	93.61(5)
N1–Fe–N5	92.11(5)	90.2(2)	88.25(4)	89.4(2)	85.41(5)
N3–Fe–N5	79.38(6)	81.2(2)	84.39(4)	85.6(2)	83.65(5)
Lₓ–Fe–N1	90.69(6)	87.4(2)	91.32(4)	85.3(1)	89.01(5)
Lₓ–Fe–N3	95.37(6)	95.3(2)	88.47(4)	84.5(1)	87.53(5)
Lₓ–Fe–N5	174.27(6)	175.7(2)	172.83(4)	168.4(1)	169.24(5)
τ–value[b]	0.35	0.60	0.55	0.64	0.58

[a] L is the N or O atom of the pendant donor of the HQ anion. [b] For a definition of the τ-value, see ref [98]. A five-coordinate complex with ideal square-pyramidal geometry would have a τ-value of 0.0, while those with ideal trigonal bipyramidal geometry would have a value of 1.0.

The coordination geometry of **1** is intermediate between square pyramidal and trigonal bipyramidal ($\tau = 0.35^{98}$), and the BIHQ ligand adopts a twisted conformation with a dihedral angle of 35° between the planes of the HQate and benzimidazolyl rings (<u>Figure 2.3</u>). This orientation is likely the result of π-stacking interactions between the benzimidazolyl moiety and a 3-phenyl substituent of the ^{Ph2}Tp ligand, in addition to steric repulsion between the HQate ring and a second phenyl group. Compared to **1**, the structures of **2** and **3** lie much further towards the trigonal-bipyramidal limit ($\tau = 0.60$ and 0.55, respectively) with the acetyl group in an axial position trans to a pyrazole donor (N5). The metric parameters for **2** and **3** are nearly identical, suggesting that the structural effects of the para hydroxyl group are minimal. The O1–C46 distances in **2** and **3** are shorter than the

corresponding distance in **1** (1.303 vs. 1.341 Å; <u>Table 2.1</u>) due to delocalization of the negative charge onto the 2-acetyl group. The O1–C46 bond of the acetophenone-derived ligands therefore acquires some double-bond character, whereas the twisted conformation of the HL^A ligand indicates a lack of electronic conjugation between the π-systems.

In contrast to the HL$^{1-3}$ donors of complexes **1-3**, the 2-methoxyhydroquinonate ligand in **4** forms a five-membered ring chelate with the Fe(II) center. This fact, coupled with the intrinsically weak donating ability of methoxy substituents, results in a rather lengthy Fe1–O3 distance of 2.317(3) Å. Thus, in certain respects, **4** can be considered to possess an intermediate coordination number between 4 and 5. As evidence, the O1–Fe1–N5 angle increases from an average of 97.8° in **1-3** to 115.6° in **4** (with a corresponding decrease in the O3–Fe1–N$_{Tp}$ angles), as the HQate donor shifts out of the equatorial plane (Table 2.1). Thus, if the weakly-bound –OCH$_3$ group is ignored, **4** appears to adopt a distorted trigonal pyramidal geometry with the O1 donor in the axial position. Notably, complex **4** co-crystallizes with one equivalent of [HNEt$_3$]OTf salt, and the triflate anion participates in a hydrogen-bonding interaction with the distal –OH group in the solid state (<u>Figure 2.3</u>; the O2▪▪▪O4 distance is 2.782(6)). This feature is reminiscent of acid/base interactions between HQ substrates and conserved second-sphere residues that have been proposed to play an important role in HQDO catalysis.[50,52]

The diiron(II) μ-HQate complexes were never observed in preparations of **1-4**, and we initially attributed the lack of dinuclear side-products to the steric demands of the ^{Ph2}Tp ligand. To evaluate this hypothesis, we generated the compound 2,5-dimethoxyhydroquinone, which is capable of coordinating two metal centers in a bidentate fashion. Interestingly, use of this ligand provides the diiron(II) complex **5** as the

only isolated product even when the reactants are mixed in equimolar ratios, thereby proving that the ^{Ph_2}Tp framework is capable of supporting dinuclear complexes. The X-ray structure of **6** is shown in <u>Figure 2.4</u> and key metric parameters are listed in the caption. The complex is centrosymmetric with an Fe▪▪▪Fe distance of 8.15 Å. The Fe–O/N distances of **5** are nearly identical to those of the analogous monoiron(II) complex **4**, although the position of the HQate ligand with respect to the N_{Tp} donors is somewhat different (e.g., ∠O1–Fe1–N5 = 98.1(2)° and 115.6(1)° in **5** and **4**, respectively). The fact that the 2,5-dimethoxyhydroquinonate ligand exclusively yields **5**, whereas the HQate ligands incorporated by complexes **1-4** favor monomeric species, suggests that the thermodynamic benefit of bidentate chelation at both Fe(II) centers is able to overcome the steric barrier to dimerization.
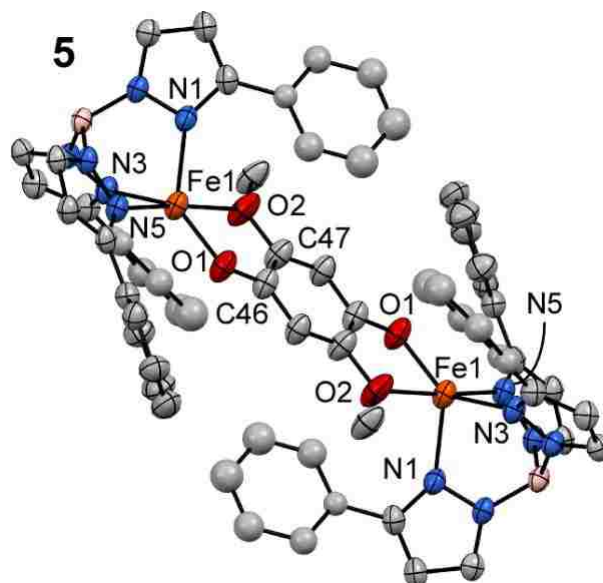
Figure 2.4. Thermal ellipsoid plot (50% probability) derived from the X-ray structure of **5**·CH_2Cl_2. Non-coordinating solvent molecules and hydrogen atoms have been omitted for clarity, in addition to Ph-rings at the 5-positions of the ^{Ph2}Tp ligand. Ellipsoids are not shown for four Ph rings due to disorder. [note: the complex is centrosymmetric] Metric parameters are provided in Chapter 6.

2.B.ii. Fe(II) complexes with an untethered hydroquinonate ligand

As noted in previously, several HQDOs oxidize "untethered" HQs that lack additional metal-coordinating groups. To replicate the monodentate binding mode of these HQ substrates, we employed the ligand 2,6-dimethylhydroquinone. Reaction of H_2L^6 with equimolar amounts of $K(^{Ph2}Tp)$, $FeCl_2$, and NaOMe in MeCN generates a bright orange solid, which was recrystallized by slow diffusion of MeCN into a concentrated 1,2-dichloroethane (DCE) solution. X-ray analysis of the crystals revealed a diiron(II) structure (**7**(MeCN); Figure 2.5). Unlike **5**, the Fe(II) centers in **7**(MeCN) are not equivalent: Fe2 is 4C due to steric hindrance from the methyl substituents of the bridging 2,6-dimethylhydroquinonate dianion, and Fe1 is 5C with an additional solvent

MeCN ligand. The Fe1 center exhibits a distorted trigonal bipyramidal coordination geometry (τ = 0.58), while the Fe2 geometry is best described as trigonal pyramidal ($\angle$O2–Fe2–N$_{Tp}$ = 125 ± 5°). The low Fe2 coordination number leads to relatively short metal–ligand bond lengths, especially the Fe2–O2 distance of 1.784(6) Å (see Figure 2.5 caption for additional metric parameters). The high-spin Fe ions are separated by 8.72 Å. While the initial synthesis of **7** employed equimolar amounts of reagents, the complex can also be prepared in greater yield by using only 0.5 equivalent of the HL^6 ligand.
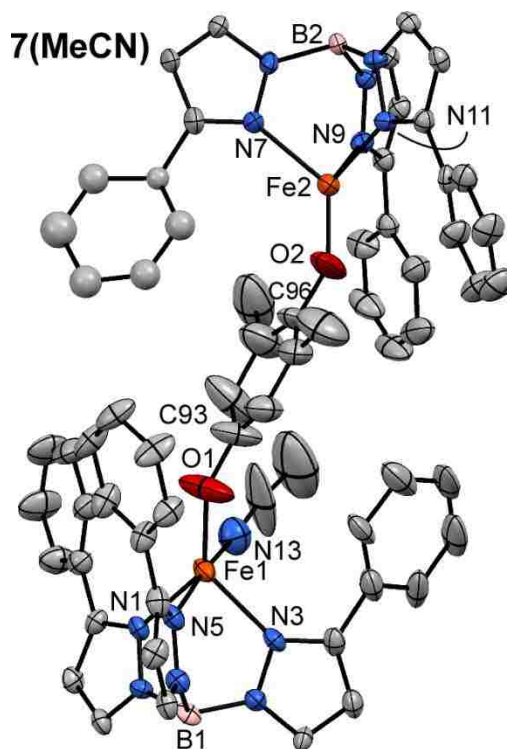
Figure 2.5. Thermal ellipsoid plot (50% probability) derived from the X-ray structure of [**7**(MeCN)]·2DCE. Non-coordinating solvent molecules, hydrogen atoms, and Ph-rings at the 5-positions of the ^{Ph2}Tp ligand have been omitted for clarity. Selected bond lengths (Å): Fe1–O1 1.852(6), Fe1–N1 2.111(5), Fe1–N3 2.136(6), Fe1–N5 2.187(5), Fe1–N13 2.289(8), O1–C93 1.348(10), Fe2–O2 1.784(6), Fe2–N7 2.105(5), Fe2–N9 2.119(5), Fe2–N11 2.136(5), O2–C96 1.352(10).

In an effort to prevent formation of **7**(MeCN), one equivalent of 3,5-diphenylpyrazole (^{Ph2}pz) was included in the reaction mixture described above. Under these conditions, the reaction provided a yellow product that was recrystallized by DCE/pentane layering. X-ray diffraction analysis revealed that the crystals contain the 5C monoiron(II) complex, [**6**(^{Ph2}pz)]. As shown in Figure 2.6, **6**(^{Ph2}pz) features a trigonal bipyramidal coordination geometry ($\tau = 0.58$) with the HQate and ^{Ph2}pz donors in equatorial and axial positions, respectively. These two ligands form an intramolecular hydrogen-bond that closes a five-membered ring, as evident in the O1–N8 distance of 2.840(2) Å and O1–H7 distance of 2.17(2) Å (the H2 and H7 atoms were found objectively and refined). The Fe1–O1 bond distance of 1.893(1) is shorter than the corresponding distances in the tethered complexes **1-4**, whereas the axial ^{Ph2}pz ligand is weakly bound with an Fe1–N7 distance of 2.341(2) Å (Table 2.1). As expected, HL^5 coordinates to the Fe(II) center via the more sterically-accessible O-atom at the 4-position of the HQ. Without the constraint of a pendant ligand, the HQate ring in **6**(^{Ph2}pz) rotates away from the Fe center, as signified by the large Fe1–O1–C46 bond angle of 148.7(1)° (compared to values of $125 \pm 5°$ for **1-4**).
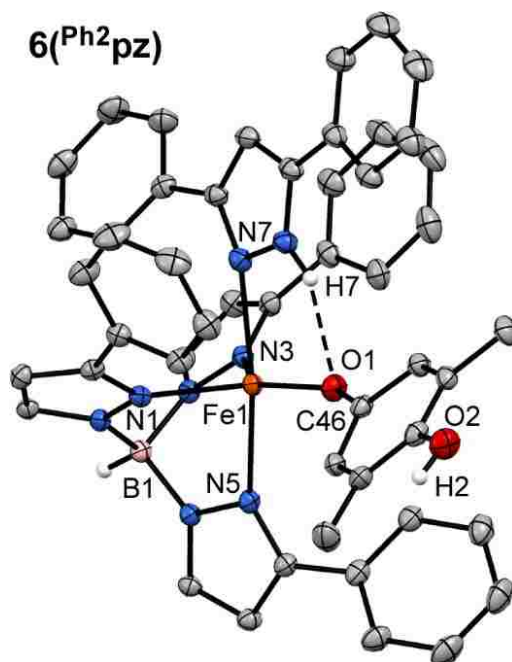
Figure 2.6. Thermal ellipsoid plot (50% probability) derived from the X-ray structure of **6(^{Ph2}pz)**. Hydrogen atoms and Ph-rings at the 5-positions of the ^{Ph2}Tp ligand have been omitted for clarity. Selected bond lengths and angles are provided in Table 2.1.

2.B.iii. Spectroscopic and electrochemical properties of Fe(II)–HQate complexes

Electronic absorption spectra of complexes **1-4** and **6** in CH$_2$Cl$_2$ are shown in Figure 2.7. Complexes **2** and **3** are both brightly colored due to a weak absorption manifold (ε ■0.7 mM^{-1} cm^{-1}) in the visible region and an intense peak in the near-UV (ε ■5.5 mM^{-1} cm^{-1}). The application of time-dependent density functional theory (TD-DFT) to **2** revealed that the lower-energy band arises from an Fe(II) $\rightarrow$ HL^B MLCT transition in which the acceptor molecular orbital (MO) has primarily acetyl(C■O*) character. The higher-energy feature is assigned to a HL^B-based $\pi \rightarrow \pi^*$ transition (see Experimental section for details concerning the TD-DFT calculations). While **1** does not exhibit visible-region MLCT transitions like **2** and 3, a very intense ligand-based $\pi \rightarrow \pi^*$ band is

observed with $\lambda_{max} = 369$ nm (Figure 2.7). In contrast, complexes containing ligands derived from methoxy- and alkyl-substituted HQs ($H_2L^{4,6}$) have pale yellow colors due to broad UV absorption features that tail into the visible region (Figure 2.7 and Figure 2.8).
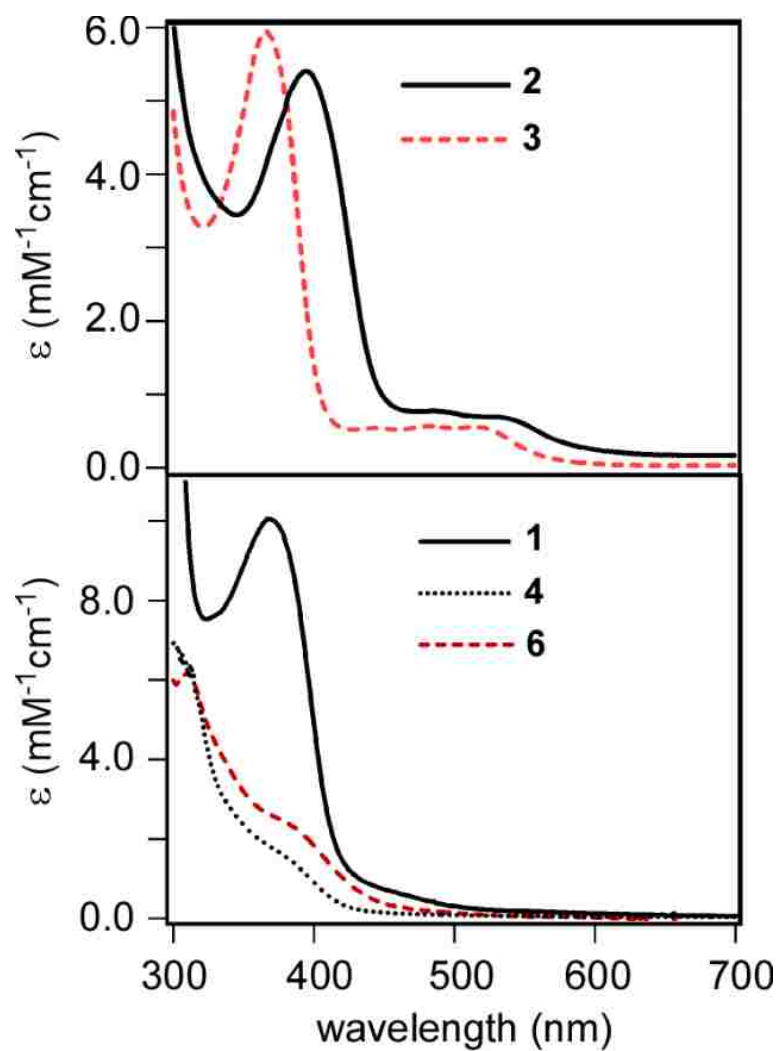
Figure 2.7. Electronic absorption spectra of complexes **1-4** and **6** in CH_2Cl_2 at 20°C.
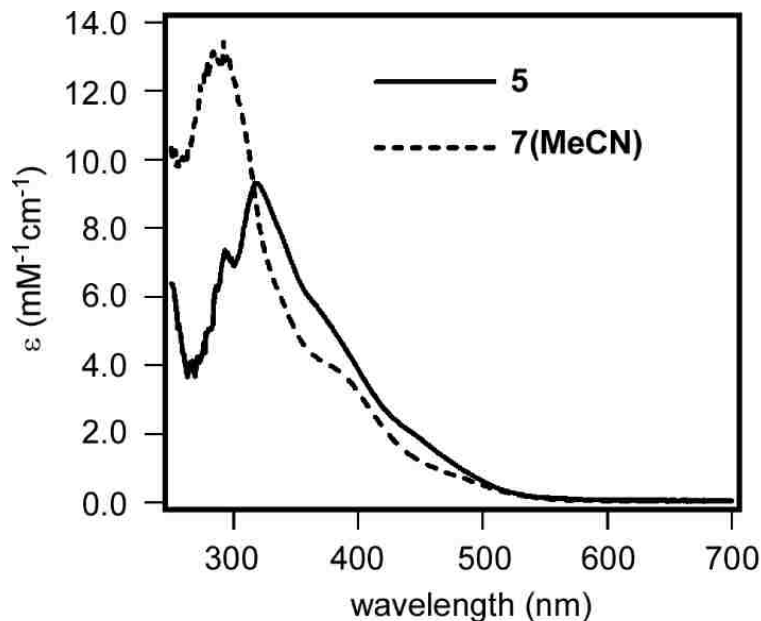
Figure 2.8. Electronic absorption spectra of **5** and **7(MeCN)** in CH_2Cl_2 at 20°C.

^{1}H NMR spectra of complexes **1-4** and **6** in CD_2Cl_2 display paramagnetically-shifted signals characteristic of high-spin monoiron(II) centers (Figure 2.9). Peaks arising from the ^{Ph2}Tp supporting ligand are easily assigned by comparison to earlier literature reports (e.g., the signal from the 4-pyrazole protons consistently appears near 55 ppm).[93,94] In each case, the resonance arising from the distal hydroxyl substituent was identified through H/D exchange with a small amount of added MeOH-d$_4$. These peaks appear downfield with chemical shifts of 23 ± 3 ppm, although the hydroxyl proton is observed at 59 ppm in the **4** spectrum (Figure 2.9) The observation of paramagnetically-shifted –OH resonances confirms that the HQate ligands do not adopt bridging positions in solution.
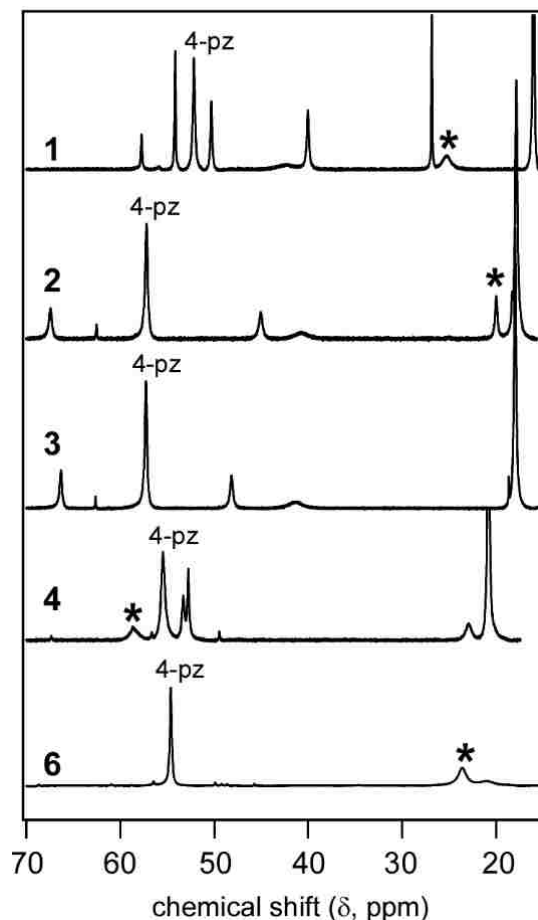
Figure 2.9. ^{1}H NMR spectra of **1-4** and **6** in CD$_2$Cl$_2$ at ambient temperature. Peaks marked with an asterisk (*) disappeared upon addition of a small amount of MeOH-*d$_4$* and are therefore assigned to the exchangeable proton of the distal –OH moiety. Resonances arising from protons at the 4-positions of the [Ph2]Tp pyrazole rings are also identified (4-pz).

The electrochemical behavior of the monoiron(II) complexes **1-4** and **6** were studied by cyclic voltammetry in CH$_2$Cl$_2$ or THF solutions containing 100 mM [NBu$_4$]PF$_6$ as the supporting electrolyte. The cyclic voltammograms are displayed in Figure 2.10 and the results are summarized in Table 2.2. All redox potentials are referenced to the ferrocenium/ferrocene couple (Fc[+]/Fc). Complexes **1-3** display quasi-reversible one-electron oxidation waves between −290 and −30 mV that correspond to the Fe(II/III) couple. The Fe redox potential of **1** is significantly lower than those of **2** and **3**, reflecting

the stronger donating ability of benzimidazolyl relative to acetyl groups. When the window is expanded to more positive potentials, both **1** and **2** exhibit a highly irreversible wave that likely corresponds to oxidation of the respective HQate ligands. The irreversible nature of the hydroquinonate-based oxidation is probably due to subsequent loss of the distal –OH proton to the surrounding medium. Notably, **3** is redox inactive at higher potentials, which is not surprising given that phenolates are intrinsically harder to oxidize than HQates.[99]

Table 2.2. Redox potentials of complexes **1-4** and **6**[a]

Complex	Solvent	Redox Potentials[b] (mV *vs.* $Fc^{+/0}$)
1	CH_2Cl_2	$E_{1/2}$ (ΔE) = -290 (110); $E_{p,a}$ = +740 mV
2	CH_2Cl_2	$E_{1/2}$ (ΔE) = -110 (140); $E_{p,a}$ = +1050 mV
3	CH_2Cl_2	$E_{1/2}$ (ΔE) = -30 (150)
4	THF	$E_{p,a}$ = -50, +370, and +780 mV
6	THF	$E_{p,a}$ = -100, +580, and +850 mV

[a] Conditions: solutions contained 100 mM $(NBu_4)PF_6$; scan rate of 100 mV s^{-1} at room temperature. [b] $E_{1/2}$ and ΔE values are provided for (quasi)reversible processes; $E_{p,a}$ values are given for irreversible oxidation events.
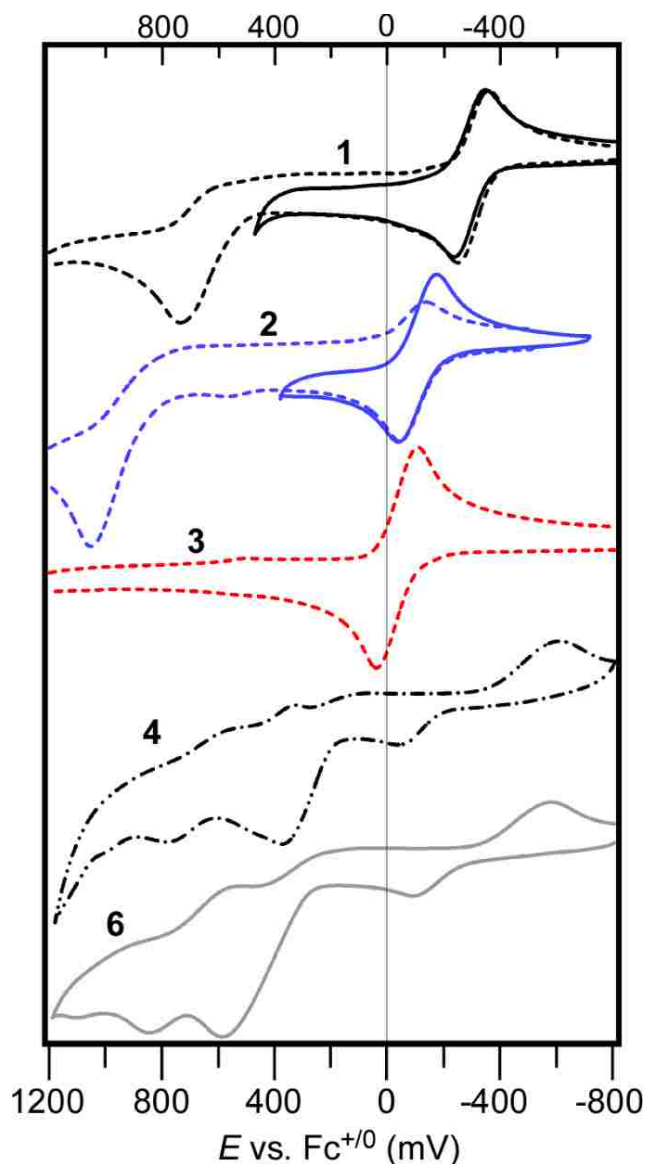
Figure 2.10. Cyclic voltammograms of **1-4** and **6**. Data was collected in CH_2Cl_2 (**1-3**) or THF (**4** and **6**) with 100 mM $(NBu_4)PF_6$ as the supporting electrolyte and a scan rate of 100 mV s^{-1}. Each voltammogram was initiated by the anodic sweep.

As shown in Figure 2.10, reversible electrochemical processes were not observed in the cyclic voltammograms of **4** and **6**; instead, each complex displays a weak anodic wave ($E_{p,a}$ = −50 and −100 mV for **4** and **6**, respectively) that is assigned to one-electron oxidation of the Fe(II) center. The corresponding cathodic waves appear at much more negative potentials ($E_{p,c}$ ■ −600 mV in both cases), suggesting an irreversible change

following oxidation to Fe(III). Additional irreversible events arising from HQate-based oxidation are evident at higher potentials for **4** and **6** (Table 2.2; Figure 2.10). As expected, the potential of the first HQate-based oxidation shifts to more negative potentials as the HQate substituents become more electron-donating: $E(HL^4) < E(HL^6) < E(HL^1) < E(HL^2)$. The ill-defined electrochemical behavior of **4** and **6** is likely a result of the greater conformational flexibility of their HQate ligands, which are not locked into a stable six-membered ring chelate like the HL^{1-3} ligands.

Given that complexes **1-3** display reversible Fe(II/III) redox couples, we sought to examine the corresponding ferric species, **X$_{ox}$**, with spectroscopic methods. As shown in Figure 2.11, treatment of the Fe(II) complexes with one equivalent of a one-electron oxidant, such as acetylferrocenium or $[N(C_6H_4Br-4)_3]^+$, yields chromophores with broad, intense absorption features centered near 480 nm. Based on literature precedents,[100,101] these bands are confidently assigned to $HL^{1-3} \rightarrow$ Fe(III) LMCT transitions. The high intensities of the LMCT bands are indicative of strong Fe1–O1 covalency in the oxidized state, arising from overlap between the out-of-plane π-orbital of the phenolate ligand and the partially-occupied Fe(xy) orbital.[102]
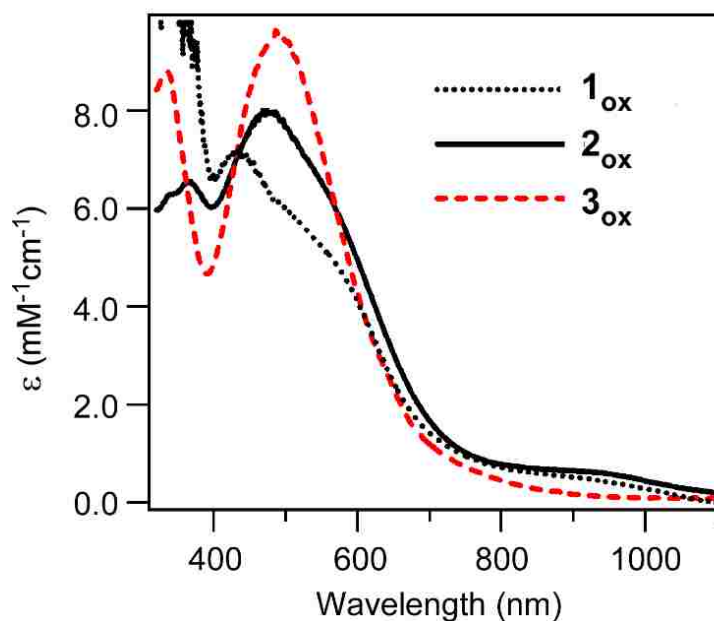
Figure 2.11. Electronic absorption spectra of $\mathbf{1_{ox}}$–$\mathbf{3_{ox}}$ in CH_2Cl_2 at room temperature. The $\mathbf{1X_{ox}}$ species were obtained by treating the Fe(II) precursors with one equivalent of acetylferrocenium ($\mathbf{1_{ox}}$) or $[N(C_6H_4Br\text{-}4)_3]^+$ ($\mathbf{2_{ox}}$ and $\mathbf{3_{ox}}$).

EPR spectra of the oxidized species $\mathbf{1_{ox}}$–$\mathbf{3_{ox}}$ (Figure 2.12) each reveal an intense derivative-shaped feature at g = 4.3 and a very weak peak near g = 9.4, characteristic of rhombic high-spin Fe(III) centers.
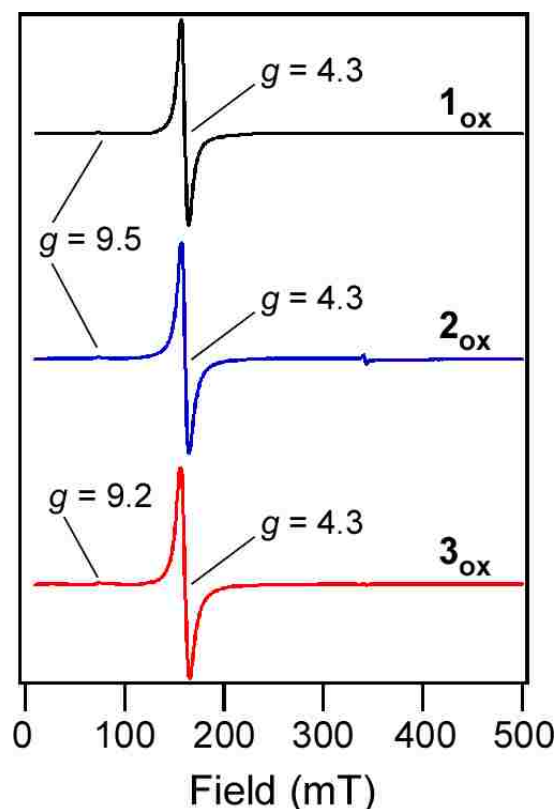
Figure 2.12. X-band EPR spectra of **1ox-3ox** in frozen CH_2Cl_2 solutions. The **Xox** species were obtained by treating the Fe(II) precursors with one equivalent of acetylferrocenium (**1Aox**) or $[N(C_6H_4Br-4)_3]$ (**2ox** and **3ox**). The spectra were collected under the following conditions: frequency = 9.63 GHz; power = 2.0 mW; modulation = 12 G; temperature = 10 K.

2.C. Conclusion

We have reported the synthesis and X-ray structure analysis of a series of

monoiron(II) hydroquinonate complexes (**1-4**, **6**) that represent the first

crystallographically-characterized models of Fe/HQate interactions in HQDO active sites.

The spectroscopic and electrochemical properties of the complexes were also described.

The models employed bidentate ("tethered") and monodentate ("untethered") HQate

ligands, since HQDOs oxidize both types of substrates. Although HQate ligands are

known to bridge multiple metal centers, the tethered ligands (H_2L^{1-4}) cleanly provided 5C

mononuclear complexes supported by the tridentate Ph2Tp framework. It was possible,

though, to obtain the diiron(II) complex 2E by inclusion of an additional donor

substituent at the 5-position of the HQate ring. Compared to the bidentate HQates, the

untethered ligand, H_2L^6, readily adopted a bridging position between Fe(II) centers, as

evident in the facile formation of **7**. Addition of one equivalent of free pyrazole (^{Ph2}pz) to

the reaction mixture, however, provided the complex **6**(^{Ph2}pz) – the only structurally-

characterized example of a monoiron(II) complex with an untethered HQate ligand

reported to date. The stability of **6**(^{Ph2}pz) isundoubtedly enhanced by an intramolecular

hydrogen bond between the HQate and ^{Ph2}pz ligands (Figure 2.6). While crystallographic

studies of substrate-bound HQDOs are not currently available, structures of ECDO :

substrate complexes have revealed similar hydrogen-bonding interactions between the

deprotonated O-atom of the catecholate ligand and second sphere residues.[6,10,23] Thus,

6(^{Ph2}pz) replicates important aspects of the enzymatic coordination environment. The

results presented here provide a basis for future modeling studies of the HQDOs. As

noted in the introduction, the noninnocent nature of HQate ligands is thought to play an

important role in the HQDO mechanism. Indeed, the cyclic voltammograms of **1** and **2**

reveal an irreversible wave that likely corresponds to HQate oxidation coupled to loss of

the distal –OH proton. Detailed studies of the electron- and proton-transfer capabilities of

our mono- and dinuclear HQate complexes with the aim of generating novel Fe benzo

(semi)quinone species are reported in subsequent chapters. In addition, O_2 reactivity

studies of complexes **1** and **2** are reported in Chapter 4.

Table 2.3. Summary of X-ray Crystallographic Data Collection and Structure Refinement

	$1 \cdot CH_2Cl_2$	$2 \cdot 2CH_2Cl_2$ [a]	3	$4 \cdot [HNEt_3]OTf$	$5 \cdot 2Et_2O$	6	$[7(MeCN)] \cdot 2DCE$ [b]
empirical formula	$C_{60}H_{47}BCl_2FeN_8O_2$	$C_{55}H_{45}BCl_4FeN_6O_3$	$C_{53}H_{41}BFeN_6O_2$	$C_{59}H_{57}BF_3FeN_7O_6S$	$C_{106}H_{96}B_2Fe_2N_{12}O_6$	$C_{68}H_{55}BFeN_8O_2$	$C_{104}H_{87}B_2Cl_4Fe_2N_{13}O_2$
formula weight	1049.62	1046.46	860.58	1115.84	1767.27	1082.86	1826.02
crystal system	Monoclinic	Orthorhombic	Monoclinic	Triclinic	Triclinic	Monoclinic	Monoclinic
space group	$P2_1/c$	$P2_12_12_1$	$P2_1/n$	$P\bar{1}$	$P\bar{1}$	$P2_1/c$	Pn
a, Å	14.5859(5)	11.2362(4)	10.4129(2)	9.6832(4)	9.6359(10)	17.8034(7)	13.4895(3)
b, Å	13.6416(4)	17.7643(6)	30.8300(5)	9.8868(5)	13.4413(14)	22.3235(10)	10.0544(3)
c, Å	25.2090(8)	25.2782(8)	13.1758(2)	28.3671(15)	18.205(2)	13.6123(6)	32.9607(9)
α, deg	90	90	90	85.740(4)	95.633(9)	90	90
β, deg	93.779(3)	90	90.634(2)	86.952(4)	105.298(10)	99.746(4)	96.806(3)
γ, deg	90	90	90	81.003(4)	99.002(9)	90	90
V, Å^3	5005.0(3)	5045.6(3)	4229.6(1)	2672.5(2)	2222.1(4)	5331.9(4)	4438.9(2)
Z	4	4	4	2	1	4	2
D_{calc}, g/cm^3	1.393	1.351	1.351	1.387	1.321	1.349	1.342
λ, Å	1.5418	1.5418	0.7107	1.5418	1.5418	0.7107	1.5418
μ, mm^{-1}	3.831	4.518	0.408	3.209	3.131	0.340	4.018
θ-range, deg	7 to 148	7 to 148	7 to 59	9 to 148	7 to 148	7 to 59	7 to 148
reflections collected	35336	19096	58359	15029	15573	62124	23318
independent reflections	9913 [R_{int} = 0.0382]	8984 [R_{int} = 0.0435]	10931 [R_{int} = 0.0402]	15029	8687 [R_{int} = 0.0622]	13600 [R_{int} = 0.0409]	12059 [R_{int} = 0.0406]
data/restraints/ parameters	9913 / 0 / 672	8984/0/634	10931 /0 / 569	15029 / 0 / 709	8687 / 24 / 569	13600/ 0 / 731	12059 / 31 / 1132
GOF (on F^2)	1.041	1.103	1.027	1.074	1.026	1.058	1.024
$R1/wR2$ ($I > 2\sigma(I)$) [c]	0.0354/0.0891	0.0814/0.2410	0.0375/0.0891	0.0864/0.2278	0.0718/0.1807	0.0414/0.1005	0.0638/0.1662
$R1/wR2$ (all data)	0.0449/0.0954	0.0838/0.2437	0.0462/0.0953	0.1008/0.2402	0.1152/0.2227	0.0552/0.1083	0.0821/0.1826

[a] One of the solvate molecules in $1B \cdot 2CH_2Cl_2$ is only partially (77%) populated. [b] One of the solvate molecules in $[2F(MeCN)] \cdot 2DCE$ is only partially (68%) populated [c] $R1 = \Sigma ||F_o| - |F_c|| / \Sigma|F_o|$; $wR2 = [\Sigma w(F_o^2 - F_c^2)^2 / \Sigma w(F_o^2)^2]^{1/2}$

2.D. Experimental

2.D.i. General methods

Unless otherwise noted, all reagents and solvents were purchased from commercial sources and used as received. Acetonitrile, dichloromethane, and tetrahydrofuran were purified and dried using a Vacuum Atmospheres solvent purification system. The synthesis and handling of air-sensitive materials were performed under inert atmosphere using a Vacuum Atmospheres Omni-Lab glovebox. The ligands $K(^{Ph2}Tp)$[103] and 2,5-dimethoxyhydroquinone (H_2L^5)[104] were prepared according to literature procedures.

Elemental analyses were performed at Midwest Microlab, LLC in Indianapolis, IN. UV-vis absorption spectra were obtained with an Agilent 8453 diode array spectrometer equipped with a cryostat from Unisoku Scientific Instruments (Osaka, Japan) for temperature control. Fourier-transform infrared (FTIR) spectra of solid samples were measured with a Thermo Scientific Nicolet iS5 FTIR spectrometer equipped with the iD3 attenuated total reflectance accessory. ^{1}H spectra were collected at room temperature with a Varian 400 MHz spectrometer. EPR experiments were performed using a Bruker ELEXSYS E600 equipped with an ER4415DM cavity resonating at 9.63 GHz, an Oxford Instruments ITC503 temperature controller, and an ESR-900 He flow cryostat. Electrochemical measurements were conducted in the glovebox with an epsilon EC potentiostat (iBAS) at a scan rate of 100 mV s^{-1} with 100 mM (NBu$_4$)PF$_6$. A three-electrode cell containing a Ag/AgCl reference electrode, a platinum auxiliary electrode, and a glassy carbon working electrode was employed for

cyclic voltammetric (CV) measurements. Under these conditions, the

ferrocene/ferrocenium (Fc$^{+/0}$) couple has an E$_{1/2}$ value of +0.52 V in CH$_2$Cl$_2$ and +0.61 V

in THF.

2.D.ii. Synthetic procedures:

2-(1-Methyl-1H-benzimidazol-2-yl)hydroquinone (**H$_2$L^1**). To 2,5-dihydroxy-

benzaldehyde (690 mg, 5.0 mmol) dissolved in 25 mL of ethanol, N-methyl-1,2-

benzenediamine (0.56 mL, 5.0 mmol) in 15 mL of ethanol was added dropwise over the

course of 30 min. The mixture was then stirred at 50 °C for two days. After cooling, 30

mL of H$_2$O was added and the mixture was placed overnight in a freezer. The resulting

brown precipitate was filtered and dried under vacuum to give the product (0.79 g, 66%).

Anal. Calcd for C$_{14}$H$_{12}$N$_2$O$_2$ (Mw = 240.26 g mol^{-1}): C, 69.99; H, 5.03; N, 11.66. Found:

C, 69.84; H, 5.15; N, 11.70. ^{1}H NMR (δ, DMSO): 3.81 (s, 3H, NCH$_3$), 6.83 (m, 2H), 7.02

(d, 1 H), 7.27 (m, 2H), 7.63 (m, 2H), 9.10 (br s, 1H, –OH), 10.43 (br s, 1H, –OH).

^{13}C[^{1}H] NMR (δ, DMSO): 31.6, 110.4, 116.0, 116.1 117.2, 118.5, 118.6, 121.9, 122.4,

135.8, 141.5, 149.1, 149.6, 151.9.

[Fe(^{Ph2}Tp)(HL^1)] (**1**). 2-(1-Methyl-1H-benzimidazol-2-yl)hydroquinone (H$_2$L^1) (120 mg,

0.50 mmol) was deprotonated by reaction with one equivalent of NaOMe in 10 mL of

MeCN. To this solution was added FeCl$_2$ (64.2 mg, 0.50 mmol) and K(^{Ph2}Tp) (350 mg,

0.49 mmol). The mixture was stirred for overnight and the solvent removed under

vacuum to give a yellow-brown solid. The crude product was dissolved in CH$_2$Cl$_2$ and

filtered; the resulting solution yielded yellow crystals suitable for crystallographic

analysis after standing for several days (0.37 g, 77%). Anal. Calcd for $C_{59}H_{45}BFeN_8O_2$ (M_W = 964.70 g mol^{-1}): C, 73.56; H, 4.70; N, 11.62. Found: C, 73.18; H, 4.87; N, 11.72. UV-vis [λ_{max}, nm (ε, M^{-1} cm^{-1}) in CH_2Cl_2]: 369 (10 100). FTIR (cm^{-1}, solution): 3592 (OH), 3047, 2988, 2901, 2611 (BH), 1543, 1484, 1415, 1332, 1243, 1171, 1070, 1007, 963, 914, 818, 760, 692.

[Fe(^{Ph2}Tp)(HL^2)] (2). Under an inert atmosphere, 182 mg (1.20 mmol) of 2′,5′-dihydroxyacetophenone (H_2L^2) was deprotonated by mixing with one equivalent of NaOMe in THF for 30 min, after which the solvent was removed to yield the Na(HL^B) salt as a white solid. To this compound was added anhydrous $FeCl_2$ (146 mg, 1.15 mmol) and K(^{Ph2}Tp) (815 mg, 1.15 mmol) in 15 ml of MeCN. After stirring the reaction mixture overnight, the resulting solid was collected by vacuum filtration, dried, and redissolved in CH_2Cl_2. Layering with pentane provided reddish brown crystals suitable for X-ray diffraction (0.26 g, 26%). Anal. Calcd for $C_{53}H_{41}BFeN_6O_3$ (M_W = 876.59 g mol^{-1}): C, 72.62; H, 4.71; N, 9.59. Found: C, 72.49; H, 4.79; N, 9.73. UV-vis [λ_{max}, nm (ε, M^{-1} cm^{-1}) in CH_2Cl_2]: 394 (5410), 485 (780), 527 (690). FTIR (cm^{-1}, solid): 3559 (OH), 3058, 2608 (BH), 1604 (CO$_{acetyl}$), 1547, 1475, 1462, 1430, 1411, 1359, 1340, 1327, 1299, 1197, 1164, 1062, 1006, 965, 917, 810, 759, 693.

[Fe(^{Ph2}Tp)(HL^3)] (3). The method of preparation was similar to the one described for **2**, except that 2′-hydroxyacetophenone (H_2L^3) was substituted for H_2L^2. Orange crystals were obtained by layering a concentrated CH_2Cl_2 solution with MeCN. Yield = 24%. Anal. Calcd for $C_{53}H_{41}BFeN_6O_2$ (M_W = 860.59 g mol^{-1}): C, 73.97; H, 4.80; N, 9.77. Found: C, 74.15; H, 4.92; N, 9.83. UV-vis [λ_{max}, nm (ε, M^{-1} cm^{-1}) in CH_2Cl_2]: 368 (5950), 441 (540), 485 (570). FTIR (cm^{-1}, solid): 3060, 2618 (BH), 1613 (CO$_{acetyl}$), 1529,

1479, 1463, 1432, 1414, 1361, 1346, 1331, 1225, 1167, 1063, 1010, 966, 912, 863, 804, 753, 692.

[Fe(^{Ph2}Tp)(HL^4)] (4). This compound was prepared via two methods. Method A: 2-methoxyhydroquinone (H$_2$L^4), 151 mg, 1.1 mmol) and triethylamine (1.1 mmol) were stirred in MeCN, followed by addition of K(^{Ph2}Tp) (710 mg, 1.0 mmol) and Fe(OTf)$_2$ (372 mg, 1.05 mmol) dissolved in CH$_2$Cl$_2$ and MeCN, respectively. The mixture was stirred overnight, filtered, and the solvent removed under vacuum. The resulting solid was washed multiple times with MeCN to remove triflate salts and other impurities and then dried again. The solid was dissolved in CH$_2$Cl$_2$ and layered with hexane to yield a yellow crystalline powder (0.28 g, 33%). Anal. Calcd for C$_{52}$H$_{41}$BFeN$_6$O$_3$ (M$_W$ = 864.58 g mol^{-1}): C, 72.24; H, 4.78; N 9.72. Found: C, 69.69; H, 5.65; N 10.63 (the discrepancies indicate the presence of small amounts of impurities). UV-vis [λ_{max}, nm (ε, M^{-1} cm^{-1}) in CH$_2$Cl$_2$]: 383 (1490). FTIR (cm^{-1}, solid): 3563 (OH), 3056, 2931, 2615 (BH), 1543, 1495, 1477, 1461, 1410, 1357, 1305, 1260, 1226, 1164, 1060, 1008, 913, 818, 754, 690. Method B: Equimolar amounts of the four reagents – Fe(OTf)$_2$, K(^{Ph2}Tp), H$_2$L^D, and NEt$_3$ – were mixed in CH$_2$Cl$_2$ and stirred overnight. The solution was filtered and the solvent removed under vacuum. The solid was taken up in CH$_2$Cl$_2$ and layered with pentane to yield yellow crystals suitable for X-ray diffraction.

[Fe$_2$(^{Ph2}Tp)$_2$(μ-L^5)] (5). 2,5-Dimethoxyhydroquinone (H$_2$L^5, 91 mg, 0.53 mmol) was first deprotonated by treatment with two equivalents of NaOMe in THF. After removal of the solvent, the resulting white solid Na$_2$(L^5) was mixed with FeCl$_2$ (131 mg, 1.03 mmol) and K(^{Ph2}Tp) (715 mg, 1.01 mmol) in MeCN, and the solution was stirred overnight. After removal of the solvent under vacuum, the yellow solid was taken up CH$_2$Cl$_2$ and the

solution filtered to remove unwanted salts. Vapor diffusion of Et_2O into this CH_2Cl_2 solution provided yellow-orange needles suitable for X-ray crystallography (0.11 g, 13%). Anal. Calcd for $C_{98}H_{76}B_2Fe_2N_{12}O_4$ (M_W = 1619.07 g mol^{-1}): C, 72.70; H, 4.73; N 10.38. Found: C, 72.45; H, 4.67; N, 10.36. UV-vis [λ_{max}, nm (ε, M^{-1} cm^{-1}) in CH_2Cl_2]: 317 (9300), 370 (sh), 444 (sh). FTIR (cm^{-1}, solid): 3058, 2926, 2614 (BH), 1541, 1478, 1465, 1438, 1407, 1359, 1260, 1221, 1194, 1167, 1154, 1061, 1008, 888, 802, 756, 690.

[Fe(^{Ph2}Tp)(HL^6)(^{Ph2}pz)] (6). 3,5-Diphenylpyrazole (236 mg, 1.04 mmol), K(^{Ph2}Tp) (714 mg, 1.01 mmol), and 2,6-dimethylhydroquinone (H_2L^6, 164 mg, 1.19 mmol) were dissolved in a 3:1 mixture of DCE–MeCN. To this solution was added $FeCl_2$ (129 mg, 1.02 mmol) in MeCN and NaOMe (0.23 mL of 4.37 M MeOH solution, 1.00 mmol). The reaction was stirred overnight. The solvent was evaporated under vacuum to give a pale orange solid. The crude solid was taken up into DCE and filtered, providing a bright yellow solution. Yellow crystals were obtained by layering this DCE solution with pentane. Anal. Calcd for $C_{68}H_{55}BFeN_8O_2$ (M_W = 1082.88 g mol^{-1}): C, 75.42; H, 5.12; N 10.35. Found: C, 75.22; H, 5.00; N 10.21. UV-vis [λ_{max}, nm (ε, M^{-1} cm^{-1}) in CH_2Cl_2]: 374 (2530). FTIR (cm^{-1}, solid): 3355 (OH), 3060, 3038, 2912, 2631 (BH), 1598, 1543, 1477, 1465, 1430, 1410, 1339, 1306, 1212, 1165, 1062, 1004, 967, 913, 851, 810, 754, 688.

[Fe$_2$(^{Ph2}Tp)$_2$(μ-L^6)(MeCN)] [7(MeCN)]. Anhydrous $FeCl_2$ (130 mg, 1.02 mmol) and K(^{Ph2}Tp) (715 mg, 1.01 mmol) were combined with 0.5 equivalent of 2,6-dimethylhydroquinone (H_2L^F, 70.0 mg, 0.51 mmol) in 10 mL of MeCN. To this mixture was added 0.23 mL of 4.37 M solution of NaOMe (1.01 mmol). The reaction was stirred overnight, and the solvent removed under vacuum. The resulting solid was dissolved in

DCE, filtered, and then layered with MeCN to provide reddish-brown needles (0.21 g, 26%) suitable for crystallographic analysis. The X-ray structure revealed two uncoordinated DCE molecules in the asymmetric unit, and elemental analysis suggest that a small amount of solvent (■0.8 equiv.) remains even after drying. Anal. Calcd for $C_{100}H_{79}B_2Fe_2N_{13}O_2 \cdot 0.8DCE$ ($M_W = 1707.27$ g mol^{-1}): C, 71.48; H, 4.85; N 10.67. Found: C, 71.47; H, 4.77; N, 10.37. UV-vis [λ_{max}, nm (ε, M^{-1} cm^{-1}) in CH_2Cl_2]: 288 (11 500), 377 (3600). FTIR (cm^{-1}, solid): 3052, 2925, 2608 (BH), 1542, 1465, 1477, 1431, 1412, 1358, 1242, 1162, 1065, 1029, 1009, 969, 916, 847, 810.

2.D.iii. Crystallographic studies

Each complex was characterized with X-ray crystallography; details concerning the data collection and analysis are summarized in <u>Table 2.4</u>. The X-ray diffraction data were collected at 100 K with an Oxford Diffraction SuperNova kappa-diffractometer equipped with dual microfocus Cu/Mo X-ray sources, X-ray mirror optics, Atlas CCD detector and a low-temperature Cryojet device. The data were processed with CrysAlisPro program package (Oxford Diffraction Ltd, 2010) typically using a numerical Gaussian absorption correction (based on the real shape of the crystal) followed by an empirical multi-scan correction using SCALE3 ABSPACK routine. The structures were solved using the SHELXS program and refined with the SHELXL program[105] within the Olex2 crystallographic package.[106] All computations were performed on an Intel PC computer with Windows 7 OS. Some structures contain disorder that was detected in difference Fourier syntheses of electron density and accounted for using capabilities of

the SHELX package. In most cases, hydrogen atoms were localized in difference synthesES of electron density but were refined using appropriate geometric restrictions on the corresponding bond lengths and bond angles within a riding/rotating model (torsion angles of methyl hydrogens were optimized to better fit the residual electron density).

Chapter 3

Synthetic Models of Intermediates in the Hydroquinone Dioxygenase Mechanism: Generation of Fe(II)-*p*SQate Species via Proton-Induced Valence Tautomerization
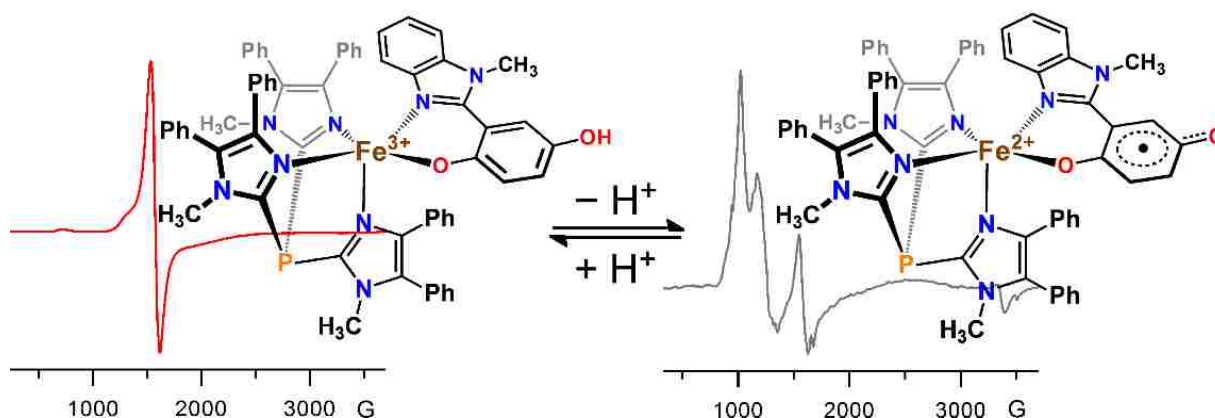
Abstract: While the nonheme Fe center in nearly all HQDOs is coordinated to one Asp (or Glu) and two His residues, 1,2-gentisate dioxygenase (GDO) is unique in featuring a three His triad instead. A synthetic GDO model was therefore prepared with the neutral tris(4,5-diphenyl-1-methylimidazol-2-yl)phosphine (^{Ph2}TIP) ligand. The gentisate substrate was mimicked with the bidentate ligand 2-(1-methylbenzimidazol-2-yl)hydroquinonate (BIHQ) to yied complex **[8]OTf**, [Fe(^{Ph2}TIP)(BIHQ)]OTf. Structural and electrochemical data collected for **[8]OTf** were compared to those previously reported for [Fe(^{Ph2}Tp)(BIHQ)] **[1]**, which features an anionic hydrotris(3,5-diphenylpyrazol-1-yl)borate (^{Ph2}Tp) ligand. Oxidation of **[8]OTf** and **[1]** provides the corresponding Fe(III) complexes ([**8b**]$^{2+}$/[**1b**]$^{+}$) and the crystal structure of [**1b**]PF$_6$ is reported. Both complexes undergo reversible deprotonation to yield the brown chromophores, **[8c]**$^{+}$ and **[1c]**. Detailed studies of **[8c]**$^{+}$ and **[1c]** with spectroscopic (UV-vis absorption, EPR, resonance Raman) and computational methods determined that each complex consists of a high-spin Fe(II) center ferromagnetically coupled to a *p*-semiquinonate radical (BISQ). The (de)protonation-induced valence tautomerization described here resembles key steps in the putative HQDO mechanism.

3.A. Introduction

In the past, biomimetic studies have proven to be fruitful in the investigation of metalloenzymes as the geometry, function and ultimately, the electronic structure of reactive intermediates can be examined especially considering that models have the capability to be modified and studied in a straightforward and systematic manner. In order to gain a better understanding of the structure and function of a specific class of mononuclear non-heme iron dioxygenases (MNIDs), we chose to pursue the study of small molecule mimics of the enzyme-substrate complex with an ultimate goal of trapping catalytically-relevant species. These metalloenzymes are responsible for catalyzing the incorporation of dioxygen into a variety of aromatic substrates upon ring cleavage in their respective pathways of catabolism. A vast majority of MNIDs incorporate a high-spin Fe(II) center bound by one Asp (or Glu) and two His residues in a facial orientation – namely, the canonical 2-His-1-carboxylate (2H1C) facial triad.[7] Numerous studies have employed the [R]Tp scaffold to replicate the monoanionic charge, facial arrangement, and ligand-field strength of the 2H1C triad.[85,107] Other chemists have prepared *N,N,O*-heteroscorpionates with one carboxylate and two nitrogen donors to more accurately reproduce the enzymatic ligand set.[108,109]

Given the prevalence of the 2H1C coordination motif among MNIDs, it was rather surprising when two crystal structures of mammalian cysteine dioxygenase (CDO), published in 2006, revealed a mononuclear iron site with a neutral 3-histidine (3His) facial triad instead.[60,61] Other members of the "3His family" were subsequently reported and structurally characterized, including β-diketone dioxygenase (Dke1),[62,63] salicylate

1,2-dioxygenase (SDO),[19] and gentisate 1,2-dioxygenase (GDO).[50,64] Of particular

relevance to this chapter is GDO, which catalyzes the oxidative cleavage of the C1−C2

bond within the hydroquinone ring of its substrate (Figure 3.1).[14,110] Interestingly, GDO is

the only known example of a hydroquinone dioxygenase (HQDO) featuring the 3His

triad;[111] all other HQDOs, including *homo*gentisate dioxygenase, possess the canonical

2H1C triad.[51]
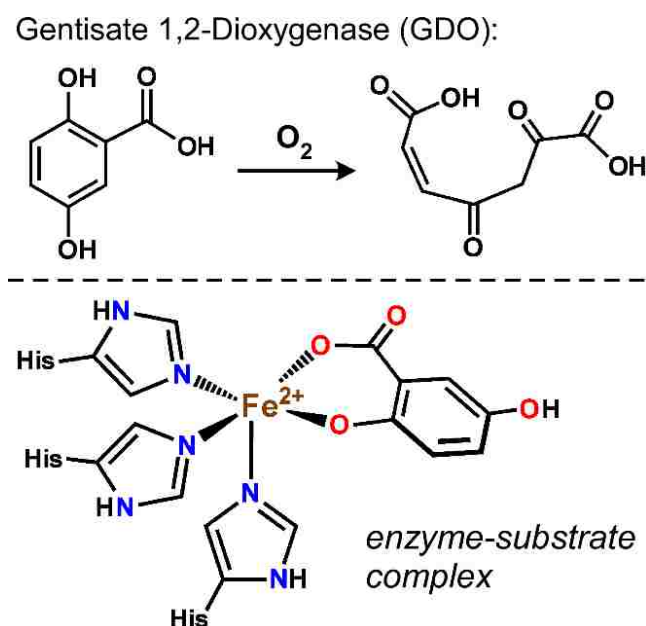
Figure 3.1. (top) Overall bond cleavage reaction facilitated by gentisate 1,2-dioxygeanse. (bottom) Enzyme-substrate complex formed upon binding of gentisate to the ferrous center of the GDO active site.

The HQDO family is unique in containing both 2H1C and 3His enzymes, and the

catalytic implications of this variation in first-sphere coordination environment currently

remains unclear. Biomimetic studies involving both neutral and anionic scorpionates

have the potential to elucidate the role of the facial triad in tuning the electronic structure

of nonheme iron sites. In the previous chapter, we reported a series of HQDO model

complexes using the hydridotris(3,5-diphenylpyrazol-1-yl)borate (^{Ph2}Tp) supporting

ligand to mimic the 2H1C triad found in most HQDOs.[112] Each complex featured a

mono- or bidentate hydroquinonate (HQate) ligand attached to the [Fe^{2+}(^{Ph2}Tp)]$^+$

scaffold, thereby replicating the structure of substrate-bound HQDOs in which the

deprotonated HQ coordinates directly to iron. The discovery of a 3His triad in the GDO

active site has since prompted us to prepare HQDO models using a neutral, imidazole-

based scorpionate ligand, specifically, tris(4,5-diphenyl-1-methylimidazol-2-

yl)phosphine (^{Ph2}TIP; Figure 3.2).
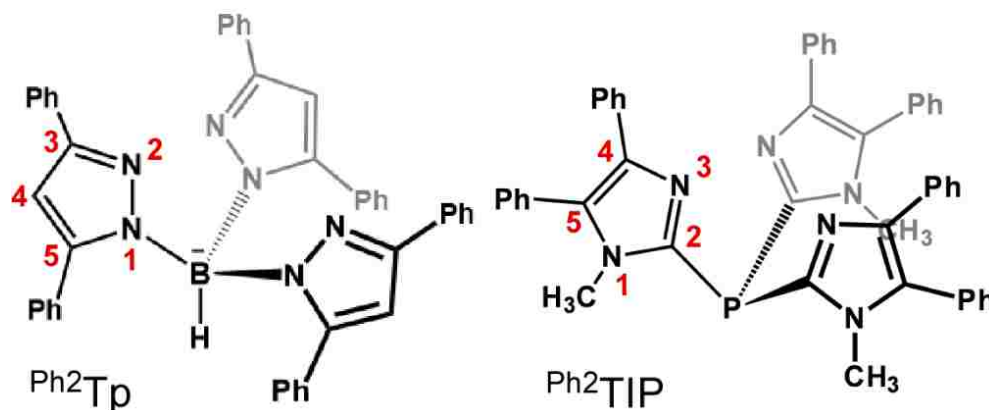
Figure 3.2. Shown here are the anionic ^{Ph2}Tp and neutral ^{Ph2}TIP ligands utilized in this chapter to model the 2H1C and 3His binding motifs, respectively.

Tris-(imidazolyl)phosphine ligands were initially developed in the 1980s to model

the active sites of Zn and Cu enzymes.[113-120] Our previous spectroscopic studies of Dke1

models found that TIP ligands accurately reproduce the coordination environment and

donor strength of the 3His triad, whereas the properties of Tp ligands align better with the

2H1C triad.[94] The ^{Ph2}Tp- and ^{Ph2}TIP-based complexes are therefore complimentary

models of the two types of HQDO active sites.
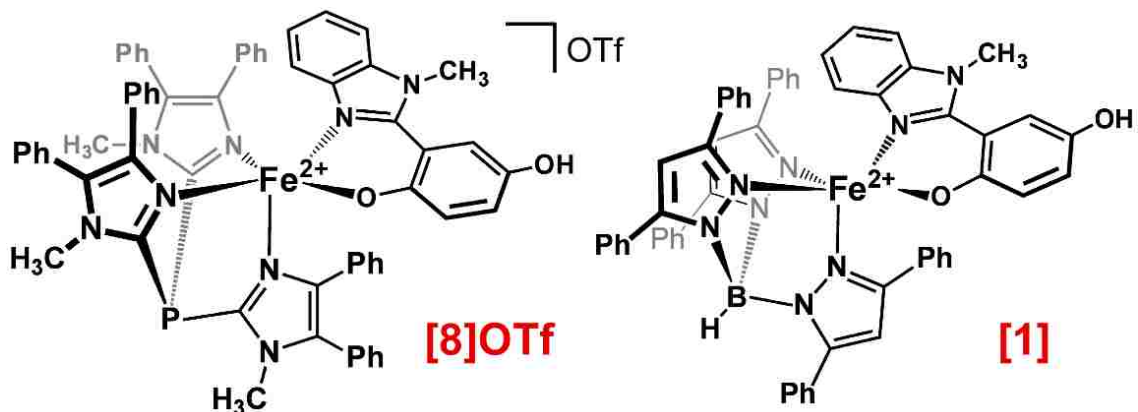
Figure 3.3. Pictorial representation of complexes **[8]OTf** and **[1]**. Both complexes contain a high-spin Fe(II) center bound to the BIHQ ligand and supported by the ^{Ph2}TIP or ^{Ph2}Tp scaffold, respectively, to mimic the metalloenzyme-derived facial binding motifs.

This chapter describes the synthesis and X-ray crystal structure of

[Fe(^{Ph2}TIP)(BIHQ)]OTf (**[8]OTf**, where BIHQ is the monoanion of 2-(1-methyl-1H-

benzimidazol-2-yl)hydroquinone; Figure 3.3). The BIHQ ligand forms a six-membered

chelate ring upon metal binding, which resembles the bidentate coordination of gentisate

to iron in the GDO mechanism. The structural and electrochemical properties of **[8]OTf**

are then compared to those previously reported for [Fe(^{Ph2}Tp)(BIHQ)] (**[1]** in Figure 3.3;

^{Ph2}TIP-based complexes are designated a **[8x]** and ^{Ph2}Tp-based complexes are labeled

[1x]). In addition, we have explored the ability of these complexes to perform proton-

and electron-transfers via stepwise or concerted processes. For **[8]OTf** and **1**, one-

electron oxidation generates the corresponding Fe(III)-HQate complexes **[8b]$^{2+}$** and

[1b]⁺. Interestingly, both **[8b]²⁺** and **[1b]⁺** undergo reversible deprotonation to yield

metastable species (**[8c]⁺** and **[1c]**, respectively) in which the Fe(II) center is bound to a

p-semiquinonate (*p*SQ$^{\bullet-}$) radical. The existence of this proton-induced valence

tautomerization has been confirmed through extensive spectroscopic and computational

studies. Complexes **[8c]⁺** and **[1c]** serve as a models of the elusive Fe(II)-*p*SQ$^{\bullet-}$

intermediate proposed for the enzymatic mechanisms of HQDOs.[52,87,121] Moreover, the

pairs of valence tautomers highlight the interplay of "noninnocent" behavior and

protonation state for ligands associated with nonheme iron centers.

3.B. Results and Discussion

3.B.i. Preparation, Solid-State Structures, and Electrochemical Properties.

Complex **[8]OTf** was synthesized by the reaction of

[Fe(^{Ph2}TIP)(MeCN)₃](OTf)₂[122] with an equimolar amount of Na(BIHQ) salt in THF.

Yellow crystals, of sufficient quality for X-ray diffraction (XRD) analysis, were grown

by vapor diffusion of diethyl ether into a concentrated 1,2-dichloroethane (DCE)

solution. The asymmetric unit of the X-ray structure consists of the cationic monoiron

complex, the triflate counteranion, and two Et₂O solvates. As shown in Figure 3.4(a), the

five-coordinate (5C) Fe(II) center of **[8]OTf** is attached to a facially-capping ^{Ph2}TIP

ligand and bidentate BIHQ anion. The distorted coordination geometry is intermediate

between square-pyramidal and trigonal-pyramidal. The two rings of the BIHQ chelate are

rotated by 27° with respect to each other, largely to accommodate the π-π stacking

interaction between the benzimidazole unit and a nearby 4-phenyl substituent of ^{Ph2}TIP. The distal –OH moiety of BIHQ forms a hydrogen bond with one of the Et_2O solvates.

The Fe-N$_{TIP}$ bond lengths of **[8]OTf** range from 2.11 Å for N3 to 2.22 Å for the pseudo-axial N5 donor (Table 3.1). The anionic BIHQ ligand exhibits Fe1-O1 and Fe1-N7 distances of 1.91 and 2.15 Å, respectively, typical of phenolate[68,123,124] and benzimidazole[125-127] donors in high-spin ferrous complexes. The observed magnetic moment of $\mu_{eff} = 4.93$ μ_B at room temperature (RT) is also proof that **[8]OTf** possesses a high-spin ($S = 2$) Fe(II) center.

Table 3.1 compares the metric parameters of ^{Ph2}TIP-based **[8]OTf** to those previously reported for ^{Ph2}Tp-based **[1]**. The coordination geometries of the two complexes are quite similar, as evident in the overlay of solid-state structures shown in Figure 3.4(b). The structure of **1** falls somewhat closer to the square-pyramidal limit than **[8]OTf**, as indicated by the respective τ-values[98] of 0.35 and 0.43 (Table 3.1). The average Fe-N$_{TIP}$ bond length in **[8]OTf** is about 0.03 Å longer than the average Fe-N$_{Tp}$ bond length in **[1]**, in line with our previous comparisons of Fe(II) Tp/TIP pairs.[24,94]

The redox properties of **[8]OTf** were examined using electrochemical methods in CH_2Cl_2 solution with 0.1 M [NBu$_4$]PF$_6$ as the supporting electrolyte. All redox potentials are referenced to the ferrocene (Fc$^{+/0}$) couple. Two features are evident in the cyclic voltammogram (CV): a quasi-reversible couple at -190 mV ($\Delta E = 200$ mV) and an irreversible oxidation at $E_{p,a} = 950$ mV (Figure 3.5). Based on our prior experience with **[1]** and related complexes, the lower-potential event is assigned to the Fe$^{2+/3+}$ couple, while the high-potential peak is attributed to oxidation of the BIHQ ligand.[24,94,112] CV data obtained for **[1]** is provided in Figure 3.5 for the sake of comparison. The Fe$^{2+/3+}$

potential of **[8]OTf** is shifted positively by 100 mV relative to **[1]** due to the weaker

donor strength of neutral ^{Ph2}TIP relative to anionic ^{Ph2}Tp.
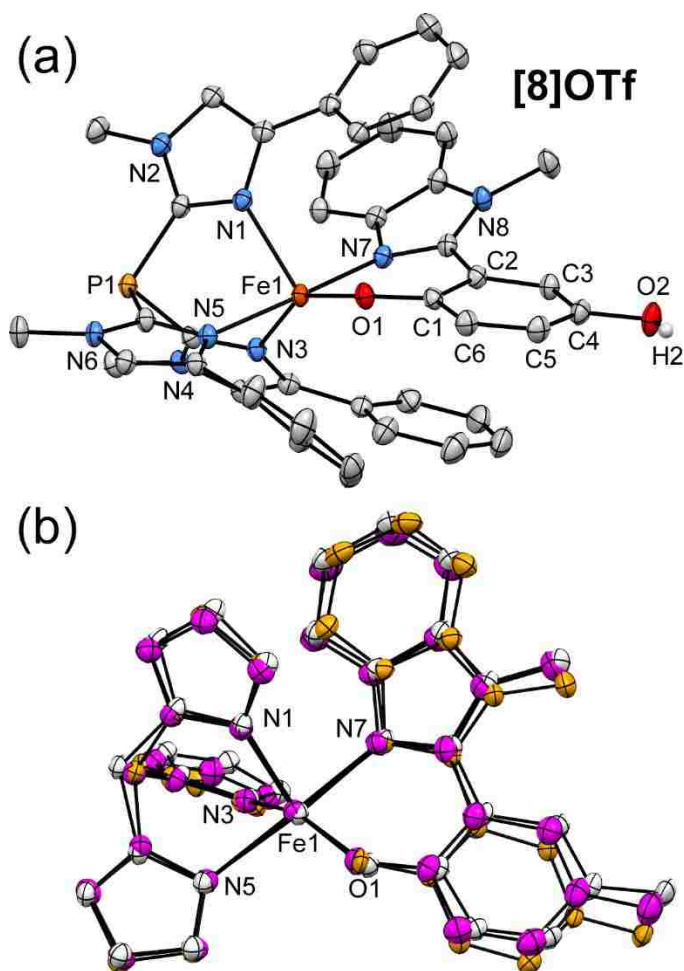
Figure 3.4. (a) Thermal ellipsoid plot (50% probability) obtained from the X-ray crystal structure of **[8]OTf**. The phenyl rings at the 5-positions of the ^{Ph2}TIP ligand have been omitted for clarity, as well as non-coordinating solvent molecules and most hydrogen atoms. (b) Overlays of the crystallographically-derived structures of **[8]OTf** (white), [**1**] (orange), and **[1b]PF₆** (magenta). The phenyl and methyl substituents of the ^{Ph2}Tp and ^{Ph2}TIP ligands are not shown.

Table 3.1. Selected Bond Distances (Å) and Bond Angles (°) for Complexes **[8]OTf**, **[1]**, and **[1b]PF₆** as Measured by X-ray Crystallography.

Bond Distances	[8]OTf	[1]ᵃ	[1b]PF₆
Fe–N1	2.1681(12)	2.1218(14)	2.0409(17)
Fe–N3	2.1149(12)	2.1481(15)	2.0464(18)
Fe–N5	2.2214(12)	2.1470(15)	2.1138(17)
Fe–O1	1.9144(10)	1.9609(12)	1.8292(15)
Fe–N7	2.1503(13)	2.1393(15)	2.0693(17)
Fe–N$_{Tp/TIP}$ (ave)	2.168	2.139	2.067
Fe–L (ave)	2.114	2.103	2.020
O1–C1	1.321(2)	1.341(2)	1.337(2)
O2–C4	1.377(2)	1.370(2)	1.373(3)
C1–C2	1.423(2)	1.417(2)	1.412(3)
C1–C6	1.409(2)	1.405(2)	1.399(3)
C2–C3	1.410(2)	1.410(2)	1.403(3)
C3–C4	1.380(2)	1.379(2)	1.384(3)
C4–C5	1.393(2)	1.397(2)	1.390(3)
C5–C6	1.385(2)	1.383(2)	1.376(3)
C–C (ave)	1.400	1.399	1.394
C–C (dev) ᵇ	0.017	0.015	0.013
Bond Angles			
O1–Fe–N1	117.31(5)	110.64(5)	115.58(7)
O1–Fe–N3	147.79(5)	153.34(5)	147.84(7)
O1–Fe–N5	98.33(4)	94.78(5)	94.80(7)
O1–Fe–N7	88.20(5)	88.90(5)	88.92(7)
N1–Fe–N3	94.87(5)	95.65(6)	96.52(7)
N1–Fe–N5	88.04(5)	92.11(5)	90.95(7)
N1–Fe–N7	89.69(5)	90.69(6)	91.19(7)
N3–Fe–N5	83.23(5)	79.38(6)	82.10(7)
N3–Fe–N7	90.82(5)	95.37(6)	92.54(7)
N5–Fe–N7	173.42(5)	174.27(6)	174.42(7)
τ-value ᶜ	0.43	0.35	0.44

ᵃ The structure of **1** was originally reported in reference 112. ᵇ This number reflects the standard deviation of C-C bond distances. ᶜ See reference 98 for the definition of the τ-value.

On the basis of the CV data, we sought to isolate the ferric complexes **[8b]²⁺** and **[1b]⁺** using chemical means of oxidation. To this end, treatment of the yellow Fe(II) complexes with one equivalent of a ferrocenium (Fc⁺) salt in CH_2Cl_2 gives rise to dark brown chromophores with intense absorption bands in the visible region (<u>Figure 3.6</u>). The spectrum of **[8b]²⁺** exhibits a broad feature with λ_{max} = 630 nm (ε = 2600 $M^{-1}cm^{-1}$), while **[1b]⁺** displays two intense, overlapping bands between 400 and 600 nm. These features likely arise from phenolate-to-Fe(III) charge transfer (CT) transitions.[100,101] Indeed, both complexes exhibit EPR signals characteristic of rhombic, high-spin Fe(III) centers; namely, an intense derivative-shaped feature at g = 4.3 and a much weaker peak at g = 9.4 (<u>Figures 3.7 and 3.8</u>).
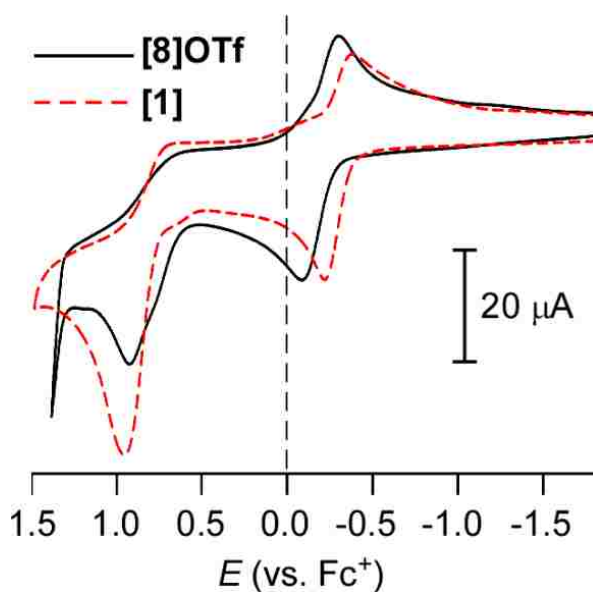
Figure 3.5. Cyclic voltammograms of **[8]OTf** and **[1]** in CH_2Cl_2 (conc. = 2.0 mM) with 0.1 M (NBu₄)PF₆ as the supporting electrolyte.

Crystals of **[1b]PF₆** suitable for XRD studies were generated by oxidation with [Fc]PF₆, followed by diffusion of pentane into a concentrated DCE solution (to date, we have not been able to grow crystals of **[8b]²⁺** with any counteranion). Metric parameters derived from the resulting crystal structure are shown in <u>Table 3.1</u>. Complex **[1b]PF₆** retains the five-coordinate geometry of its ferrous precursor, as illustrated by the high degree of overlap between the **[1]** and **[1b]PF₆** structures depicted in <u>Figure 3.4(b)</u>. The presence of the distal –OH moiety of BIHQ is evident from the hydrogen bond it forms with the PF_6^- counteranion. Compared to **[1]**, the average $Fe-N_{Tp}$ and Fe-O1 bond distances in **[1b]PF₆** are contracted by 0.07 and 0.13 Å, respectively, while the O–C and C–C distances of the BIHQ ligand are unchanged within experimental error (<u>Table 3.1</u>). Therefore, the XRD data confirm that conversion of **[1]** into **[1b]PF₆** involves an iron-centered oxidation, and there is no detectable amount of radical character on the BIHQ ligand. Although XRD data is lacking for **[8b]²⁺**, the spectroscopic results (*vide supra*) indicate that this complex also contains an Fe(III) center bound to a HQate ligand.
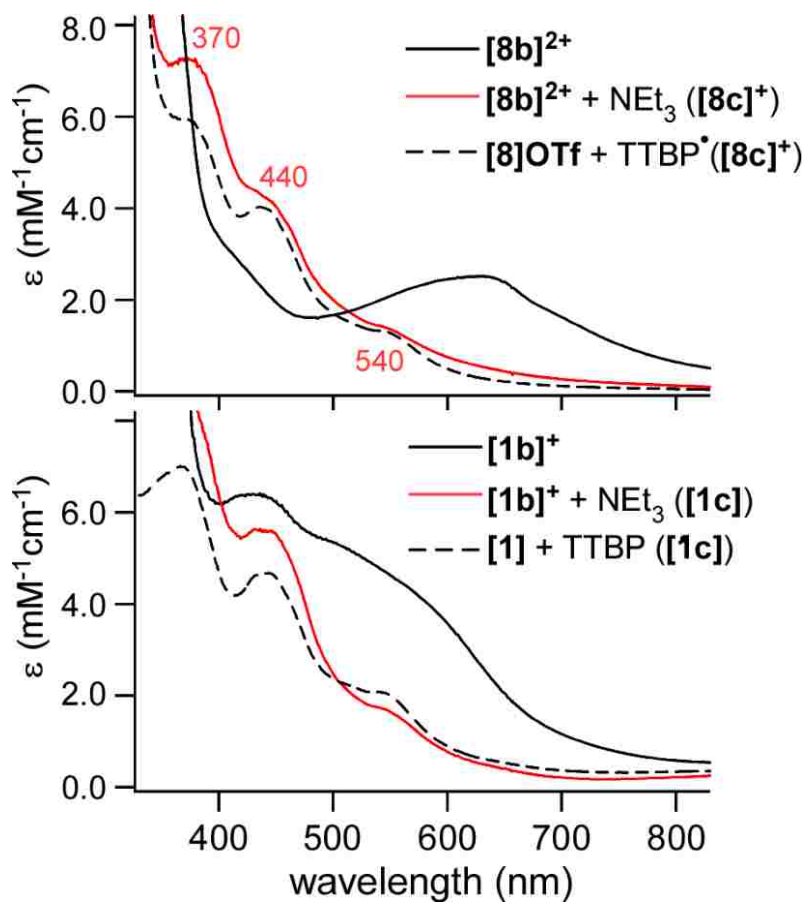
Figure 3.6. UV-visible absorption spectra measured in CH_2Cl_2. The red spectra of [**8c**]⁺/[**1c**] were obtained by treating solutions of **[8b]²⁺**/**[1b]⁺** (black solid lines) with 5 equiv. of NEt₃ at -30 °C. The black spectra of **[8c]⁺**/**[1c]** (dashed lines) were collected after treating solutions of **[8]OTf**/**[1]** with one equiv. of the TTBP• radical at RT.
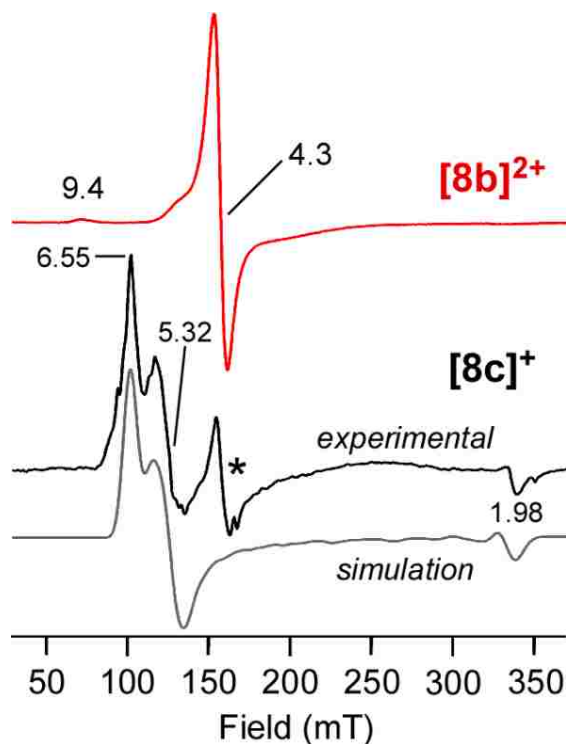
Figure 3.7. X-band EPR spectra of **[8b]$^{2+}$** (red line) and **[8c]$^+$** (black line) in frozen CH$_2$Cl$_2$ solution ([Fe] = 1.4 mM) at 15 K. The intensity of the **[8b]$^{2+}$** spectrum has been reduced by 50%. The feature labeled with an asterisk (*) in the **[8c]$^+$** spectrum arises from residual **[8b]$^{2+}$**. The simulated **[8c]$^+$** spectrum (grey line) was obtained with the following parameters: $D = 0.63$ cm^{-1}, $E/D = 0.03$, and $g = 2.02, 2.0, 2.0$.
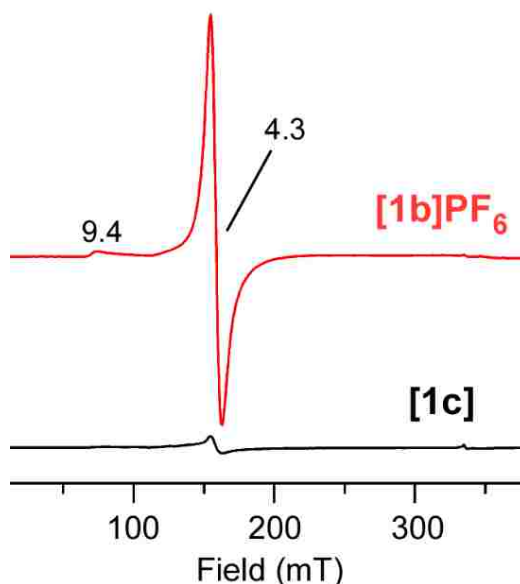
Figure 3.8. X-band EPR spectra of **[1b]PF$_6$** (red line) and **[1c]** (black line) in frozen CH$_2$Cl$_2$ solution ([Fe] = 1.2 mM) at 10 K.

3.B.ii. Formation and Spectroscopic Features of [8c]$^+$ and [1c].

Treatment of complexes **[8b]$^{2+}$** and **[1b]$^+$** with 5-10 equivalents of triethylamine in CH$_2$Cl$_2$ immediately yields the golden-brown chromophores **[8c]$^+$** and **[1c]**, respectively (Figure 3.6). The absorption spectra of the new species are nearly identical, with each displaying three bands of increasing intensity at 540, 440, and 370 nm. The reaction is reversible, as addition of excess acid (HBF$_4$) to solutions of **[8c]$^+$/[1c]** regenerates the **[8b]$^{2+}$/[1b]$^+$** spectra with only 15% reduction in intensity (Figure 3.9).
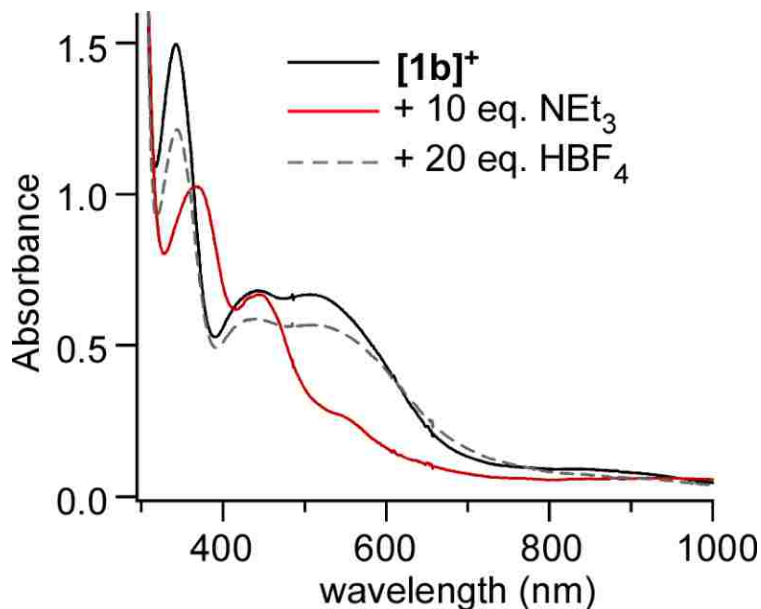
Figure 3.9. UV-visible absorption spectra demonstrating the reversible deprotonation of complex **[1b]PF$_6$**. The black solid line corresponds to the spectrum of **[1b]PF$_6$** [conc. = 0.11 mM] at -60 $^{\circ}$C in CH$_2$Cl$_2$. Addition of 10 equivalents of NEt$_3$ at -60 $^{\circ}$C yielded the red (solid line) spectrum characteristic of **[1c]**. Finally, treatment with excess acid (HBF$_4$ in Et$_2$O, 20 equivalents) at -60 $^{\circ}$C, followed by warming to RT, provided the grey (dashed line) spectrum, indicating nearly complete regeneration of **[1b]$^+$**. All three spectra were collected using the same sample, which was prepared by dissolving crystalline **[1b]PF$_6$** in CH$_2$Cl$_2$.

Given the structure of the Fe(III) complexes, it is reasonable to assume that the

Xb → Xc conversion involves deprotonation of the distal –OH group of the BIHQ ligand.

In support of this conclusion, **[8c]$^+$** and **[1c]** can also be prepared by treatment of the

ferrous precursors (**[8]OTf** and **[1]**) with 2,4,6-tri-tert-butylphenoxy radical (TTBP$^{\bullet}$) – a

well-established H-atom transfer (HAT) agent (Figure 3.6).[128] Thus, the three complexes

in each series (**[8]OTf/[1]**, **[8b]$^{2+}$/[1b]$^+$**, **[8c]$^+$/[1c]**) can be interconverted by concerted or

stepwise transfers of one electron and/or one proton, as indicated in Figure 3.10.
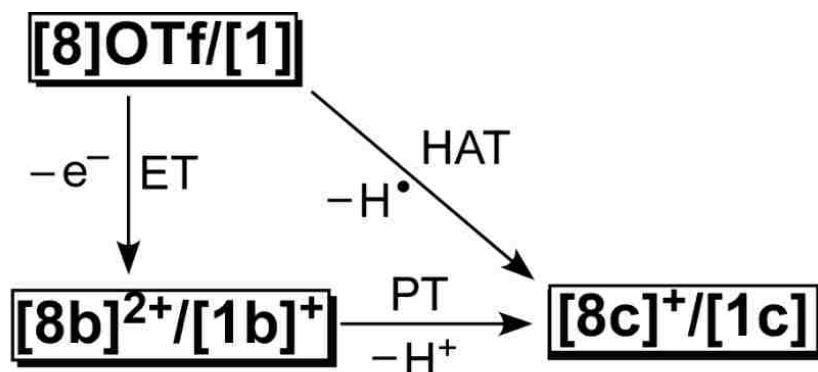
Figure 3.10. Summary of interconversion of species examined in this chapter via concerted or stepwise transfers of one electron and one proton.

Bases other than NEt_3 were used in an attempt to estimate the pK_a of **[8b]$^{2+}$** and **[1b]$^+$**. For both complexes, addition of the weaker base 2,6-lutidine in CH_2Cl_2 failed to generate the corresponding **[8c]$^+$**/**[1c]** species. Similar results were observed for **[8b]$^{2+}$** in MeCN solutions, where the pK_a-values of triethylammonium ($HNEt_3^+$) and 2,6-lutidinium (2,6-LutH$^+$) are known to be 18.6 and 14.0, respectively.[129] Bordwell and Mayer have proven that the bond dissociation free energy (BDFE) of an X–H bond is a function of both pK_a and redox potential (E^o), according to the following equation: BDFE (X–H) = 1.37 pK_a + 23.06 E^o + $C_{G,solv}$, where $C_{G,solv}$ is a solvent-dependent constant equal to 54.9 kcal mol^{-1} in MeCN.[99] Using the experimental redox potential, and assuming that a pK_a-value halfway between $HNEt_3^+$ and 2,6-LutH$^+$, provides a BDFE of 72.9 kcal mol^{-1} for **[8]OTf**. This bond energy is reasonable given that **[8]OTf** transfers a H-atom to TTBP$^\bullet$ (BDFE = 77.1 kcal mol^{-1}) but not to the TEMPO$^\bullet$ radical (BDFE = 66.5 kcal mol^{-1}; all values in MeCN).[99]

Unfortunately, it was not possible to grow crystals of **[8c]$^+$** or **[1c]** for XRD studies; therefore, electronic-structure insights were gathered using spectroscopic

methods, in conjunction with the DFT calculations described in the next section. Two limiting descriptions are possible: **[8c]**[+]/**[1c]** could consist of an Fe(III) center bound to a closed-shell hydroquinonate dianion (HQate^{2-}), or an Fe(II) center bound to a *p*-semiquinonate radical anion (*p*SQ$^{\bullet-}$). Significantly, the UV-vis absorption spectra of **[8c]**[+]/**[1c]** closely resemble those published for *para*- and *ortho*-semiquinone radicals in various contexts.[130,131] For example, our group recently prepared a ^{Ph2}Tp-based Fe(II) complex that features a 1,4-naphthosemiquinone ligand. This complex displays a three-band pattern between 380 and 560 nm with intensities very similar to those observed for **[8c]**[+]/**[1c]**.[131] Transient absorption studies of "free" *p*-semiquinones likewise report a series of π-π* transitions in the near-UV region.[132-134] Indeed, the close similarity of the **[8c]**[+] and **[1c]** spectra suggests that the observed transitions are primarily ligand-based – a hypothesis supported by time-dependent DFT calculations (*vide infra*).

EPR samples of **[8c]**[+] and **[1c]** were prepared via stepwise oxidation and deprotonation of **[8]OTf/[1]**. Interestingly, it was observed that CH_2Cl_2 solutions of **[1c]** change color from golden-brown to green upon freezing, whereas **[8c]**[+] maintains its brown color at all temperatures. Variable-temperature absorption studies found that the 440 and 540 nm bands of **[1c]** diminish as the temperature is lowered to -70 °C, while a new chromophore (labeled **[1d]**) appears with a broad band at $\lambda_{max} = 825$ nm. This thermochromic behavior is reversible, as **[1d]** converts back to **[1c]** when the temperature is returned to 25 °C (Figure 3.11).
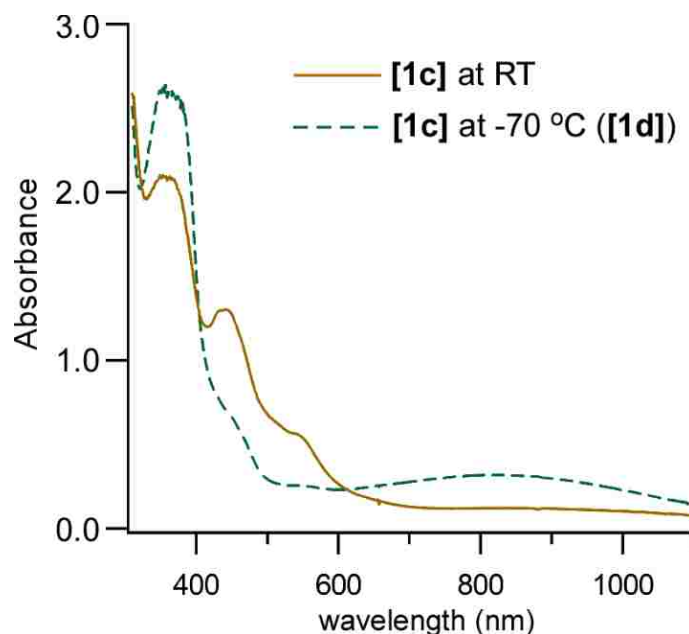
Figure 3.11. Thermochromism of complex **[1c]**. A solution of **[1]** in CH_2Cl_2 (conc. = 0.25 mM) was treated with one equivalent of the TTBP$^\bullet$ radical at -70 $^\circ$C, providing the absorption spectrum of **[1d]** (green dashed line). The sample changed color from green to brown upon warming to RT, eventually yielding a spectrum characteristic of **[1c]** (brown solid line).

The EPR spectrum of **[1d]** measured at 15 K is featureless apart from a weak peak at $g = 4.3$ due to residual **[1b]**$^+$ (Figure 3.8). While further studies are required, we postulate that **[1d]** arises from dimerization of **[1c]** at low temperatures, which would yield the EPR-silent species observed experimentally.

Thankfully, the absence of thermochromism for **[8c]**$^+$ indicates that the structure of this complex is maintained upon freezing. Unlike **[1d]**, complex **[8c]**$^+$ exhibits an intense EPR signal at 10 K with features at $g = 6.55$, 5.32, and 1.98, along with a small derivative at $g = 4.3$ from residual **[8b]**$^{2+}$ (Figure 3.7). This spectrum is characteristic of a $S = 5/2$ paramagnet with an axial **D**-tensor; the data was nicely simulated with spin-Hamiltonian parameters of $g = 2.02$, 2.0, 2.0; $D = 0.63$ cm^{-1}, $E/D = 0.03$ (Figure 3.7;

where D and E are the axial and rhombic zero-field splitting parameters, respectively).

Given the rhombic nature of the **[8b]$^{2+}$** spectrum ($E/D \sim 0.33$) noted above, the EPR

results make it clear that the **[8b]$^{2+}$**→**[8c]$^{+}$** conversion causes a dramatic rearrangement of

unpaired spin-density within the $S = 5/2$ manifold. The origin of this change has been

elucidated with the aid of DFT calculations described in the next section.

3.B.iii. Geometric and Electronic Structures of DFT-optimized Models.

Table 2 provides relevant metric parameters for energy-minimized structures of

complexes **[1b]$^{+}$**, **[8c]$^{+}$**, and **[1c]** obtained via DFT geometry optimizations. Truncated

versions of the complexes were employed in which the Ph rings at the 5-positions of the

^{Ph2}Tp and ^{Ph2}TIP ligands were removed. Unless otherwise noted, all calculations

employed the hybrid B3LYP functional and assumed a $S = 5/2$ ground state. The

accuracy of our computational approach was gauged by comparing the XRD and DFT

structures of complex **[1b]$^{+}$**. While DFT slightly overestimates the Fe(III)-N/O bond

lengths (by 0.05 Å on average), it accurately reproduces the C-C and O-C bond distances

of the HQate ligand, with a root-mean-square deviation of only 0.01 Å (*i.e.*, near the

experimental 3σ error of the XRD measurement). We therefore felt confident in

proceeding with calculations of **[8c]$^{+}$** and **[1c]**, for which structural data are lacking.

Table 3.2. DFT-Calculated Bond Distances (Å) for Models of **[1b]⁺**, **[1c]**, **[8c]**, and the BISQ Radical

		[1b]⁺	**[1c]**	Δᵃ	**[8c]**	Free BISQ•ᵇ
Bond	Fe–N1	2.110	2.180	0.070	2.214	
Distances	Fe–N3	2.084	2.177	0.093	2.186	
	Fe–N5	2.162	2.250	0.088	2.348	
	Fe–O1	1.861	1.982	0.121	1.952	
	Fe–N7	2.152	2.190	0.038	2.185	
	Fe–L (ave)	2.074	2.156	0.082	2.177	
	O1–C1	1.320	1.293	-0.027	1.303	1.327
	O2–C4	1.360	1.256	-0.104	1.254	1.253
	C1–C2	1.421	1.444	0.023	1.438	1.441
	C1–C6	1.409	1.432	0.023	1.428	1.416
	C2–C3	1.404	1.386	-0.018	1.386	1.383
	C3–C4	1.388	1.442	0.054	1.441	1.444
	C4–C5	1.401	1.448	0.047	1.448	1.447
	C5–C6	1.409	1.361	-0.048	1.362	1.362
	C–C (ave)	1.400	1.419	0.019	1.417	1.416
	C–C (dev)ᶜ	0.016	0.036		0.035	0.036
Mulliken	Fe	4.14	3.81	-0.33	3.80	—
spins	O,N-ligand	0.34	1.09	+0.75	1.13	1.04

ᵃ Difference between corresponding **[1b]⁺** and **[1c]** bond lengths. ᵇ Geometry-optimized model of the BISQ radical (H-atom removed from the 4-OH position). ᶜ Standard deviation of the six C-C bond distances within the BIHQ or BISQ ring.

The structural differences between **[1b]⁺** and **[1c]/[8c]⁺** are highlighted in Table 3.2. The iron-ligand bonds in **[1c]** are longer than their counterparts in **[1b]⁺** by an average of 0.082 Å; indeed, the computed Fe-L distances in **[8c]⁺** and **[1c]** are more similar to those observed experimentally for the Fe(II) complexes **[8]OTf** and **[1]**.ᵃ The bidentate *O,N*-ligand derived from BIHQ also experiences sizable changes. The closed-shell nature of the HQate donor in **[1b]⁺** is evident in the uniformity of its six C-C bond

---

ᵃ This statement is true even when accounting for the systematic overestimation of Fe-L bonds by DFT.

lengths (standard deviation of 0.016 Å). In the **[8c]**⁺ and **[1c]** models, however, this deviation increases to 0.035 Å and the C–C bonds display the "four long/two short" pattern characteristic of semiquinones.[35,135] This quinoidal-type distortion is also apparent in the dramatic shortening of the O2–C4 bond from 1.360 Å in **[1b]**⁺ to ~1.255 Å in **[8c]**⁺/**[1c]**. Significantly, the metric parameters of the bidentate *O,N*-ligand in **[8c]**⁺/**[1c]** are very similar to those computed for the "free" 2-(1-methylbenzimidazol-2-yl)semiquinone radical (BISQ•; Table 2). Collectively, the DFT results indicate that deprotonation of the distal –OH moiety triggers an electron transfer (ET) from BIHQ to the Fe center, giving rise to an Fe(II)-BISQ configuration. This conclusion is further supported by the Mulliken spin populations of the Fe center (3.8 α spins) and BISQ ligand (1.1 α spins) in the **[8c]**⁺/**[1c]** models (Table 3.2).

DFT calculations of **[1c]** were used to generate the molecular orbital (MO) diagram shown in Figure 3.12. The most critical orbitals for evaluating the electronic configuration of this complex are the frontier MOs in the spin-down (β) manifold. The highest-occupied β MO (203β) possesses 81% Fe character with electron density primarily located in the Fe d_{yz} orbital, confirming the presence of a high-spin Fe(II) ion. By contrast, the lowest-unoccupied β MO (204β) has 84% ligand character localized in a π*-orbital on the *p*SQ•⁻ unit, clear evidence of a ligand-based radical. Ferromagnetic coupling between the Fe(II) center ($S = 2$) and BISQ radical ($S = 1/2$) yields the axial $S = 5/2$ paramagnet observed in the EPR spectrum of **[8c]**⁺.
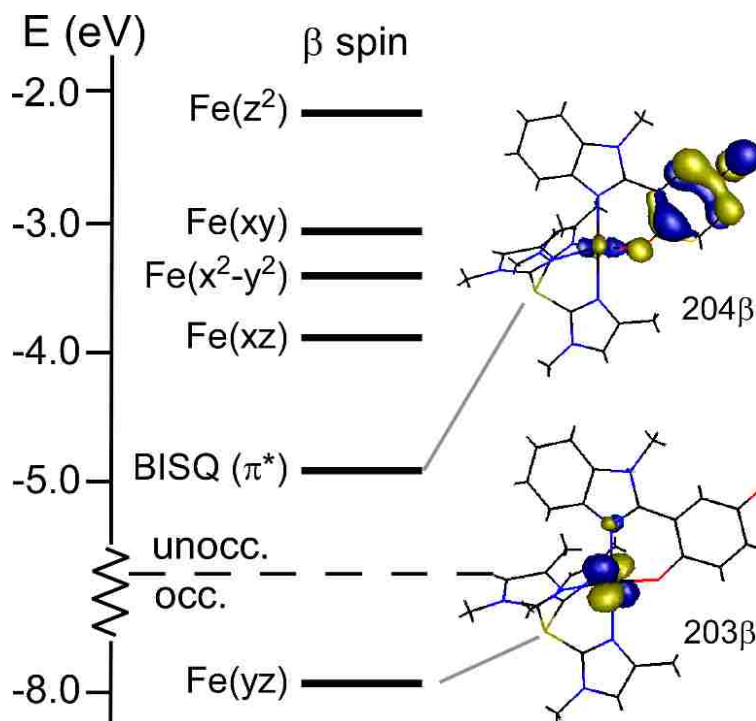
Figure 3.12. Energy-level diagram for the spin-down (β spin) MOs obtained from an unrestricted DFT calculation of **[8c]**$^+$. MOs are labeled according to their principal contributor. Surface contour plots for the highest-occupied and lowest-unoccupied orbitals are also shown.

The time-dependent DFT (TD-DFT) approach was employed to compute the absorption spectrum of **[8c]**$^+$. As shown in Figure 3.13, the calculated spectrum adequately reproduces the energies and intensities of the experimental absorption features, suggesting that our DFT model of **[8c]**$^+$ provides an accurate description of the complex's electronic structure. Analysis of the computed transitions indicate that the lowest-energy feature near 550 nm arises from an Fe(II)→BISQ charge transfer (CT) transition, while the higher-energy peaks (350 nm < λ_{max} < 450 nm) are due to BISQ-based π→π* transitions. These findings are consistent with our prior studies of a monoiron(II) complex containing a 1,4-naphthosemiquinone ligand.[131]

To ensure that our computational results were not simply due to our chosen methodology, we also performed parallel calculations of **[8c]**$^+$ and **[1c]** with the *non-hybrid* Becke Perdew 86 functional (BP). As shown in Table 3.3, the ligand metric parameters of the BP optimized structures are nearly identical to those obtained with B3LYP (rms deviation of 0.009 Å), although the Fe-N/O distances computed by BP are shorter by ~0.04 Å on average. Importantly, the bonding descriptions and spin-density distributions provided by the BP calculations are indicative of an Fe(II)-BISQ electronic configuration for **[8c]**$^+$/**[1c]**, in agreement with the B3LYP results.

Table 3.3. DFT-Calculated Bond Distances (Å) for Models of **[8c]**[+] and **[1c]** Using the BP and B3LYP Functionals.

		3a (B3LYP)	3a (BP)	Δ [a]	3b (B3LYP)	3b (BP)	Δ [a]
Bond	Fe–N1	2.214	2.137	-0.077	2.180	2.141	-0.039
Distances	Fe–N3	2.186	2.157	-0.029	2.177	2.152	-0.025
	Fe–N5	2.348	2.285	-0.063	2.250	2.213	-0.037
	Fe–O1	1.952	1.928	-0.024	1.982	1.930	-0.052
	Fe–N7	2.185	2.139	-0.046	2.190	2.148	-0.042
	Fe–L (ave)	2.177	2.129	-0.048	2.156	2.117	-0.039
	O1–C1	1.303	1.313	0.010	1.293	1.313	0.020
	O2–C4	1.254	1.263	0.009	1.256	1.266	0.010
	C1–C2	1.438	1.447	0.009	1.444	1.445	0.001
	C1–C6	1.428	1.423	-0.005	1.432	1.431	-0.001
	C2–C3	1.386	1.396	0.010	1.386	1.398	0.012
	C3–C4	1.441	1.449	0.008	1.442	1.448	0.006
	C4–C5	1.448	1.454	0.006	1.448	1.454	0.006
	C5–C6	1.362	1.370	0.008	1.361	1.372	0.011
	C–C (ave)	1.417	1.423	0.006	1.419	1.425	0.006
	C–C (dev) [b]	0.035	0.034		0.036	0.033	
Mulliken	Fe	3.80	3.77		3.81	3.83	
spins	O,N-ligand	1.13	1.13		1.09	0.99	

[a] Difference between BP- and B3LYP-computed bond distances. [b] Standard deviation of the six C-C bond distances within the BIHQ or BISQ ring.
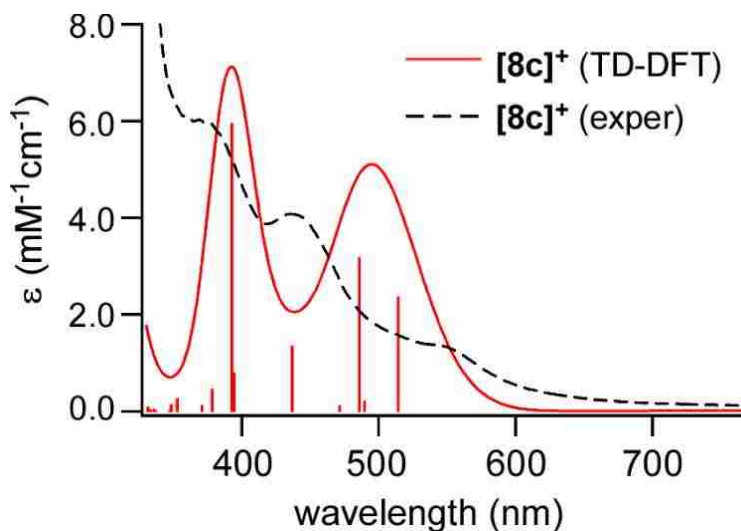
Figure 3.13. Experimental (black dashed line) and TD-DFT computed (solid red line) absorption spectra of **[8c]⁺**. The experimental spectrum was obtained by treating **[8]OTf** with the TTBP⁺ radical in CH_2Cl_2. The red sticks mark the wavelengths and intensities of computed transitions.

3.B.iv. Resonance Raman Spectroscopic Studies

The electronic structures of complexes **[8c]⁺** and **[1c]** were further examined with resonance Raman (rR) spectroscopy – a well-established method for the characterization of semiquinone radicals. The experiments employed 457.9 nm laser excitation, in resonance with the ligand-based π-π* transition observed near 440 nm. Spectra of **[1c]** and its **[1b]⁺** precursor were measured at 273 K due to the thermochromic nature of the former complex (*vide supra*), whereas the **[8c]⁺** spectrum was collected at 77 K on a frozen sample. Figure 3.14 highlights the 1200-1700 cm⁻¹ region where peaks due to aromatic C–C and O–C stretching modes are typically found. The **[8c]⁺** and **[1c]** spectra exhibit an intense feature near 1527 cm⁻¹ that is not apparent in the **[8b]²⁺** spectrum, and it arises regardless of the route of preparation (concerted H-atom transfer or sequential

oxidation/deprotonation). A series of peaks is also evident between 1400 and 1500 cm^{-1}, especially in the low-temperature **[8c]$^+$** spectrum.

To aid in assignment of the observed rR peaks, DFT frequency calculations were performed for the BIHQ ligand in three oxidation states: the hydroquinonate anion (**BIHQate**; deprotonated at 4-OH position), semiquinone radical (**BISQ**; H-atom removed from 4-OH position), and benzoquinone (**BIBQ**). We focused specifically on the predicted frequency of the distal O-C stretching mode [ν(O2−C4)], since studies of *ortho*-dioxolene compounds have demonstrated that ν(O-C) modes give rise to intense rR peaks that are diagnostic of ligand oxidation state.[136-142] The computed ν(O2−C4)-based mode appears at 1414 and 1681 cm^{-1} for **BIHQate** and **BIBQ**, respectively, following the expected increase in frequency as the ligand becomes more oxidized. The **BISQ** calculation predicts two modes with significant ν(O2−C4) character at intermediate frequencies of 1449 and 1521 cm^{-1}. The 1449 cm^{-1} vibration couples the ν(O2−C4) stretch with the breathing motion of the *p*SQ ring, while the 1521 cm^{-1} vibration couples the ν(O2−C4) stretch to nearby bending motions. Significantly, these calculated ν(O2−C4) frequencies are consistent with previous studies of *p*SQ radicals[143] and remarkably close to the experimentally-observed peaks at 1527 and ~1450 cm^{-1} in the **[8c]$^+$**/**[1c]** spectra (Figure 3.14). Thus, the rR data provide further evidence that complexes **[8c]$^+$** and **[1c]** possess a BISQ ligand.
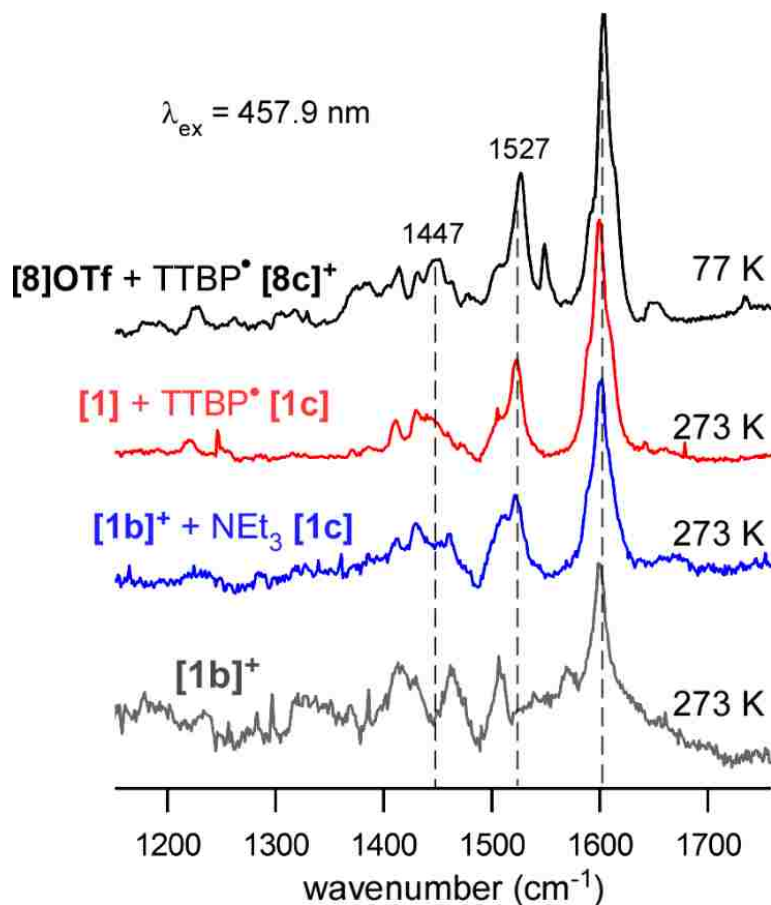
Figure 3.14. Resonance Raman spectra obtained with 457.9 nm excitation (40 mW at sample) of **[1b]⁺**, **[8c]⁺**, and **[1c]** in CD_2Cl_2 solutions. The **[8c]⁺** sample was prepared by treatment of the **[8]OTf** precursor with TTBP•. The rR spectrum of **[8c]⁺** (black line) was collected at 77 K. Samples of **[1c]** were prepared via two routes: treatment of **[1]** with TTBP• (red spectrum) or addition of 5 equiv. of NEt_3 to **[1b]⁺** (blue spectrum). rR spectra of **[1c]** and **[1b]⁺** (gray line) were measured at 273 K (ice/water bath).

3.C. Conclusion

This chapter has described the preparation and X-ray structural characterization of complex **[8]OTf** (Figure 3.3) – the first synthetic model of the nonheme iron enzyme GDO. The mononuclear Fe(II) center in the GDO active site is coordinated by a 3His facial triad (Figure 3.2), in contrast to the 2H1C triad found in all other HQDOs.[50,64] Complex **[8]OTf** features a neutral ^{Ph2}TIP scorpionate ligand to mimic the enzymatic

3His triad, while the bidentate BIHQ ligand models the coordination of gentisate to the Fe(II) ion. The structural and electrochemical properties of **[8]OTf** were compared to those previously reported for the analogous complex **[1]**, which contains a monoanionic ^{Ph2}Tp scorpionate ligand (Figure 3.3) that better resembles the 2H1C triad. Overall, the differences between **[8]OTf** and **[1]** are modest: the Fe$-$N$_{TIP}$ bonds are longer than the Fe$-$N$_{Tp}$ distances by an average of 0.03 Å (Table 1), and the Fe$^{3+/2+}$ redox potential of **[8]OTf** is shifted positively by ~100 mV relative to **[1]** (Figure 3.5).

Spectroscopic and crystallographic methods confirmed that one-electron oxidation of **[8]OTf** and **1** yields the Fe(III)-HQate complexes **[8b]$^{2+}$** and **[1b]$^{+}$**. Treatment of the Fe(III) complexes with excess NEt$_3$ gives rise to the brown chromophores **[8c]$^{+}$** and **[1c]**, which can also be generated by treatment of **[8]OTf/[1]** with the H-atom abstracting agent, TTBP$^{•}$ (Scheme 4). Extensive spectroscopic (UV-vis, EPR, rR) and computational (DFT) studies provided overwhelming evidence that **[8c]$^{+}$** and **[1c]** feature a high-spin Fe(II) center ferromagnetically coupled to a pSQ$^{•-}$ ligand (BISQ). Thus, the conversion of **[8b]$^{2+}$**/**[1b]$^{+}$**→**[8c]$^{+}$**/**[1c]** involves both deprotonation of the distal hydroxyl group and intra-molecular ligand-to-metal ET, as illustrated in Figure 3.15(a). The ET occurs because loss of the distal proton destabilizes of the frontier MOs of the HQate ligand relative to those of the iron center; indeed, it has been shown that deprotonation of free p-hydroquinonate lowers its redox potential by more than 0.9 V in DMSO.[99,144] Keramidas and coworkers have similarly demonstrated that tetranuclear vanadium(V) complexes with bridging HQate ligands undergo deprotonation to give the corresponding V(IV)-SQate species.[145] Thus, there is literature precedent for the type of reversible, proton-induced valence tautomerization described presently in this chapter.

Noninnocent (i.e., redox-active) ligands have garnered increasing attention due to their ability to function as electron reservoirs in the cycles of (bio)inorganic catalysts, thereby permitting multi-electron transformations.[146-151] By comparison, less attention has been paid to ligands, such as HQates, that are capable of donating (or accepting) both electrons *and protons*. The advantage of this type of noninnocent ligand is its potential to participate in proton-coupled electron transfers (PCETs), which play a critical role in numerous biological and synthetic processes.[99,152] The interconversions of **[8b]$^{2+}$**/**[8c]$^+$** and **[1b]$^+$**/**[1c]** highlight the ability of protonation state to modulate the noninnocent nature of ligands such as BIHQ.

Significantly, this series of complexes (**[8]OTf/[1]**, **[8b]$^{2+}$/[1b]$^+$**, **[8c]$^+$/[1c]**) replicates key aspects of the proposed GDO mechanism, as shown in <u>Figure 3.15</u>. The active site of GDO contains a conserved second-sphere Asp residue that forms a hydrogen bond to the distal –OH group of the coordinated gentisate substrate.[50,64] It has been proposed that this second-sphere carboxylate moiety deprotonates gentisate during (or immediately after) O_2 binding to the Fe center, thereby giving rise to a superoxo-Fe(II)-pSQ$^{\bullet-}$ intermediate (<u>Figure 3.15(b)</u>).[50,52,64,87,121] While this intermediate has not been observed experimentally, the synthetic results described here suggest that formation of an Fe(II)-pSQ$^{\bullet-}$ intermediate via transfer of 1e$^-$ and 1H$^+$ is a viable option for the GDO catalytic cycle.
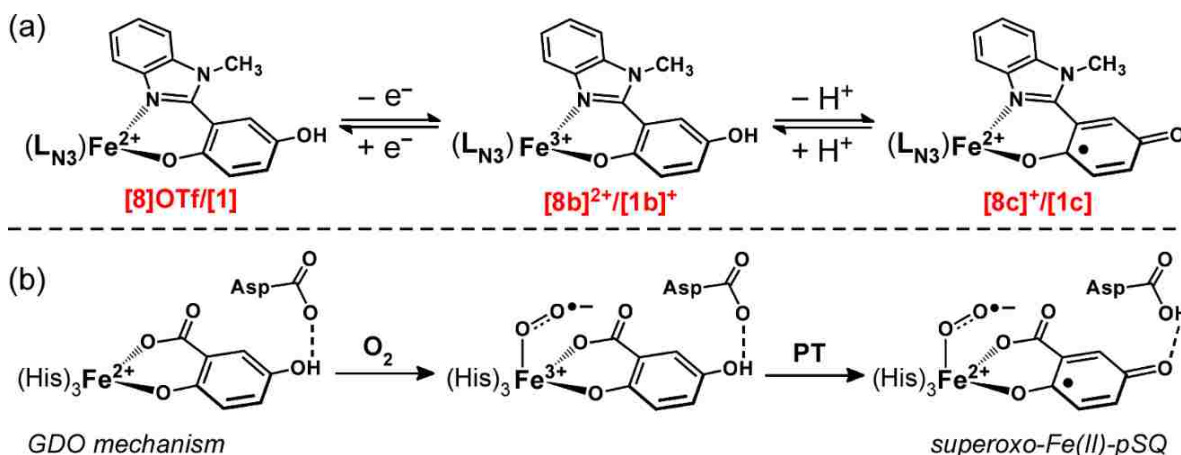
Figure 3.15. **(a)** Interconversion of **[8]OTf-** and **1-**derived species via reversible stepwise transfer of one electron and one proton. (b) Proposed reaction mechanism of GDO to form the putative superoxo-Fe(II)-pSQ$^{\cdot-}$ intermediate.

3.D. Experimental

3.D.i. General Methods

Unless otherwise noted, all reagents and solvents were purchased from commercial sources and used as received. Solvents CH_2Cl_2 and MeCN were purified and dried using a Vacuum Atmospheres solvent purification system. The synthesis and handling of air-sensitive materials were performed under inert atmosphere using a Vacuum Atmospheres Omni-Lab glovebox. The compounds ferrocenium hexaflurorphosphate ([Fc]PF$_6$),[153] 2,4,6-tri-*tert*-butylphenoxyl radical (TTBP$^{\cdot}$),[128] ^{Ph2}TIP[122] and 2-(1-methyl-benzimidazol-2-yl)hydroquinone[112] were prepared according to published procedures. The syntheses and X-ray crystal structures of complexes

[Fe(^{Ph2}TIP)(MeCN)$_3$](OTf)$_2$ and **1b** were reported previously.[112,122] Elemental analyses were performed at Midwest Microlab, LLC in Indianapolis, IN.

UV-vis absorption spectra were collected with an Agilent 8453 diode array spectrometer equipped with a cryostat from Unisoku Scientific Instruments (Osaka, Japan) for experiments at reduced temperatures. Infrared (IR) spectra were measured with a Thermo Scientific Nicolet iS5 FTIR spectrometer equipped with the iD3 attenuated total reflectance accessory for solid-state samples. EPR experiments were performed using a Bruker EleXsys E650 instrument equipped with an ER4415DM cavity, an Oxford Instruments ITC503 temperature controller, and an ESR-900 He flow cryostat. The program *EasySpin4* was used to simulate the experimental spectra.[154] Resonance Raman (rR) spectra were measured with 457.9 nm excitation from a Coherent I-305 Ar$^+$ laser using ~40 mW of power at the sample. The scattered light was collected using a 135° backscattering arrangement, dispersed by an Acton Research triple monochromator and detected with a Princeton Instruments Spec X 100BR CCD camera. The samples were held in a dewar cooled with either water/ice (273 K) or liquid nitrogen (77 K).

Electrochemical measurements were performed with an epsilon EC potentiostat (iBAS) under nitrogen atmosphere at a scan rate of 100 mV/s with 0.1 M (NBu$_4$)PF$_6$ as the electrolyte. A three-electrode cell containing a Ag/AgCl reference electrode, a platinum auxiliary electrode, and a glassy carbon working electrode was employed for cyclic and square-wave voltammetric measurements. Under these conditions, the ferrocene/ferrocenium (Fc$^{+/0}$) couple has an $E_{1/2}$ value of +0.52 V in CH$_2$Cl$_2$.

3.D.ii. Synthetic Procedures

[Fe(^{Ph2}TIP)(BIHQ)]OTf ([8]OTf): Under an inert atmosphere, 2-(1-methyl-1H-benzimidazol-2-yl)hydroquinone (33 mg, 0.14 mmol) as deprotonated by stirring with one equivalent of NaOMe in THF. After 30 minutes, a solution of [Fe(^{Ph2}TIP)(MeCN)$_3$](OTf)$_2$ (165 mg, 0.14 mmol) in THF was added to the reaction vial. The mixture was stirred overnight, and the solvent was then removed under vacuum. The crude product was taken up in 1,2-dichloroethane and filtered through Celite. Vapor diffusion of Et$_2$O into this solution provided yellow crystals suitable for X-ray diffraction (113 mg, 71 %). Anal. Calcd for C$_{63}$H$_{50}$F$_3$FeN$_8$O$_5$PS (MW = 1175.02 g mol^{-1}): C, 64.40; H, 4.29; N, 9.54. Found: C, 63.80; H, 4.82; N, 9.04. UV-Vis (CH$_2$Cl$_2$): λ_{max} (ε, M^{-1}cm^{-1}) = 378 (7800), 440 (2200) nm. FTIR (solid): ν = 3590 [ν(O-H)], 3047, 2985, 2871, 1604, 1578, 1504, 1488, 1461, 1444, 1386, 1325, 1253, 1155, 1074, 1031, 949, 833, 638 cm^{-1}.

[Fe(^{Ph2}Tp)(BIHQ)]PF$_6$ ([1b]PF$_6$): Complex **1** (149 mg, 0.15 mmol) was treated with one equivalent of [Fc]PF$_6$ (50 mg, 0.15 mmol) in MeCN (10 mL) for 30 minutes. The resulting dark brown solution was filtered through Celite to eliminate any unreacted precursor complex, and the solvent was removed under vacuum. The resulting brown solid was washed twice with a pentane (3 mL each time) to extract the ferrocene byproduct. The crude product was then taken up in 1,2-dichloroethane (4 mL), and vapor diffusion of pentane into this solution yielded dark brown needles suitable for X-ray crystallography (145 mg, 87%). Anal. Calcd for C$_{59}$H$_{45}$BF$_6$FeN$_8$O$_2$P (MW = 1109.68 g mol^{-1}): C, 63.86; H, 4.09; N, 10.10. Found: C, 63.49; H, 4.25; N, 10.05. UV-Vis (CH$_2$Cl$_2$): λ_{max} (ε, M^{-1}cm^{-1}) = 339 (12800), 441 (6250), 506 (5800) nm. FTIR (solid):

3529 [ν(O-H)], 3057, 2987, 2626 [ν(B-H)], 1545, 1479, 1425, 1354, 1255, 1165, 1067, 1013, 848, 781, 559 cm^{-1}.

3.D.iii. Crystallographic Studies

X-ray diffraction (XRD) data were collected with an Oxford Diffraction SuperNova kappa-diffractometer (Agilent Technologies) equipped with dual microfocus Cu/Mo X-ray sources, X-ray mirror optics, Atlas CCD detector, and low-temperature Cryojet device. The data were processed with CrysAlis Pro program package (Agilent Technologies, 2011), followed by an empirical multi-scan correction using SCALE3 ABSPACK routine. Structures were solved using SHELXS program and refined with SHELXL program[105] within Olex2 crystallographic package.[106] X-ray crystallographic parameters are provided in Table 3 and experimental details are available in the CIFs.

3.D.iv. DFT Computations

DFT calculations were performed using the ORCA 3.0 software package developed by Dr. F. Neese (MPI for Chemical Energy Conversion).[155] Geometry optimizations employed either (i) Becke's three-parameter hybrid functional for exchange along with the Lee-Yang-Parr correlation functional (B3LYP),[156,157] or (ii) the Becke-Perdew (BP86) functional.[158,159] All calculations used Ahlrichs' valence triple-ζ basis set (TZV) and TZV/J auxiliary basis set, in conjunction with polarization functions

on all atoms.[160,161,162] In the geometry optimized models, the ^{Ph2}TIP and ^{Ph2}Tp ligands were modified by replacing the Ph-groups at the 5-positions of the imidazolyl and pyrazolyl rings, respectively, with H-atoms. Time-dependent DFT (TD-DFT) calculations of **3a** used a truncated version of the optimized model with Me groups (instead of Ph groups) at the 4-positions of the imidazolyl rings. TD-DFT calculations[163,164,165,] calculated absorption energies and intensities for 60 excited states with the Tamm-Dancoff approximation.[166,167] Vibrational frequency calculations were performed on the BIHQ ligand in various oxidation state; calculation of the harmonic force fields proved that the optimized structure is a local minima on the potential energy surface. Isosurface plots of molecular orbitals and electron-density difference maps (EDDMs) were prepared with Laaksonen's gOpenMol program.[168]

Table 3.4. Summary of X-ray Crystallographic Data Collection and Structure Refinement for **[8]OTf** and **[1b]PF₆**.

	[8]OTf·2Et$_2$O ^{a}	**[1b]PF₆**·C$_2$H$_4$Cl$_2$
empirical formula	C$_{71}$H$_{70}$F$_3$FeN$_8$O$_7$PS	C$_{61}$H$_{49}$BCl$_2$F$_6$FeN$_8$O$_2$P
formula weight	1323.26	1208.61
crystal system	monoclinic	triclinic
space group	$P2_1/c$	P-1
a, Å	21.2966(19)	12.8542(5)
b, Å	20.2553(16)	14.8267(4)
c, Å	15.4880(15)	16.1415(5)
α, deg	90	75.336(6)
β, deg	101.9938(8)	68.675(3)
γ, deg	90	88.313(3)
V, Å^3	6535.20(10)	2765.67(15)
Z	4	2
ρ_{calc}, g/cm^3	1.348	1.451
λ, Å	1.5418	1.5418
μ, mm^{-1}	3.042	3.970
θ-range, deg	6 to 149	6 to 149
reflections collected	63087	52535
independent reflections	13122 [R_{int} = 0.0320]	11084 [R_{int} = 0.0418]
data/restraints/parameters	13122 / 0 / 868	11084 / 0 / 777
GOF (on F^2)	1.021	1.078
$R1/wR2$ ($I > 2\sigma(I)$)	0.0348 / 0.0907	0.0460 / 0.1234
$R1/wR2$ (all data)	0.0378 / 0.0932	0.0495 / 0.1271

^{a} One of the Et$_2$O solvates is partially (11%) occupied by 1,2-dichloroethane solvent.

Chapter 4

Dioxygen Reactivity of Fe(II)-Hydroquinonate Complexes: Generation of Catalytically-Relevant Intermediates of the Hydroquinone Dioxygenases
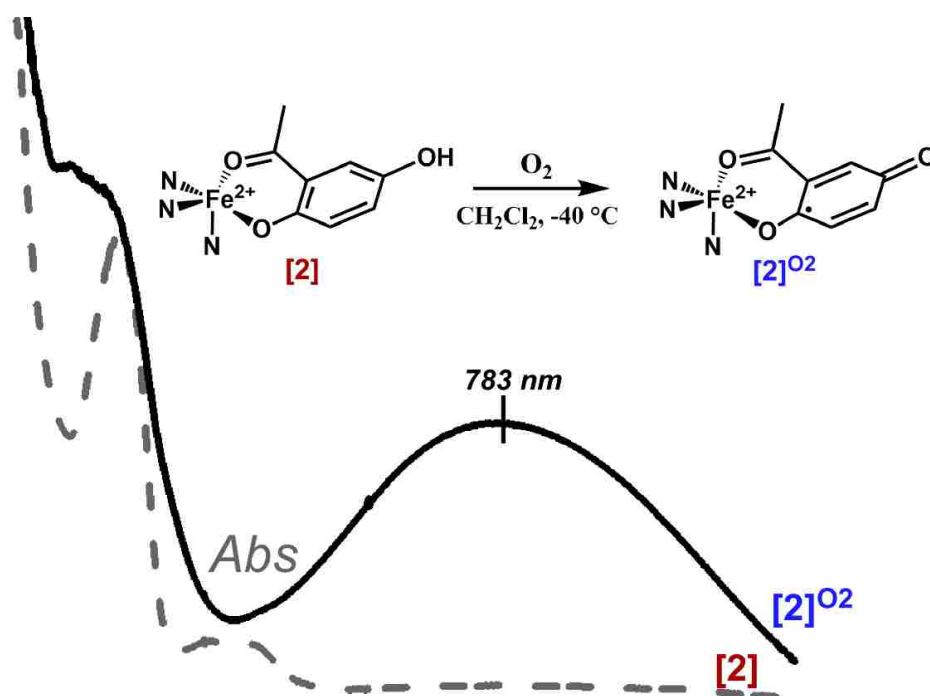
Abstract: This chapter describes the initial dioxygen reactivity studies of a series of mononuclear iron(II)-hydroquinonate complexes featuring the facially coordinating hydridotris(3,5-diphenylpyrazol-1-yl)borate (^{Ph2}Tp) ligand. These complexes have been previously reported as biologically-relevant models that nicely replicate the geometric structure of the enzyme-substrate complex formed during the mechanism of hydroquinone dioxygenases (HQDOs). The O_2 reactivity of these complexes was monitored via UV-vis absorption spectroscopy and attempts were made to isolate organic products formed upon reaction with O_2. The results described here indicate upon treatment with O_2, complexes **1** and **2** (Chapter 2) undergo a one-electron oxidation and deprotonation of their HQate ligands to generate Fe(II)-pSQ$^{.-}$ species, providing interesting implications for the mechanism of the HQDOs in nature.

4.A. Introduction

Mononuclear non-heme iron dioxygenases (MNIDs) are involved in the catabolism of a wide variety of aromatic substrates in biological systems.[13-14,16-21,28,50-51] A crucial feature of the non-heme iron active sites of these enzymes is their ability to simultaneously bind dioxygen and substrate, effectively activating O_2 and facilitating the oxidative C-C bond cleavage reaction of each MNID. To better understand the electronic structures of reactive intermediates formed during the catalytic mechanisms of particular MNIDs, researchers have performed modeling studies using biomimetic complexes that can be modified in a straightforward and systematic manner. The ultimate goal of this work is to determine structure-reactivity correlations that can be applied back to the biological system to elucidate their exquisite mechanism of action.

The literature describes several studies of model complexes that aim to replicate the observed function of MNIDs. Associated reactivity studies of these species have indicated that the reaction of a proposed non-heme Fe dioxygenase model with O_2 tends to follow three major trends (Figure 4.1). While studies of mononuclear Fe(II)-HQate complexes are rare, we can envision our HQDO models reacting in an analogous fashion.
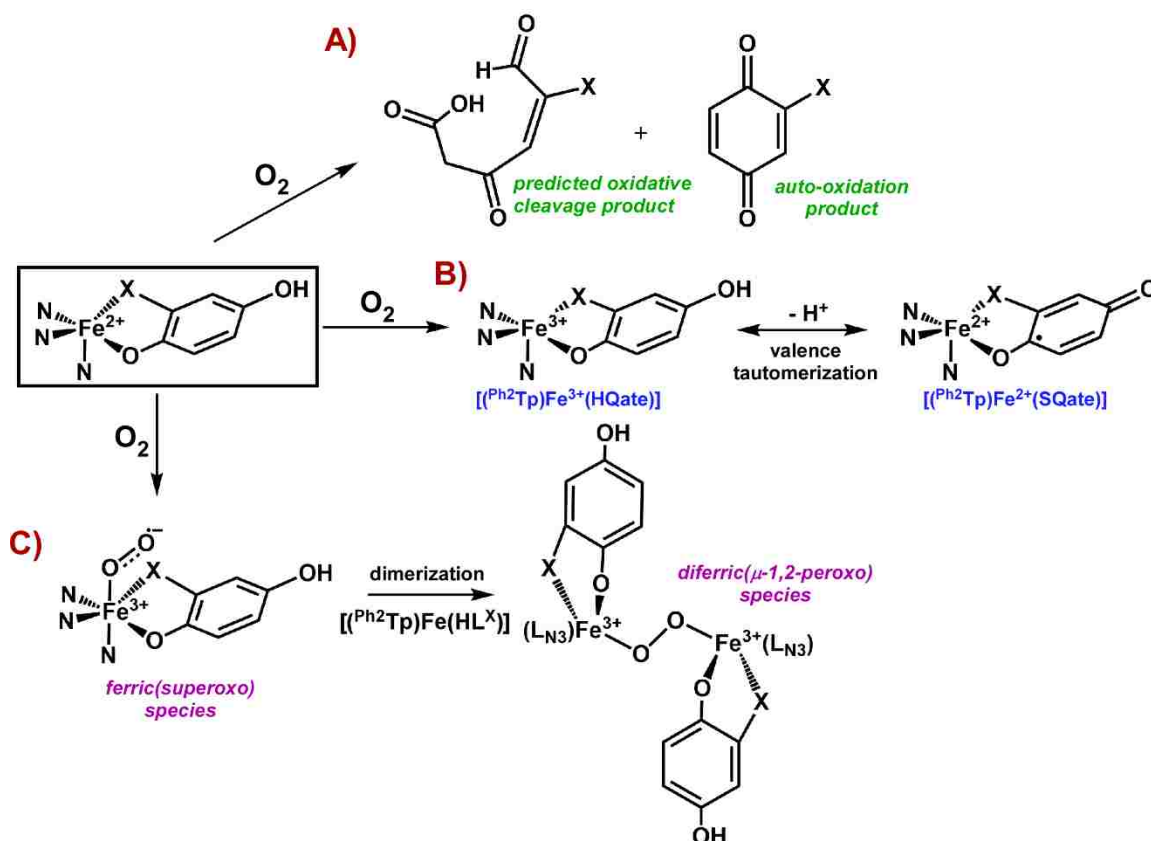
Figure 4.1. Possible outcomes of reaction of mononuclear Fe-HQate model complexes, **1** and **2**: (A) oxidative cleavage of bound model substrate and generation of possible auto-oxidation product(s) (B) metal- or ligand-centered oxidation of species facilitated by O_2 (C) generation of an Fe-$O_2^{\cdot-}$ adduct upon binding of dioxygen to the metal center.

The first predicted outcome of the O_2 reaction is that the model will exhibit the reactivity that mirrors the function of the corresponding metalloenzyme in nature, resulting in oxidative cleavage of an incorporated model substrate. An early example of biomimetic extradiol cleavage was demonstrated by the complex [Fe^III(tacn)Cl(dbc)] (tacn = 1,4,7-triazacyclononane; dbc = 3,5-di-*tert*-butylcatecholate) as reported by Dei et al.[169] Upon treatment of the starting iron complex with O_2 in either a MeCN or DMF solution, they noted that the oxygenation reaction is virtually complete within 6 h, as monitored by UV-vis absorption spectroscopy. Upon examination of the final reaction

mixture, Dei et al. noted a 35% yield of extradiol cleavage products, as confirmed by NMR and mass spectrometry. While the literature presents an abundance of additional examples of complexes that can carry out both intra- and extradiol cleavage of catechols, recent attention has focused on the development of models that instead aim to facilitate the ring cleavage reactions of other substrates, such as aminophenols and β-diketones.[170-173]

Interestingly, MNID model complexes have also demonstrated the ability to undergo direct metal- or ligand-based oxidation(s) upon treatment with O_2. Several examples of Fe(II)-catecholate complexes exist that are observed to undergo oxidation to the corresponding Fe(III) form. Que, et al. report an example of a pale yellow Fe(II)-catecholate complex [Fe^{2+}(6TLA)(DBCH)](ClO_4), (6TLA = tris[(6-methyl-2-pyridyl)methyl]amine) that undergoes loss of an electron to generate the corresponding ferric species upon treatment with dioxygen.[174] By monitoring the oxygenation reaction, Que, et al. observe the formation of a deep purple-blue species that displays two intense bands at 600 and 1020 nm, characteristic of catecholate → Fe(III) charge transfer transitions.[175-177] The generation of a high-spin ferric species was further confirmed via EPR spectroscopy. Similar reactivity was reported and spectroscopically confirmed by Fiedler and Bittner. upon treatment of the complex [(^{Ph2}TIP)Fe^{2+}(^{tBu}CatH)]$^+$ (^{tBu}CatH = 4-*tert*-butylcatecholate) with dioxygen.[178] Notably, both of these ferric species have been demonstrated to react further with an additional equivalent of O_2 to yield extradiol cleavage products. In contrast, Bittner et al. also report two complexes similar to the aforementioned 4-*tert*-butylcatecholate species that can undergo two-electron oxidation processes facilitated by dioxygen. The first of these complexes is

$[(^{Ph2}TIP)Fe^{2+}(^{tBu}PDA)]^{2+}$ which displays a two-electron ligand-based oxidation to yield

$[(^{Ph2}TIP)Fe^{2+}(^{tBu}DIBQ)]^{2+}$ ($^{tBu}DIBQ$ = o-diiminobenzoquinone). Conversely, they report

the preparation of a similar complex, $[(^{Ph2}TIP)Fe^{2+}(^{tBu2}APH)]^+$ (^{tBu2}APH = 2-amino-4,6-

di-*tert*-butylphenolate), that undergoes a two-electron oxidation process upon exposure to

dioxygen, however, in this case, the final product arises from oxidation of both the Fe(II)

center and the bound ligand to yield a species best described as $[(^{Ph2}TIP)Fe^{3+}(^{tBu}ISQ)]$

(^{tBu}ISQ = o-iminobenzosemiquinone).[178] These studies highlight the interesting dioxygen

reactivity of non-heme iron models which results in metal- and/or ligand-based

oxidation(s). In particular, the last two species mentioned demonstrate the ability of

model species to undergo oxidative processes in aerobic solutions without incorporation

of either atom of dioxygen in the final oxidized product.

The last major trend that has been observed upon the reaction of dioxygen with a

model non-heme iron dioxygenase complex is the formation of (quasi)stable Fe-

superoxo or Fe-peroxo adducts. The literature includes several examples of species that

incorporate dioxygen bound directly to the iron center of a complex. Kitajima et al first

described the dioxygen reactivity of the complex, $[(^{iPr2}Tp)Fe(OBz)]$ (OBz = benzoate),

which was observed to generate a deep-green chromophore at -50 °C with λ_{max} = 682 nm

(ε = 3450 M^{-1} cm^{-1}).[179] Further studies utilizing rRaman spectroscopy revealed two new

bands (876 and 418 cm^{-1}) upon treatment of $[(^{iPr2}Tp)Fe(OBz)]$ with $^{16}O_2$, characteristic of

ν(O-O) and ν(Fe-O) frequencies, respectively, diferric-peroxo species. They noted an

isotopic shift upon incorporation of $^{18}O_2$ (827 and 409 cm^{-1}, respectively), in reasonable

agreement with predicted values based on the diatomic harmonic-oscillator

approximation (shifts of 50 and 15 cm^{-1}, respectively). They note that based on their

rRaman results, they did not observe isotopically-active bands in the range of 1000-1200 cm^{-1} characteristic of ν(O-O) of a superoxide complex, further supporting the generation of a μ-peroxo dinuclear ferric complex. Que et al. observed formation of a similar species upon oxygenation of [(^{iPr2}Tp)Fe(PRV)] (PRV = pyruvate) at -40 °C which exhibits a broad absorption band with λ_{max} = 680 nm (ε = 1600 M^{-1} cm^{-1}).[180] Interestingly, because the pyruvate-bound complex demonstrates similar behavior to that reported previously by Kitajima et al., Que et al. noted that these complexes are remarkable due to the fact that, while there are many (μ-η^1:η^1-peroxo)diiron(III) complexes present in the literature, very few are derived from mononuclear ferrous complexes that bind O_2 in a bridging fashion.[180]

Additional reports described formation of mononuclear Fe-superoxo species upon treatment of a non-heme iron model complex with dioxygen. Lee et al. reported the synthesis of a non-heme Fe^{2+}(BDPP) (BDPP = 2,6-bis[((S)-2-(diphenylhydroxymethyl)-1-pyrrolidinyl)methyl]pyridine) complex that readily reacts with O_2 at -80 °C to form a paramagnetic Fe^{3+}-superoxo species.[181] A solution of the precursor complex in THF undergoes a drastic color change (from red to bright yellow) upon introduction of O_2 and displays an intense absorption feature at 330 nm. Literature precedent indicates that this new feature corresponds to the formation of an Fe(III)-$O_2^{\cdot-}$ adduct.[182] rRaman spectroscopy confirmed the binding of dioxygen to the metal center as a resonance-enhanced mode at 1125 cm^{-1} is displayed in the spectrum obtained for the oxygenated species (introduction of $^{18}O_2$ induces a reasonable isotopic shift to 1062 cm^{-1}). Additional evidence for the generation of a Fe^{3+}-superoxo adduct was derived from the use of Mössbauer and EPR spectroscopies.

Inspired by the aforementioned investigations and the continuing questions regarding the identity of catalytic intermediates, we chose to study the dioxygen reactivity of a series of complexes that accurately mimic the structure of the enzyme-substrate complex of the hydroquinone dioxygenases (HQDOs), as described in Chapter 2. In order to establish the ability of these complexes to act as viable functional models, we explored the O_2 reactivity of each complex and monitored the subsequent reaction via UV-vis spectroscopy. Further studies were completed to assess the capacity of these complexes to facilitate oxidative ring cleavage of their respective model substrates. While the work reported here is somewhat preliminary, we believe these results lay the foundation for future studies of the viability of our systems to act as functional models of the HQDOs.

4.B. Results and Discussion

This chapter details the dioxygen reactivity of complexes **1** and **2**. Both complexes feature a monoiron(II) center supported by the facially capping hydridotris(3,5-diphenylpyrazol-1-yl)borate (^{Ph2}Tp) ligand. The monoanion of 2-(1-methyl-1H-benzimidazol-2-yl)hydroquinone (**1**) or 2′,5′-dihydroxyacetophenone (**2**) bind in a bidentate manner. As reported in Chapter 2, each complex consists of a 5C high-spin Fe(II) center with distorted geometries between square planar and trigonal bipyramidal; however, the coordination geometry of **2** lies closer to the trigonal bipyramidal limit ($\tau =$ 0.35 and 0.60, respectively[98]). In order to assess the ability of **1** and **2** to react with

dioxygen, we exposed each complex to O_2 in DCM solutions at low temperatures. The

resulting reactions were monitored via UV-vis absorption spectroscopy.

4.B.i. Dioxygen reactivity of complex 1 – [(^{Ph2}Tp)Fe(2-BIHQ)]

Upon treatment of **1** with dioxygen at -50 °C, the generation of **[1]^{O2}** is signified

by formation of a new absorption band at λ_{max} = 445 nm in addition to a weak shoulder

centered at approximately 530 nm (Figure 4.2). In conjunction with the appearance of the

two new features, the intense $\pi \rightarrow \pi^*$ transition of the starting ferrous complex **1** (λ_{max} =

365 nm) noticeably decreases in intensity.
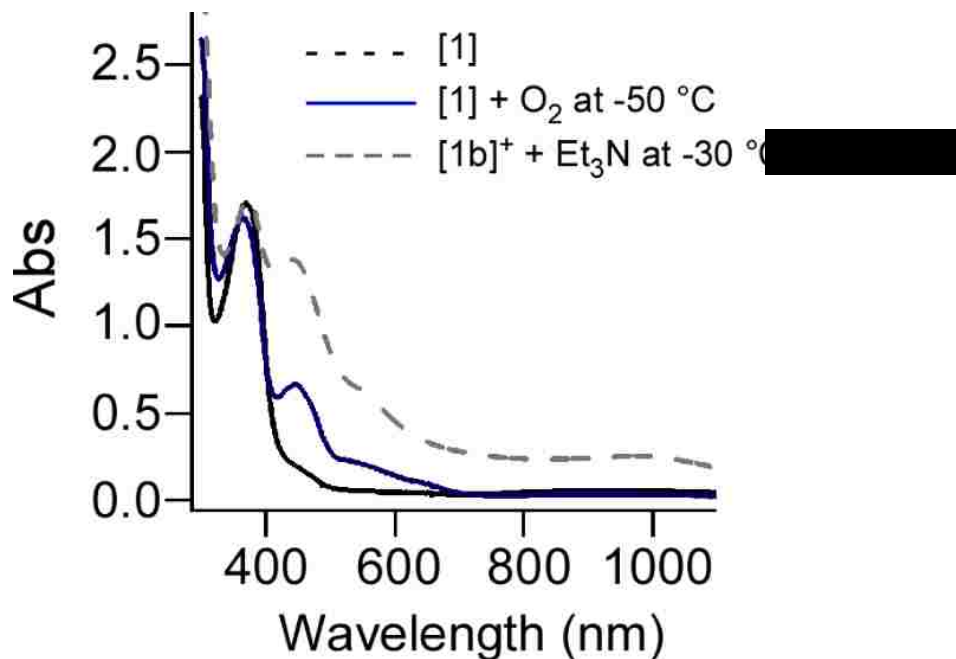
Figure 4.2. Electronic absorption spectra demonstrating formation of **[1]^{O2}** upon addition of O_2 to complex **1** in CH_2Cl_2 at -50 °C. The spectrum for **[1c]** is included for comparison

Addition of O_2 to **1** at room temperature first generates the **[1]^{O2}** species observed at low temperature which slowly decays overnight to a brown species with a broad absorption band between 400-800 nm (Figure 4.3). Attempts to isolate and characterize oxidative cleavage products from the reaction of **1** with O_2 have been made, but the resulting NMR and GC-MS data have not provided conclusive evidence for specific products.
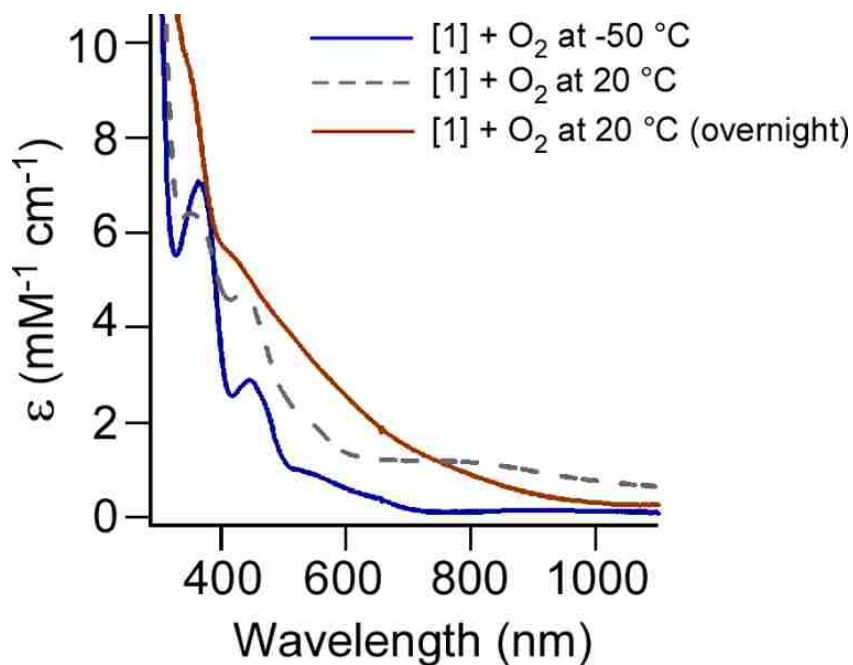
Figure 4.3. Electron absorption data of the reaction of **1** with O_2 at 20 °C in CH_2Cl_2 overnight (grey dashed line – starting spectrum; brown solid line – reaction of **1** with O_2 after approximately 12 hours). The absorption data for **[1]^{O2}** generated at -50 °C is also included for comparison.

Interestingly, the band shapes of newly generated **[1]^{O2}** are reminiscent of those observed in the absorption spectrum of **[1c]**, the previously reported Fe^{2+}-pSQ$^{\cdot-}$ species (Chapter 3). However, the absorption intensity of the dioxygen-treated form of **1** are somewhat diminished with respect to **[1c]**. Addition of 5 equivalents of Et_3N at -50 °C leads to an increase in intensity of each feature (Figure 4.4).
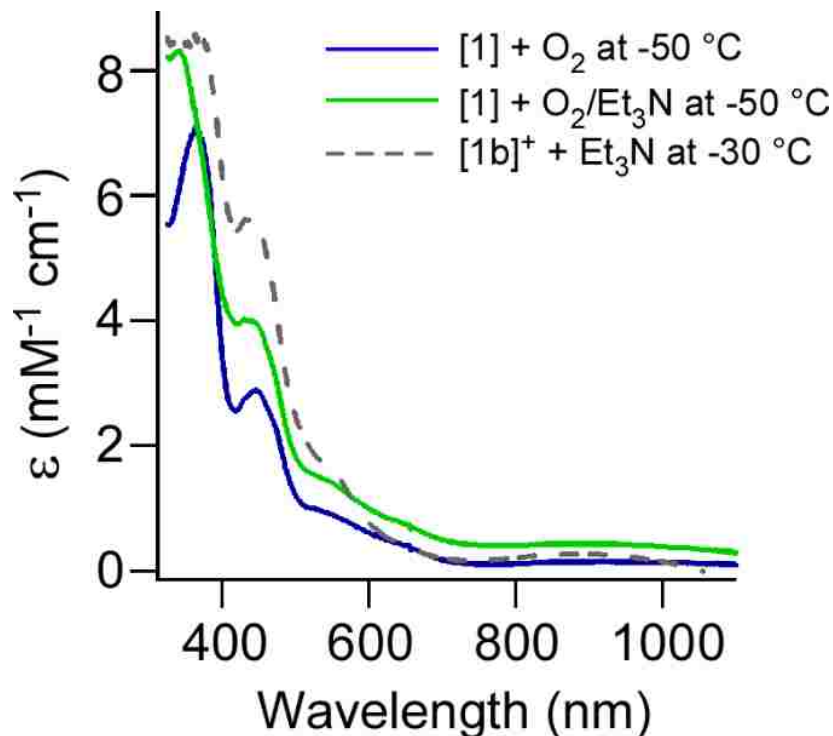
Figure 4.4. Electronic absorption data comparing the reaction of **[1]** with O_2 and Et_3N and **[1b]**$^+$ with Et_3N in CH_2Cl_2. The starting spectrum of **[1]**^{O2} is included for comparison.

Based on these results, we surmised that addition of O_2 does not result in formation of the corresponding Fe^{3+}-HQate species (UV-vis absorption data for the ferric species is reported in Figure 3.6), but instead leads to the generation of a new species that is spectroscopically similar to **[1c]**, especially upon addition of base at low temperatures. Reversing the order of addition of dioxygen and base only yields minor changes in the resulting electronic absorption data. Formation of a ligand-based radical assumes that dioxygen is acting as a one-electron oxidant in the presence of Et_3N. While further spectroscopic evidence is required to confirm this assignment (*vide infra*), if this prediction holds, it has interesting implications for the HQDO mechanism.

4.B.ii. Dioxygen reactivity of complex 2 – [(^{Ph2}Tp)Fe(2′,5′-DHAP)]

Because complexes **3, 4** and **7** displayed very little change upon exposure to O_2 in solution, we instead pursued further studies of the dioxygen reactivity of complex **2**. Significant spectral changes are observed upon exposure of a solution of **2** in CH_2Cl_2 to O_2 at -40 °C, as demonstrated by the absorption spectrum of **[2]^{O2}** displayed in Figure 4.5.
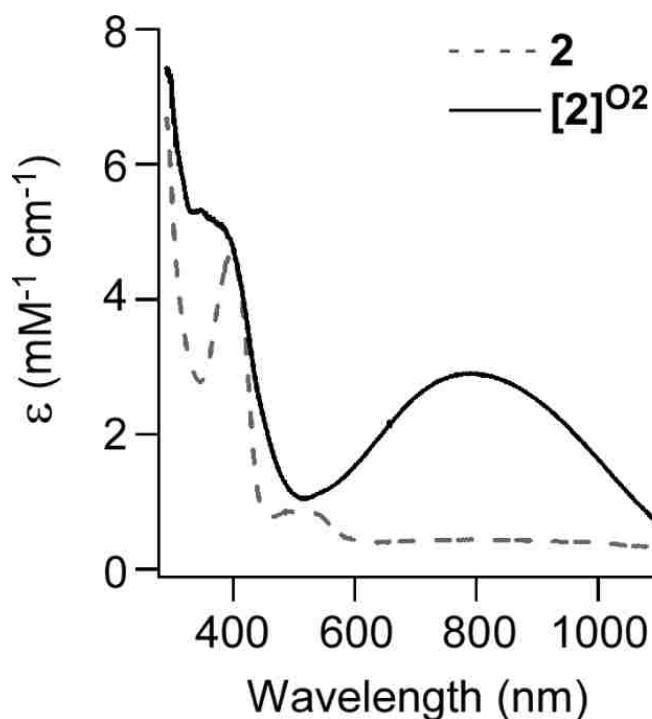
Figure 4.5. Electronic absorption spectra of the species formed upon treatment of complex **2** with O_2 in CH_2Cl_2 at -40 °C.

As shown previously, the absorption spectrum of **2** contains a sharp band with λ_{max}= 397 nm (ε= 4710 M^{-1} cm^{-1}). Addition of O_2 to a solution of **2** in DCM at -40 °C generates a dark green chromophore that exhibits two new absorption bands: one at λ_{max}=

360 nm (ε= 5220 M^{-1} cm^{-1}), as well as a broad feature centered around λ_{max}= 783 nm (ε= 2900 M^{-1} cm^{-1}). Due to the observation that this new species did not persist at room temperature, attempts to crystallize **[2]^{O2}** at low temperature (< -70 °C) were made, but these trials proved unsuccessful.

Based on the observed absorption features of **[2]^{O2}** and their similarity to those reported by Kitajima[179] and Que[180] upon formation of a diferric-(μ-1,2-peroxo) species, we investigated the ability of dioxygen to bind to the ferrous center of complex **2**. Specifically, the electronic structure of **[2]^{O2}** was probed with resonance Raman (rRaman) spectroscopy . Two oxygenated samples were prepared in DCM at low temperature; one sample was exposed to naturally-abundant O$_2$ and the other to ^{18}O$_2$. The resulting spectrum of **[2]^{ox}**, obtained with 647 nm excitation, failed to display any isotopically-active peaks, providing evidence against the incorporation of dioxygen in **[2]^{O2}**. While **2** is EPR silent, the X-band EPR spectrum of **[2]^{O2}** revealed an intense signal corresponding to a $S = 5/2$ system with rhombic zero-field splitting parameters (Figure 4.6). The preliminary spectral data suggests that the complex is undergoing a one-electron oxidation facilitated by the addition of dioxygen. Comparison of the absorption features of the ferric form of **2** (*vide supra*) and **[2]^{O2}** indicates that the two species are not spectroscopically similar and we therefore surmise that the oxygenation of **2** involves a ligand-based oxidation. In order to provide further evidence for the generation of a ligand-based radical, we treated **2** with one equivalent of AcFc$^+$ followed by an excess of Et$_3$N and monitored the reaction via UV-vis spectroscopy. As illustrated in Figure 4.7, the resulting chromophore is similar in appearance to the oxygenation product **[2]^{O2}**.
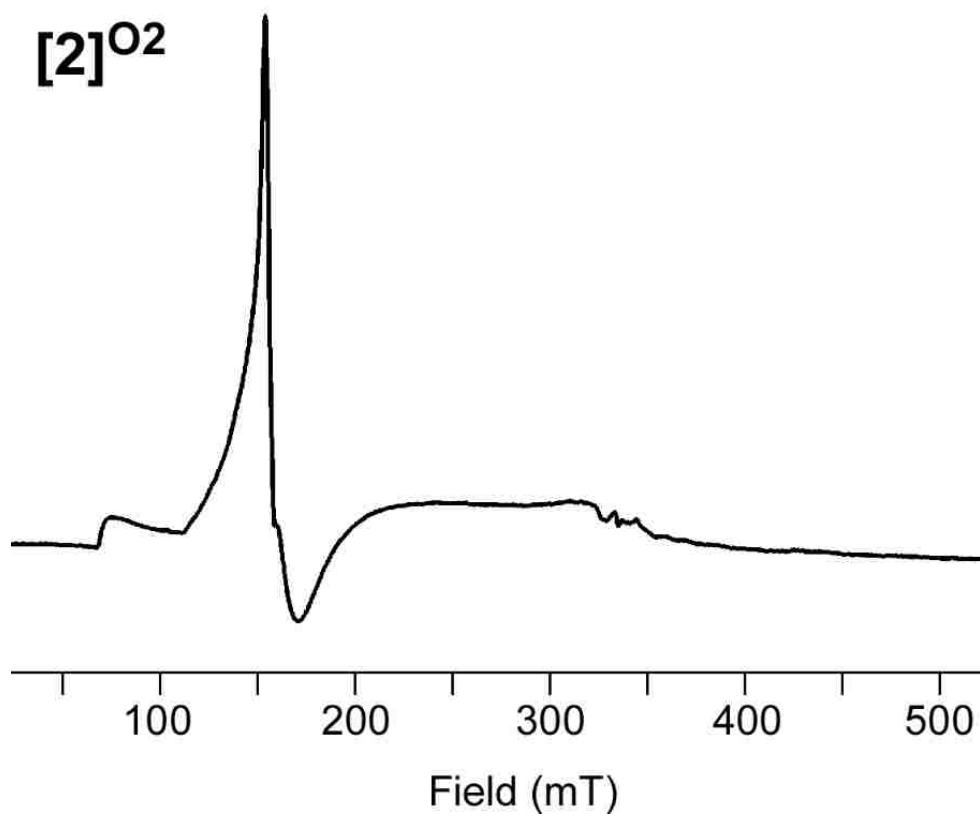
Figure 4.6. X-band EPR spectrum of $[2]^{O_2}$ in frozen CH_2Cl_2 solution at 10 K.
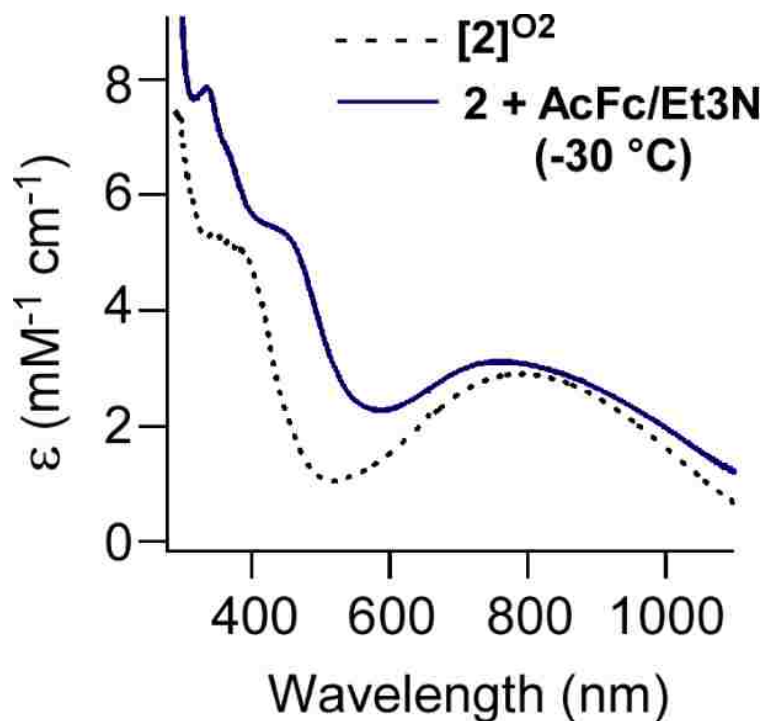
Figure 4.7. Electronic absorption spectra comparing features observed for species $[2]^{O2}$ generated at -40 °C and the reaction of **2** with $AcFc^+$ and Et_3N at -30 °C. Both spectra were obtained with CH_2Cl_2 solutions.

To further confirm that the chromophore observed upon the oxygenation of **2** involves a ligand-based process, we first studied the dioxygen reactivity of complex **3** which incorporates the monoanion of 2-hydroxyacetophenone. The lack of the distal -OH group makes it difficult to oxidize the ligand to the corresponding (phenoxy) radical. The complex remained unreactive toward the proposed oxygenation reaction, indicating the distal –OH group of 2′,5′-DHAP is necessary for conversion of **2** → $[2]^{ox}$. To further study the reactivity of the 2′,5′-DHAP ligand when bound to a ferrous center, we chose to develop an additional analog of **2** that incorporates 2-hydroxy-5-methoxyacetophenone as its ligand (complex **9**). Crystals suitable for X-ray structure determination were obtained from vapor diffusion of pentane into a solution of the complex in 1,2-dichloroethane.

Details concerning data collection and analysis are provided in Table 4.2. Selected bond lengths and angles determined for **9** are given in Table 4.1 and compared to previously established parameters collected for **2** and **3**. The new complex, [(^{Ph2}Tp)Fe(2-hydroxy-5-methoxyacetophenone)] **9**, shown in Figure 4.8, is similar to the previously synthesized mononuclear Fe-hydroquinonate complexes reported in this paper. Complex **9** displays a 5C, Fe(II) center facially bound by the ^{Ph2}Tp ligand as well as the bidentate 2-hydroxy-5-methoxyacetophenone ligand. The average Fe-N$_{Tp}$ bond length is 2.14 Å, which is indicative of a high spin ferrous center. The Fe-O1 bond length of 1.9087 Å falls within the previously mentioned range of Fe(II)-phenolate distances of 5C complexes.

Table 4.1. Selected bond distances (Å) and bond angles (°) from the X-ray structures of monoiron(II) hydroquinonate complexes **2**, **3** and **9.**

	2·2CH₂Cl₂	**3**	**9**
Fe–O1	1.937(4)	1.927(1)	1.9087(10)
Fe–N1	2.131(5)	2.108(1)	2.0990(11)
Fe–N3	2.089(5)	2.093(1)	2.0957(11)
Fe–N5	2.185(5)	2.228(1)	2.2375(11)
Fe–L^a	2.079(4)	2.103(1)	2.1097(10)
O1–C46	1.303(7)	1.304(2)	1.3118(17)
O2–C49	1.370(7)		1.3730(17)
O1–Fe–N1	129.5(2)	128.04(5)	129.90(5)
O1–Fe–N3	139.9(2)	140.01(5)	137.43(5)
O1–Fe–N5	97.9(2)	100.61(4)	98.23(4)
O1–Fe–L$_X$	86.4(2)	85.28(4)	85.70(4)
N1–Fe–N3	90.6(2)	91.50(4)	92.55(4)
N1–Fe–N5	90.2(2)	88.25(4)	87.59(4)
N3–Fe–N5	81.2(2)	84.39(4)	84.98(4)
L$_X$–Fe–N1	87.4(2)	91.32(4)	91.98(4)
L$_X$–Fe–N3	95.3(2)	88.47(4)	90.27(4)
L$_X$–Fe–N5	175.7(2)	172.83(4)	175.21(4)
τ-value^b	0.60	0.55	0.63

^{a} L is the N or O atom of the pendant donor of the HQ anion. ^{b} For a definition of the τ-value, see ref. 98. A five-coordinate complex with ideal square-pyramidal geometry would have a τ-value of 0.0, while those with ideal trigonal bipyramidal geometry would have a value of 1.0.
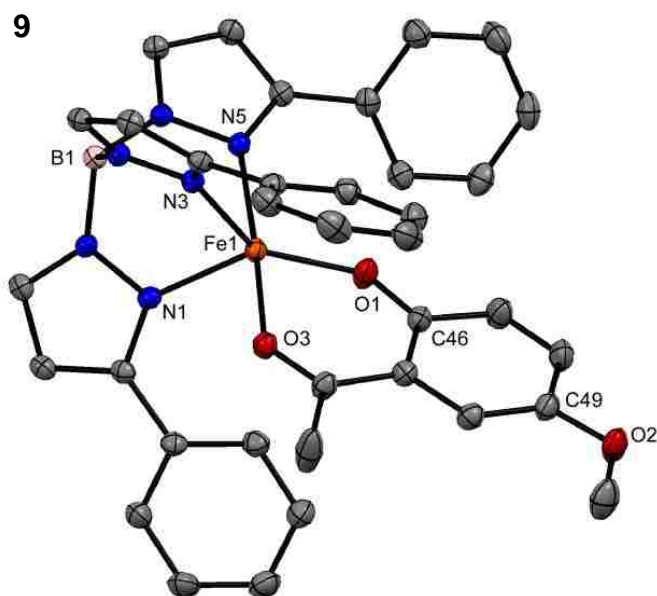
Figure 4.8. Thermal ellipsoid plot (50% probability) derived from the X-ray structure of **9**. Hydrogen atoms, and Ph-rings at the 5-positions of the ^{Ph2}Tp ligand have been omitted for clarity.

Reaction of **9** with O_2 in DCM at room temperature was monitored via UV-Vis spectroscopy. The resulting spectra indicate that **9** does not react readily with dioxygen, as previously observed for complex **3**. This study was further augmented by electrochemical investigation of **9** which measured an irreversible oxidation at $E_{p,a}$= 1132 mV and a quasi-reversible couple at $E_{1/2}$= -5 mV (ΔE=142 mV) corresponding to the Fe(II)/Fe(III) couple (Figure 4.9).
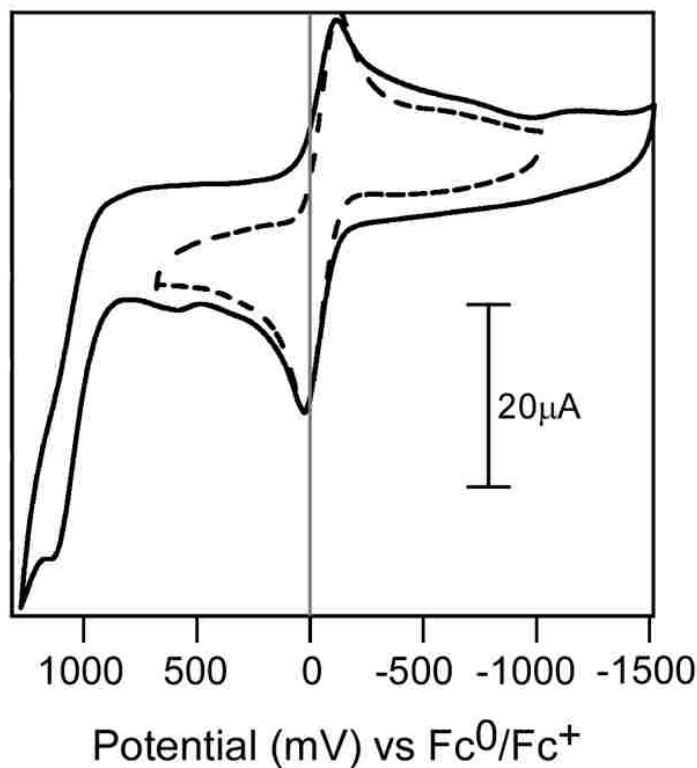
Figure 4.9. Cyclic voltammogram of **9**. Data was collected in CH$_2$Cl$_2$ with 100 mM (NBu$_4$)PF$_6$ as the supporting electrolyte and a scan rate of 100 mV s^{-1}. The voltammogram was initiated by the anodic sweep.

Comparison of the electrochemical data for **9** versus that collected for complex **2** indicates that the HL^B ligand and 2-hydroxy-5-methoxyacetophenone ligands have approximately equal electron-donating abilities. This trend is demonstrated by the fact that the redox potential for the Fe(II)/Fe(III) couple of **2** and **9** differ by only 100 mV (E$_{1/2}$ = -110 mV and -5 mV, respectively). It is interesting to note this observation when considering the reactivity of these complexes toward dioxygen as it further underlines the necessity of a distal –OH group for generation of the observed green chromophore **[2]^{O2}**.

Due to the inability of complexes **3** and **9** to react with O$_2$ in comparison to complex **2**, it is clear the observed oxygenation reaction is due to a ligand-based process

rather than formation of a diferric-(μ-peroxo) species despite the similarities in observed features of the absorption spectra. As mentioned previously, rRaman data collected for **[2]^{O2}** fails to display isotopically-active modes further refuting the incorporation of dioxygen into **[2]^{O2}**. Considering previous reports by Fiedler and Bittner regarding the dioxygen reactivity of non-heme Fe(II) models of β-diketo dioxygenase (Dke1), this observation is not surprising.[183] In this study, O$_2$ incorporation into a model complex, leading to dimerization, was only observed for complexes utilizing a ^{Me2}Tp ligand scaffold, which is much less sterically demanding than the ^{Ph2}Tp ligand utilizing in our model complexes.

Based on the spectroscopic evidence and control studies described here, we are confident that treatment of **2** with dioxygen at -40 °C in CH$_2$Cl$_2$ yields a complex with a ligand-based radical. Upon initial consideration of the significant differences in the absorption features of **[1]^{O2}** and **[2]^{O2}**, we were surprised by the apparent ability of each precursor complex to exhibit similar behavior towards reaction with O$_2$. However, as previously reported, the absorption features observed for the Fe(II)-pSQ$^{.-}$ species **[1c]** arise primarily from ligand-based transitions. This result indicates that it is reasonable for the absorption spectra of **[1]^{O2}** and **[2]^{O2}** to vary so much based on the intrinsic difference of the pendant donors of each ligand (i.e., benzimidazolyl group versus the acetyl donor, respectively). Further proof for the generation of a substrate-based radical was derived from the rRaman spectrum of **[2]^{O2}** (Figure 4.10). While further computational work must be done to aid in the assignment of the principal vibrational modes of **[2]^{O2}**, the spectrum clearly displays a series of intense features in the range of 1200-1600 cm^{-1}.

Previous work with similar complexes indicates that intense modes observed in the range

of 1400-1500 cm^{-1} correspond to stretching motions of (semi)quinonate ligands.[136,139,184]
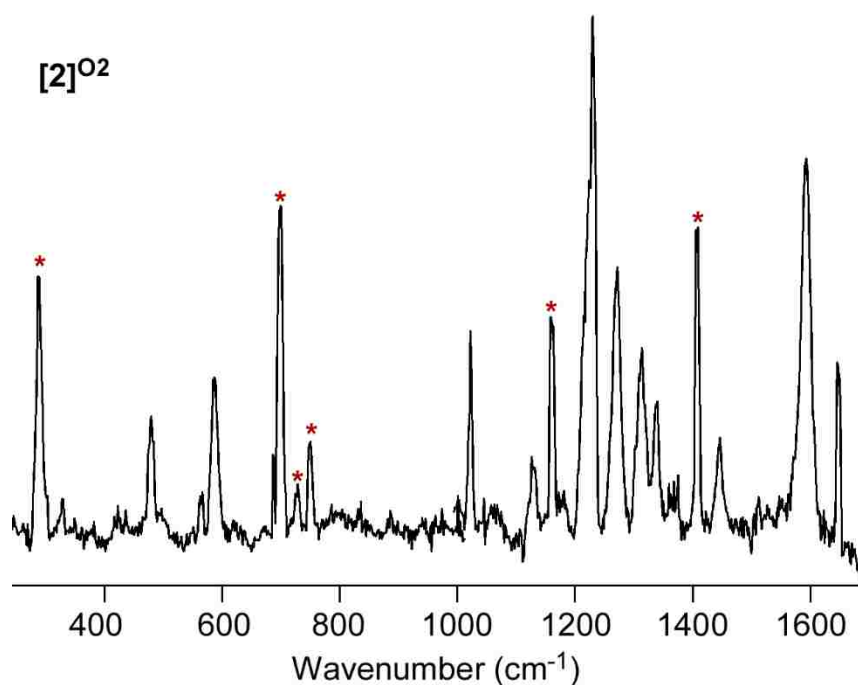
Figure 4.10. rRaman spectrum of **[2]^{O2}** obtained with 647 nm (10 mW) excitiation in frozen CD$_2$Cl$_2$ solution. Peaks labeled with an asterisk (*) arise from solvent.

4.C. Conclusion

The dioxygen reactivity of mononuclear Fe(II)-hydroquinonate models **1** and **2** was described in this chapter. Treatment of each complex with dioxygen at low temperatures (-30 and -40 °C, respectively) in CH$_2$Cl$_2$ has been shown to result in one-electron oxidation and deprotonation of the ligand rather than incorporation of O$_2$. Further comparison of the absorption spectra of the oxygenated species with data

collected for the stepwise treatment of each complex with $AcFc^+$ followed by Et_3N indicates the product of the oxygenation reaction is the $Fe(II)$-$SQ^{\cdot-}$ form of each complex. The results presented here have interesting implications for the mechanism of function of the HQDOs in nature. Previous biomimetic studies of the extradiol catechol dioxygenases (ECDOs – a similar MNID) indicated that treatment of model $Fe(II)$-CatH complexes with O_2 first yielded a one-electron oxidized $Fe(III)$-catecholate species.[175-178] It was the observed that further reaction of the $Fe(III)$-catecholate species with an additional equivalent of O_2 lead to formation of oxidatively cleaved products upon an appropriate chemical work up. It is interesting to consider that the *o*-substituted ECDO models indicate the necessity for formation of a ferric species before further reaction with O_2 to facilitate oxidative ring cleavage; however, we instead observe generation of a *p*$SQ^{\cdot-}$ ligand-based radical. The difference in reactivity is due to the variance in substitution of the respective dioxolene ligands. With regards to the catecholate system, the oxidation facilitated by dioxygen is metal-based, due to the bidentate binding mode of the catecholate ligand, which stabilizes the π-system of the ligand. Conversely, the HQate models (and by extension, the HQDOs) instead incorporate hydroquinonate ligands whose characteristic *p*-hydroxy substitution pattern leaves the distal -OH group of the ligand unbound. This arrangement favors formation of the $Fe(II)$-$SQ^{\cdot-}$ species upon exposure of O_2. The unreactive nature of the "control complexes" (**3** and **9**) highlights the importance of a free distal -OH group to allow the oxygenation reactions to occur. While further investigations of the final reaction products are required, the results reported here set an interesting precedent for future biomimetic studies of the hydroquinone dioxygenases.

4.D. Experimental

4.D.i. General methods

Unless otherwise noted, all reagents and solvents were purchased from commercial sources and used as received. Dichloromethane was purified and dried using a Vacuum Atmospheres solvent purification system. The synthesis and handling of air-sensitive materials were performed under inert atmosphere using a Vacuum Atmospheres Omni-Lab glovebox. Complexes **1**, **2** and **3** were prepared according to literature procedures.[112] Elemental analyses were performed at Midwest Microlab, LLC in Indianapolis, IN. UV-vis absorption spectra were obtained with an Agilent 8453 diode array spectrometer equipped with a cryostat from Unisoku Scientific Instruments (Osaka, Japan) for temperature control. Fourier-transform infrared (FTIR) spectra of solid samples were measured with a Thermo Scientific Nicolet iS5 FTIR spectrometer equipped with the iD3 attenuated total reflectance accessory. ^{1}H spectra were collected at room temperature with a Varian 400 MHz spectrometer. EPR experiments were performed using a Bruker ELEXSYS E600 equipped with an ER4415DM cavity resonating at 9.63 GHz, an Oxford Instruments ITC503 temperature controller, and an ESR-900 He flow cryostat. Electrochemical measurements were conducted in the glovebox with an epsilon EC potentiostat (iBAS) at a scan rate of 100 mV s^{-1} with 100 mM $(NBu_4)PF_6$. A three-electrode cell containing a Ag/AgCl reference electrode, a platinum auxiliary electrode, and a glassy carbon working electrode was employed for

cyclic voltammetric (CV) measurements. Under these conditions, the

ferrocene/ferrocenium ($Fc^{+/0}$) couple has an $E_{1/2}$ value of +0.52 V in CH_2Cl_2.

4.D.ii. Synthetic Procedures

[Fe(^{Ph2}Tp)(2-hydroxy-5-methoxyacetophenone)] [9] : Under an inert atmosphere in glove box, 174 mg (1 mmol) of 2-hydroxy-5-methoxyacetophenone was deprotonated with one equivalent of NaOMe in approximately 10 mL of THF for one hour. Solvent was removed under vacuum to yield the Na(2-hydroxy-5-methoxyaceophenone) salt as a bright yellow powder. This salt was then combined with anhydrous $FeCl_2$ (138 mg, 1 mmol) and K(^{Ph2}Tp) (741 mg, 1 mmol) in 20 mL of MeCN. After stirring the reaction mixture overnight, the solvent was removed under vacuum to yield a pale red solid which was dried thoroughly. The product was then taken up in 1,2-dichloroethane and filtered though celite to yield a dark red solution. Vapor diffusion with pentane yielded dark red crystals suitable for X-ray crystallography. Anal. Calcd for $C_{54}H_{43}BFeN_6O_3$ (MW = 890.60 g mol^{-1}): C, 72.82; H, 4.87; N, 9.44. UV-vis [λ_{max}, nm (ε, M^{-1} cm^{-1}) in CH_2Cl_2]: 395 (2411), 506 (290).

Chapter 5

Synthesis and Spectroscopic Characterization of High-Spin Mononuclear Iron(II) *p*-Semiquinonate Complexes
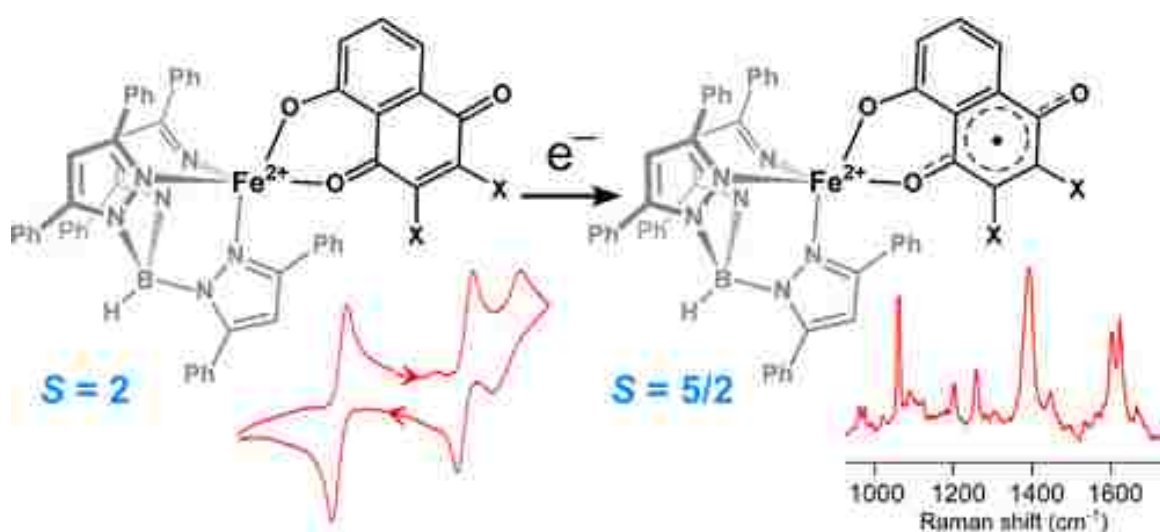
Abstract: The synthesis and characterization of a series of mononuclear Fe(II) complexes supported by the tris(3,5-diphenylpyrazol-1-yl)borate (^{Ph2}Tp) ligand and bearing substituted quinone ligands is detailed in this chapter. Upon successful generation of an Fe(II)-quinonate species, we explored the abilities of these compounds to generate novel Fe(II)-*p*-semiquinone species upon chemical reduction in order to further investigate the role of a radical species in the catalytic mechanism of the hydroquinone dioxygenases. The existence of a ligand-based radical was confirmed by extensive spectroscopic and computational analysis. These results represent the first examples of mononuclear iron complexes containing *p*-SO$^{\cdot-}$ ligands and therefore provide a solid foundation for further investigation of metal-ligand radical interactions similar to those observed in nature.

5.A. Introduction

The utilization of substituted p-benzoquinones to facilitate redox reactions is a common theme in biological processes. The ability of these cofactors to carry out reversible redox reactions allows them to participate in a variety of processes such as respiration, photosynthesis, catalytic transformations and protection against oxidative stress.[99, 152] Quinones can take part in one- and two-electron reactions, usually coupled with proton transfer(s), to generate the corresponding semiquinone and hydroquinone species, respectively (Figure 5.1).
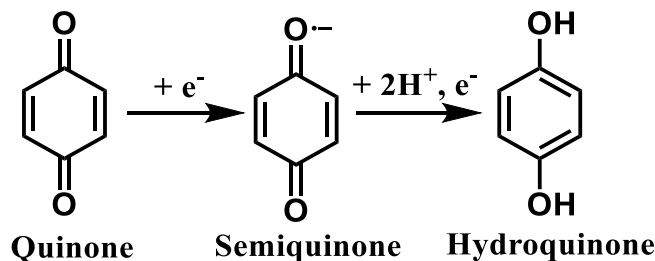
Figure 5.1. Net reduction of quinone to hydroquinone.

In biological systems, quinones generally function in unison with redox active metal centers, such as iron and copper. A specific example of a metal-quinone system found in nature is cytochrome bc_1, an essential complex in the electron transport chain. This complex facilitates the transfer of two electrons from p-hydroquinone ubiquinol to a Rieske cluster and a heme (b_L) site within the ET chain.[185] The close proximity of ubiquinol with the iron centers allows for electronic coupling between sites. Electronic

paramagnetic resonance (EPR) has recently confirmed the interaction of the ubi-semiquinone ($SQ^{\cdot-}$) radical and a reduced Fe-S cluster following the primary electron transfer via detection of a triplet electronic state arising from ferromagnetic interactions between each paramagnetic moiety.[186] In addition, a nonheme ferrous center in Photosystem II (PSII) operates in conjunction with two p-quinones (Q_A and Q_B) that shuttle electrons away from the photoexcited cofactor, P_{680}^{*} resulting the formation of transient Fe^{II}-$p$$SQ^{\cdot-}$ as elucidated via EPR studies.[187] Most relevant to this document, a superoxo-Fe^{II}-$SQ^{\cdot-}$ intermediate has been proposed as a key intermediate in the degradative pathways of the hydroquinone dioxygenases, which facilitate the catabolism of p-hydroquinones in nature.[52]

Despite these biological precedents of iron-quinone interactions, few synthetic Fe complexes with bound p-quinone or p-semiquinone ligands have been reported in the literature. The lack of reported synthetic analogues can be attributed to the weak donor ability of the carbonyl moieties of p-quinones, which can only bind to metal centers in a monodentate manner. This difficulty can be overcome by the placement of an anionic donor adjacent to the carbonyl moiety of the quinone to assist in ligation to a metal center.

This chapter details our success in the synthesis and characterization of metastable Fe(II)-$p$$SQ^{\cdot-}$ species with relevance towards similar metal-radical intermediates found in biological applications – particularly those observed in metalloenzymes. In order to achieve our goal, we first sought to synthesize a series of monoiron(II) complexes which incorporate the monoanion of substituted quinone ligand derivatives [juglone (**H J**), 2,3-dibromojuglone (**Br J**), lawsone (**H L**), 3-chlorolawsone (**Cl L**)

and 1-hydroxyanthraquinone (AQ)] (Figure 5.2). In order to facilitate binding of each

ligand to the metal center, each naphthoquinone moiety incorporates a pendant phenolate

donor which allows formation of a favorable six-membered ring chelate. The high-spin

Fe(II) center of each mononuclear complex is further supported by the hydrotris(3,5-

diphenylpyrazol-1-yl)borate (^{Ph2}Tp) facially-capping ligand scaffold.
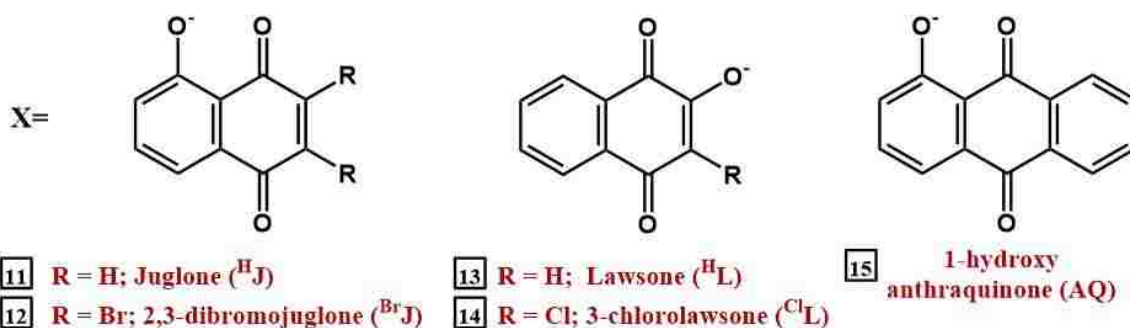
Figure 5.2. Substituted naphthoquinone ligands utilized in this study. Each incorporates a hydroxyl group pendant to the carbonyl moiety to facilitate binding.

Upon successful generation of our Fe(II)-quinonate precursors, we explored the

ability of these species to undergo chemical reduction to form Fe(II)-pSQ$^{\cdot-}$ species. We

noted that upon addition of an appropriate one-electron reductant at low temperatures to

11 and **12**, we generated two new brown chromophores, **11^{red}** and **12^{red}**, respectively.

These species were studied extensively via spectroscopic [UV-vis absorption, EPR and

rRaman (rR)] and computational methods, which confirmed the presence of a substrate-

based radical in the newly-generated Fe(II)-pSQ$^{\cdot-}$ species – which, to the best of our

knowledge, are the first to be reported in literature. Thus, our synthetic efforts lay

precedent for further detailed explorations of biologically-relevant iron-(semi)quinone interactions.

5.B. Results and Discussion

5.B.i. Synthesis and Characterization of monoiron(II) complexes incorporating substituted quinonate-derived ligands

In our course to develop synthetic models of the HQDOs (Chapter 2), our survey of bidentate hydroquinonate ligands initially included a naphthalene-derivative, 1,4,5-naphthatlenetriol (**1,4,5-NTO**). Upon generation a mononuclear Fe(II) complex supported facially by the ^{Ph2}Tp ligand and bound to the monoanion of (**1,4,5-NTO**), we determined our complex incorporated the unexpected diketo- tautomer of the triol ligand, even in the presence of base (Figure 5.3).
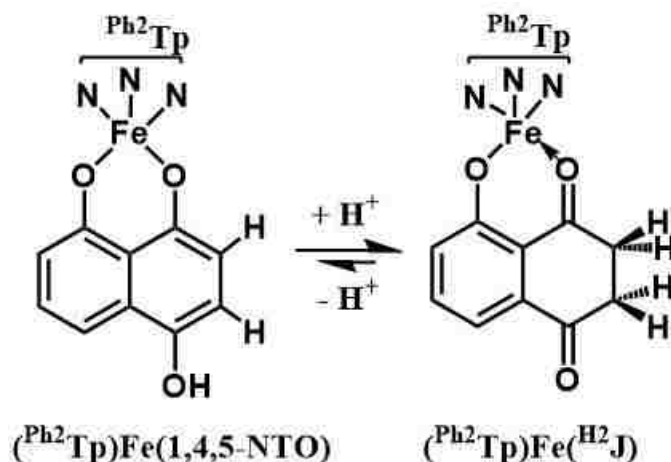
Figure 5.3. Suggested tautomerization of 1,4,5-naphthalenetriol ligand to 2,3-dihydrojugalone (**^{H2}J**).

Crystals suitable for X-ray crystallographic analysis were obtained by layering a concentrated solution of the complex in DCM with MeCN. X-ray diffraction analysis (XRD) revealed a 5-coordinate complex with an Fe center bound to the anion of 2,3-dihydrojugalone formulated as [(^{Ph2}Tp)Fe(2,3-dihydrojugalone)], (**10**) (Figure 5.4). The saturation of the C-C bond is evident by the presence of two H-atoms and the twisted ring conformation of the bound ligand. Details concerning data collection and analysis are provided in Table 5.4 and selected bond lengths and angles for **10** are given in Table 5.1.
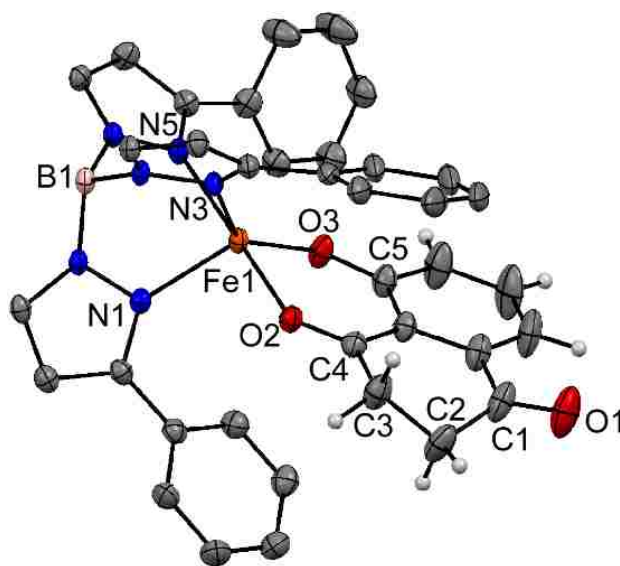
Figure 5.4. Thermal ellipsoid plot (50% probability) derived from the X-ray crystal structure of [**Fe(^{Ph2}Tp)(2,3-dihydrojugalone)] (10)**. Non-coordinating solvent molecules, hydrogen atoms, and Ph-rings at the 5-positions of the ^{Ph2}Tp ligand have been omitted for clarity.

Table 5.1. Selected bond distances (Å) and bond angles (°) from the X-ray structures of monoiron(II) napthoquinone-derivative complexes **10-14**.

	10	11	12	13	14
Fe–N1	2.1082(17)	2.1022(13)	2.102(4)	2.100(4)	2.072(5)
Fe–N3	2.0959(17)	2.0892(14)	2.084(4)	2.086(4)	2.054(5)
Fe–N5	2.2036(17)	2.2047(14)	2.229(4)	2.191(4)	2.166(5)
Fe–O2	2.0904(14)	2.0624(12)	2.080(3)	2.226(3)	2.217(5)
Fe–O3	1.9384(15)	1.9262(13)	1.933(3)	1.955(3)	1.963 (4)
O1–C1	1.221(3)	1.222(2)	1.221(6)	1.232(6)	1.218(8)
O2-C4	1.241(3)	1.234(2)	1.244(6)	1.218(6)	1.232(7)
O3–C5	1.293(3)	1.298(2)	1.297(6)	1.310(5)	1.279(8)
C2-C3	1.521(3)	1.333(3)	1.337(7)		
O3–Fe–N1	129.69(7)	130.60(6)	127.16(2)	130.78(15)	129.12(2)
O3–Fe–N3	137.84(7)	137.32(6)	139.90(2)	134.04(15)	133.70(2)
O3–Fe–N5	100.53(6)	96.74(5)	96.42(1)	105.99(14)	110.33(19)
O3–Fe–O2	85.56(6)	86.05(5)	85.20(1)	76.99(12)	77.00(18)
N1–Fe–N3	91.84(6)	91.98(5)	92.93(1)	92.22(15)	92.85(2)
N1–Fe–N5	89.43(6)	89.17(5)	84.90(1)	88.41(15)	87.10(2)
N3–Fe–N5	84.71(6)	84.95(5)	87.90(1)	87.98(14)	87.35(2)
O2–Fe–N1	90.04(6)	90.15(5)	93.34(1)	89.81(14)	88.63(18)
O2–Fe–N3	87.79(6)	92.18(5)	92.06(1)	89.69(13)	86.86(18)
O2–Fe–N5	172.46(6)	174.97(5)	176.77(1)	177.01(14)	172.64(17)
τ-value[b]	0.58	0.63	0.62	0.72	0.65

[a] For a definition of the τ-value, see ref 98. A five-coordinate complex with ideal square-pyramidal geometry would have a τ-value of 0.0, while those with ideal trigonal bipyramidal geometry would have a value of 1.0.

Due to the tautomeric flexibility of the triol ligand, further studies were aimed at the synthesis of the dehydro analog, namely [Fe(^{Ph2}Tp)(^{H}J)] (**11**). We also generated the Fe(II)/quinone complexes [Fe(^{Ph2}Tp)(^{Br}J)] (**12**), [Fe(^{Ph2}Tp)(^{H}L)] (**13**) and [Fe(^{Ph2}Tp)(^{Cl}L)] (**14**). Complexes **11-14** were prepared under anaerobic conditions by mixing equimolar amounts of the [(^{Ph2}Tp)Fe(OBz)] precursor complex with the corresponding ligands (**^{H}JH**, **^{Br}JH**, **^{H}LH** and **^{Cl}LH**, respectively) treated with one equivalent of NaOMe in DCM. Layering concentrated solutions of **11-14** with either MeCN or pentane afforded crystals suitable for XRD analysis. Details concerning data collection and analysis are

provided in Table 5.3 and selected bond lengths and angles for **11-14** are given in Table 5.1. As illustrated in Figure 5.5, all three complexes feature a 5C Fe(II) center bound facially by the Ph2Tp ligand and the bidentate **HJ, BrJ**, **HL** or **ClL** napthoquinone-derived ligands.
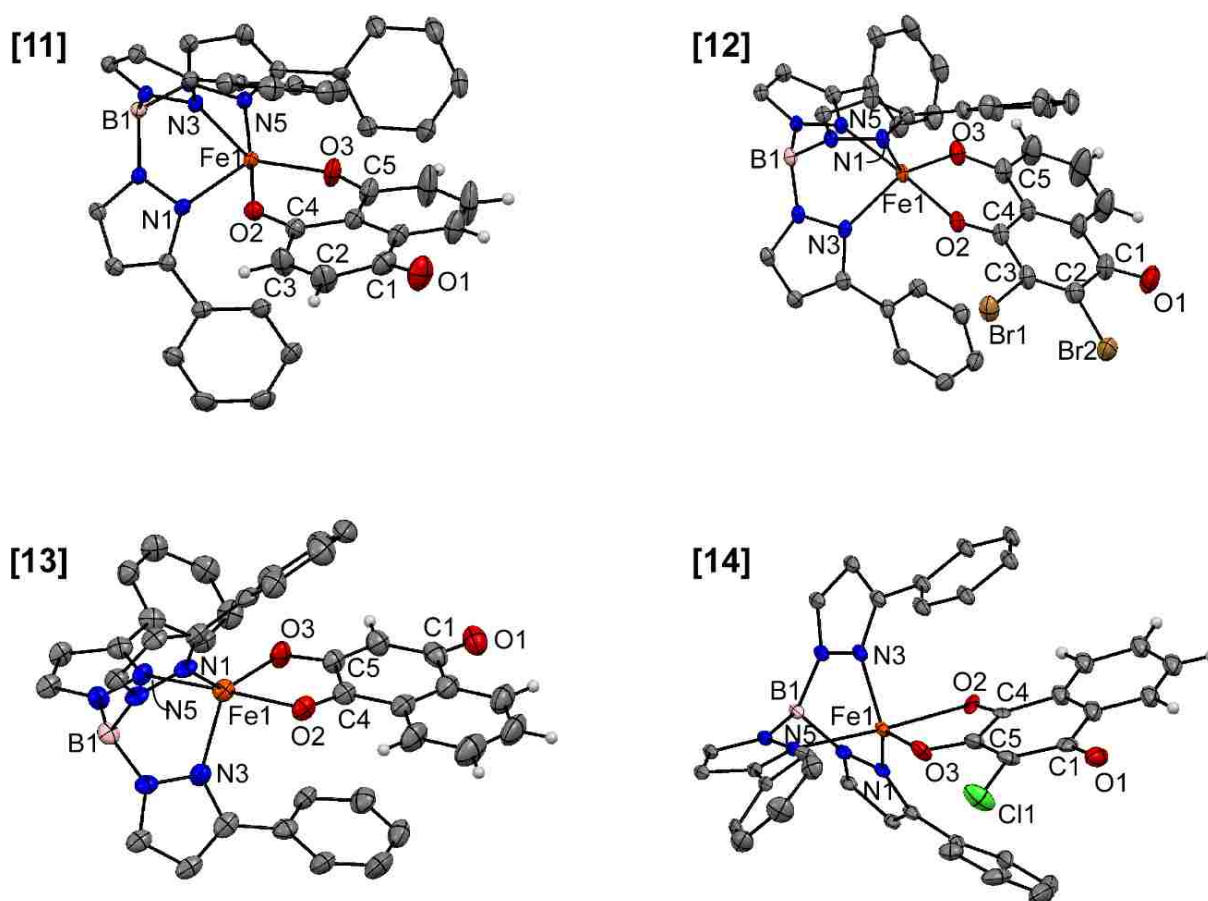
Figure 5.5. Thermal ellipsoid plots (50% probability) derived from the X-ray structures of complexes **11-14**. Non-coordinating solvent molecules, scorpionate-derived hydrogen atoms and the Ph-rings at the 5-positions of the Ph2Tp ligand have been omitted for clarity.

Comparison of the Fe-N_{Tp} bond lengths of complexes **11-14** indicate an average value of 2.13 Å, characteristic of high spin, Fe(II) (S=2) centers. Further support for the formation of ferrous complexes is demonstrated by the Fe-O3 distances which range between 1.926 Å-1.963 Å, indicative of Fe(II)-phenolate units within 5C iron complexes.[96,97,112] Despite the weak donor ability of quinone ligands toward metal centers, the presence of pendant anionic donors located on the bidentate ligand positions the quinone in close proximity to the iron center, ultimately facilitating a binding interaction. This observation is demonstrated by the bond distances found between the Fe(II) center and the carbonyl moieties (Fe–O2, Table 5.1) of the naphthalene-derived ligands, ranging from 2.062 Å-2.226 Å. The coordination geometry of **11**, **12** and **13** are closer to the trigonal bipyramidal limit (τ = 0.63, 0.62 and 0.72, respectively) with the phenolate (O3) and carbonyl (O2) donors of the **^{R}J^{-}/^{R}L^{-}** ligands bound in equatorial and axial positions, respectively. Complexes **10** and **11** display very similar metric parameters beyond the difference in the C2-C3 bond distance due to the varying degree of saturation between the ligands. The donor ligands of **10**, **11** and **12** form six-membered ring chelates with the iron center whereas the **^{R}L**-derived ligands form a five-membered chelate in **13** and **14** due to the varied position of the pendant hydroxyl donor.

In addition to complexes **11-14**, the synthesis of a similar mononuclear (^{Ph2}Tp)Fe^{2+} species incorporating 1-hydroxyanthraquinone (AQ; **15**) was synthesized. While crystals suitable for X-ray diffraction analysis were unable to be isolated, an ^{1}H-NMR spectrum of **15** obtained in CD$_2$Cl$_2$ displays a number of paramagnetically shifted and broadened peaks between δ -40-80 ppm, similar to the spectrum observed for **11**, confirming the presence of high-spin Fe(II) (S=2) centers in each complex (Figure 5.6).
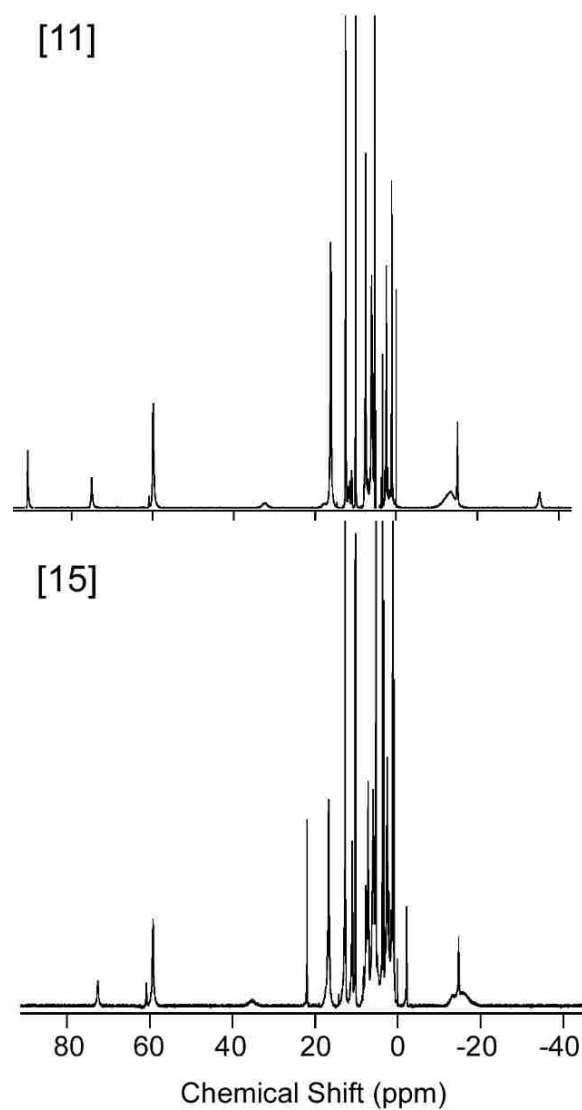
Figure 5.6. ^{1}H-NMR spectra of complexes **11** and **15** in CD_2Cl_2.

5.B.ii. Spectroscopic and Electrochemical Investigation of Fe(II)-quinonate Complexes

Electronic absorption spectra of complexes **10-15** are shown in Figure 5.7(a)-(c).

Complex **10**; Figure 5.7(a). exhibits an intense feature at λ_{max} = 343 nm (ε = 3.8 mM^{-1} cm^{-1}) as well as a weak absorption manifold centered at 550 nm (ε = 0.6 mM^{-1} cm^{-1}). The

spectrum is strikingly similar to that obtained previously for the Fe(II)-HQate complexes

2 and **3** (Figure 2.8). This is not surprising, given the similar electronic structures of these

ligands which incorporate similar acetyl moieties. The lower energy band of this

spectrum is likely to arise from an Fe(II) → (2,3-^{H2}J) MLCT transition whereas the

higher energy feature can be assigned to a ligand-based $\pi \to \pi^*$ transition. The electronic

spectra of complexes **11**-**14** display similar band shapes; Figure 5.7(b)-(c), however these

naphthoquinone-based ligands exhibit lower energy bands compared to complex **10**.

Complex **11** exhibits a deep-violet color in solution due to the presence of two absorption

bands at 510 and 910 nm (ε = 5.7 and 2.4 mM^{-1} cm^{-1}, respectively; Figure 5.7). Time-

dependent (TD) density functional theory (DFT) calculations attribute the lower-energy

band to a Fe^{II} → ^{H}J^{-} metal-to-ligand charge transfer (MLCT) transition while the higher-

energy feature arises from an intraligand $\pi \to \pi^*$ transition on ^{H}J^{-} (Figure 5.8).

Both transitions red-shift by approximately 700 cm^{-1} in the spectrum of **12**

because of the presence of electron-withdrawing Br substituents. The absorption spectra

of complexes **13** and **14** bear resemblance to those of **11** and **12**, however vary

significantly in band intensity. Complexes **13** and **14** exhibit intraligand transitions at λ_{max}

= 448 nm (ε = 1.5 mM^{-1} cm^{-1}) and 473 nm (ε = 2.7 mM^{-1} cm^{-1}), respectively, while

simultaneously displaying broad, low energy features between 680-820 nm (ε < 0.6 mM^{-1}

cm^{-1}) likely representing weak Fe^{II}→^{R}L^{-} MLCT transitions.
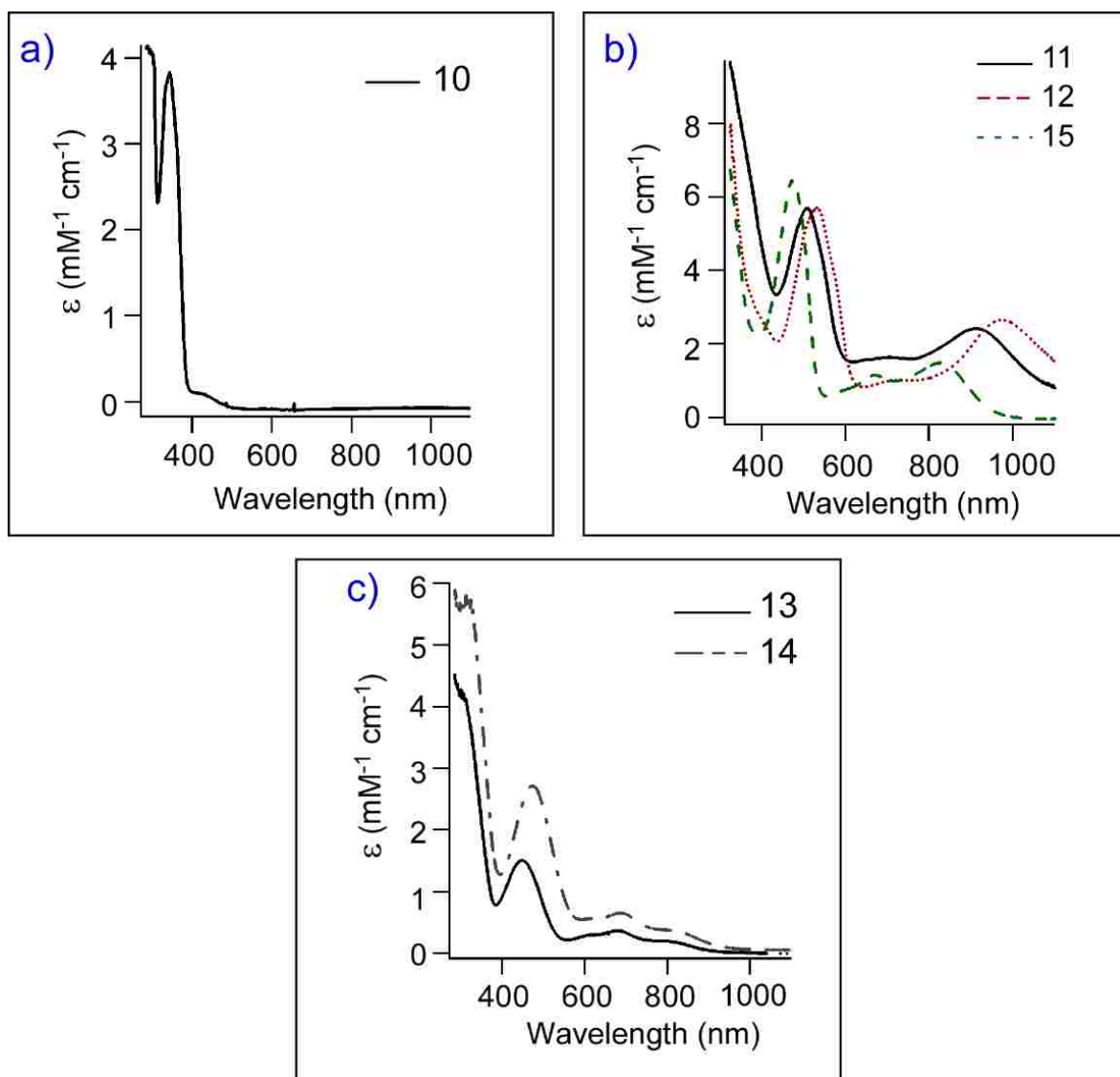
Figure 5.7. Electronic absorption spectra for complexes **10-15** obtained in CH_2Cl_2 at 20°C.
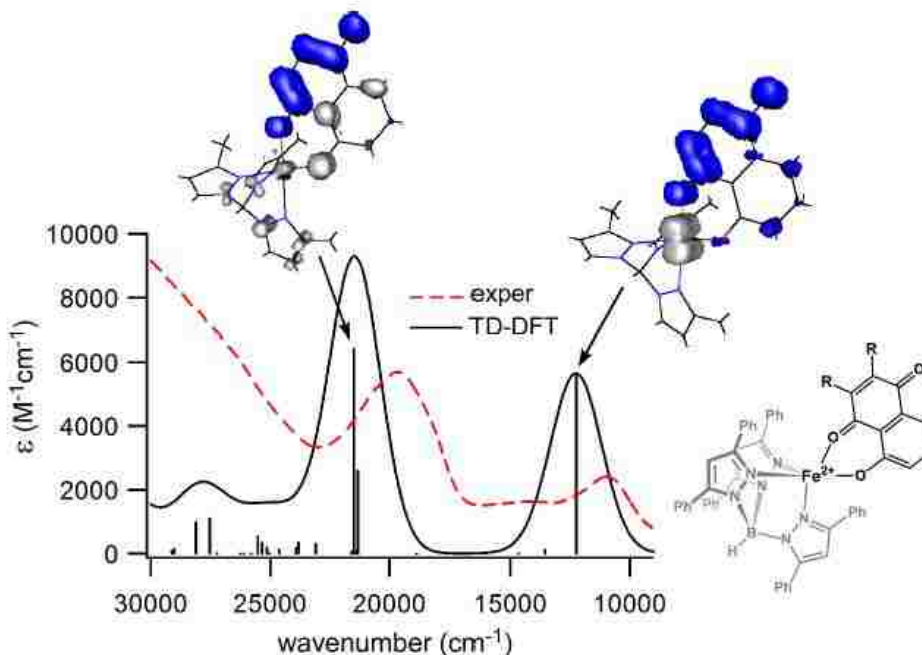
Figure 5.8. Experimental (red, dashed line) and TD-DFT computed (black, solid line) absorption spectra for complex **11**. The experimental spectrum was measured at room temperature in CH_2Cl_2. Electron density difference maps (EDDMs) for two computed transitions are also provided. The blue and grey regions indicate gain and loss of electron density, respectively.

Based on the structural similarity of the naphthoquinone- and anthraquinone-derived ligands, it is reasonable that complex **15** displays an intense $\pi \rightarrow \pi^*$ intraligand transition at λ_{max} = 471 nm (ε = 6.4 mM^{-1} cm^{-1}) as well as a series of weaker features at lower energy corresponding to Fe(II)$\rightarrow$ quinone MLCT transitions: λ_{max} = 666 nm (ε = 1.1 mM^{-1} cm^{-1}) and λ_{max} = 819 nm (ε = 1.5 mM^{-1} cm^{-1}). Besides a slight blue shift in energy, this data closely resembles the absorption spectra observed for **11** and **12**. In general, the MLCT bands displayed by complexes **11-15** appear at lower energies compared to those of **10** due to the ability of quinones to act as better electron acceptors with respect to acetyl moieties.

To assess the feasibility of generating iron(II) semiquinonate species via one-electron reduction, the electrochemical properties of complexes **11**-**15** were examined in DCM solutions with 0.1 M [NBu$_4$]PF$_6$ as the supporting electrolyte. In each case, cyclic voltammetry (CV) exhibits quasi-reversible one-electron oxidations between 0.07 – 0.33 V versus Fc$^{+/0}$ (Figure 5.9), assigned to the Fe$^{2+/3+}$ redox couple of each species based on our experience with related complexes.[112] At lower potentials, complex **11** displays a quasi-reversible couple at -1.33 V and an irreversible peak at -1.97 V. A comparison to redox potentials measured for 1,4-napthoquinone in MeCN (-1.11 V and -1.74 V)[188] indicates that these low-potential events arise from successive one-electron reductions of the ^{H}**J**$^{-}$ ligand. The corresponding features in the CV of **12** are shifted to more positive potentials by 0.23 V (Figure 5.9), reflecting the electron-poor nature of the ^{Br}**J**$^{-}$ ligand. A similar pattern is observed upon comparison of the ^{R}**L**$^{-}$ ligand-based reductions for complexes **13** and **14**; the first semireversible ligand redox event for **13** occurs at -1.37 V while this feature is shifted to a more positive potential in the CV of **14** (-1.26 V) due to the presence of the electron deficient ^{Cl}**L**$^{-}$ ligand relative to ^{H}**L**$^{-}$. Irreversible peaks are observed for **13** and **14** at -2.12 V and -2.02 V. A list of all electrochemical data is provided in Table 5.2.
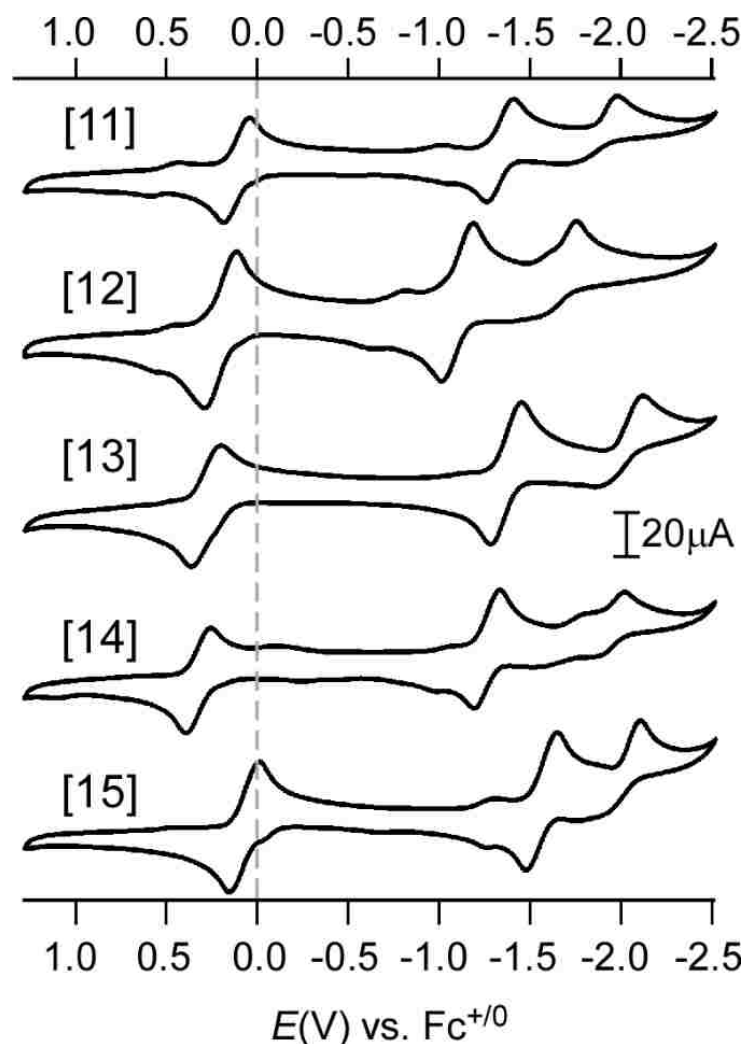
Figure 5.9. Cyclic voltammograms of **11-15** in CH_2Cl_2 with 0.1 M $(NBu_4)PF_6$ as the supporting electrolyte. Each CV was collected at a scan rate of 0.1 V/s.

Similar redox potentials were observed in the CV of **15** (Figure 5.9, Table 5.2). Two quasi-reversible couples were displayed at +0.073V and -1.56 V. An additional irreversible peak was observed at -2.11 V. It is interesting to note that compared to the complexes incorporating **RJ**- derived ligands (**11** and **12**), the redox events of **15** occur at more negative potentials, highlighting the difference in electron density localized on the naphthoquinone- and anthraquinone-derived ligands, respectively. The apparent ability of

complexes **11-15** to undergo reduction at potentials lower than that of their respective

Fe(II)/Fe(III) redox couples correlates well with the increased ability of quinones to act

as excellent electron acceptors when bound to a metal center as previously demonstrated

by the low energy bands present in their absorption spectra (Figure 5.7).

Table 5.2. Redox potentials of complexes **11-15**.

Complex	Solvent	Redox Potentials[b] (V *vs.* Fc$^{+/0}$)
11	CH_2Cl_2	$E_{1/2}$ (ΔE) = -1.33 (0.15), +0.11 (0.14); $E_{p,c}$ = -1.97 V
12	CH_2Cl_2	$E_{1/2}$ (ΔE) = -1.10 (0.17), +0.20 (0.18); $E_{p,c}$ = -1.76 V
13	CH_2Cl_2	$E_{1/2}$ (ΔE) = -1.37 (0.17), +0.28 (0.16); $E_{p,c}$ = -2.12 V
14	CH_2Cl_2	$E_{1/2}$ (ΔE) = -1.26 (0.14), +0.33 (0.14); $E_{p,c}$ = -2.02 V
15	CH_2Cl_2	$E_{1/2}$ (ΔE) = -1.56 (0.17), +0.07 (0.17); $E_{p,c}$ = -2.11 V

[a]Conditions: solutions contained 100 mM (NBu$_4$)PF$_6$; scan rate of 100 mV s^{-1} at room temperature. [b] $E_{1/2}$ and ΔE values are provided for (quasi)reversible processes; $E_{p,c}$ values are given for irreversible reduction events.

5.B.iii. Acidification Reaction of Complex 11

Based on our electrochemical investigation of **11-15**, we sought to generate novel

iron species bound to a semiquinonate ligand. Our initial studies involved the treatment

of **11** with acid, such as trifluoromethanesulfonic acid (HOTf) or HBF$_4$·O(CH$_2$CH$_3$)$_2$,

which we predicted would lead to the protonation of the distal carbonyl moiety of **^{H}J$^-$**,

facilitating an electronic rearrangement to the proposed semiquinone-oxidation level

(Figure 5.10). Due to protonation of ligand in absence of a chemical reductant, the target

complex is proposed to be a ferric-semiquinone species.
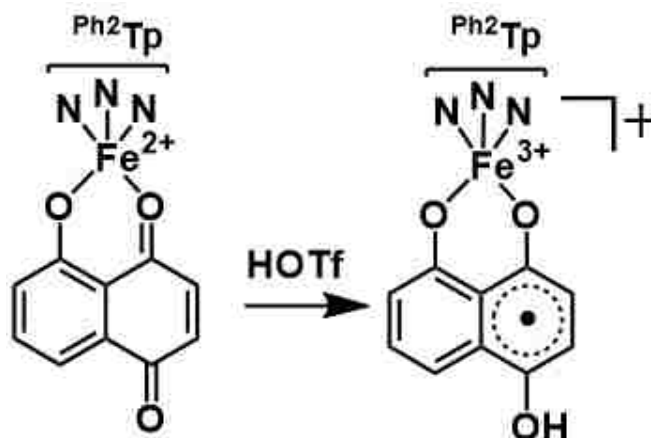
Figure 5.10. Proposed reaction for acidification of **11** to form an Fe(III)-semiquinone species.

Reaction of **11** with HOTf was monitored via UV-Vis spectroscopy. Initially, the reaction was carried out in pure DCM but it was observed that the reaction products upon addition of acid were not stable in solution. Further studies were carried out in methanol solution or a 1:1 mixture of DCM/MeCN which allowed for formation of stable, yellow species (**11^{H+}**) at room temperature. The formation of **11^{H+}** was observed to occur only in the presence of MeOH or MeCN which seems to indicate a coordinating solvent is necessary during reaction to stabilize the final product. The initial absorption spectrum of **11** in 1:1 DCM/MeCN displays an intense band at $\lambda_{max} = 507$ nm ($\varepsilon = 0.9$ mM^{-1} cm^{-1}) as well as two broad features at $\lambda_{max} = 707$ nm ($\varepsilon = 0.3$ mM^{-1} cm^{-1}) and $\lambda_{max} = 908$ nm ($\varepsilon = 0.8$ mM^{-1} cm^{-1}). Upon acidification, a new band is observed at $\lambda_{max} = 425$ nm ($\varepsilon = 1.6$ mM^{-1} cm^{-1}). (Figure 5.11).
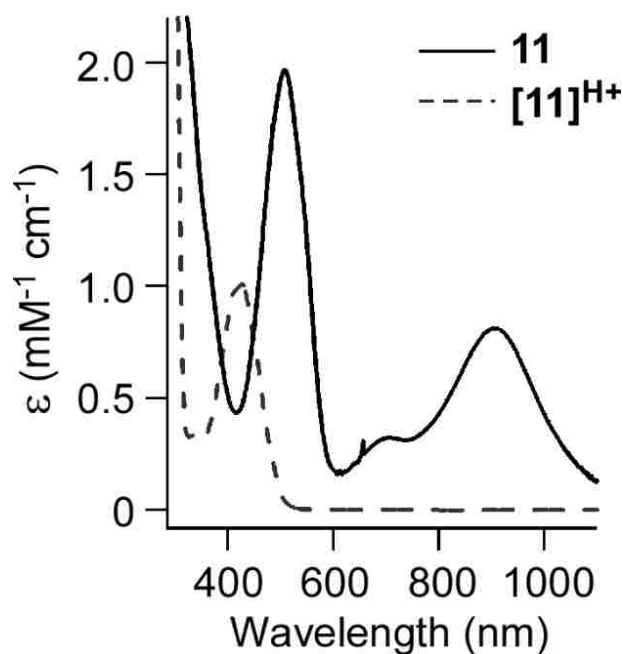
Figure 5.11. Electronic absorption spectra of **11** and final acidification product **[11]$^{H+}$** in a mixture of CH_2Cl_2/MeCN at room temperature.

Attempts to isolate solid material, especially crystalline solids, of **[11]$^{H+}$** were unsuccessful. Additionally, we attempted to characterize **[11]$^{H+}$** by ^{1}H-NMR, but all collected spectra were contaminated with signals arising from the added acid or excess solvent. In order to confirm the generation of the protonated species, **[11]$^{H+}$**, rather than potential complex degradation in solution, reversibility tests were carried out and monitored via UV-Vis spectroscopy. Addition of 2 equivalents of $HBF_4 \cdot O(CH_2CH_3)_2$ to **11** in methanol generated **[11]$^{H+}$**. Subsequent addition of 6 equivalents of tetrabutylammonium methoxide to the protonated species lead to the regeneration of **11**.

Comparison of **[11]$^{H+}$** with protonation of a similar species containing carbonyl donors in a β-position to the phenolate donor, namely [(^{Ph2}Tp)Fe(2,3-dihydrojugalone)] (**10**), was conducted via UV-Vis spectroscopy. The observed spectrum for **10** displayed a

similar high energy band at λ=339 nm (ε = 3.9 mM^{-1} cm^{-1}) upon treatment with HOTf (Figure 5.12).
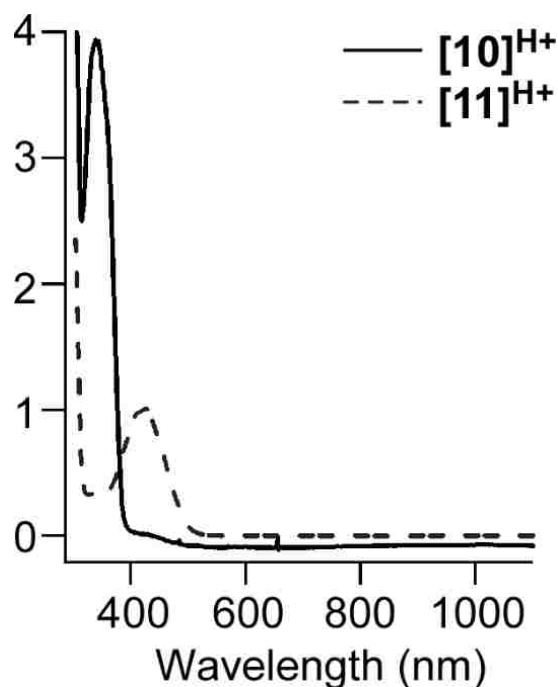
Figure 5.12. Electronic absorption spectra of complexes **10** and **11** treated with HOTf in a 1:1 mixture of CH$_2$Cl$_2$/MeCN at room temperature.

Interestingly, complex **10** displayed a change upon acidification, which indicates protonation must be occurring at either the proximal carbonyl donor or more likely, the anionic phenolate donor, due to the lack of aromaticity within the 2,3-^{H2}J ligand which would prevent tautomerization upon addition of acid. We therefore surmised that **[11]$^{H+}$** does not coincide with our previously predicted ferric-semiquinonate intermediate.

5.B.iv. Formation and Spectroscopic Analysis of Fe(II)-*p*SQ Species via One-Electron Reduction

In a further attempt to generate Fe-*p*SQ$^{\cdot-}$ species, we proceeded to monitor the reactivity of **11-15** with chemical reductants. Guided by the CV data we collected, complexes **11**, **13** and **15** were treated with one equivalent of CoCp$^*_2$ ($E° = $ -1.94 V in CH$_2$Cl$_2$), while the more-easily reduced complexes, **12** and **14**, were treated with CoCp$_2$ ($E° = $ -1.33 V).[189] The addition of reductants to solutions of **11-15** instantly generates new chromophores (**X**$^{\text{red}}$). Complexes **11**, **12** and **15** display two intense absorption features in the near-UV region (ε values of 8-10 mM^{-1} cm^{-1}; Figure 5.13). In addition, **11** and **12** display a shoulder near 600 nm and a broad near-IR feature. Complexes **13** and **14** also display the formation of a single intense band upon addition of one equivalent of reductant as well as a series of broad features at lower energies. According to further UV-vis analysis, the features observed upon addition of reductant to generate the **X**$^{\text{red}}$ species of **11** and **12** do not arise from (decamethyl)cobaltocene or its oxidized derivative (Figure 5.14). The **X**$^{\text{red}}$ species are stable for several minutes under anaerobic conditions and low temperatures (<-30 °C) but decay rapidly at room temperature to the starting material. The sizable intensities and sharp nature of the near-UV bands suggest they arise from ligand-based π-π^* transitions, consistent with transient absorption features in the same region.[132] Moreover, the **X**$^{\text{red}}$ absorption spectra bear close similarities to the one reported for Riordan's Fe^{II}-*o*SQ$^{\cdot-}$ complex.[130]
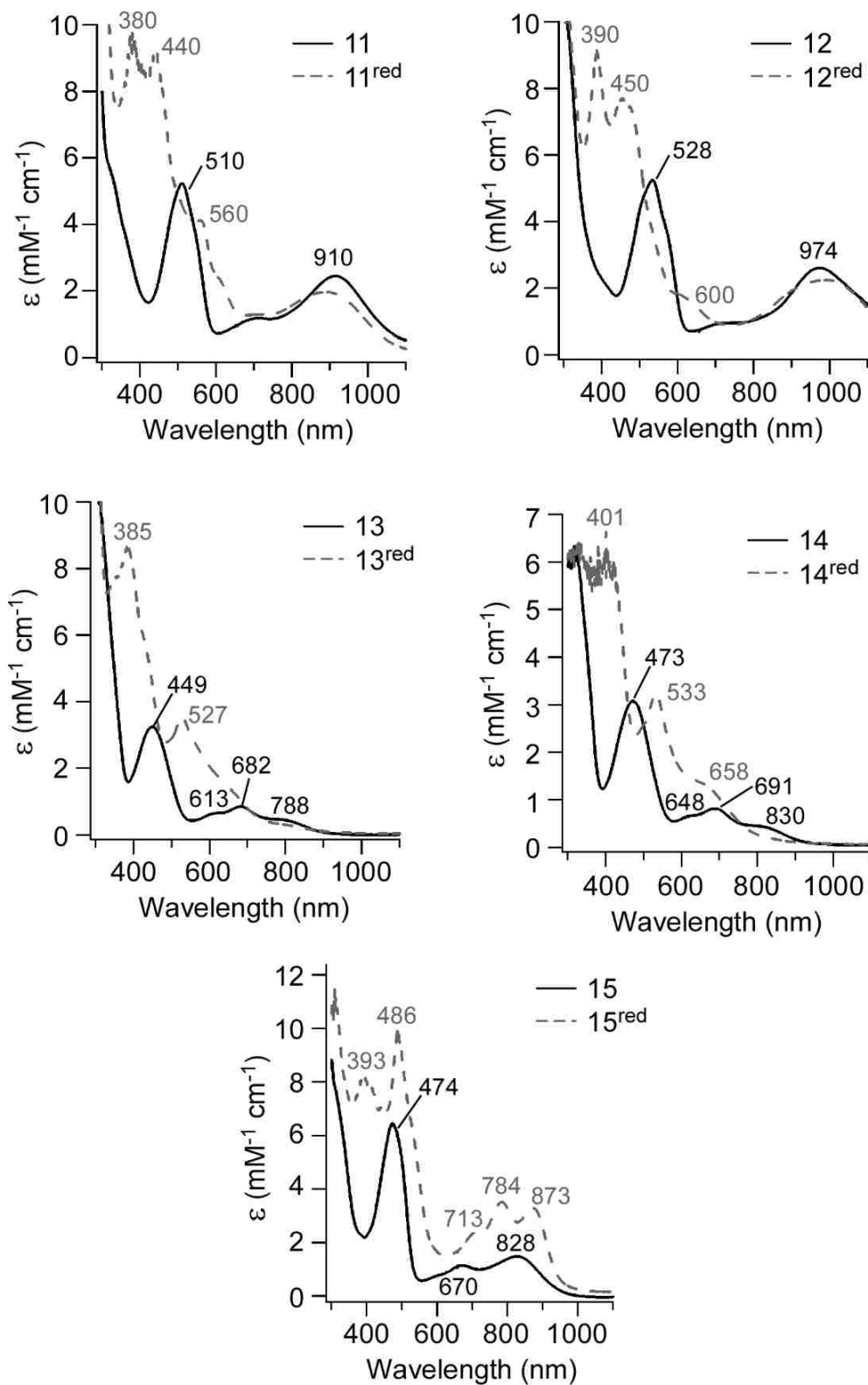
Figure 5.13. Solid lines: Electronic absorption spectra of **11**-**15** in CH$_2$Cl$_2$ at room temperature. Dashed lines: Spectra measured after the addition of 1 equiv of CoCp$^*_2$ (**11**, **13**, **15**) or CoCp$_2$ (**12**, **14**) at -30 °C in CH$_2$Cl$_2$ to give corresponding **X^{red}** species.
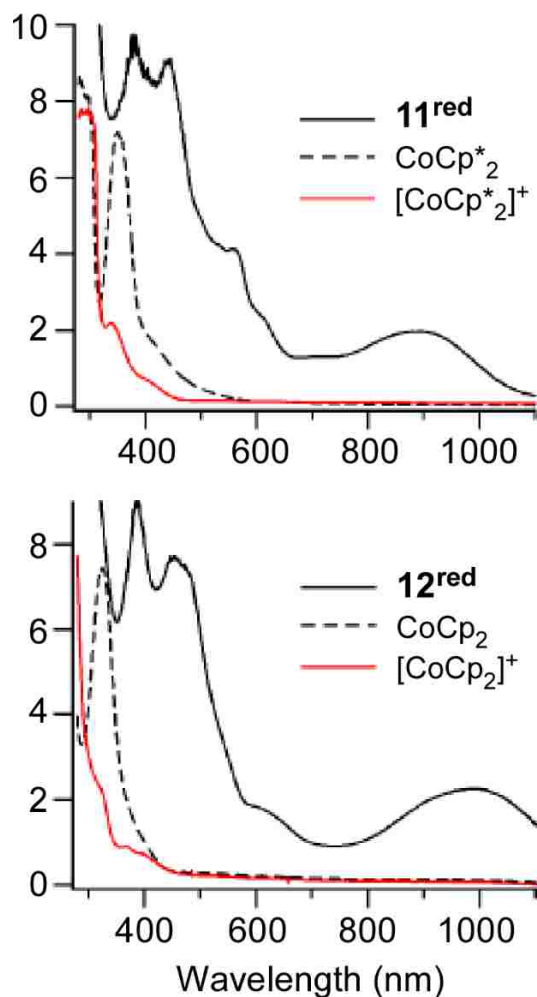
Figure 5.14. Electronic absorption spectra of 11^{red} (top) and 12^{red} (bottom) in CH_2Cl_2 at -30 °C. Spectra of the cobaltocene reductants and their oxidized cobaltocenium derivatives in CH_2Cl_2 are also shown. From this juxtapositon of spectra it is evident that the cobalt-containing complexes are not responsible for the intense absorption features assigned to the X^{red} species.

The X-band EPR spectra of **11** and **12** were obtained in order to study the electronic structure of the reduced species. The spectrum of 12^{red}, collected at 20 K in frozen CH_2Cl_2, consists of two $S = 5/2$ signals, as is evident by the low-field peaks at $g = 8.6$ and 10.1 (Figure 5.15).
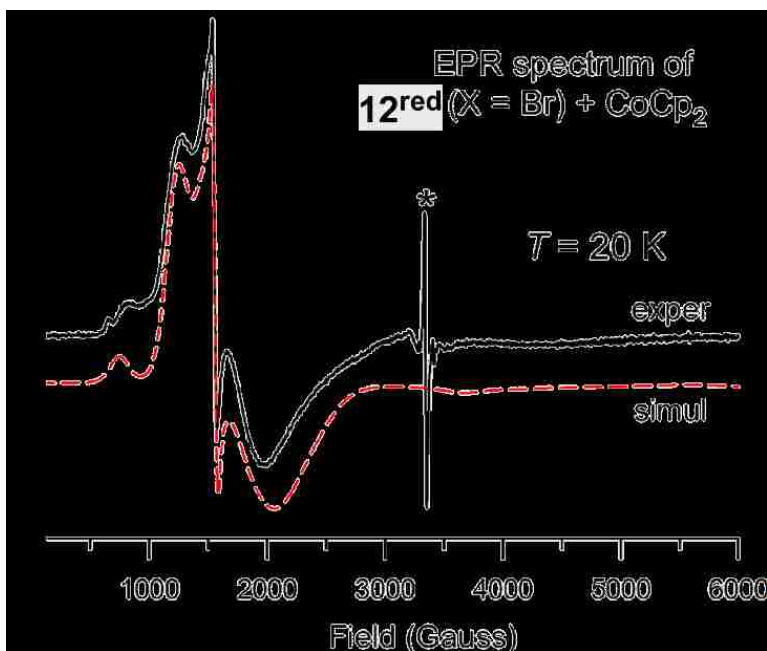
Figure 5.15. X-band EPR spectrum of **12$^{\text{red}}$** in frozen CH_2Cl_2 at 20 K. The sharp feature (*) arises from a radical impurity. Simulation of the data required two $S = 5/2$ species with the following parameters: major (92%), D = -4.0 cm^{-1}, E/D = 0.18, g = 2.0, 2.0, 2.1; minor (8%), D = 1.6 cm^{-1}, E/D = 0.33, g_{iso} = 2.0.

Simulation of the **12$^{\text{red}}$** data at multiple temperatures (Figure 5.16) determined that the dominant $S = 5/2$ species, accounting for 92% of the total intensity, has a negative D value and moderate rhombicity (E/D = 0.18). The minor $S = 5/2$ species is highly rhombic, characteristic of Fe$^{\text{III}}$ ions in low-symmetry environments.
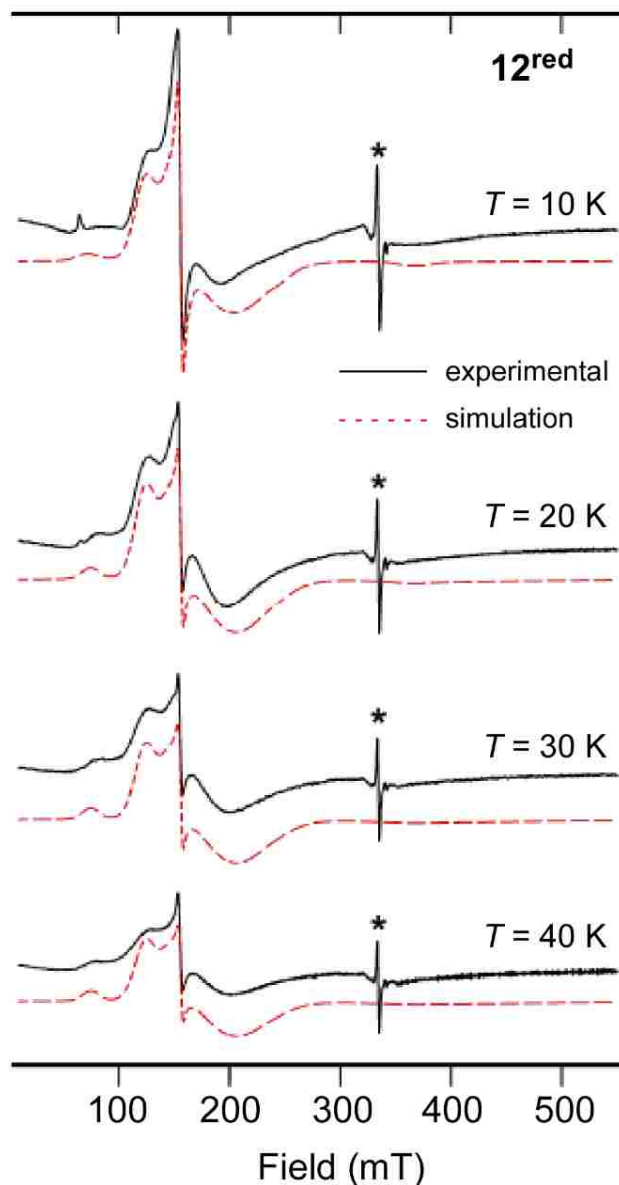
Figure 5.16. X-band EPR spectra of **12^{red}** collected at various temperatures in frozen CH$_2$Cl$_2$ solution. Experimental parameters: frequency = 9.387 GHz; microwave power = 2.0 mW; modulation amplitude = 10.0 Gauss; modulation frequency = 100 kHz. The sharp feature at 334 mT (*) arises from a radical impurity. Simulation parameters are provided in **Figure 5.11**.

This species accounts for the sharp feature at $g = 4.3$. Likewise, the **11^{red}**

spectrum (Figure 5.17) has contributions from major (88%) and minor (12%) $S = 5/2$

species with spin-Hamiltonian parameters nearly identical with their **12^{red}** counterparts. For both species, we propose that the major $S = 5/2$ signal corresponds to **X^{red}**, while the minor signal is attributed to ferric impurities generated from trace amounts of O_2. The EPR results therefore suggest that the putative pSQ$^{\cdot-}$ ligand is ferromagnetically coupled to the high-spin Fe^{II} center.
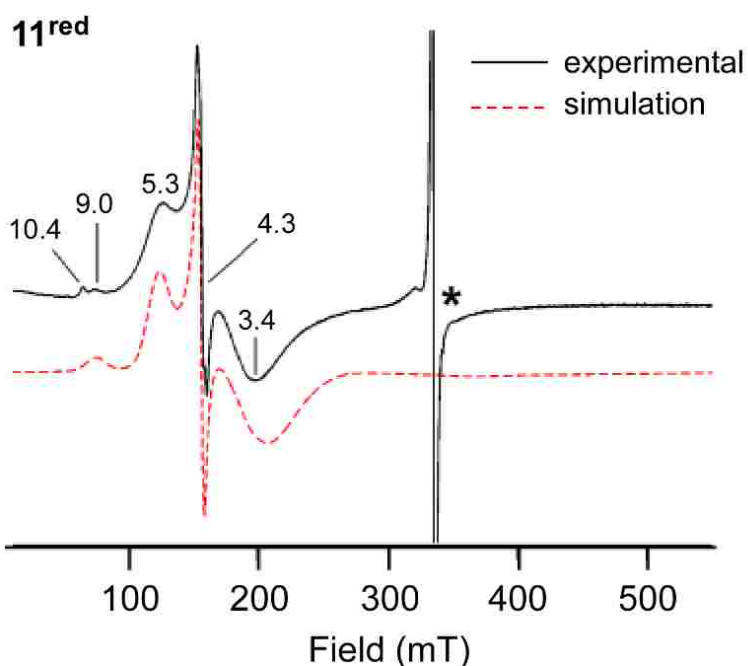
Figure 5.17. X-band EPR spectrum of **11^{red}** in frozen CH$_2$Cl$_2$ at 20 K. Experimental parameters: frequency = 9.387 GHz; microwave power = 2.0 mW; modulation amplitude = 10.0 Gauss; modulation frequency = 100 kHz. The sharp feature at 334 mT (*) arises from a radical impurity. Simulation of the data required two $S = 5/2$ species with the following spin Hamiltonian parameters: major (88%), $D = -3.0$ cm^{-1}, $E/D = 0.18$, $g = 2.0$, 2.0, 2.1; minor (12%), $D = 1.6$ cm-1, $E/D = 0.33$, $g_{iso} = 2.0$.

In addition, evidence for the generation of a ligand-based radical in complex **14** upon one-electron reduction observed via EPR spectroscopy. An X-band EPR spectrum

of **14**^{red} was obtained at 20 K (<u>Figure 5.18</u>) and exhibits a similar $S = 5/2$ signal as

previously observed for species **11**^{red} and **12**^{red}, indicating the Cl-substituted 2-

hydroxynaphthoquinone ligand of **14** (3-chlorolawsone) is able to facilitate redox

reactions similar to those observed for the 5-hydroxynaphthoquinone ligands of **11** and

12 (^HJ and ^{Br}J, respectively), despite the difference in substitution position of the

phenolate donor.
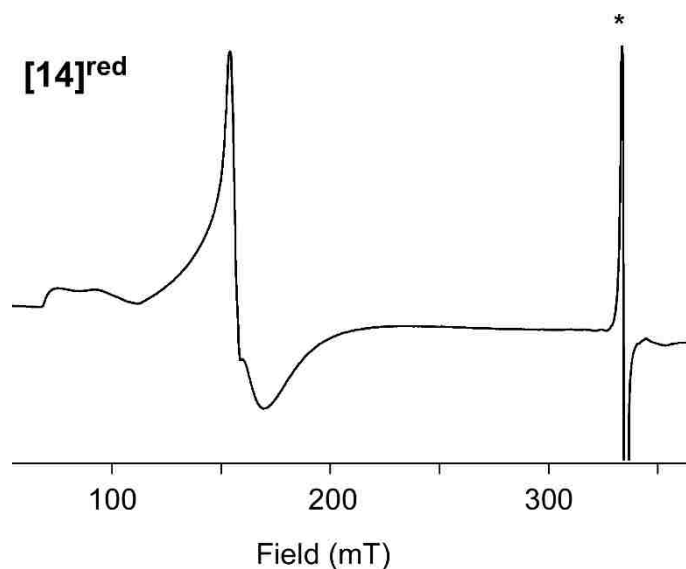
Figure 5.18. X-band EPR spectrum obtained for **[14]**^{red} in a frozen solution of CH_2Cl_2 at 20 K. The sharp feature at 334 mT (*) arises from a radical impurity.

5.B.v. Computational Analysis of X^{red} Species

Because we were unable to grow X-ray quality crystals of **11**^{red} and **12**^{red},

structural models of the reduced species with $S = 5/2$ were derived from DFT

calculations; <u>Table 5.3</u> compares the metric parameters for the **11/11**^{red} and **12/12**^{red} pairs

of geometry-optimized models. One-electron reduction of **11** to **11^{red}** causes the O2-C4

and O1-C1 bonds to elongate by 0.049 and 0.033 Å, respectively. In addition, the

quinoidal character of the ligand is diminished because of the lengthening of the C2-C3

(by 0.037 Å) and comparable shortening of the C1-C2 and C3-C4 bonds. Similar

differences in the ligand bond lengths are observed for the **12/12^{red}** pair (Table 5.3). Such

dramatic changes in the O-C and C-C bond distances upon conversion of **X→X^{red}** are

indicative of a change in the ligand oxidation state from a closed-shell quinone to a

semiquinone radical.[190] This conclusion is further supported by the Mulliken spin

populations of the iron center (3.78) and the **^{H}J** ligand (1.20) in the **11^{red}** model.

Table 5.3. Computed Bond Distances (Å) Obtained from DFT Geometry-Optimizations of Complexes **X** and **X^{red}** (**X** = **11** or **12**).

Bond Distances	11	11^{red} (DFT)	Δ	12 (DFT)	12^{red} (DFT)	Δ
Fe1-N1	2.150	2.218	0.068	2.135	2.210	0.075
Fe1-N3	2.157	2.190	0.033	2.148	2.177	0.029
Fe1-N5	2.297	2.491	0.194	2.294	2.491	0.197
Fe1-O2	2.086	2.031	-0.055	2.101	2.034	-0.067
Fe1-O3	1.942	1.914	-0.028	19.45	1.918	-0.027
O1-C1	*1.222*	*1.255*	*0.033*	*1.216*	*1.245*	*0.029*
O2-C4	*1.251*	*1.300*	*0.049*	*1.242*	*1.285*	*0.043*
O3-C5	1.298	1.323	0.025	1.298	1.319	0.021
C1-C2	*1.474*	*1.434*	*-0.040*	*1.496*	*1.448*	*-0.048*
C2-C3	*1.366*	*1.373*	*0.037*	*1.347*	*1.380*	*0.033*
C3-C4	*1.471*	*1.422*	*-0.049*	*1.494*	*1.434*	*-0.060*
C4-C10	1.444	1.451	0.007	1.445	1.451	0.006
C9-C10	1.423	1.430	0.007	1.420	1.424	0.004
C1-C9	1.491	1.481	-0.010	1.489	1.481	-0.008
C5-C6	1.423	1.404	-0.019	1.424	1.405	-0.019
C5-C10	1.430	1.437	0.007	1.434	1.439	0.005
C6-C7	1.373	1.391	0.018	1.373	1.388	0.015
C7-C8	1.402	1.383	-0.019	1.402	1.385	-0.017
C8-C9	1.380	1.399	0.019	1.381	1.398	0.017
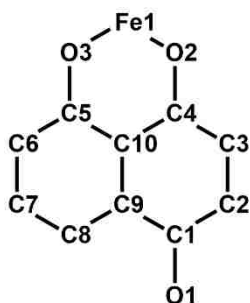
In agreement with the EPR data, broken-symmetry (BS) calcuations found that the iron- and ligand-based spins are ferromagnetically coupled, with computed J values of ~65 cm^{-1} ($H = -2JS_A \cdot S_B$). Moreover, absorption spectra computed using TD-DFT nicely reproduce key features of the experimental spectra (Figure 5.19); in particular, the calculations predict that each $\mathbf{X^{red}}$ model will display two pSQ-based $\pi \rightarrow \pi^*$ transitions in the near-UV region, resulting in an intense absorption band with λ_{max} near 410 nm. The computed spectra also exhibit a moderate Fe$^{II} \rightarrow p$SQ$^{\cdot-}$ MLCT band at 530 nm ($\mathbf{11^{red}}$) or 645 nm ($\mathbf{12^{red}}$).
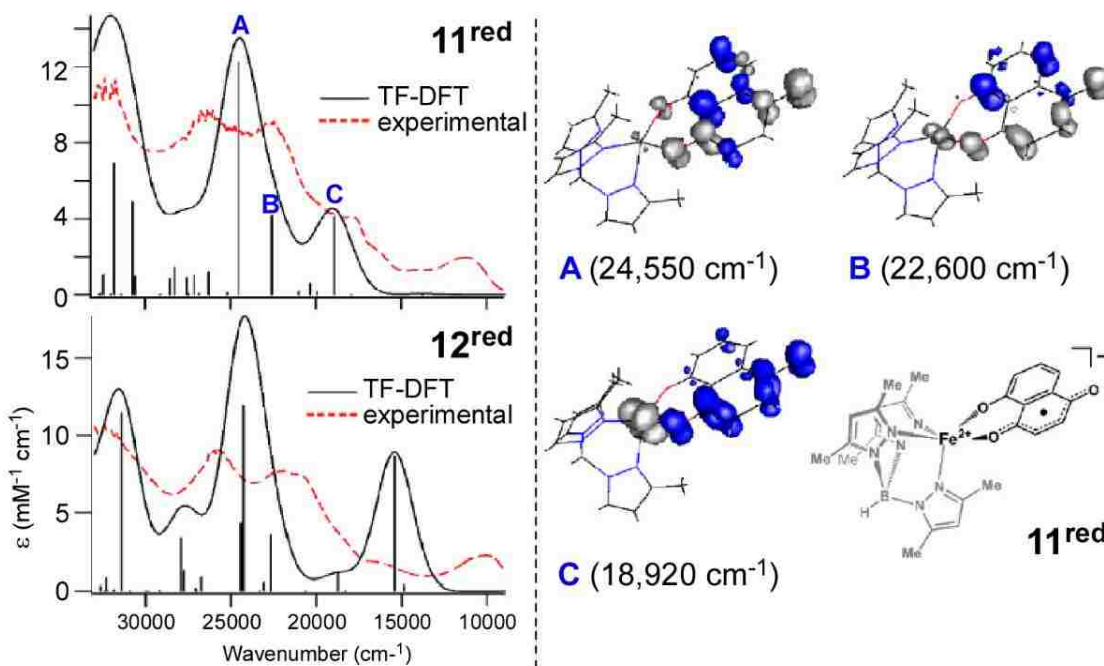
Figure 5.19. (Left) Experimental (red, dashed line) and TD-DFT computed (black, solid line) absorption spectra for $\mathbf{11^{red}}$ and $\mathbf{12^{red}}$. The experimental spectra were measured at -30 °C in CH$_2$Cl$_2$. (Right) Electron density difference maps (EDDMs) for three transitions in the computed $\mathbf{11^{red}}$ spectrum. The blue and grey regions indicate gain and loss of electron density, respectively.

5.B.vi. Resonance Raman Spectroscopic Studies of X^{red}

Direct evidence for the presence of a semiquinonate ligand in the **11^{red}/12^{red}** complexes was provided by rR studies. The rR spectrum of **11^{red}** (Figure 5.20) displays an intense peak at 1392 cm^{-1} that is not evident in the precursor spectrum; **2^{red}** exhibits a similar feature at 1382 cm^{-1} (Figure 5.21). Both peaks are strongly enhanced by excitation into the near-UV absorption bands. Coordinated SQ radicals typically display an intense peak in the 1400-1500 cm^{-1} region that arises primarily from stretching motions of the C-O bonds.[136, 139, 184] While the observed **11^{red}** and **12^{red}** frequencies fall slightly below this range, the C-O bonds of the semiquinonate ring are likely weakened by charge donation from the phenolate moiety of the **$^RJ^{2-}$** ligand. This conclusion is supported by DFT frequency calculations with the **11^{red}** mode, which predict a mode at 1407 cm^{-1} with mixed ν(C-O) and ring breathing character (Figure 5.22).
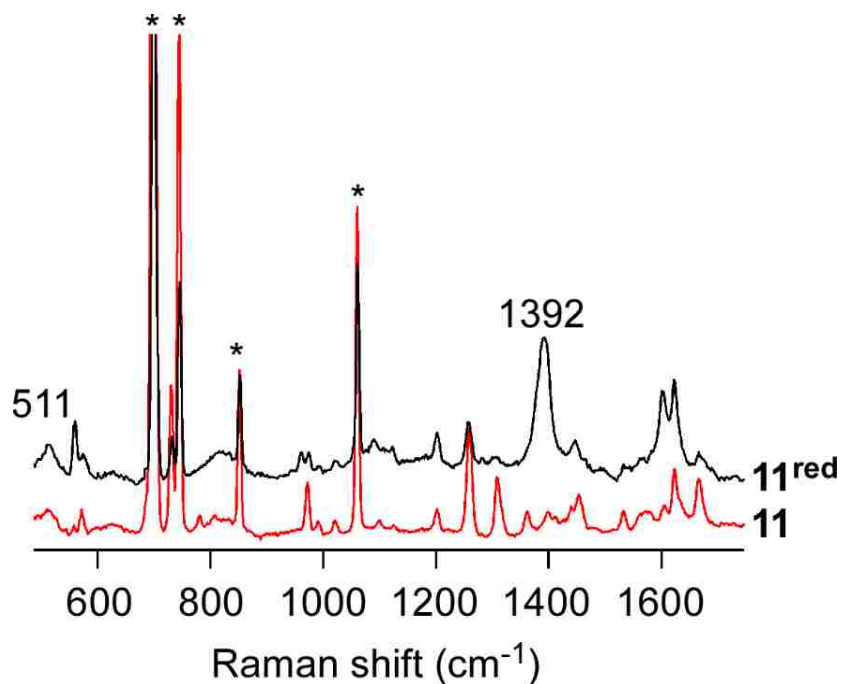
Figure 5.20. rRaman spectra obtained with 413.1 nm excitation (40 mW) of **11$^{\text{red}}$** (black; top) and **11** (red; bottom) in frozen CD_2Cl_2 solutions. Peaks with an asterisk (*) arise from solvent.
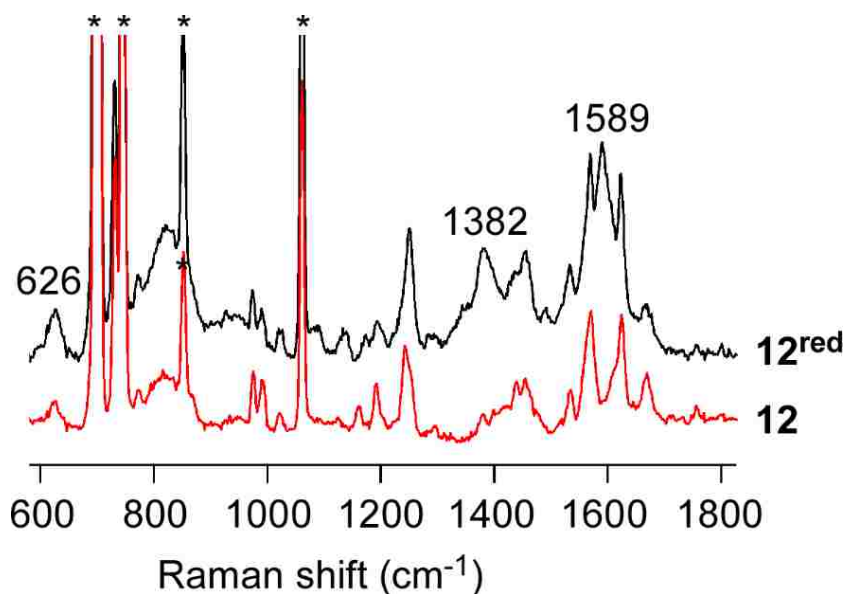
Figure 5.21. rRaman spetra obtained with 413.1 nm excitation (40 mW) of **12$^{\text{red}}$** (black; top) and **12** (red; bottom) in frozen CD_2Cl_2 solutions. Peaks marked with an asterisk (*) arise from solvent.
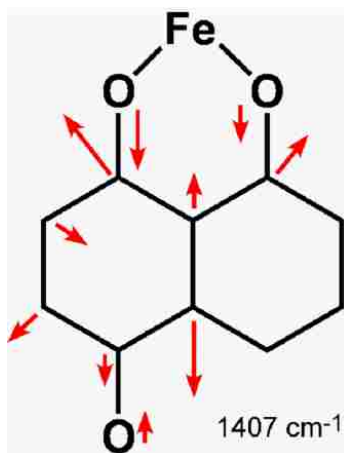
Figure 5.22. Pictorial representation of mixed ν(C-O) and ring breathing character at a predicted mode of 1407 cm^{-1} as derived from DFT frequency calculations.

Further evidence that the newly observed peak at 1392 cm^{-1} in the rRaman spectrum of **11^{red}** arises from the formation of a ligand-based radical, a spectrum of **11^{red}** upon warming the original sample to room temperature was taken, resulting in the decomposition of this species (Figure 5.23). Upon warming to room temperature, the sample was refrozen and rR data was collected under the same conditions as the initial **11^{red}** spectrum. The new spectrum indicates that the peak at 1392 cm^{-1} is dramatically diminished in the "decomposed" trial, indicating that it arises from **11^{red}** not CoCp$^{*}_{2}$ or [CoCp$^{*}_{2}$]$^{+}$. Interestingly, the rRaman spectrum of **14^{red}** did not provide direct evidence for the formation of a ligand-based radical as observed for the analogous complexes incorporating juglone ligands (**11^{red}** and **12^{red}**) due to the varied position of the phenolate donor of the lawsone-derived ligand of **14/14^{red}**.
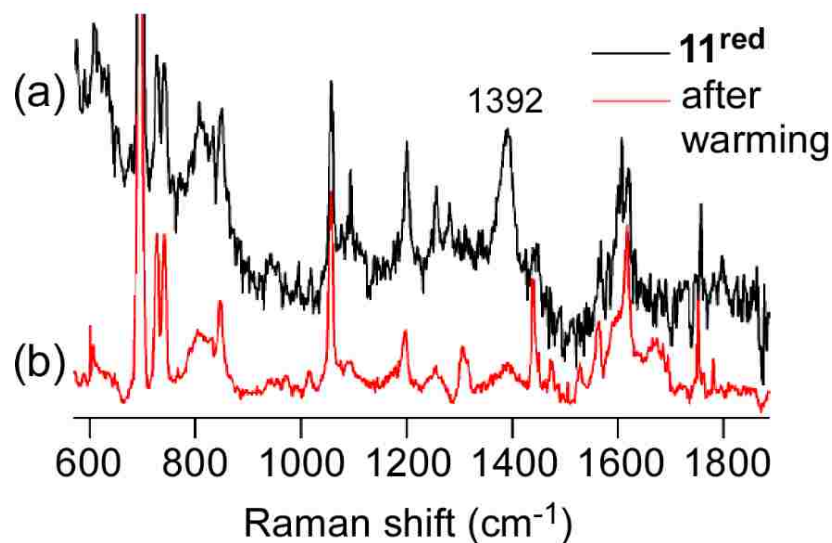
Figure 5.23. (a) Resonance Raman spectrum of **11^{red}** obtained with 413.1 nm excitation (40 mW). (b) Spectrum obtained after warming sample to room temperature, resulting in the decomposition of **11^{red}**.

5.B.vii. Nitric Oxide Reactivity Studies of Complex 11

In an effort to generate a comprehensive model of an enzymatic Fe/O$_2$$^{\cdot-}$-radical intermediate, we chose to employ nitric oxide as a functional model of dioxygen. Upon treatment of the ferrous precursor complex **11** in DCM solutions with nitric oxide we observed formation of a new purple-brown species that is stable at room temperature under anaerobic conditions (Figure 5.24).
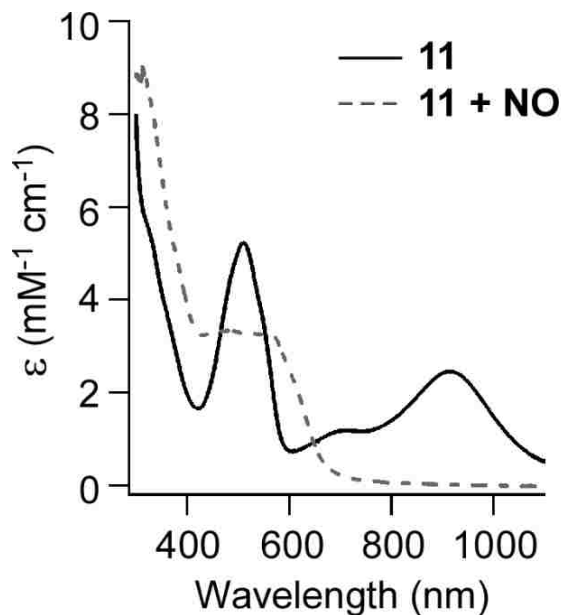
Figure 5.24. Comparison of UV-vis absorption spectra of **11** and species formed upon bubbling NO through a solution of **11** in DCM at room temperature (**11 + NO**).

Direct evidence for formation of an Fe-NO adduct upon addition of gaseous nitric oxide to DCM solutions of **11** was derived from the use of FTIR spectroscopy. Figure 5.25 displays a new peak at ~1740 cm^{-1} upon bubbling NO through a sample of **11** for several minutes in DCM. Isotopic labelling studies using ^{15}NO were completed and FTIR indicated a reasonable isotopic shift of ~32 cm^{-1} (1708 cm^{-1}) for **11^{15NO}**. XRD quality crystals of **11NO** were obtained by bubbling NO through a concentrated solution of **11** in for five minutes and transferring the sample to a -10 °C freezer to initiate crystallization. Despite significant disorder in the juglone ligand, XRD indicates the binding of NO to the iron center with an Fe-N$_{NO}$ distance of 1.797 Å (Figure 5.26).
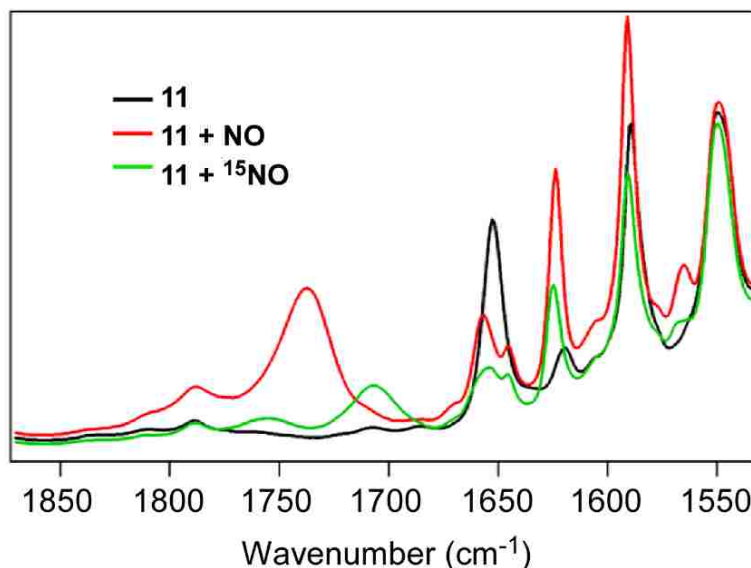
Figure 5.25. Solution FTIR spectra of **11** and the NO adducts formed upon bubbling either NO (red spectrum) or ^{15}NO (green spectrum) through a CH_2Cl_2 solution of **11** at room temperature.
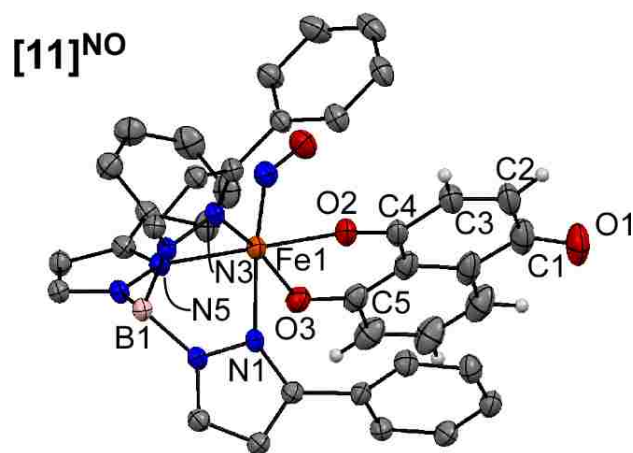
Figure 5.26. Thermal ellipsoid plot (50% probability) derived from the X-ray structure of complex **11NO**. Non-coordinating solvent molecules, scorpionate-derived hydrogen atoms and the Ph-rings at the 5-positions of the ^{Ph2}Tp ligand have been omitted for clarity. Selected bond lengths (Å) and angles (°): Fe1–O2 2.000(16), Fe1–O3 2.041(15), Fe1–N1 2.210(17), Fe1–N3 2.163(18), Fe1–N5 2.148(17), Fe1-N$_{NO}$ 1.799(19), O3–Fe1–N1 86.0(7), O3–Fe1–N3 165.5(7), O3–Fe1–N5 96.6(7), O2–Fe1–N1 88.9(6), O2–Fe1–N3 89.9(6), O2–Fe1–N5 176.7(7), N1–Fe1–N3 82.0(7), N1–Fe1–N5 89.2(6), N3–Fe1–N5 87.1(7).

In our effort to trap biologically relevant reactive intermediates similar to those proposed to exist in the catalytic mechanism of the HQDOs, we predicted that treatment of the NO adduct of **11** with one equivalent of an appropriate chemical reductant would generate an NO-Fe-SQ$^{\cdot-}$ type species. We first aimed to generate this species by a stepwise treatment of **11** with NO, followed by addition of one equivalent of a chemical reductant. Upon addition of CoCp$^{*}_{2}$ to the NO adduct of **11**, it is clear that a new species is formed as evidenced by UV-vis absorption spectroscopy. However, upon further analysis of this data, we confirmed that reaction of excess NO with CoCp$^{*}_{2}$ lead to the generation of the newly observed chromophore rather than formation of the predicted ligand-based radical (Figure 5.27).
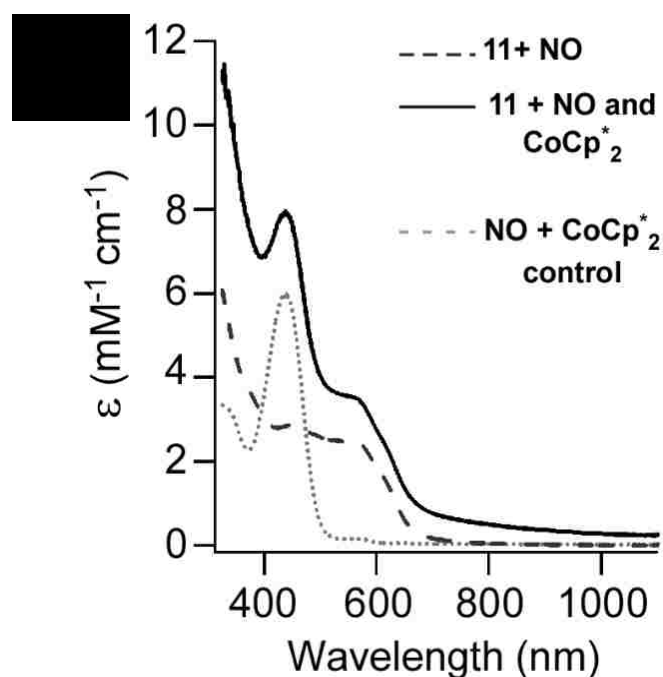
Figure 5.27. UV-vis absorption spectra of **11** treated with NO at -70 °C and a combination of NO and CoCp$^{*}_{2}$ in THF. Data obtained from a control experiment in which CoCp$^{*}_{2}$ was added to a solution of THF treated with nitric oxide is included for comparison.

In an attempt to avoid reaction of NO with CoCp$^*_2$, we sought to utilize an organic chemical reductant rather than a metal-based one, specifically sodium naphthalenide. UV-vis spectroscopy indicated treatment of **11** with 5 equivalents of sodium napthalenide in THF at room temperature allowed for conversion of **11** to **11^{red}** in THF. However, upon treatment of **11^{red}** with nitric oxide, UV-vis spectroscopy seemed to indicate loss of the electron, leading to generation of previously observed NO-bound form of **11** (Figure 5.28).
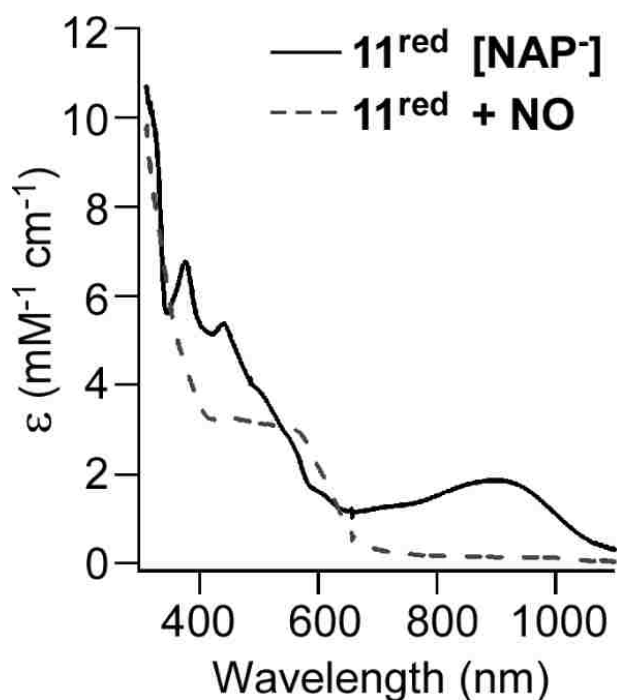
Figure 5.28. UV-vis absorption spectra indicating the formation of **11^{red}** upon addition of 5 equivalents of sodium napthalenide to **11** in THF at room temperature (solid line). NO was then bubbled through the solution, resulting in formation of the Fe-NO adduct (dashed line).

We therefore attempted to treat a solution of the previously isolated Fe-NO adduct, **11NO**, with sodium napthalenide in THF. Unfortunately, upon monitoring the

reaction via UV-vis spectroscopy, we observed that the addition of reductant to 11^{NO}

caused the complex to revert back to the precursor ferrous complex, **11** (Figure 5.29).
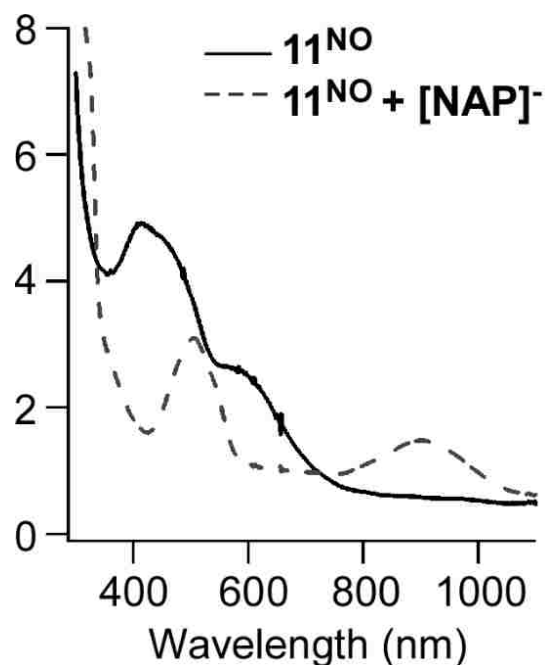
Figure 5.29. The addition of 5 equivalents of sodium napthalenide to 11^{NO} in THF at -40 °C seems to cause the complex to release NO and revert to starting material.

5.C. Conclusion

In this chapter, we reported the synthesis and structural analysis of a series of

mononuclear ferrous complexes that incorporate a variety of substituted 1,4-

naphthoquinone ligands (**11-14**). In order to facilitate a binding interaction between the

iron center and the quinone moiety, each naphthoquinone ligand includes an anionic

group pendant to a carbonyl donor of the quinone unit. Each complex features a 5C high-

spin ferrous center supported facially by the ^{Ph2}Tp scorpionate ligand and incorporates a

naphthoquinone ligand (^{H}J, ^{Br}J, ^{H}L or ^{Cl}L) bound in a bidentate fashion. A similar mononuclear complex featuring 1-hydroxyanthraquinone (**15**) as a ligand donor was synthesized, but crystals suitable for X-ray structural analysis were unable to be isolated.

The electrochemical and spectroscopic properties of complexes **11-15** were investigated in order to explore their propensity to undergo a 1 electron reduction in order to generate biologically-relevant Fe^{II}-pSQ$^{·-}$ species. We observed that treatment of complexes **11** and **12** with strong 1 electron reductants gives rise to species, X^{red}, with coordinated pSQ$^{·-}$ radicals ferromagnetically coupled to the high spin ferrous centers.

A similar procedure was used in an attempt to generate a similar Fe-pSQ species from **15,** which incorporates a substituted anthraquinone ligand**.** While similar absorption features are displayed in the UV-vis spectrum of **15** upon treatment with 1 equivalent of $CoCp^{(*)}_{2}$, further spectroscopic confirmation of this electronic assignment has not been completed. In addition, complexes **13** and **14** were included in this study to explore the effects of the position of the phenolate donor with respect to the carbonyl moiety of the naphthoquinone ligand. Rather than utilize a juglone-derived ligand, complexes **13** and **14** instead incorporate lawsone-derived ligands (^{H}L and ^{Cl}L) which incorporate a hydroxyl donor at the 2-position of the naphthoquinone ring. As demonstrated by UV-vis absorption spectroscopy, each complex displays new sharp features upon addition of an appropriate chemical reductant. The generation of a ligand-based radial, specifically in **14^{red}**, is supported by an X-band EPR spectrum of $CoCp_{2}$ which displays an $S = 5/2$ signal, similar to that observed for **11^{red}** and **12^{red}**. Unfortunately, rRaman spectroscopy did not provide evidence for the presence of a ligand-based radical as the measured spectra did not indicate resonance enhancement of any observed modes upon chemical

reduction of **14.** This could be due to the varied substitution of the lawsone-derived ligand with respect to the juglone ligands of **11** and **12**, and further characterization is required to confirm the presence of a ^{Cl}**L**-based radical.

Additional studies were focused on the generation of biologically-relevant intermediates, with regards to the reactive intermediates of the HQDOs, by the stepwise treatment of the Fe(II)-quinonate precursor **11** with nitric oxide and an appropriate chemical reductant. Up to this point in time, we have not been able to identify an appropriate method of preparation and future studies should focus on the determination of a more suitable chemical reductant.

Table 5.4. Summary of X-ray Crystallographic Data Collection and Structure Refinement of Complexes **10-14**.

	10	**11**	**12·DCE**	**13·2(MeCN)**	**14·2(DCM)**
empirical formula	$C_{55}H_{41}BFeN_6O_2$	$C_{55}H_{39}BFeN_6O_3$	$C_{57}H_{41}BFeN_6O_3Br_2Cl_2$	$C_{59}H_{45}BFeN_8O_3$	$C_{57}H_{42}BFeN_6O_3Cl_5$
formula weight	900.60	898.58	1155.34	980.69	1102.88
crystal system	Monoclinic	Monoclinic	Monoclinic	Orthorhombic	Monoclinic
space group	$P2_1/n$	$P2_1/n$	$P2_1/n$	$Pna2_1$	Pc
a, Å	10.3510(2)	10.4080(3)	9.7856(14)	36.3957(5)	13.4477(7)
b, Å	31.0420(7)	30.9033(9)	37.3826(4)	9.82077(13)	9.8666(6)
c, Å	13.5971(3)	13.4858(4)	13.4121(14)	13.53469(17)	97.8770(3)
α, deg	90	90	90	90	90
β, deg	93.6876(19)	91.703(3)	92.196(12)	90	90.882(7)
γ, deg	90	90	90	90	90
V, Å^3	4359.94(16)	4335.7(2)	4902.7(10)	4837.8(11)	5025.0(6)
Z	4	4	4	4	4
D_{calc}, g/cm^3	1.372	1.377	1.565	1.346	1.458
λ, Å	1.5418	0.7017	1.5418	1.5418	0.7017
μ, mm^{-1}	3.208	0.403	5.811	2.949	0.620
θ-range, deg	7 to 148	7 to 59	7 to 147	7 to 148	5 to 59
reflections collected	24148	32339	46439	34799	34047
independent reflections	8558 [R_{int} = 0.0414]	10656 [R_{int} = 0.0300]	9717 [R_{int} = 0.0456]	9487 [R_{int} = 0.0588]	34047 [R_{int} = 0.0000]
data / restraints / parameters	8558/12/635	10656/12/644	9717/0/649	9487/1/624	34047/695/1318
GOF (on F^2)	1.022	1.039	1.142	1.024	1.034
R1/wR2 ($I > 2\sigma(I)$) [a]	0.0434 / 0.1038	0.0409 / 0.0922	0.0647/0.1598	0.0660 / 0.1551	0.0822/0.2083
R1/wR2 (all data)	0.0532 / 0.1104	0.0524 / 0.0993	0.0691/0.1624	0.0737 / 0.1606	0.1094/0.2245

[a] $R1 = \Sigma\,||F_o| - |F_c||\,/\,\Sigma|F_o|$; $wR2 = [\Sigma w(F_o^2 - F_c^2)^2\,/\,\Sigma w(F_o^2)^2]^{1/2}$

5.D. Experimental

5.D.i. General methods

Unless otherwise noted, all reagents and solvents were purchased from commercial sources and used as received. Acetonitrile and dichloromethane were purified and dried using a Vacuum Atmospheres solvent purification system. The synthesis and handling of air-sensitive materials were performed under inert atmosphere using a Vacuum Atmospheres Omni-Lab glovebox. The ligands K(^{Ph2}Tp)[103], 1,4,5-naphthalenetriol[191-192], 2,3-dibromojuglone[193] as well as the precursor complex [(^{Ph2}Tp)Fe(OBz)][93] and chemical reductant sodium naphthalenide[189] were prepared according to literature procedures. Elemental analyses were performed at Midwest Microlab, LLC in Indianapolis, IN. UV-vis absorption spectra were obtained with an Agilent 8453 diode array spectrometer equipped with a cryostat from Unisoku Scientific Instruments (Osaka, Japan) for temperature control. Fourier-transform infrared (FTIR) spectra of solid samples were measured with a Thermo Scientific Nicolet iS5 FTIR spectrometer equipped with the iD3 attenuated total reflectance accessory. All solution FTIR data was collected using a Thermo Scientific Nicolet spectrophotometer (Model 670 Nexus) with an MCT detector. ^{1}H spectra were collected at room temperature with a Varian 400 MHz spectrometer. EPR experiments were performed using a Bruker ELEXSYS E600 equipped with an ER4415DM cavity resonating at 9.63 GHz, an Oxford Instruments ITC503 temperature controller, and an ESR-900 He flow cryostat. Electrochemical measurements were conducted in the glovebox with an epsilon EC

potentiostat (iBAS) at a scan rate of 100 mV s^{-1} with 100 mM (NBu$_4$)PF$_6$. A three-electrode cell containing a Ag/AgCl reference electrode, a platinum auxiliary electrode, and a glassy carbon working electrode was employed for cyclic voltammetric (CV) measurements. Under these conditions, the ferrocene/ferrocenium (Fc$^{+/0}$) couple has an E$_{1/2}$ value of +0.52 V in CH$_2$Cl$_2$.

5.D.ii. Synthetic Procedures

[Fe(^{Ph2}Tp)(^{H2}J)] (**10**): In glove box, 367 mg of [(^{Ph2}Tp)Fe(OBz)] (0.43 mmol) was combined with 77.6 mg of 1,4,5-naphthalenetriol in DCM and stirred overnight. Once reaction had completed, mixture was filtered through celite to isolate a purple solution. Layering with MeCN yielded purple crystals suitable for X-ray diffraction (261mg) Yield = 67%. Anal. Calcd* for C$_{55}$H$_{41}$BFeN$_6$O$_3$ (M$_W$ = 900.60 g mol^{-1}): C, 73.35; H, 4.59; N, 9.33. UV-vis [λ_{max}, nm (ε, M^{-1} cm^{-1}) in CH$_2$Cl$_2$]: 343 (3830).

[Fe(^{Ph2}Tp)(^{H}J)] (**11**): Under an inert atmosphere, 79.0 mg (0.45 mmol) of 5-hydroxy-naphthoquinone (^{H}JH) was stirred for 5 minutes with 1 equivalent of NaOMe in CH$_2$Cl$_2$, at which point a solution of [(^{Ph2}Tp)Fe(OBz)] (377 mg, 0.45 mmol) in CH$_2$Cl$_2$ was added to the reaction vial. After stirring overnight, the solution was filtered through celite and the resulting solution was layered with MeCN to provide dark violet crystals suitable for X-ray diffraction (249 mg). Yield = 62%. Anal. Calcd. for C$_{55}$H$_{39}$BFeN$_6$O$_3$ (M$_W$ = 898.58 g mol^{-1}): C, 73.51; H, 4.37; N, 9.35. Found: C, 73.24; H, 4.47; N, 9.41. UV-vis [λ_{max}, nm (ε, M^{-1} cm^{-1}) in CH$_2$Cl$_2$]: 510 (5230), 910 (2460). FTIR (cm^{-1}): 2961, 2618 [ν(BH)], 1654 [ν(C=O)], 1618, 1418, 1165, 802, 754, 691, 666. μ_{eff} = 4.79 μ_B

[Fe(^{Ph2}Tp)(^{Br}J)] (**12**): The synthesis of complex **12** followed the same procedure as the one described above for **11**, with the exception that 2,3-dibromojuglone (^{Br}JH) was substituted for 5-hydroxynaphthoquinone. Reddish-violet crystals were isolated by layering a 1,2-dichloroethane (DCE) solution of the crude solid with pentane. Yield = 54%. Anal. Cald. for $C_{55}H_{37}BBr_2FeN_6O_3$ (MW = 1056.38 g mol^{-1}): C, 62.53; H, 3.53; N, 7.96. Found: C, 62.01; H, 3.63; N, 7.68. UV-vis [λ_{max}, nm (ε, M^{-1} cm^{-1}) in CH_2Cl_2]: 528 (5240), 974 (2620). FTIR (cm^{-1}): 3038, 2601 [ν(BH)], 1653 [ν(C=O)], 1589, 1414, 1163, 811, 758, 691, 665. μ_{eff} = 4.91 μ_B

[Fe(^{Ph2}Tp)(lawsone)] (**13**): Under an inert atmosphere, 120 mg of [(^{Ph2}Tp)Fe(OBz)] (0.2 mmol) was dissolved in 10 mL of DCM and combined with an equimolar amount of lawsone (27 mg; 0.2 mmol) in approximately 5 mL of MeOH. The reaction was stirred overnight. Solvent was then removed under vacuum and the resulting solid was dried. The product was taken up in 1,2,-dichloroethane and filtered through celite. Layering with MeCN yielded feathery green crystals suitable for X-ray diffraction. Anal. Calcd.[*] for $C_{55}H_{39}BFeN_6O_3 \cdot 2MeCN$ (M_W = 980.69 g mol^{-1}): C, 72.26; H, 4.63; N 11.43. UV-vis [λ_{max}, nm (ε, M^{-1} cm^{-1}) in CH_2Cl_2]: 449 (3250), 613 (650), 682 (850), 788 (460).

[Fe(^{Ph2}Tp)(3-chlorolawsone)] (**14**): Complex **14** was synthesized in a manner similar to **13** except that 3-chlorolawsone was used in place of lawsone. Dark brown needles suitable for X-ray diffraction were isolated from layering a concentrated solution of **14** in DCM with hexane. Anal. Calcd.[*] for $C_{55}H_{38}BFeN_6O_3Cl$ (M_W = 933.05 g mol^{-1}): C, 70.80; H, 4.11; N, 9.01. UV-vis [λ_{max}, nm (ε, M^{-1} cm^{-1}) in CH_2Cl_2]: 473 (3080), 648 (700), 691 (820), 830 (410).

[Fe(^{Ph2}Tp)(1-HAQ)] (**15**): In glove box, 378 mg of [(^{Ph2}Tp)Fe(OBz)] (0.5 mmol)

dissolved in 10 mL of DCM. To this solution, 106 mg of 1-hydroxyanthraquinone (0.5

mmol) in 5 mL of MeOH was added. Once the reaction was stirred overnight, the solvent

was removed and the resulting solid was dried. The product was taken up in 1,2-

dichloroethane and filtered through celite. All attempts to isolate crystalline material have

proven to be unsuccessful. (Predicted $M_W = 948.64$ g mol^{-1}). UV-vis [λ_{max}, nm (ε, M^{-1}

cm^{-1}) in CH_2Cl_2]: 474 (6460), 670 (1150), 828 (1490).

Generation of X^{red} species. Under anaerobic conditions, 4 mL of a 0.32 mL solution of

11 (or **12**) in CH_2Cl_2 was added to a quartz cuvette equipped with a stir bar. The cuvette

was sealed with a rubber septum and transferred to an Agilent 8453 diode array UV-vis

spectrometer, where it was cooled to -30 °C in the cryostat. Using a gas-tight syringe,

200 μL of CoCp$_2$ (or CoCp$^*_2$) in air-free MeCN (9 mM, 1.5 eq) was injected into the

cuvette and the formation of **X^{red}** was monitored at low temperature. To prepare

resonance Raman samples, more concentrated solutions of **11** or **12** (~5 mM) in CD_2Cl_2

were added to solid CoCp$_2$ (or CoCp$^*_2$) at -40 °C under anaerobic conditions. After

formation of the **X^{red}** species, the solutions were rapidly transferred to cooled NMR tubes

and immediately frozen in liquid N$_2$.

5.D.iii. Crystallographic studies

Each complex was characterized with X-ray crystallography; details concerning

the data collection and analysis are summarized in Table 5.4. The X-ray diffraction data

were collected at 100 K with an Oxford Diffraction SuperNova kappa-diffractometer

equipped with dual microfocus Cu/Mo X-ray sources, X-ray mirror optics, Atlas CCD detector and a low-temperature Cryojet device. The data were processed with CrysAlisPro program package (Oxford Diffraction Ltd, 2010) typically using a numerical Gaussian absorption correction (based on the real shape of the crystal) followed by an empirical multi-scan correction using SCALE3 ABSPACK routine. The structures were solved using the SHELXS program and refined with the SHELXL program[105] within the Olex2 crystallographic package.[106] All computations were performed on an Intel PC computer with Windows 7 OS. Some structures contain disorder that was detected in difference Fourier syntheses of electron density and accounted for using capabilities of the SHELX package. In most cases, hydrogen atoms were localized in difference syntheses of electron density but were refined using appropriate geometric restrictions on the corresponding bond lengths and bond angles within a riding/rotating model (torsion angles of methyl hydrogens were optimized to better fit the residual electron density).

5.D.iv. DFT Computations

DFT calculations were performed using the ORCA 2.9 software package developed by Dr. F. Neese (MPI for Chemical Energy Conversion).[194] All calculations employed Becke's three-parameter hybrid functional for exchange along with the Lee-Yang-Parr correlation functional (B3LYP).[156-157] These calculations utilized Ahlrichs' valence triple-ζ basis set (TZV) snf TZV/J auxiliary basis set, in conjunction with polarization functions on all atoms.[160-162] In the geometry optimized models, the ^{Ph2}Tp ligand was modified by replacing the Ph-groups on the 5-position of the imidazolyl rings

with H-atoms. To avoid spurious transitions, time-dependent DFT (TD-DFT) calculations used a truncated version of the optimized model with Me groups (instead of Ph groups) at the 3-positions of the pyrazolyl rings. TD-DFT calculations[163-165] calculated absorption energies and intensities for 50 excited states with the Tamm-Dancoff approximation.[166-167] Vibrational frequency calculations were performed using truncated models with hydrogen atoms at the 3- and 5-positons of the Tp ligand. Calculation of the harmonic force fields proved that the optimized structure is a local minimum on the potential energy surface. Exchange coupling constants (J) were obtained using Noodleman's broken symmetry approach ($H = -2JS_A \cdot S_B$).[195-196] Isosurface plots of molecular orbitals and electron-density maps (EDDMs) were prepared with Laaksonen's gOpenMol program.[168]

Chapter 6

Preparation of a Semiquinonate-Bridged Diiron(II) Complex and Elucidation of its Geometric and Electronic Structures
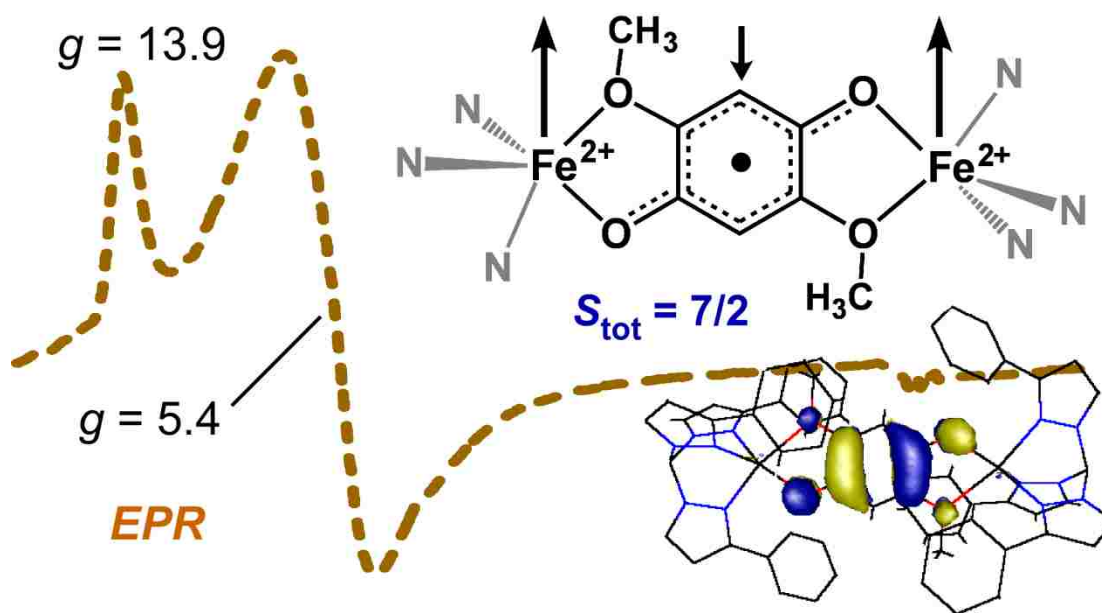
Abstract: The synthesis and crystal structure of a diiron(II) complex containing a bridging semiquinonate radical are presented. The unique electronic structure of this $S =$ 7/2 complex is examined with spectroscopic (absorption, EPR, resonance Raman) and computational methods.

6.A. Introduction

p-Hydroquinone (1,4-dihydroxybenzene; HQ) and its substituted derivatives are important biological cofactors due to the ability to participate in multiple proton- and electron-transfers.[152, 197] HQs undergo reversible one- and two-electron oxidations to yield semiquinone radicals (SQs) and quinones (Qs), respectively. These redox events typically involve loss of proton(s), such that the net reaction is H-atom transfer.[99, 198] In biochemical processes, HQ cofactors are often associated with one or more redox-active metal ions. For instance, photosystem II incorporates two quinones (Q_A and Q_B) that shuttle electrons away from the primary electron donor, P_{680}.[187, 199] In close proximity to both quinones is a nonheme mononuclear Fe center, and recent spectroscopic studies have detected significant magnetic interactions between the high-spin Fe(II) center and semiquinone forms of Q_A and Q_B.[200-201] In addition, substituted HQs are generated as part of the microbial breakdown of halogenated and nitro aromatic compounds. In these cases, the HQs are oxidatively degraded by ring-cleaving dioxygenases (HQ dioxygenases, HQDOs) with nonheme monoiron active sites.[6] Even in these enzymes the electroactive nature of HQs is critical, since the key intermediate in the putative catalytic cycle is a superoxo–Fe(II)–semiquinonate complex.[52]

In the course of our efforts to develop synthetic models of HQDOs, we have prepared the diiron(II) complex [Fe_2(^{Ph2}Tp)$_2$(μ-DMHQ)] (**5**; <u>Figure 6.1</u>), where DMHQ is the dianion of 2,5-dimethoxyhydroquinone and^{Ph2}Tp is hydrotris(3,5-diphenylpyrazol-1-yl)-borate(1-).[112]
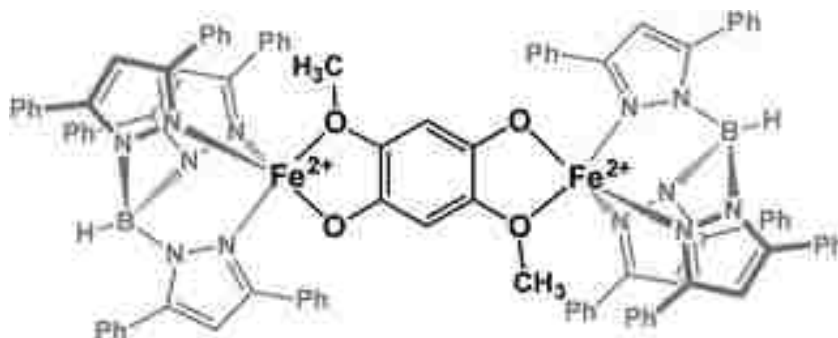
Figure 6.1. Schematic representation of the structure of the diiron(II) complex, **5,** formulated as [(^{Ph2}Tp)$_2$Fe$_2$(μ-DMHQ)].

X-ray diffraction (XRD) analysis revealed that **5** is a centrosymmetric complex with two high-spin, five-coordinate Fe(II) centers linked by a closed-shell *p*-hydroquinonate ligand (the Fe▬Fe separation is 8.15 Å). We examined the magnetic and electrochemical properties of **1** and observed that the one-electron oxidation of **5** yields a unique diiron(II) complex, [**5b**]$^+$, containing a bridging *p*-semiquinonate ligand (DMSQ$^{•−}$). The geometric and electronic structures of [**5b**]$^+$ are verified on the basis of crystallographic, spectroscopic, and computational methods. To the best of our knowledge, [**5b**]$^+$ is the first crystallographically-characterized complex to feature Fe(II) center(s) bound to a SQ radical.[a,70] The results therefore have the potential to advance our fundamental understanding of metal–SQ interactions in biological systems. Moreover, dinuclear complexes with "noninnocent" bridging ligands have attracted considerable attention lately due to their novel electronic and magnetic behavior;[202-204] this chapter contributes a new member to this fascinating class of compounds.

---

[a] Min et al. reported a diiron(II) complex bridged by a chloranilate radical (ref. 176). However, this complex did not provide suitable crystals for X-ray crystallography.

6.B. Results and Discussion

6.B.i. Synthesis and Characterization of a Diiron(II)-hydroquinonate Complex

Complex **16** is easily generated by mixing equimolar amounts of $FeCl_2$ and K(^{Ph2}Tp) with 0.5 equiv. of Na_2(DMHQ) in MeCN, followed by recrystallization from CH_2Cl_2/Et_2O.[112] The ^1H NMR spectrum of **5** in CD_2Cl_2, (shown in <u>Figure 6.2</u>) reveals an abundance of paramagnetically-shifted peaks between $\delta = +60$ and -20 ppm. Using the Evans method, an effective magnetic moment (μ_{eff}) of 6.3 μ_B was measured at room temperature for **5**, which is reasonably close to the spin-only value of 6.93 μ_B expected for a molecule with two uncoupled high-spin ($S = 2$) Fe(II) centers. Consistent with this result, broken symmetry (BS) calculations[196] using density functional theory (DFT) computed a J-value (exchange coupling parameter) of -2 cm^{-1} for **5**, indicative of very weak antiferromagnetic interactions.[205]
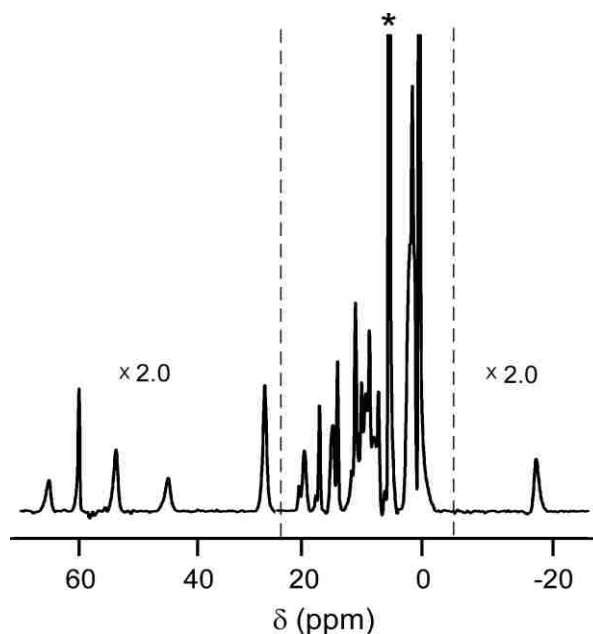
Figure 6.2. ^{1}H NMR spectrum of **5** in CD$_2$Cl$_2$. Peak intensities for the outer portions of the spectra were enlarged (X 2) for the sake of clarity. The solvent-derived peak is indicated with an asterisk(*).

The redox activity of **5** was examined in CH$_2$Cl$_2$ with 0.1 M [NBu$_4$]PF$_6$ as the supporting electrolyte. The cyclic voltammogram (CV) exhibits a reversible couple at $E_{1/2} = -570$ mV *versus* Fc$^{+/0}$ ($\Delta E = 130$ mV), along with several irreversible events at more positive potentials (Figure 6.3). It is instructive to compare this CV to the one reported previously for [Fe(^{Ph2}Tp)(2-MHQ)] (**4**; where 2-MHQ is the anion of 2-methoxyhydroquinone).
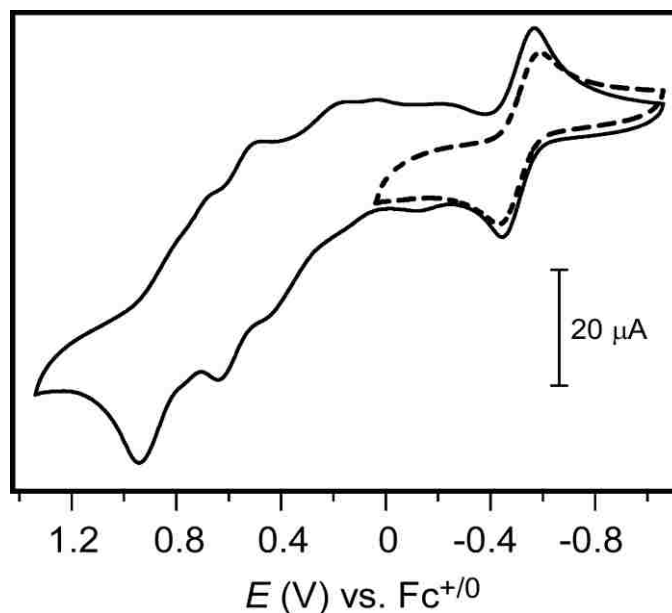
Figure 6.3. Cyclic voltammograms of complex **5** measured in CH_2Cl_2 with 100 mM $(NBu_4)PF_6$ as the supporting electrolyte and a scan rate of 100 mVs^{-1}

Even though **5** and **4** feature nearly identical Fe coordination environments, the latter complex is oxidized at a much higher potential (-50 mV).[112] We therefore surmised that the -570 mV redox couple of **5** corresponds to a ligand-based event.

6.B.ii. Isolation and Characterization of a Semiquinonate-Bridged Diiron (II) Complex via One-Electron Oxidation

To explore this possibility, complex **5** was treated with 1.0 equivalent of AgPF$_6$ in CH_2Cl_2. The resulting orange-brown species, [**5b**]$^+$, displays two intense absorption features with $\lambda_{max} = 365$ and 440 nm ($\varepsilon = 13.2$ and 8.0 mM^{-1} cm^{-1}, respectively), along with shoulders at ■480 and 540 nm (Figure 6.4). Needle-like crystals of [**5b**]PF$_6$ were obtained by layering a concentrated CH_2Cl_2 solution with pentane.
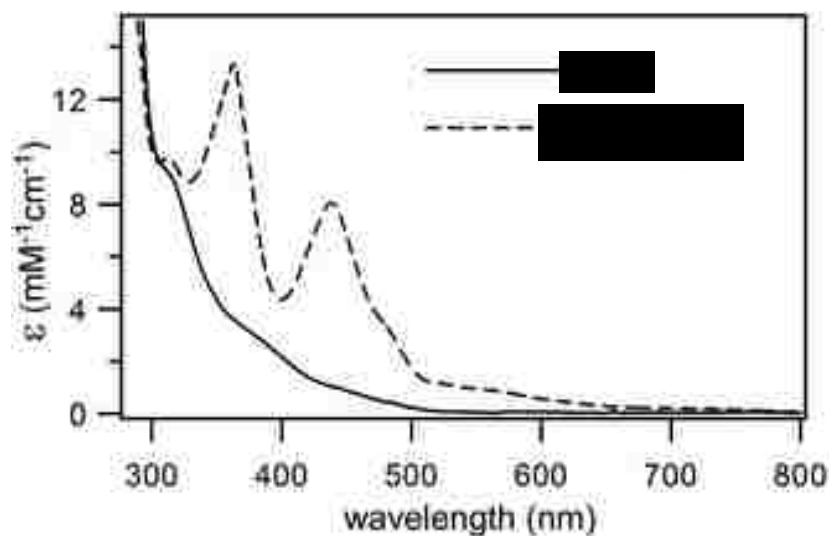
Figure 6.4 Electronic absorption spectra of **5** and [**5b**]PF$_6$ measured in CH$_2$Cl$_2$ at 20 °C.

The X-ray structure of [**5b**]$^+$ reveals a centrosymmetric diiron unit with the same atomic composition as **5** (Figure 6.5) Metric parameters for both complexes are provided in Table 6.1. The average Fe–N$_{Tp}$ bond length of [**17**]$^+$ (2.094 Å) is only slightly shorter than the value observed for **5** (2.143 Å), suggesting that both Fe centers belong to the ferrous state. The Fe coordination environments are distorted between trigonal-bipyramidal and square pyramidal (τ^{98} = 0.34). The most dramatic structural changes upon conversion of **5** → [**5b**]$^+$ involve the bridging ligand. In the crystal structure of **5**, the C–C bond lengths of the DMHQ^{2-} ligand are essentially identical (1.391 ± 0.004 Å) and the O1–C1 distance is 1.329(5) Å – typical values for *p*-hydroquinonate anions.[112] By contrast, the corresponding ring in [**5b**]$^+$ displays a pronounced quinoid distortion involving elongation of the C1–C2 and C1–C3 bonds and shortening of the C2–C3 bond. In addition, the O1–C1 distance of [**5b**]$^+$ contracts to 1.287(2) Å (Table 6.1). Such metric parameters require a semiquinone assignment for the bridging ligand in [**5b**]$^+$, based on well-established guidelines for the evaluation of dioxolene oxidation states.[136, 206-207]

Thus, the X-ray diffraction data support our hypothesis that oxidation of **5** is a ligand based process, such that [**5b**]$^+$ is best formulated as [(Fe^{2+})$_2$(^{Ph2}Tp)$_2$(μ-DMSQ)]$^+$.
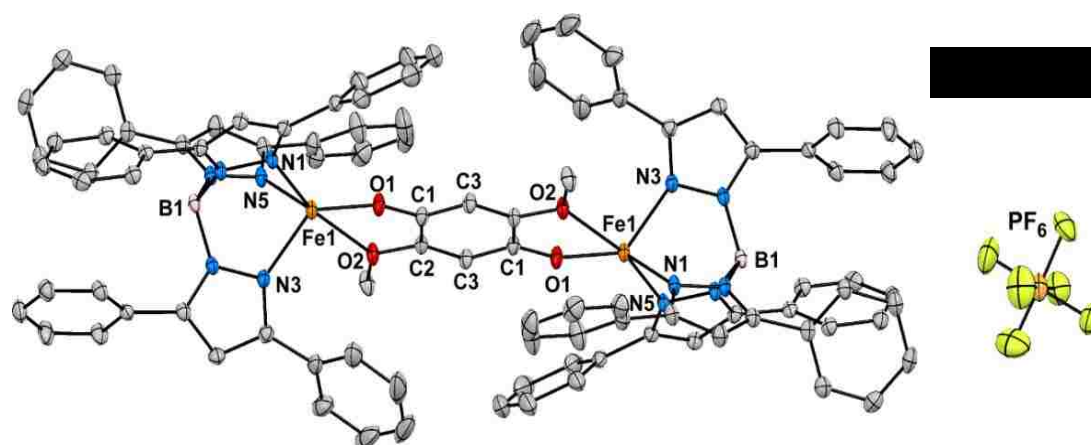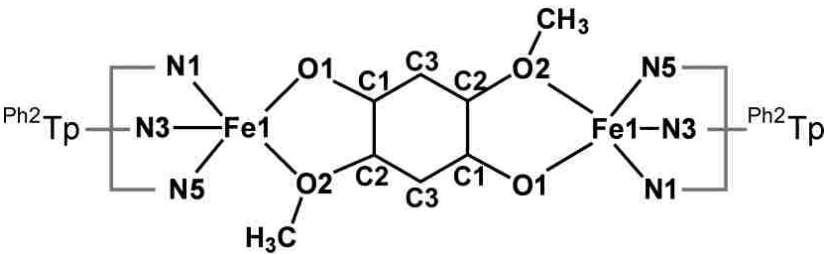
Figure 6.5. Thermal ellipsoid plot (50% probability) derived from the X-ray structure of [**5b**]PF$_6$·CH$_2$Cl$_2$. Non-coordinating solvent molecules and hydrogen atoms have been omitted for clarity. Key metric parameters are provided in Table 6.1.

Table 6.1. Experimental and computed bond distances (Å) for **5** and **[5b]**$^+$ [b]

	5 (XRD)	**[5b]**PF$_6$ (XRD)	**[5b]**PF$_6$ (DFT)
Fe1–N1	2.107(4)	2.125(2)	2.072
Fe1–N3	2.108(3)	2.076(2)	2.051
Fe1–N5	2.213(4)	2.082(2)	2.067
Fe1–O1	1.904(3)	1.940(1)	1.909
Fe1–O2	2.328(3)	2.403(1)	2.682
O1–C1	1.329(5)	1.287(2)	1.303
O2–C2	1.388(6)	1.358(2)	1.360
C1–C2	1.395(7)	1.446(2)	1.449
C1–C3	1.388(6)	1.415(2)	1.419
C2–C3	1.389(7)	1.366(2)	1.381
τ-Value[98]	0.59	0.34	0.74

The electronic structure of [**5b**]PF$_6$ was examined with spectroscopic and computational techniques. The X-band EPR spectrum exhibits a peak at g_{eff} = 13.9 and a derivative-shaped feature at g_{eff} = 5.4 (Figure 6.6). Since half-integer spin systems cannot give rise to features with g_{eff} > 4S (assuming real g-values near 2.0),[208] the EPR results suggest that [**5b**]$^+$ possesses a spin of 7/2. Indeed, as shown in Figure 6.6, the data is nicely simulated assuming S = 7/2 and the following spin-Hamiltonian parameters: D = +7(2) cm^{-1}, E/D = 0.11(2), and g_{real} = 2.3, 2.2, 2.1.[c]

---

[b] Both **5** and [**5b**]PF$_6$ are centrosymmetric compounds.
[c] Attempts to reproduce the data assuming a spin of 5/2 required unrealistically large g_{real} values.
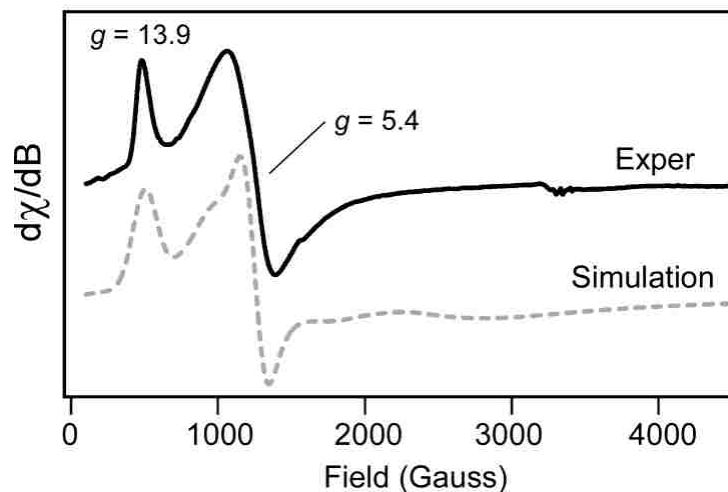
Figure 6.6. X-band EPR spectrum of [**5b**]PF$_6$ in a frozen CH$_2$Cl$_2$ solution (4 mM) collected at 10 K. Parameters used to generate the simulated spectrum are provided in the text.

These values were obtained by fitting EPR spectra measured at temperatures ranging from 5 to 20 K. The g = 13.9 peak therefore arises from the lowest-energy M_S = ±1/2 doublet, while the derivative signal at 5.4 is due to the M_S = ±3/2 doublet;[109] as expected, the former diminishes at higher temperatures while the latter gains in relative intensity (Figure 6.7).
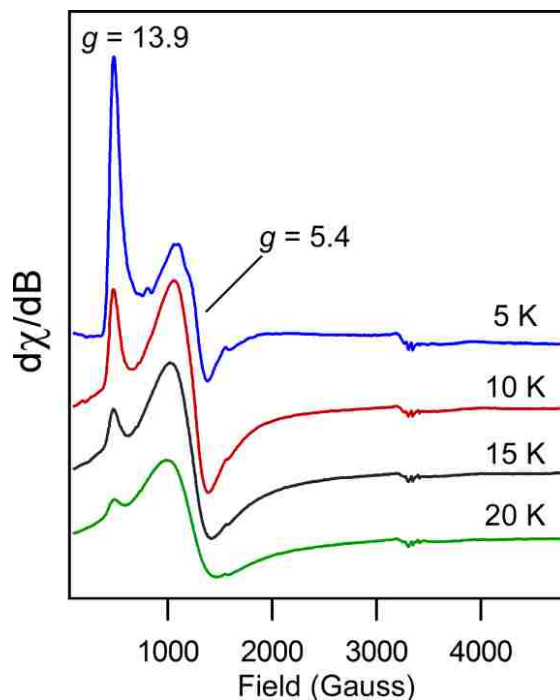
Figure 6.7. X-band EPR spectra of [**5b**]PF$_6$ at various temperatures (5, 10, 15 and 20 K) in frozen CH$_2$Cl$_2$ solution (4 mM). Experimental parameters: frequency = 9.38 GHz; microwave power = 2.0 mW; modulation amplitude = 10.0 Gauss; modulation frequency = 100 kHz.

The electronic origin of this unique EPR signal was elucidated with the aid of

DFT. Using the crystallographic coordinates, a calculation with $S = 7/2$ converged to a

wavefunction consisting of two high-spin Fe(II) centers antiferromagnetically coupled to

the bridging DMSQ radical (Figure 6.8, left). Geometry optimizations indicate that this

electronic configuration is the most stable one on the $S = 7/2$ surface (bond distances for

the optimized model are shown in Table 6.1). A J-value of -83 cm^{-1} per Fe–DMSQ

interaction was computed using the BS formalism.[d] Thus, unlike the closed-shell DMHQ

ligand, the bridging radical in [**5b**]$^+$ is capable of mediating significant exchange

[d] Experimentally, the variable-temperature EPR data (Figure 6.6) provides a lower-limit for the J-value. Since a signal from the $S = 5/2$ excited state is not observed in the 20 K spectrum, we can assume its population is less than ~ 1% at this temperature. This requires a J-value greater than -40 cm^{-1}.

interactions between the Fe-based spins, which are separated by 8.22 Å in the crystal structure. A similar spin topology was observed by Dei and Gatteschi for a *diferric* complex containing a bridging SQ ligand.[69] In this case, the overall spin is 9/2 and the *J*-value is considerably larger at −370 cm^{-1}.
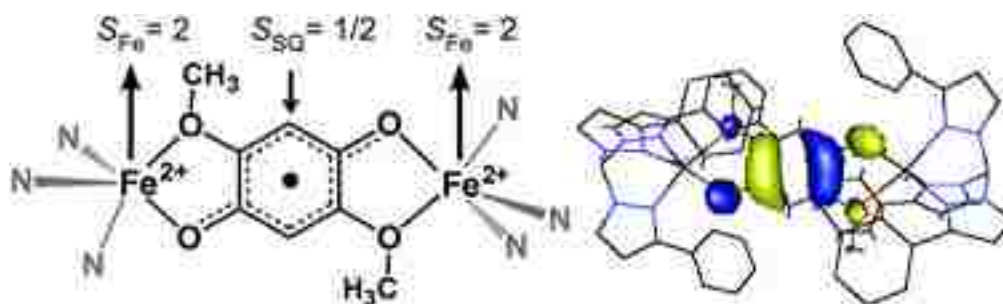
Figure 6.8. (Left) Spin coupling topology for [**5b**]$^+$ that gives rise to overall spin of 7/2. (Right) DFT-generated isosurface plot of the [**5b**]$^+$ SOMO.

The radical character of the [**5b**]$^+$ bridging ligand is illustrated by the singly-occupied molecular orbital (SOMO) shown in Figure 6.8, which is almost exclusively localized on DMSQ. This MO contributes to the intense electronic transitions that appear in the visible region, according to time-dependent DFT (TD-DFT) calculations that reproduce the experimental [**5b**]$^+$ spectrum reasonably well (Figure 6.9). TD-DFT attributes the absorption manifold centered at 440 nm to multiple Fe(II) → DMSQ metal-to-ligand charge transfer (CT) transitions, while the higher-energy feature at 365 nm arises from a single DMSQ → Fe(II) ligand-to-metal CT transition. It appears that the existence of a ligand radical in [**5b**]$^+$ is favored by the presence of low-symmetry, five-

coordinate Fe(II) geometries, which stabilize the Fe 3d-orbitals and remove their degeneracy.[209]
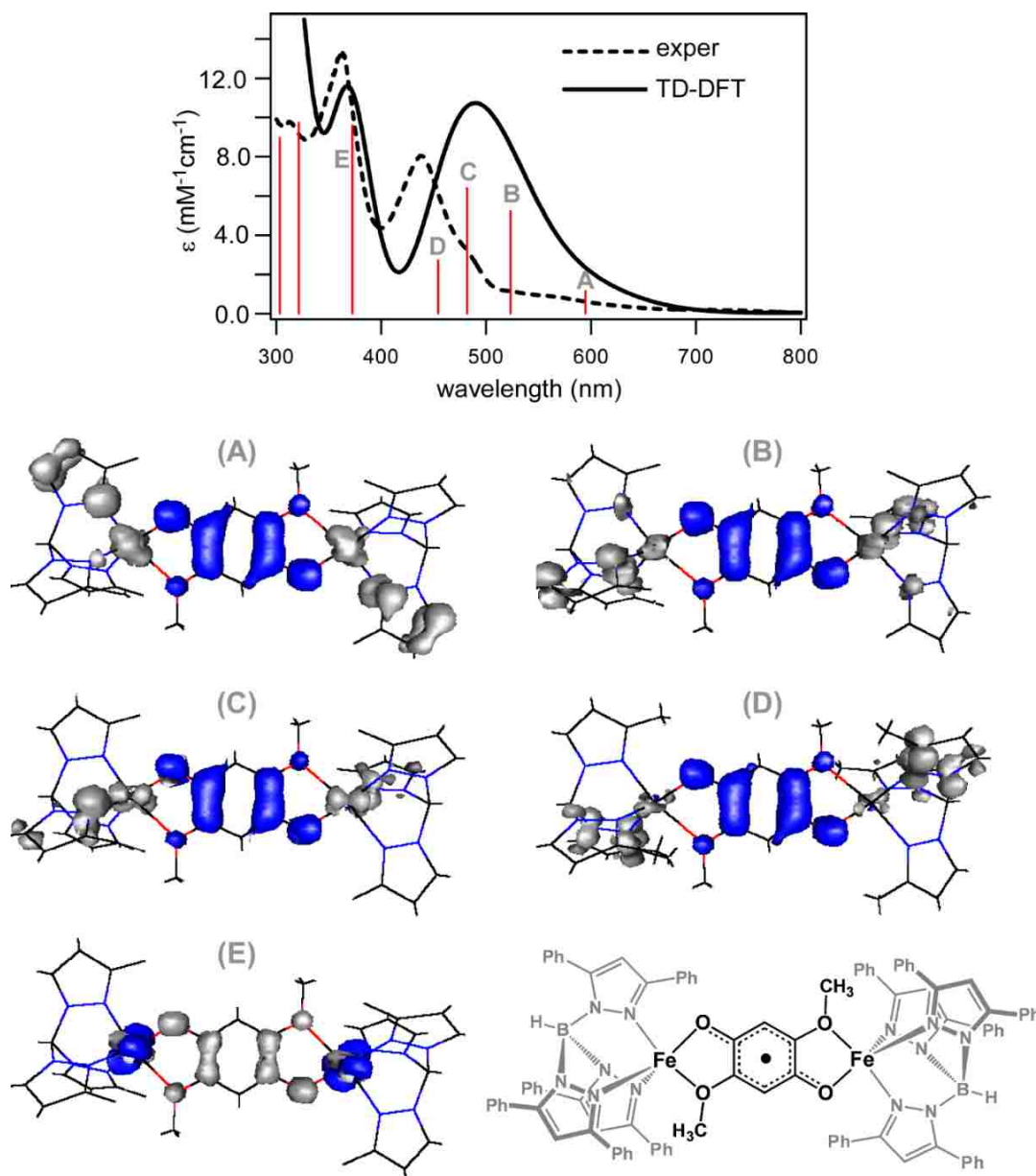
Figure 6.9. Top: Experimental (dashed) and TD-DFT computed (solid line) absorption spectra for **[5b]**PF$_6$. Red sticks represent the energies and intensities of prominent transitions in the TD-DFT spectrum. Bottom: Electron density difference maps (EDDMs) for the computed transitions labeled in the upper spectrum. Blue and grey regions indicate gain and loss of electron density, respectively.

The nature of the bridging ligand was further probed *via* resonance Raman (rR) spectroscopy. As shown in <u>Figure 6.10</u>, the [**5b**]$^+$ spectrum exhibits several intense peaks that are not evident in the precursor spectrum. The dominant feature at 1466 cm^{-1} is strongly enhanced by excitation into 440 nm absorption feature (<u>Figure 6.11</u>) indicating that it corresponds to a DMSQ-based mode. The rR spectra of metal-bound *o*-dioxolenes typically display prominent peaks arising from C–O stretching modes. The frequencies of these modes are diagnostic of ligand oxidation state, appearing at 1250–1275 cm^{-1} for catecholates, 1400–1500 cm^{-1} for *o*-semiquinones, and 1620–1640 cm^{-1} for *o*-benzoquinones.[207] It is therefore reasonable to assign the dominant feature at 1466 cm^{-1} to the symmetric ν(O1–C1) mode of [**5b**]$^+$. Literature precedents indicate that the 575 cm^{-1} peak corresponds to the breathing mode of the five-membered chelates formed by each Fe center and the DMSQ ligand, while the resonance-enhanced peaks at 1412 and 1480 cm^{-1} likely involve modes that strongly mix ν(O1–C1) and intraligand C–C bond motions.[137, 210] The rR data thus provides additional evidence for the presence of a DMSQ ligand in [**5b**]$^+$.
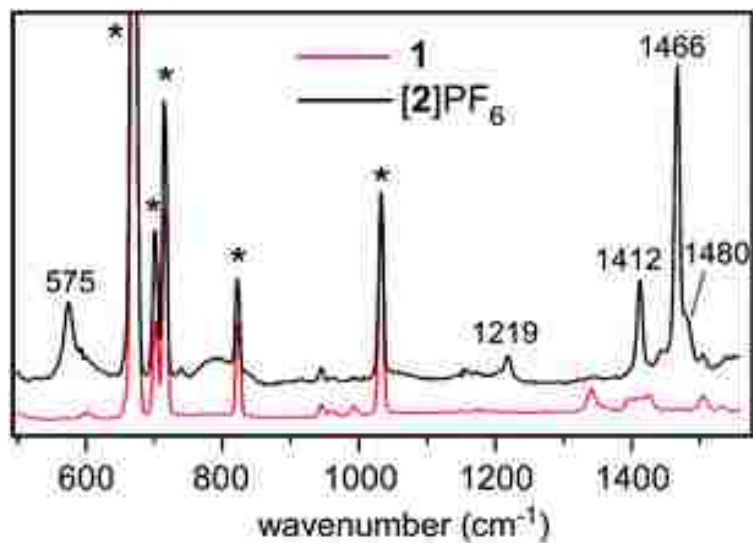
Figure 6.10. rR spectra of frozen CD_2Cl_2 solutions of **5** (red, bottom) and [**5b**]PF_6 (black, top) obtained with 457.9 nm excitation. * = solvent peaks.
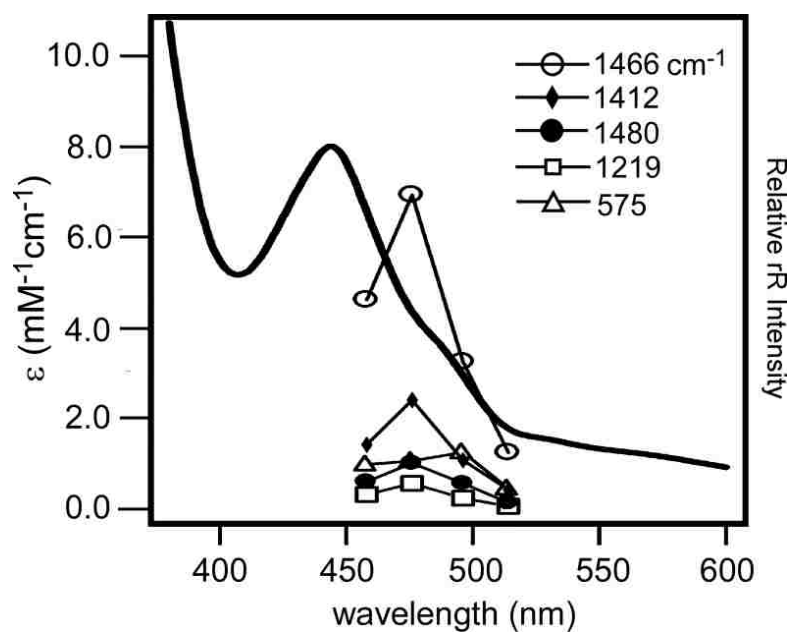
Figure 6.11. rR excitation profiles of various modes of [**5b**]PF_6 measured with a frozen CD_2Cl_2 solution ([Fe] = 3.1 mM) at 77 K. Profiles are superimposed on the room temperature absorption spectrum of [**5b**]PF_6 in CH_2Cl_2.

6.C. Conclusion

The results presented here open up intriguing possibilities for future research. The fact that the ligand-to-metal and metal-to-ligand CT bands of [**5b**]$^+$ appear in close proximity (*vide supra*) indicates that the Fe- and DMSQ-based orbitals are nearly isoenergetic, making it difficult to predict whether further oxidations would be ligand- or iron-centered. Further oxidiation of **[5b]**$^+$ was briefly studied through trials to synthetically isolate the two-electron oxidized species. Initially, the oxidation of **5** by two equivalents of AgPF$_6$ was attempted, but it was determined that Ag$^+$ is not a strong enough reagent to oxidize this complex by two electrons. Recent studies involved attempts to synthesize the [(^{Ph2}Tp)Fe$_2$(μ-DMHQ)] complex using two equivalents of ferric salts [Fe(ClO$_4$)$_3$ or FeCl$_3$] in place of FeCl$_2$ in the previously reported procedure.[112] It was hypothesized that if a stable product could be isolated, perhaps the redox activity of the 2,5-dimethoxyhydroquinone ligand would lead to the creation of a mixed valent [(^{Ph2}Tp)Fe(II)Fe(III)-(μ-DMSQ)] complex thorough an internal electron transfer. Unfortunately, attempts to generate this species were unsuccessful as they led to the isolation of a powdery blue solid determined to be insoluble in all available organic solvents (DCM, MeCN, toluene, acetone, ether, DMF, THF, pentane/hexane, etc) as well as H$_2$O and further characterization was not completed.

6.D. Experimental

6.D.i. General methods

All reagents and solvents were purchased from commercial sources and used as received unless otherwise noted. Dichloromethane was purified and dried using a Vacuum Atmospheres solvent purification system. The compounds 2,5-dimethoxyhydroquinone[104] and K(^{Ph2}Tp)[103] were prepared according to literature procedures. The synthesis of complex **5** was reported preciously in Chapter 2.[112] The synthesis and handling of air-sensitive materials were carried out under an inert atmosphere using a Vacuum Atmospheres Omni-Lab glovebox. Elemental analyses were performed at Midwest Microlab, LLC in Indianapolis, IN. Infrared (IR) spectra of solid samples were measured with a Thermo Scientific Nicolet iS5 FTIR spectrometer equipped with the iD3 attenuated total reflectance accessory. UV-vis spectra were obtained with an Agilent 8453 diode array spectrometer. Magnetic susceptibility measurements were carried out using the Evans NMR method. Cyclic voltammetric (CV) measurements were conducted in the glovebox with an epsilon EC potentiostat (iBAS) at a scan rate of 100 mV/s with 100 mM (NBu$_4$)PF$_6$. A three-electrode cell containing a Ag/AgCl reference electrode, a platinum auxiliary electrode, and a glassy carbon working electrode was employed. Under these conditions, the ferrocene/ferrocenium (Fc$^{+/0}$) couple has an E$_{1/2}$ value of +0.52 V in CH$_2$Cl$_2$. EPR experiments were performed using a Bruker ELEXSYS E600 equipped with an ER4415DM cavity resonating at 9.63 GHz, an Oxford Instruments ITC503 temperature controller and ESR-900 He flow cryostat. The

program EasySpin[154] was used to simulate the experimental spectra. Resonance Raman (rR) spectra were obtained upon excitation with a Coherent I-305 Ar^+ laser with ~45 mW of laser power at the sample. The scattered light was collected using a 135° backscattering arrangement, dispersed by an Acton Research triple monochromator equipped with a 1200 grooves/mm grating and analyzed with a Princeton Instruments Spec X 100BR deep depletion, back-thinned CCD camera. Solution samples of **5** and [**5b**]PF_6 were prepared in CD_2Cl_2 with concentrations of 4.8 and 3.1 mM, respectively. Spectra were accumulated at 77 K by inserting the samples (contained in an NMR tube) in an EPR dewar filled with liquid N_2. rR excitation profiles were measured by quantifying the sample peak intensities relative to the 1032 cm^{-1} peak of frozen CD_2Cl_2.

6.D.ii. Synthetic Procedures

Preparation of [5b]PF₆: [$Fe_2(^{Ph2}Tp)_2(\mu\text{-DMHQ})$] (**5**, 98.0 mg, 0.0605 mmol) was treated with one equivalent of $AgPF_6$ (16.1 mg, 0.0637 mmol) in CH_2Cl_2 (10 mL) for one hour. The resulting dark brown solution was filtered through celite and concentrated to approximately half of its original volume. Layering of this solution with pentane provided dark brown needles suitable for X-ray crystallography (69 mg, 62%). The X-ray structure found one uncoordinated CH_2Cl_2 molecule per unit cell, and elemental analysis indicates that some solvent (~0.4 equiv.) remains after drying. Anal. Calcd for $C_{98}H_{76}B_2F_6Fe_2N_{12}O_4P\cdot0.4CH_2Cl_2$ (MW = 1797.99 gmol^{-1}): C, 65.73; H, 4.31; N, 9.35. Found: C, 65.77; H, 4.00; N, 9.54. FTIR (cm^{-1}, solid): 3051, 2616 [ν(B-H)], 1516, 1495, 1477, 1464, 1431, 1414, 1207, 1163, 1065, 1009, 833, 759, 694, 668.

6.D.iii. Crystallographic studies

X-ray diffraction (XRD) data were collected with an Oxford Diffraction SuperNova kappa-diffractometer (Agilent Technologies) equipped with dual microfocus Cu/Mo X-ray sources, X-ray mirror optics, Atlas CCD detector, and low-temperature Cryojet device. The data were processed with CrysAlis Pro program package (Agilent Technologies, 2011) typically using a numerical Gaussian absorption correction (based on the real shape of the crystal), followed by an empirical multi-scan correction using SCALE3 ABSPACK routine. The structures were solved using SHELXS program and refined with SHELXL program[105] within Olex2 crystallographic package.[106] B- and C-bonded hydrogen atoms were positioned geometrically and refined using appropriate geometric restrictions on the corresponding bond lengths and bond angles within a riding/rotating model (torsion angles of methyl hydrogens were optimized to better fit the residual electron density).

Crystallographic data for [**5b**]$PF_6 \cdot CH_2Cl_2$: $C_{99}H_{78}B_2Cl_2F_6Fe_2N_{12}O_4P$, $M_r = 1848.95$ g mol^{-1}, triclinic, space group P-1, $a = 9.7382(3)$, $b = 13.2530(4)$, $c = 18.0619(7)$ Å, $\alpha = 103.453(3)$, $\beta = 104.559(3)$, $\gamma = 97.098(3)°$, $V = 2152.89(13)$ Å^3, $Z = 1$, $\rho = 1.428$ g cm^{-3}, total data 42432, independent reflections 8566 ($R_{int} = 0.0395$), 624 parameters, $R_1 = 0.0393$ for I $\geq 2\sigma$(I) and $wR_2 = 0.1024$.

6.D.iv. DFT Computations

DFT calculations were performed using the ORCA 2.8 software package developed by Dr. F. Neese.[155] Geometry optimizations employed the Becke-Perdew (BP86) functional,[158-159] while single-point (SP) and time-dependent DFT (TD-DFT) calculations used Becke's three-parameter hybrid functional for exchange along with the Lee-Yang-Parr correlation functional (B3LYP).[156-157] SP and TD-DFT calculations were based on modified crystallographic coordinates in which the phenyl groups at the 5-position of the pyrazole ligands were replaced by hydrogen atoms. Ahlrichs' valence triple-ζ basis set (TZV), in conjunction with the TZV/J auxiliary basis set,[160-161] were used for all calculations TD-DFT calculations[163, 165] computed absorption energies and intensities within the Tamm-Dancoff approximation.[166-167] In each case, at least 60 excited states were calculated. The gOpenMol program[168] developed by Laaksonen was used to generate isosurface plots of molecular orbitals.

Chapter 7

Preparation of (Hydro)quinonate-bridged Dimetal(II) Complexes with Relevance Towards the Generation of Unique Magnetic Materials
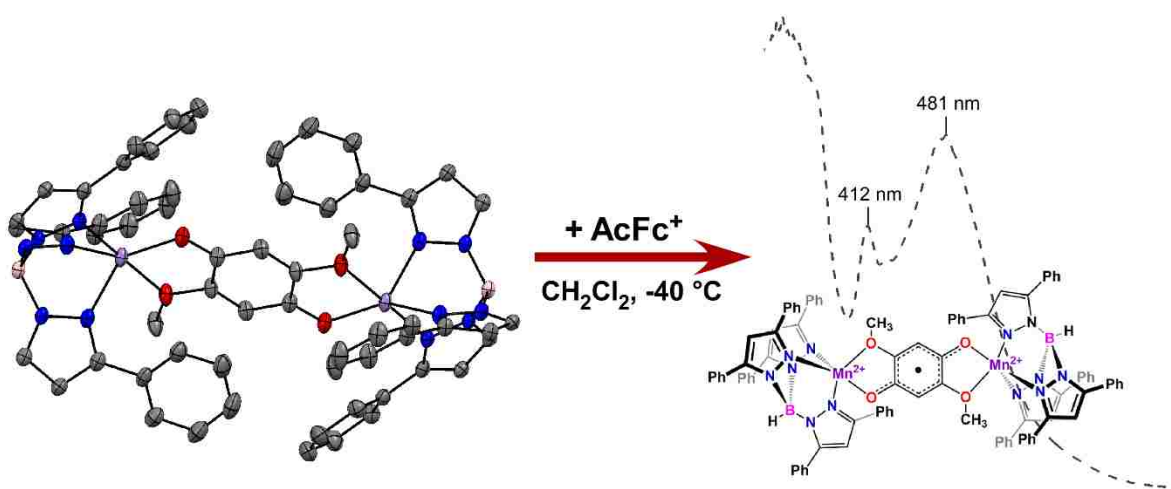
Abstract: The ability of single molecules to exhibit magnetic hysteresis of purely molecular origin at low temperature is currently of great interest. While many magnetic materials studied in this field are best represented as large, polynuclear metal clusters bridged by closed-shell ligands, the incorporation of radical ligands bridging two metal centers has allowed for the generation of a new class of single molecule magnets (SMMs). This chapter details the synthesis and preliminary characterization of a series of dimetal(II) complexes that incorporate a variety of bridging (hydro)quinone ligands with metal centers supported by either the hydridotris(3,5-diphenylpyrazol-1-yl)borate (^{Ph2}Tp) or the tris(4,5-diphenyl-1-methylimidazol-2-yl)phosphine (^{Ph2}TIP) ligand scaffold. Motivated by previous work with a similar complex (**5**; Chapter 6), we aim to generate one-electron oxidized/reduced species that incorporate a ligand-based radical between two divalent metal centers. Because the incorporation of a bridging ligand radical has been observed to increase the amount of electronic coupling between the paramagnetic centers, we anticipate that these high-spin complexes will have unique magnetic and electronic properties.

7.A. Introduction

Over the past few decades, a significant amount of interest has been paid to the development of a class of molecular materials known as single molecule magnets (SMMs) due to their potential applications in molecular spintronics and quantum information storage and processing.[72-75] By definition, SMMs are compounds that possess a slow relaxation of magnetization, below a certain blocking temperature (T_b), derived purely from the molecule itself and not long-range magnetic ordering. The ability of these molecules to maintain magnetization in the absence of an applied field makes them perfect candidates for utilization as novel materials in applications such as quantum computing. Because the intrinsic spin of a SMM can be recognized as one quantum bit (qubit), unparalleled data densities can be achieved allowing for the development of efficient solid state and other useful nanoscale devices.[211-213] However, one of the major challenges facing the development of this technology is the low temperatures required for the observation of this magnetic behavior.

The inherent slow relaxation of magnetization of a single molecule magnet is derived from the essential magnetic spin of the material. For each SMM, a thermal energy barrier, or anisotropy barrier, exists that describes the amount of energy required to reverse the orientation of the molecule's anisotropy, thereby causing the compound to lose magnetization.[214] This therefore suggests that a compound with a larger anisotropy barrier would function more efficiently as a single molecular magnet.[215] The anisotropy of each SMM is based upon key physical parameters of the compound, particularly the magnitude of the ground state spin (S) and zero-field splitting parameter (D).[215] To

improve SMMs, higher relaxation barriers must be accomplished. Harris, et al. suggest that while key parameters such as spin ground state (S) and the zero field splitting parameter (D) of each complex must be considered when attempting to design a successful SMM, more attention should be paid to the exchange coupling constant (J) of the system. This value numerically describes the degree of separation between the ground and excited spin-states of the molecule. Harris notes that this factor must be significantly large enough in magnitude to enforce slow magnetic relaxation dynamics at high temperatures while also blocking fast quantum tunneling pathways within the manifold of a single spin state.[215-216]

To date, much of the effort devoted to the development of transition metal single molecule magnets has focused on species incorporating paramagnetic metal centers bridged by closed-shell, diamagnetic ligands. While molecular magnetization has been of interest for many years, SMM behavior was first observed in 1993 by Sessoli, et al.[76] They reported the synthesis of a high spin $[Mn_{12}O_{12}(O_2CMe)_{16}(H_2O)_4]$ cluster compound [8Mn(III), 4Mn(IV)] that displays a high degree of magnetic coupling with an overall $S =$ 10 ground state mediated by indirect superexchange coupling interactions. The advent of this novel cage compound attracted a great deal of interest in the generation of other transition metal complexes, high in nuclearity and spin state, in order to study their unique spectroscopic and magnetic properties.[217-219] In pursuit of increased global anisotropy and therefore SMM behavior at higher temperatures, it is logical to focus efforts on the generation of polynuclear complexes with large predicted spin states; however their formation presents a challenge as the synthesis of these large clusters tends to be unpredictable. Furthermore, the use of closed-shell, diamagnetic bridging ligands by

researchers in the development of these compounds seems to remain a common theme despite their inability to facilitate strong magnetic exchange. Recently, efforts focused on the generation of species incorporating radical ligands linking paramagnetic centers in low nuclearity complexes have garnered success.[77-79] While limiting the number of metal nuclei in the target system may seem counterintuitive, the incorporation of radical ligands bridging the centers can functionally increase the observed spin state of the molecule while increasing the magnitude of the magnetic exchange coupling between metals.[77-78, 220]

During our efforts to develop Fe^{II}-HQate species as small molecule mimics of the enzyme-substrate complex of the HQDOs, we synthesized a diiron(II) species bridged by the closed-shell dianion of 2,5-dimethoxyhydroquinone (**5**; <u>Chapter 6</u>).[139] We observed that upon one-electron oxidation, we could isolate a new species [**5b**]$^+$ which is best described as a dinuclear ferrous complex bridged by a semiquinonate radical. Interestingly, upon oxidation of **5** → **[5b$^+$]**, we noted a substantial change in the exchange coupling parameter (J-value). Using broken symmetry (BS) DFT methods, we calculated J-values of -2 cm^{-1} and -83 cm^{-1}, for complexes **5** and **[5b]$^+$**, respectively. This increase in magnitude of the computed J-values indicates that the bridging ligand radical mediates larger exchange interactions between the Fe^{2+} centers (separated by 8.22 Å) as compared to the closed-shell HQate ligand of **5**. Inspired by the development of this interesting $S = 7/2$ species, we sought to pursue additional homodinuclear divalent transition metal complexes bridged by a variety of (semi)quinone radical ligands in order to study their unique physical properties, particularly compounds that incorporate bridging ligands derived from naphthoquinone and anthraquinone. We hypothesized that by preparing

compounds that incorporate a ligand such as 5,8-dihydroxynaphthoquinone (**5,8-DHNQ**), which functionally incorporates both a hydroquinone and quinone moiety, we could potentially observe both ligand oxidation and reduction through separate redox reactions. Our goal was to ultimately generate a series of related complexes with distinct spin-states and therefore, differing amounts of magnetic exchange. This chapter reports the synthesis and characterization of such compounds followed by brief descriptions of preliminary electrochemical and spectroscopic investigations. The intention of this study was to develop dinuclear compounds that exhibited explicit redox behavior similar to that observed for complex **5** (Chapter 6) in order to generate a series of species which represented varying degrees of magnetic coupling which we aimed to study spectroscopically as we predicted they would exhibit interesting electronic and magnetic properties. Unfortunately, we observed that the incorporation of substituted naptho- and anthraquinone ligands into our dinuclear systems lead to the generation of a series of complexes that display extremely ill-defined redox behavior, as evidenced by electrochemical experiments. We were, therefore, unable to isolate stable oxidized or reduced species to investigate further and this project was not pursued to completion.

7.B. Results and Discussion

7.B.i. Synthesis and Characterization of Dinuclear-(H)Qate Complexes

In an attempt to generate $(M)_2^{2+}$-SQ type complexes ($M = Fe^{2+}$, Mn^{2+}), we first sought to synthesize a series of complexes supported by either the hydridotris(3,5-

diphenylpyrazol-1-yl)borate (^{Ph2}Tp) or tris(4,5-diphenyl-1-methylimidazol-2-yl)phosphine (^{Ph2}TIP) ligands and bridged by a variety of (hydro)quinone ligands shown in Figure 7.1.
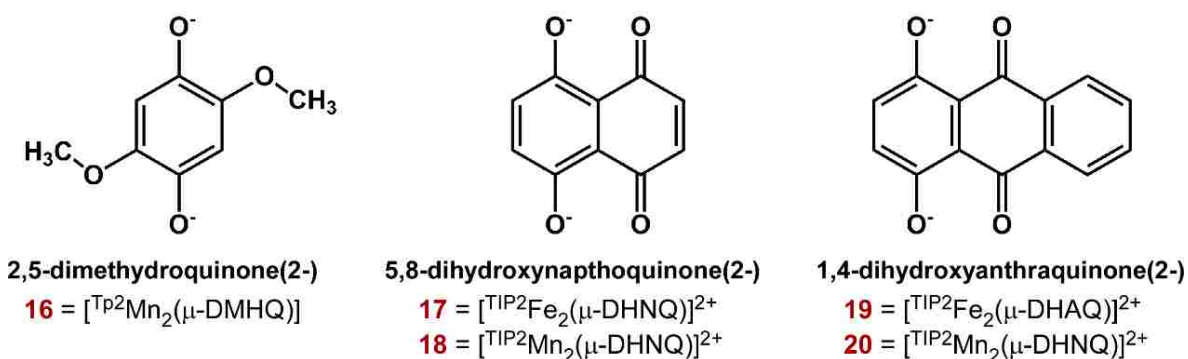
Figure 7.1. Series of (hydro)quinone ligands used in this study. The dianion of each ligand was utilized to facilitate binding of two metal centers (M = Fe^{2+}, Mn^{2+}) in a bidentate fashion.

Complex **16** is a dimanganese(II) analog of complex **5** and was prepared in a similar fashion by mixing 0.5 equiv of Na$_2$(2,5-DMHQ) with equimolar amounts of MnClO$_4$·6H$_2$O and K(^{Ph2}Tp) in MeCN followed by recrystallization from DCM/pentane (Figure 7.2). Complexes **17-20**, however, instead feature two divalent metal centers (Fe^{2+} or Mn^{2+}) bound facially by the neutral ^{Ph2}TIP scorpionate ligand and bridged by either 5,8-DHNQ (**17,18**) or 1,4-DHAQ (**19,20**). Each [(^{Ph2}TIP)Fe$_2$$^{2+}$]-species (**17,19**) was generated by combining 0.5 equiv of the corresponding ligand with the previously reported [(^{Ph2}TIP)Fe(MeCN)$_3$](OTf)$_2$ precursor complex in THF followed by recrystallization from a vapor diffusion of either Et$_2$O into MeCN or pentane into DCE, respectively (Figure 7.3). The [(^{Ph2}TIP)Mn$_2$$^{2+}$]-complexes were prepared by mixing 0.5 equiv of the appropriate ligand with equimolar amounts of MnClO$_4$·6H$_2$O and (^{Ph2}TIP) in

MeCN followed by a salt anion metathesis reaction in MeOH with 2 equivalents of

NaBPh$_4$. Each complex was easily recrystallized from DCM/MeOH (Figure 7.4). Metric

parameters for complexes **16-20** are presented in Table 7.1.

Table 7.1. Selected bond distances (Å) and bond angles (°) from the X-ray structures of dimetal(II) (hydro)quinone-bridged complexes **16-20**. (M = Fe, Mn)

	16	[17](OTf)₂·4Et₂O	[18](BPh₄)₂·2DCM	[19](OTf)₂·DCE	[20](BPh₄)₂·5DCM[b]
M–N1	2.175(18)	2.136(13)	2.191(2)	2.129(3)	2.194(4) / 2.149(5)
M–N3	2.172(17)	2.143(12)	2.202(2)	2.128(3)	2.188(5) / 2.178(5)
M–N5	2.250(16)	2.199(12)	2.236(2)	2.198(2)	2.230(5) / 2.242(5)
M–O1	1.969(14)	1.956(10)	2.038(19)	1.950(2)	2.023(5) / 2.026(4)
M–O2	2.321(15)	1.984(11)	2.064(18)	1.979(2)	2.043(5) / 2.052(4)
O2–C2	1.398(2)	1.282(17)	1.285(3)	1.277(4)	1.280(7) / 1.286(7)
O1-C1	1.336(2)	1.289(17)	1.277(3)	1.287(4)	1.278(7) / 2.026(4)
O1–M–N1	130.73(7)	106.62(5)	107.69(8)	108.33(10)	118.06(19) / 112.70(18)
O1–M–N3	140.06(7)	162.95(5)	157.71(8)	158.09(10)	158.10(18) / 155.64(18)
O1–M–N5	104.18(6)	92.78(4)	91.56(8)	94.69(9)	95.51(18) / 95.88(17)
O1–M–O1	74.56(6)	86.28(4)	83.54(7)	86.52(9)	84.37(18) / 84.18(17)
N1–M–N3	87.32(7)	90.26(5)	94.31(8)	93.46(10)	90.84(17) / 91.66(18)
N1–M–N5	88.66(6)	90.65(5)	90.85(8)	89.88(9)	89.59(18) / 92.59(18)
N3–M–N5	85.73(6)	84.44(5)	84.37(8)	82.80(10)	84.60(19) / 83.06(19)
O2–M–N1	91.49(6)	100.21(5)	110.69(8)	97.71(10)	99.47(18) / 100.43(19)
O2–M–N3	95.84(6)	93.22(4)	92.21(8)	92.94(10)	91.92(18) / 91.08(18)
O2–M–N5	178.43(5)	168.91(5)	158.40(8)	171.53(10)	170.36(19) / 165.88(29)
τ-value[a]	0.64	0.10	0.01	0.22	0.20 / 0.17

[a] For a definition of the τ-value, see ref 98. A five-coordinate complex with ideal square-pyramidal geometry would have a τ-value of 0.0, while those with ideal trigonal bipyramidal geometry would have a value of 1.0. [b] Complex [**20**](BPh₄)₂ is quasi-centrosymmetric, values corresponding to each Mn center (A and B) are given on the left and right sides of the column, respectively.
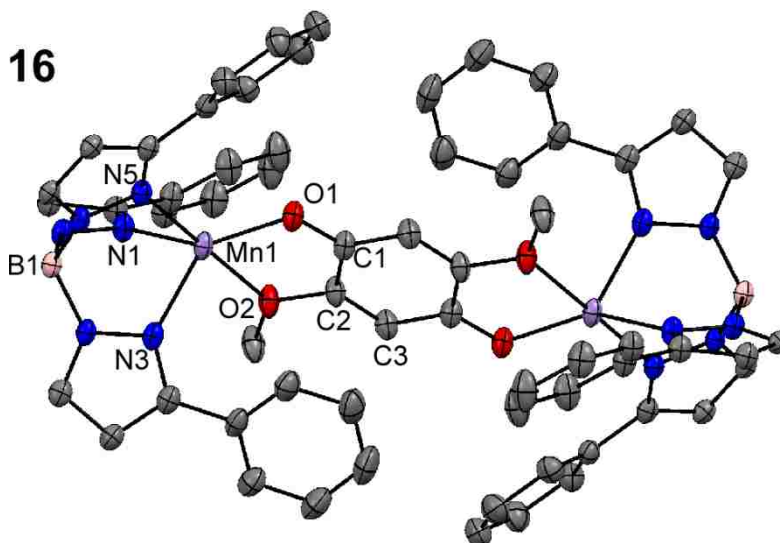
Figure 7.2. Thermal ellipsoid plot (50% probability) derived from X-ray structure of **16**, a dimanganese(II) analog of **5** (see Chapter 6). Non-coordinating solvent molecules, hydrogen atoms and the Ph-rings at the 5-positions of the Ph2Tp ligand have been omitted for clarity.
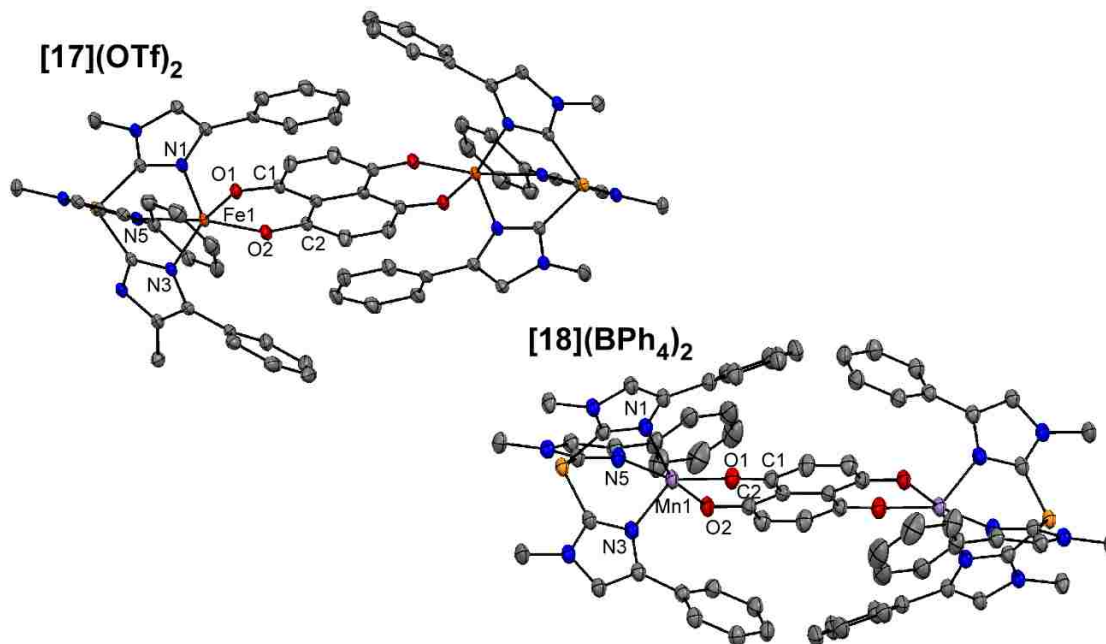
Figure 7.3. Thermal ellipsoid plots (50% probability) derived from the X-ray structures of **[17](OTf)₂** and **[18](BPh₄)₂**. Non-coordinating solvent molecules, counter anions, all hydrogen atoms and the Ph-rings at the 5-positions of the Ph2TIP ligands have been omitted for clarity.
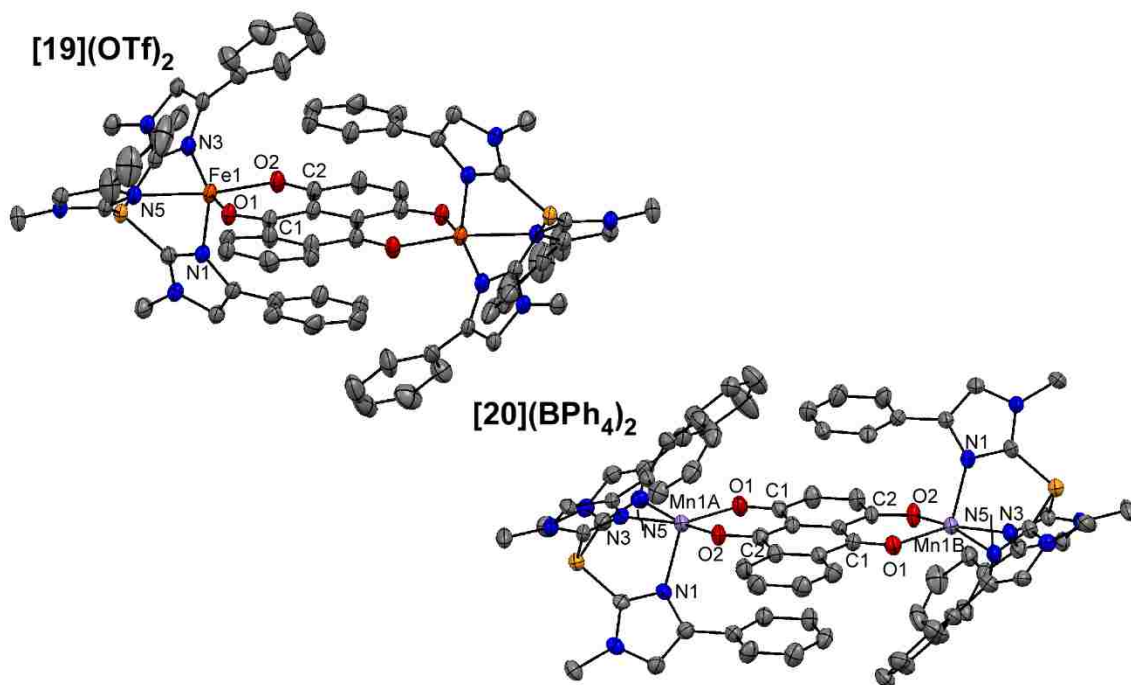
Figure 7.4. Thermal ellipsoid plots (50% probability) derived from the X-ray structures of **[19](OTf)₂** and **[20](BPh₄)₂**. Non-coordinating solvent molecules, counter anions, all hydrogen atoms and the Ph-rings at the 5-positions of the ^{Ph2}TIP ligands have been omitted for clarity.

X-ray diffraction analysis indicates that **16** is a centrosymmetric complex consisting of 2 Mn(II) centers bridged by a closed-shell *p*-hydroquinonate ligand with an Mn···Mn distance of 8.227 Å (Figure 7.2). The coordination geometry of each Mn is intermediate between square pyramidal and trigonal bipyramidal ($\tau = 0.64$).[98] An average Mn-N$_{Tp}$ bond length of 2.20 Å indicates the presence of high-spin Mn(II) centers in **16** and the Mn1-O1 and Mn1-O2 bond lengths of 2.303 and 1.969 Å nicely mirror the corresponding Fe-O bond distances in **6** representing the methoxy and phenolate donors, respectively.[139, 221]

The X-ray crystal structures of **[17](OTf)₂** and **[18](BPh₄)₂** also reveal centrosymmetric complexes featuring 5C metal centers linked by the dianion of the 5,8-

dihydroxynaphthoquinone ligand (Figure 7.3). Both complexes incorporate divalent

metals centers (Fe^{2+} and Mn^{2+}, respectively) bound to the neutral (^{Ph2}TIP) scorpionate in

a facial orientation. Complex **[17](OTf)₂** displays an average Fe-N$_{TIP}$ bond length of 2.16

Å and Fe1-O1 and Fe1-O2 distances of 1.984 and 1.956 Å, respectively, with an Fe···Fe

separation of 8.307 Å. The similarity of the four Fe-O bond lengths indicates that the

bridging ligand has a delocalized structure, further supported by the observation of

shortened C$_\beta$-C$_\beta$ bond lengths (1.351 Å versus C-C$_{ring}$ avg. length of 1.433 Å). The 5C

Fe-centers of complex **[17](OTf)₂** also display square pyramidal coordination geometries

($\tau = 0.10$)[98] which differs from the intermediate square planar/trigonal bipyramidal

geometries of the [(^{Ph2}Tp)₂(M)₂(μ-DMHQ)]-species, **5** and **16**. X-ray diffraction analysis

indicates that complex **[18](BPh₄)₂** bears resemblance to **[17](OTf)₂** except that it

incorporates two Mn(II) centers (Mn···Mn separation = 8.412 Å) in place of the diiron(II)

centers of **17** with average Mn-N$_{TIP}$ bond lengths of 2.21 Å and Mn1-O1 and Mn1-O2

distances of 2.064 and 2.038 Å, respectively. In addition, **[18](BPh₄)₂**, like complex

[17](OTf)₂, displays a square pyramidal coordination geometry ($\tau = 0.01$)[98] at each 5C

manganese center. The square planar coordination geometries displayed by complexes

[17](OTf)₂ and **[18](BPh₄)₂** in comparison to the intermediate coordination geometry of

16 is likely the result of π-stacking interactions between the naphthoquinonate moiety and

a 3-phenyl substituent of each ^{Ph2}Tp ligand.

Like complexes **16-18**, the XRD analysis confirms that **19** and **20** lay on

crystallographic inversion centers requiring the bridging anthraquinone ligand to be

disordered over two positions (as indicated in the metric parameters provided in Table

7.1). Complex **[19](OTf)₂** displays an Fe···Fe separation of 8.285 Å with an average Fe-

N_{TIP} bond length of 2.15 Å. The Fe1-O1 and Fe1-O2 bond lengths are 1.950 and 1.979 Å and **19** displays an intermediate Fe coordination geometry lying closer to the square pyramidal limit ($\tau = 0.22$).[98] Compared to complex **[19](OTf)$_2$**, the manganese(II) centers of **[20](BPh$_4$)$_2$** exhibit similar coordination geometries ($\tau = 0.20/0.17$) [98] and a Mn$\cdots$Mn distance of 8.425 Å. In addition, the X-ray crystal structure of **[20](BPh$_4$)$_2$** displays average Mn-N_{TIP} bond length of 2.20 Å and Mn1-O1 and Mn1-O2 distances of 2.043 and 2.023 Å, respectively.

7.B.ii. Spectroscopic and Electrochemical Investigation of 16

The redox behavior of **16** was examined in CH_2Cl_2 with 0.1 M [NBu$_4$]PF$_6$ as the supporting electrolyte. The resulting cyclic voltammogram exhibits a quasi-reversible couple at $E_{1/2} = -718$ mV vs Fc$^{+/0}$ ($\Delta E = 104$ mV) with several additional irreversible redox events at higher potentials (Figure 7.5). This redox behavior is similar to that of **5** including the quasi-reversible event observed at negative potentials, assigned to the oxidation of the HQate ligand to its SQate form. Interestingly, in the case of **16**, the ligand-based event is shifted to more negative potentials ($\Delta E_{1/2} = 148$ mV) with respect to **5**. In order to explore whether or not the isolation of a one-electron oxidized [(^{Ph2}Tp)$_2$Mn$_2$(μ-DMSQ)]$^+$-type species was feasible, we monitored the reaction of **16** with a chemical oxidant via UV-vis spectroscopy (Figure 7.6).
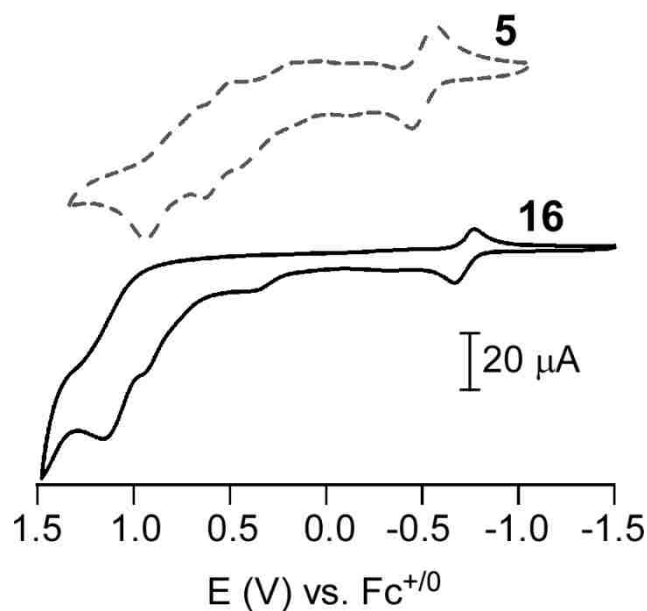
Figure 7.5. Cyclic voltammogram of **16** in CH_2Cl_2 with 0.1 M [NBu$_4$]PF$_6$ as the supporting electrolyte collected at a scan rate of 0.1 V/s. The cyclic voltammogram of **5** is provided for comparison (data was collected in similar conditions; see Chapter 6).
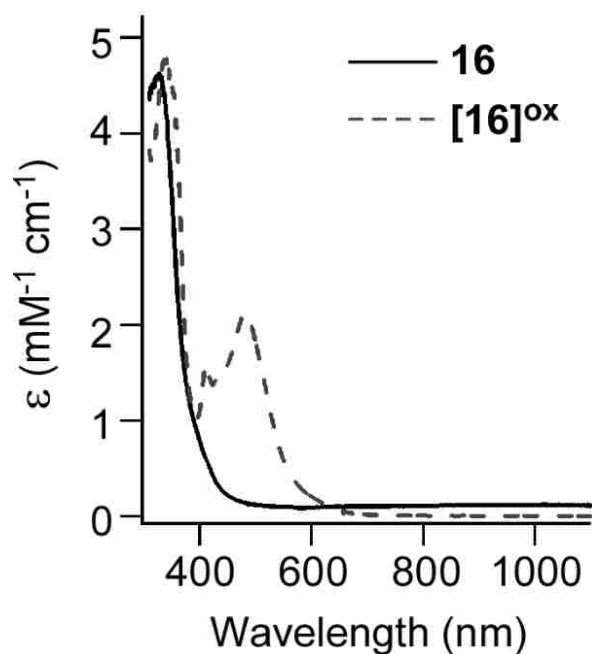
Figure 7.6. Electronic absorption data demonstrating the conversion of **16** to **[16]^{ox}** via addition of 1 equivalent of AcFc$^+$ in CH_2Cl_2 at -30 °C.

Upon addition of one equivalent of acetylferrocenium tetrafluoroborate to **16** in CH_2Cl_2 at -30 °C, a new quasi-stable species is formed, **[16]^{ox}**. Unlike **[5b]$^+$**, the $[(^{Ph2}Tp)_2Fe_2(\mu\text{-DMSQ})]^+$ analogue, **[16]^{ox}** is not stable at room temperature. The resulting red-brown chromophore displays two new absorption features with λ_{max} = 412 nm and 481 nm (ε = 1.6 and 2.1 mM^{-1} cm^{-1}, respectively). An attempt to isolate crystals of **[16]^{ox}** at low temperature was made. Under anaerobic conditions, **16** was treated with 1 equivalent of $AgPF_6$ at approximately -30 °C and the subsequent red-brown solution was layered with cold pentane placed in a -30 °C freezer to initiate crystallization. The resulting crystalline needles were submitted for X-ray diffraction analysis, however the corresponding crystallographic solution indicated over-oxidation of the bridging ligand (XRD analysis predicts an overall charge of approximately +1.27 for the dimanganese complex).

While our method of preparation for crystalline **[16]^{ox}** needs some refining, it is clear that the addition of oxidant to **16** results in a ligand-centered oxidation. Comparison of observed bond lengths of **16** and **[16]^{ox}** indicate relatively similar average Mn-N$_{Tp}$ bond lengths (2.20 vs 2.15 Å), however, upon oxidation, **[16]^{ox}** displays a pronounced change in the C-C bond lengths, namely, elongation of the C1-C2 and C1-C3 bonds and shortening of the C2-C3 bonds. Additionally, there is a noticeable shortening of the C3-O2 bond from 1.336 Å for **16 to** 1.292 Å for **[16]^{ox}**. Based on well-established guidelines for metal-ligand bond lengths with regards to dioxolene oxidation states[136, 206-207] and our previous experience with complex **5**, these changes in metric parameters suggest formation of a ligand-based radical to yield a species best described as $[(^{Ph2}Tp)_2Mn_2(\mu\text{-DMSQ})]^+$.

Attempts to collect X-band EPR spectra of **[16]^{ox}** were made and while it is clear there is a significant rearrangement of electron density upon oxidation of **16** → **[16]^{ox}**, the combination of Mn hyperfine splitting and small zero-field splitting resulted in extremely complicated EPR spectra that resisted attempts at simulation.

Further evidence for generation of a ligand-based radical was derived from rRaman spectroscopy. The spectrum of **[16]^{ox}** obtained with 514 nm excitation exhibits several new peaks that are not present in that of **16**. The intense feature at 1484 cm^{-1} is greatly enhanced by excitation into the absorption band of **[16]^{ox}** suggesting that it corresponds to a DMSQ-based mode (Figure 7.7). Based on previous studies of metal-bound dioxolenes, it has been reported that *o*-semiquinones exhibit intense peaks arising from C-O stretching modes ranging between 1400-1500 cm^{-1}, therefore, the feature observed at 1484 cm^{-1} likely corresponds to the symmetric ν(C-O) mode of **[16]^{ox}**.[136] Literature precedents suggests the peak at 580 cm^{-1} can be assigned as the breathing mode of the five-membered chelate formed by the O-donors of the DMSQ ligand and each Mn center, while the resonance-enhanced features at 1432 and 1494 cm^{-1} correspond to the mixing of ν(C-O) and C-C based modes.[137,139,210] As reported in Chapter 6, similar rRaman features were observed for **[5b]$^{+}$**.[139] We generated the dimanganese(II) version of **[5b]$^{+}$** with intention of generating a similar complex with an increased spin state, since antiferromagnetic coupling between the Mn(II) centers and the bridging DMSQ ligand would yield an overall $S = 9/2$ state. Additional investigation into the spin state of **[16]^{ox}** still remains to be done, especially with regards to solving the EPR spectra obtained in order to confirm the newly generated spin state.
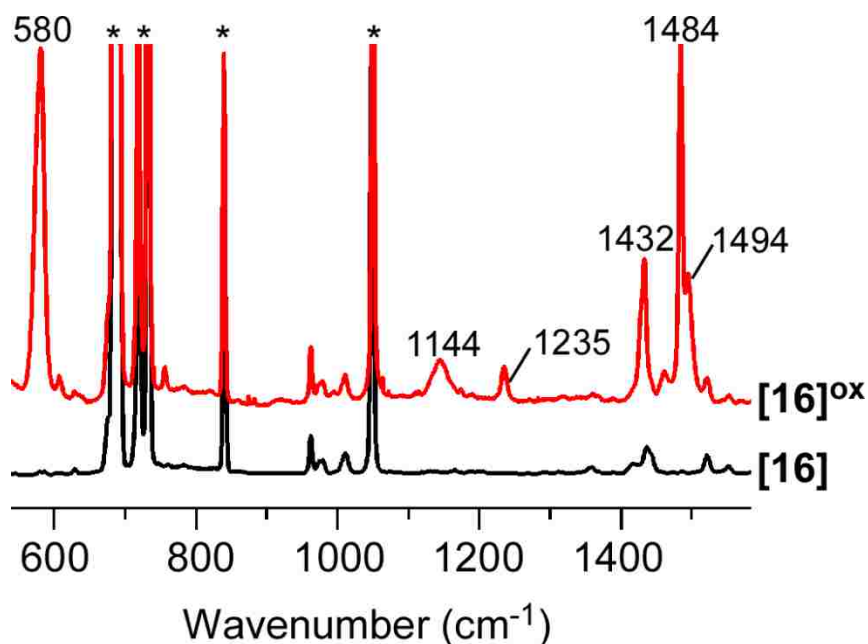
Figure 7.7. rR spectra obtained with 514 nm excitation (50 mW) of **16** (black) and **[16]ox** (red) in frozen CD_2Cl_2 solutions. Peaks with an asterisk (*) arise from solvent.

7.B.iii. Preliminary Studies of Dimetal Complexes Featuring Naphtho- and Anthraquinone-derived Bridging Ligands

The first series of complexes we aimed to synthesize are similar to **5** and **16**, but incorporate 5,8-DHNQ as the bridging ligand. Several attempts were made to generate a bis-(^{Ph}Tp) version of this complex, but crystalline material was unable to be isolated. We therefore turned to the neutral (^{Ph2}TIP) scorpionate and were able to easily isolate **[17](OTf)₂** – which has a chemical formula of [(^{Ph2}Tp)₂Fe(μ-DHNQ)](OTf)₂ according to X-ray diffraction analysis (*vide supra*). Preliminary electrochemical studies of **[17](OTf)₂** have been carried out (Figure 7.8); however the resulting data seems to be rather inconclusive as the redox behavior observed by cyclic voltammetry is somewhat ill-defined.

Figure 7.8. Cyclic voltammogram of **[17](OTf)₂** obtained in CH_2Cl_2 in the presence of 0.1 M [NBu₄]PF₆ as the counter electrolyte. Data was obtained at a sweep rate of 0.1 V/s.

While the electrochemical data obtained for **[17](OTf)₂** in DCM does not display a ligand-based (quasi)reversible redox couple as was displayed previously by complexes **5** and **16**, the CV indicates the presence of two irreversible oxidative events at E = -502 and +309 mV (vs $Fc^{+/0}$). A series of ill-defined cathodic events are displayed at more negative potentials, particularly an irreversible reduction at E = -907 mV. The absence of a distinct (quasi)reversible couple could be due to the delocalized nature of the bridging (5,8-DHNQ) ligand, as previously indicated by XRD analysis (*vide supra*).

To further investigate the ability of **[17](OTf)₂** to facilitate ligand-based electron transfers, either to or away from its ligand bridge via a chemical oxidation, we treated **[17](OTf)₂** with one equivalent of $AcFc^+$ in CH_2Cl_2 at -30 °C and monitored the resulting reaction via UV-vis absorption spectroscopy (Figure 7.9).
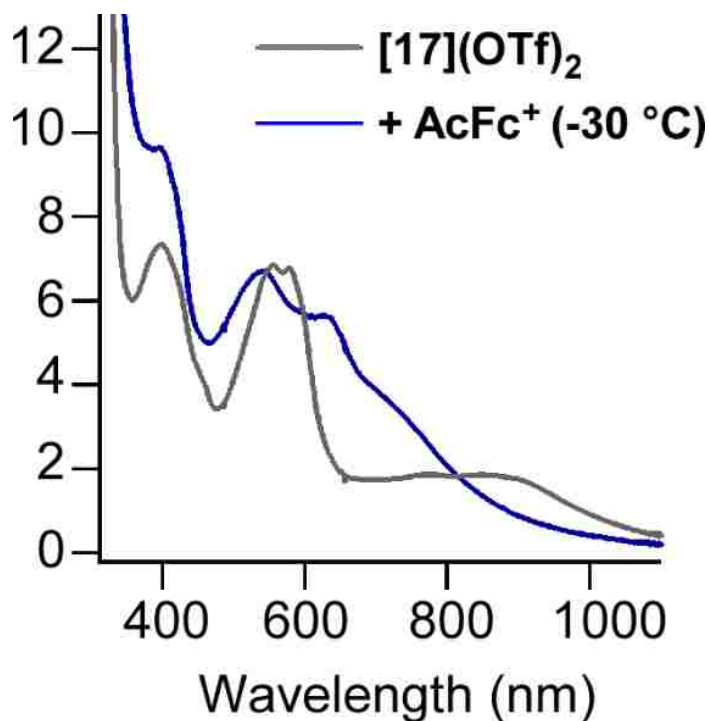
Figure 7.9. Electronic absorption spectra of **[17](OTf)$_2$** and the chromophore resulting from reaction with one equivalent of AcFcBF$_4$ in CH$_2$Cl$_2$ at -30 °C.

As demonstrated in Figure 7.9, complex **[17](OTf)$_2$** displays a series of absorption features in the visible region with λ_{max} = 399, 556 and 578 nm (ε = 7.4, 6.9 and 6.8 mM^{-1} cm^{-1}, respectively). However, upon addition of 1 equivalent of AcFc$^+$ at -30 °C, the higher energy band exhibits a slight blueshift (λ_{max} = 395 and 541 nm) while the lower energy feature with λ_{max} = 578 nm decreases slightly in intensity and experiences a redshift as it broadens (λ_{max} = 629 nm, ε = 5.7 mM^{-1} cm^{-1}). Based on our previous experience with the oxidation of complex **5**, it is predicted that the 3-band spectroscopic pattern evident in the UV-vis absorption spectrum of **[17]^{ox}** is due to the oxidation of the bridging ligand; however, further spectroscopic analysis is required to confirm this assignment, especially due to the ill-defined nature of the electrochemical data that has been collected up to this point.

Additional reactivity studies using 1 equivalent of $CoCp_2^*$ were completed as the reaction between complex **[17](OTf)$_2$** and reductant was observed via UV-vis spectroscopy (<u>Figure 7.10</u>). Addition of 1 equivalent of $CoCp_2^*$ significantly alters the absorption spectrum of **[17](OTf)$_2$** as the features between 550-580 nm completely diminish and a new, sharp absorption band appears at $\lambda_{max} = 380$ nm ($\varepsilon = 7.4$ mM^{-1} cm^{-1}) with two shoulders at approximately 428 and 466 nm. While further experimental evidence is required to determine the identity of **[17]^{red}**, it is clear that addition of one equivalent of reductant causes a substantial change in the absorption features of **[17](OTf)$_2$.** Although **[17]^{ox}** and **[17]^{red}** are both only stable at temperatures < -30 °C, attempts to crystallize these species at low temperatures should be make in order to gain insight into their geometric structures via XRD analysis. Further insight into the spin state of the molecule up removal or addition of an electron as well as the oxidation state of the bridging ligand upon oxidation or reduction can be gained from spectroscopic studies using EPR and rRaman spectroscopies.
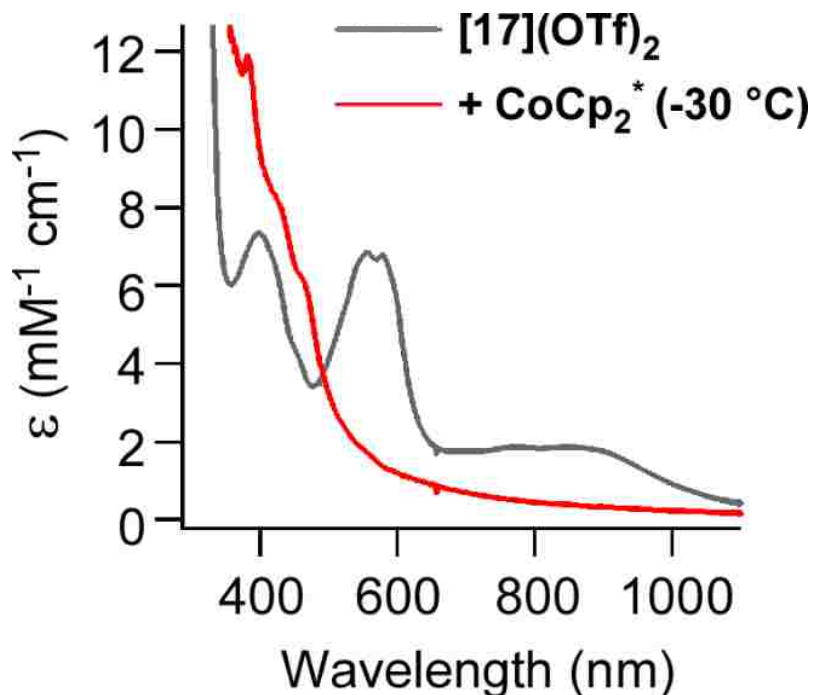
Figure 7.10. Electronic absorption spectra of **[17](OTf)₂** and the chromophore resulting from reaction with one equivalent of CoCp₂* in CH₂Cl₂ at -30 °C.

Our second class of dinuclear quinone-bridged complexes incorporates 1,4-dihydroxyanthraquinone (**1,4-DHAQ**) as the bridging ligand. We sought to use this ligand in an attempt to study the effects of incorporating a bridging substituent with an extended π-system on the ability of a radical-bridged dinuclear complex to mediate magnetic exchange interactions. Complex **[19](OTf)₂** is therefore an analog of **[17](OTf)₂**, and features two diiron(II) centers linked by the dianion of 1,4-DHAQ. Preliminary electrochemical data for **[19](OTf)₂** has been collected in CH₂Cl₂ and is presented in Figure 7.11.
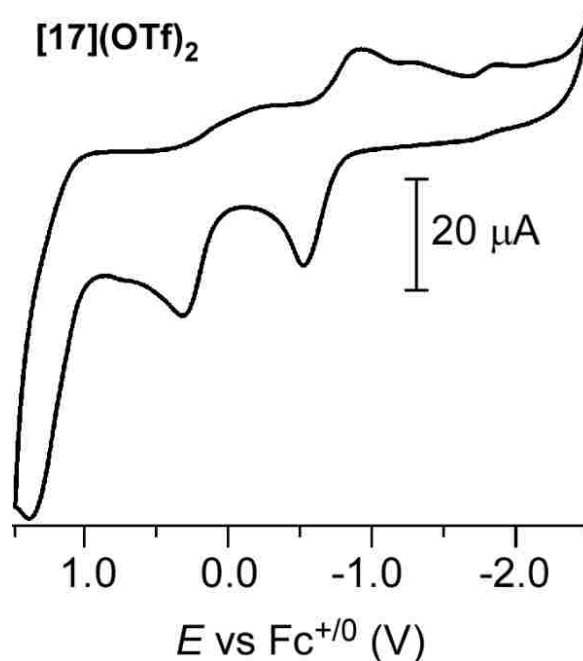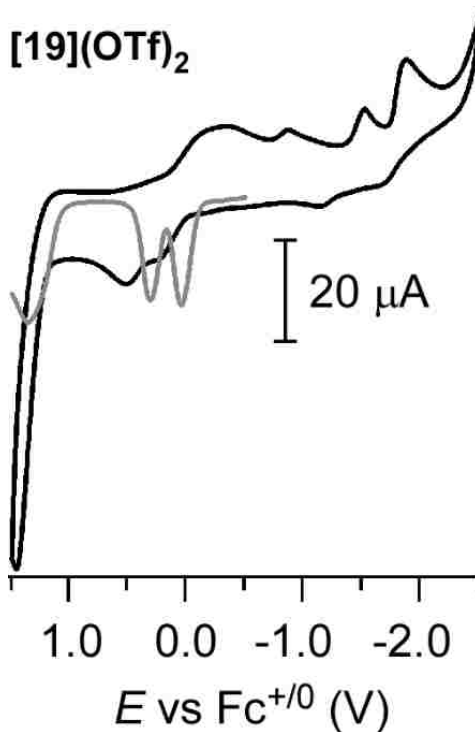
Figure 7.11. Cyclic voltammogram of **[19](OTf)₂** obtained in CH₂Cl₂ in the presence of 0.1 M [NBu₄]PF₆ as the counter electrolyte. Data was obtained at a sweep rate of 0.1 V/s.

The cyclic voltammogram of complex **[19](OTf)₂** appears to be more complicated as that obtained for **[17](OTf)₂**. Interestingly, the irreversible cathodic features of this data seem to be more resolved that those previously observed for the 5,8-DHNQ analog (E_{irrev} = -1.531 and -1.884 V vs Fc$^{+/0}$) which likely correspond to reduction of the bridging 1,4-DHAQ ligand. Irreversible oxidation events at higher potentials are poorly resolved as the potentials of the events seem to lie very close to one another. However, square wave data collected in the same region displays two discrete events with E_{irrev} = 0.035 and 0.299 V, which are tentatively assigned to the oxidation of the two diiron(II) centers. Future studies will first focus on the observation of this complex's reactivity with respect to chemical reductants in order to isolate a putative [(^{Ph2}TIP)₂Fe^{2+}₂(μ-DHSQ$^-$)]-

type species. Because of the indication that the oxidation of two Fe(II) centers lies close to one another in potential, the chemical oxidation of this complex could yield an interesting result. Unfortunately, we have yet to isolate a dinuclear species that incorporates either a mixed valent diiron core or one incorporating (di)ferric ions within our series of dinuclear Fe(II)-(H)Qate systems.

A further outgrowth of this study was aimed at the generation of complexes with larger spin systems. We therefore prepared dimanganese(II) analogs of both **[17]$^{2+}$** and **[19]$^{2+}$** (**[18]$^{2+}$** and **[20]$^{2+}$**, respectively), proposing that upon generation of a Mn(II)$_2$-SQate bridged species, each d^5, $S = 5/2$ Mn^{2+} center would couple antiferromagnetically to the SQ-bridging ligand, resulting in a $S = 9/2$ species. As previously mentioned, we have been successful in the synthesis and structural characterization of these species, however further spectroscopic characterization and reactivity studies remain to be completed.

7.C. Conclusion

The ability of ligand-based radicals to mediate significant magnetic exchange between paramagnetic metals centers has been of much interest to researchers in the development of small molecule magnets which have interesting applications towards the development of solid state storage devices.[211-213] Upon successful generation of our diiron(II) species bridged by a (semi)quinonate ligand radical (**[5b]$^+$**, Chapter 6), we chose to pursue similar dimetal(II) (M = Fe^{2+}, Mn^{2+}) species bridged by a variety of (hydro)quinonate ligands based on the ability of (hydro)quinones to facilitate multiple

electron transfers. We noted that upon oxidation of the bridging 2,5-dimethoxyhydroquinone ligand of **5**, the magnitude of the computed *J*-value (exchange coupling parameter) increased from -2 cm^{-1} to -83 cm^{-1}, indicating a net increase in magnetic exchange between the diiron(II) centers. Inspired by this observation, our ultimate goal is to generate novel species bridged by ligand-based radicals in order to study their geometric structure and their interesting electronic and magnetic properties via spectroscopy and computational methods. Up to this point, we have successfully synthesized and structurally characterized a dimanganese(II) version of **5** (complex **16**) that, according to the results described here, experiences one-electron oxidation to yield a (semi)quinonate-bridged species at low temperatures.

Additional studies were aimed at the generation of diiron(II) species that incorporate the dianion of 5,8-DHNQ or 1,4-DHAQ to generate **[17](OTf)$_2$** and **[19](OTf)$_2$**, respectively. While these complexes were synthesized and characterized with XRD, further investigation of these compounds is required. Future studies will examine the ability of these complexes to undergo one-electron oxidation or reduction reactions. Dimanganese analogs of these complexes (**[18](BPh$_4$)$_2$** and **[20](BPh$_4$)$_2$**, respectively) have been successfully prepared and structurally characterized via XRD analysis. We expect that the incorporation of two high-spin Mn^{2+} centers in these complexes will lead to species with a larger observed spin state than their diiron(II) analogs upon generation of a substrate-based radical; however additional investigation is required. The preliminary results reported here lay a foundation for the continued study of these compounds and similar dinuclear species.

Table 7.2. Summary of X-ray Crystallographic Data Collection and Structure Refinement for Complexes **16-20**.

	16	**[16]^{ox}·PF$_6$**^{a}	**[17](OTf)$_2$·4Et$_2$O**
empirical formula	$C_{98}H_{76}B_2Mn_2N_{12}O_4$	$C_{98}H_{76}B_2F_6Mn_2N_{12}O_4P_1$	$C_{124}H_{122}F_6Fe_2N_{12}O_{14}P_2S_2$
formula weight	1617.21	1800.79	2356.10
crystal system	Triclinic	Monoclinic	Triclinic
space group	P-1	P2$_{1/c}$	P-1
a, Å	9.7042(2)	13.5467(2)	12.3155(3)
b, Å	13.4568(5)	15.8981(4)	13.1640(3)
c, Å	17.8105(4)	23.4908(5)	18.5849(4)
α, deg	92.194(2)	90	80.0260(17)
β, deg	103.619(2)	96.5943(17)	75.9486(18)
γ, deg	100.236(2)	90	77.4474(17)
V, Å^3	2215.21(10)	5025.70(17)	2829.82(10)
Z	1	2	1
D_{calc}, g/cm^3	1.212	2.791	1.383
λ, Å	1.5148	1.5418	1.5418
μ, mm^{-1}	2.773	2.791	3.331
θ-range, deg	7 to 148	7 to 149	7 to 147
reflections collected	41369	48161	46785
independent reflections	8873	10134	11227
data / restraints / parameters	8873 / 0 / 533	10134 / 0 / 593	11227 / 0 / 766
GOF (on F^2)	1.073	1.048	1.026
$R1$/$wR2$ ($I > 2\sigma(I)$)^b	0.0467 / 0.1224	0.0812 / 0.2224	0.0335 / 0.0865
$R1$/$wR2$ (all data)	0.0568 / 0.1338	0.0934 / 0.2306	0.0362 / 0.0891

^{a} The PF$_6^-$ ion refined to occupation of only 0.63 and is rotationally disordered. $^b R1 = \Sigma\,||F_o| - |F_c||\,/\,\Sigma|F_o|$; $wR2 = [\Sigma w(F_o{}^2 - F_c{}^2)^2\,/\,\Sigma w(F_o{}^2)^2]^{1/2}$

Table 7.2. (cont.) Summary of X-ray Crystallographic Data Collection and Structure Refinement for Complexes **16-20**.

	[18](BPh$_4$)$_2$· 3DCM[c]	[19](OTf)$_2$·2DCE[d]	[20](BPh$_4$)·5DCM
empirical formula	C$_{158}$H$_{128}$B$_2$Cl$_6$Mn$_2$N$_{12}$O$_4$P$_2$	C$_{116}$H$_{92}$Cl$_4$F$_6$Fe$_2$N$_{12}$O$_{10}$P$_2$S$_2$	C$_{163}$H$_{134}$B$_2$Cl$_{10}$Mn$_2$N$_{12}$O$_4$P$_2$
formula weight	2677.48	2307.58	2826.05
crystal system	Triclinic	Triclinic	Triclinic
space group	P-1	P-1	P-1
a, Å	14.2755(4)	13.9219(4)	13.2692(3)
b, Å	14.8992(4)	14.9501(4)	15.8678(4)
c, Å	19.6567(4)	16.7903(4)	19.0587(4)
α, deg	94.1359(18)	100.961(2)	94.2271(18)
β, deg	106.699(2)	96.054(2)	109.855(2)
γ, deg	115.058(3)	115.833(3)	94.6975(18)
V, Å^3	3535.97(15)	3017.06(15)	3739.51(14)
Z	1	1	1
D_{calc}, g/cm^3	1.257	1.270	1.255
λ, Å	1.5418	1.5418	1.5418
μ, mm^{-1}	3.270	3.886	3.491
θ-range, deg	7 to 148	7 to 149	7 to 148
reflections collected	67185	49891	54770
independent reflections	14219	12073	24890
data / restraints / parameters	14219 / 0 / 846	12073 / 0 / 723	24890 / 1052 / 1764
GOF (on F^2)	1.079	1.098	1.055
$R1/wR2$ ($I > 2\sigma(I)$)[b]	0.0613 / 0.1839	0.0641 / 0.1874	0.0729 / 0.2048
$R1/wR2$ (all data)	0.0698 / 0.1979	0.0750 / 0.2000	0.0815 / 0.2194

[b]$R1 = \Sigma\ ||F_o| - |F_c||\ /\ \Sigma|F_o|$; $wR2 = [\Sigma w(F_o^2 - F_c^2)^2\ /\ \Sigma w(F_o^2)^2]^{1/2}$. [c]Unidentified solvent and one of the DCM solvate molecules in **[18](BPh$_4$)•3DCM** are only partially populated. [c]Only one DCE molecule was localized. [d]One DCM solvate molecule is only partially populated.

7.D. Experimental

7.D.i. General methods

Unless otherwise noted, all reagents and solvents were purchased from commercial sources and used as received. Acetonitrile and dichloromethane were purified and dried using a Vacuum Atmospheres solvent purification system. The synthesis and handling of air-sensitive materials were performed under inert atmosphere using a Vacuum Atmospheres Omni-Lab glovebox. The ligands $K(^{Ph2}Tp)$[103], (^{Ph2}TIP)[122], and 2,5-dimethoxyhydroquinone (2,5-DMHQ)[104] as well as the $[(^{Ph2}TIP)Fe(MeCN)_3](OTf)_2$[122] precursor complex were prepared according to literature procedures.

UV-vis absorption spectra were obtained with an Agilent 8453 diode array spectrometer equipped with a cryostat from Unisoku Scientific Instruments (Osaka, Japan) for temperature control. EPR experiments were performed using a Bruker ELEXSYS E600 equipped with an ER4415DM cavity resonating at 9.63 GHz, an Oxford Instruments ITC503 temperature controller, and an ESR-900 He flow cryostat. Electrochemical measurements were conducted in the glovebox with an epsilon EC potentiostat (iBAS) at a scan rate of 100 mV s^{-1} with 100 mM $(NBu_4)PF_6$. A three-electrode cell containing a Ag/AgCl reference electrode, a platinum auxiliary electrode, and a glassy carbon working electrode was employed for cyclic voltammetric (CV) measurements. Under these conditions, the ferrocene/ferrocenium (Fc$^{+/0}$) couple has an $E_{1/2}$ value of +0.52 V in CH_2Cl_2.

7.D.ii. Synthetic procedures

[Mn$_2$(^{Ph2}Tp)$_2$(μ-DMHQ)] (16). 2,5-Dimethoxyhydroquinone (0.173 g, 1.0 mmol) was first deprotonated by treatment with two equivalents of NaOMe in THF. After removal of the solvent, the resulting solid Na$_2$(2,5-DMHQ) was mixed with equimolar amounts of Mn(ClO$_4$)$_2$·6H$_2$O (0.736 g, 2.0 mmol) and K(^{Ph2}Tp) (1.450 g, 2.0 mmol) in MeCN, and the solution was stirred overnight under an inert atmosphere. After removal of the solvent under vacuum, the pale yellow solid was taken up CH$_2$Cl$_2$ and the solution filtered through celite in a syringe filter to remove unwanted salts. A concentration solution of DCM layered with pentane provided pale yellow crystals suitable for X-ray crystallography. Anal. Calcd for C$_{98}$H$_{76}$B$_2$Mn$_2$N$_{12}$O$_4$ (M$_W$ = 1616.25 g mol^{-1}): C, 72.83; H, 5.08; N 10.40. UV-vis [λ$_{max}$, nm (ε, M^{-1} cm^{-1}) in CH$_2$Cl$_2$]: 327 (4630).

[Fe$_2$(^{Ph2}TIP)$_2$(μ-DHNQ)](OTf)$_2$ [17(OTf)$_2$]. 5,8-dihydroxynapthoquinone (10.6 mg, 0.055 mmol) was deprotonated with two equivalents of Et$_3$N in 5 mLs of THF. Upon generation of the doubly deprotonated (5,8-DHNQ)$^{2-}$ ligand, two equivalents of the [(^{Ph2}TIP)Fe(MeCN)$_3$](OTf)$_2$ precursor (0.132 g, 0.11 mmol) were added in an additional 5mLs of THF and the reaction mixture was stirred overnight. The reaction solvent was removed and the crude product was taken up in MeCN and filtered through celite in a syringe filter. Vapor diffusion of Et$_2$O into a concentrated solution of **17** in MeCN provided bright violet crystals suitable for X-ray crystallography. Anal. Calcd for C$_{108}$H$_{82}$P$_2$Fe$_2$N$_{12}$O$_{10}$F$_6$S$_2$ (M$_W$ = 2059.67 g mol^{-1}): C, 62.98; H, 4.01; N 8.16. UV-vis [λ$_{max}$, nm (ε, M^{-1} cm^{-1}) in CH$_2$Cl$_2$]: 399 (7350), 556 (6850), 578 (6780).

[Mn₂(Ph2TIP)₂(μ-DHNQ)](BPh₄)₂ [18(BPh₄)₂]. 5,8-dihydroxynapthoquinone (19.3 mg, 0.1 mmol) was stirred with two equivalents of NaOMe in 5 mLs of THF. After 30 minutes, the solvent was removed under vacuum to yield Na₂(5,8-DHNQ) which was then stirred with equimolar amounts of Mn(ClO₄)₂·6H₂O (73.1 mg, 0.2 mmol) and Ph2TIP (0.144 g, 0.2 mmol) in 10 mLs of MeCN overnight. Upon removal of the reaction solvent under vacuum, the crude product was taken up in DCM and filtered through celite in a syringe filter to yield a bright blue-violet solution. The DCM was pumped off and the product was taken up in MeOH and stirred with two equivalents of NaBPh₄ to facilitate an anion metathesis reaction. Upon completion of the reaction, MeOH was stripped under vacuum and the final product was taken up in DCM. Layering a concentrated solution of **18** with MeOH provided blue-violet crystals suitable for X-ray crystallography. Anal. Calcd for $C_{150}H_{118}B_2Mn_2N_{12}O_4P_2$ (M_W = 2346.12 g mol⁻¹): C, 76.79; H, 5.07; N 7.16.

[Fe₂(Ph2TIP)₂(μ-DHAQ)](OTf)₂ [19(OTf)₂]. The method of preparation was similar as that used for complex **17** except that 1,4-dihydroxyanthraquinone was used in place of 5,8-dihydroxynaphthoquinone. Dark violet crystals suitable for X-ray diffraction were generated by vapor diffusion of pentane into a concentrated solution of **19** in 1,2-dichloroethane. Anal. Calcd for $C_{112}H_{84}P_2Fe_2N_{12}O_{10}F_6S_2$ (M_W = 2109.73 g mol⁻¹): C, 63.76; H, 4.01; N 7.97.

[Mn₂(Ph2TIP)₂(μ-DHAQ)](BPh₄)₂ [20(BPh₄)₂]. Complex **20** was prepared in a similar manner as complex **18** except 1,4-dihydroxyanthraquinone was substituted for 5.8-dihydroxynaphthoquinone. Dark violet crystals suitable for X-ray diffraction were

generated by layering a concentrated DCM solution of **20** after anion methathesis with MeOH. Anal. Calcd for $C_{112}H_{84}P_2Fe_2N_{12}O_{10}F_6S_2$ (M_W = 2396.18 g mol^{-1}): C, 77.19; H, 5.05; N 7.01.

BIBLIOGRAPHY

1. Baker, K. H., In *Bioremediation*, Inc., M.-H., Ed. New York, 1994; p 9.

2. Parales, R. E.; Haddock, J. D. *Curr. Opin. Biotechnol.* **2004,** *15*, 347.

3. Gibson, D. T.; Koch, J. R.; Kallio, R. E. *Biochem* **1968,** *7*, 2653-2662.

4. Axcell, B. C.; Geary, P. J. *Biochem J* **1975,** *146*, 173-183.

5. Axcell, B. C.; Geary, P. J. *Biochem J* **1973,** *136*, 927-934.

6. Vaillancourt, F. H.; Bolin, J. T.; Eltis, L. D. *Crit. Rev. Biochem. Mol. Biol.* **2006,** *2006* (41), 241-267.

7. Koehntop, K. D.; Emerson, J. P.; Que, L., Jr. *J. Biol. Inorg. Chem.* **2005,** *10*, 87-93.

8. Kauppi, B.; Lee, K.; Carredano, E.; Parales, R. E.; Gibson, D. T.; Eklund, J.; Ramaswamy, S. *Structure* **1998,** *6*, 571-586.

9. Han, S.; Eltis, L. D.; Timmis, K. N.; Muchmore, S. W.; Bolin, J. T. *Science* **1995,** *270*, 976-980.

10. Vaillancourt, F. H.; Barbosa, C. J.; Spiro, T. G.; Bolin, J. T.; Blades, M. W.; Turner, R. F. B.; Eltis, L. D. *J. Am. Chem. Soc.* **2002,** *124*, 2485-2496.

11. Karlsson, A.; Parales, J. V.; Parales, R. E.; Gibson, D. T.; Eklund, H.; Ramaswamy, S. *Science* **2003,** *299*, 1039-1042.

12. Kovaleva, E. G.; Lipscomb, J. D. *Science* **2007,** *316*, 453-457.

13. Lipscomb, J. D.; Orville, A. M. *Metal Ions Biol. Syst.* **1992,** *28*, 243-298.

14. Harpel, M. R.; Lipscomb, J. D. *J. Biol. Chem.* **1990,** *265*, 22187-22196.

15. Machonkin, T. E. H., P.L.; Smith, K.N.; Liberman, J.S.; Dinescu, A.; Cundari, T.R.; Rocks, S.S. *J. Biol. Inorg. Chem.* **2010,** *15*, 291-301.

16. Veldhuizen, E. J. A.; Vaillancourt, F. H.; Whiting, C. J.; Hsiao, M. M. Y.; Gingras, G.; Xiao, Y. F.; Tanguay, R. M.; Boukouvalas, J.; Eltis, L. D. *Biochemical Journal* **2005,** *386*, 305-314.

17. Lendenmann, U.; Spain, J. C. *J. Bacteriol.* **1996,** *178*, 6227-6232.

18. Li, X.; Guo, M.; Fan, J.; Tang, W.; Wang, D.; Ge, H.; Rong, H.; Teng, M.; Niu, L.; Liu, Q.; Hao, Q. *Protein Sci.* **2006,** *15*, 761-773.

19. Matera, I.; Ferraroni, M.; Buerger, S.; Scozzafava, A.; Stolz, A.; Briganti, F. *J. Mol. Biol.* **2008,** *380*, 856-868.

20. Hintner, J. P.; Reemtsma, T.; Stolz, A. *J. Biol. Chem.* **2004,** *279*, 37250-37260.

21. Hintner, J. P.; Lechner, C.; Riegert, U.; Kuhm, A. E.; Storm, T.; Reemtsma, T.; Stolz, A. *J. Bacteriol.* **2001,** *183*, 6936-6942.

22. Lipscomb, J. D. *Curr. Opin. Struct. Biol.* **2008,** *18*, 644-649.

23. Sato, N.; Uragami, Y.; Nishizaki, T.; Takahashi, Y.; Sazaki, G.; Sugimoto, K.; Nonaka, T.; Masai, E.; Fukuda, M.; Senda, T. *J. Mol. Biol.* **2002,** *321*, 621-636.

24. Bittner, M. M.; Kraus, D.; Lindeman, S. V.; Popescu, C. V.; Fiedler, A. T. *Chem. Eur. J.* **2013,** *19*, 9686-9698.

25. Schlichting, I.; Berendzen, J.; Chu, K.; Stock, A. M.; Maves, S. A.; Benson, D. E.; Sweet, R. M.; Ringe, D.; Petsko, G. A.; Sligar, S. G. *Science* **2000,** *287*, 1615-1622.

26. Tinberg, C. E.; J., L. S. *J. Acc. Chem. Res.* **2011,** *44*, 280-288.

27. Krebs, C.; Galonić Fujimori, D.; Walsh, C. T.; Bollinger, J. M. *Acc. Chem. Res.* **2007,** *40*, 484-492.

28. Zhang, Y.; Colabroy, K. L.; Begley, T. P.; Ealick, S. E. *Biochemistry* **2005,** *44*, 7632-7643.

29. Kovaleva, E. G.; Neibergall, M. B.; Chakrabarty, S.; Lipscomb, J. D. *Acc. Chem. Res.* **2007,** *40*, 475-483.

30. Bugg, T. D. H.; Ramaswamy, S. *Curr. Opin. Chem. Biol.* **2008,** *12*, 134-140.

31. Arciero, D. M.; Lipscomb, J. D. *J. Biol. Chem.* **1986,** *261*, 2170-2178.

32. Sanvoisin, J.; Langley, G. J.; Bugg, T. D. H. *J. Am. Chem. Soc.* **1995,** *117*, 7836-7837.

33. Koch, W. O.; Schünemann, V.; Gerdan, M.; Trautwein, A. X.; Krüger, H.-J. *Chem. Eur. J.* **1998,** *4*, 1255-1265.

34. Pierpont, C. G. *Coord. Chem. Rev.* **2001,** *219-221*, 415-433.

35. Pierpont, C. G. *Inorg. Chem* **2011,** *50*, 9766-9772.

36. Spence, E. L.; Langley, G. J.; Bugg, T. D. H. *J. Am. Chem. Soc.* **1996,** *118*, 8336-8343.

37. Georgiev, V.; Borowski, T.; Siegbahn, P. *J. Biol. Inorg. Chem.* **2006,** *11*, 571-585.

38. Siegbahn, P. E. M.; Haeffner, F. *J. Am. Chem. Soc.* **2004,** *126*, 8919-8932.

39. Bassan, A.; Borowski, T.; Siegbahn, P. E. M. *Dalton. Trans.* **2004**, 3153-3162.

40. Emerson, J. P.; Kovaleva, E. G.; Farquhar, E. R.; Lipscomb, J. D.; Que, L., Jr. *Proc. Natl. Acad. Sci.* **2008**, *105*, 7347-7352.

41. Mbughuni, M. M.; Chakrabarti, M.; Hayden, J. A.; Bominaar, E. L.; Hendrich, M. P.; Münck, E.; Lipscomb, J. D. *Proc. Natl. Acad. Sci.* **2010**, *107*, 16788-16793.

42. Mbughuni, M. M.; Chakrabarti, M.; Hayden, J. A.; Meier, K. K.; Dalluge, J. J.; Hendrich, M. P.; Münck, E.; Lipscomb, J. D. *Biochemistry* **2011,** *50*, 10262-102274.

43. Christian, G. J.; Ye, S.; Neese, F. *Chemical Science* **2012,** *3*, 1600-1611.

44. Dong, G.; Shaik, S.; Lai, W. *Chemical Science* **2013,** *4*, 3624-3635.

45. Klecka, G. M.; Gibson, D. T. *Appl. Environ. Microbiol.* **1981,** *41*, 1159-1165.

46. Bartels, I.; Knackmuss, H.-J.; Reineke, W. *Appl. Environ. Microbiol.* **1984,** *47*, 500-505.

47. Cerdan, P.; Wasserfallen, A.; Rekik, M.; Timmis, K. N.; Harayama, S. *J. Bacteriol.* **1994,** *176*, 6074-6081.

48. Vaillancourt, F. H.; Labbé, G.; Drouin, N. M.; Fortin, P. D.; Eltis, L. D. *J. Biol. Chem.* **2002,** *277*, 2019-2027.

49. Dai, S.; Vaillancourt, F. H.; Maaroufi, H.; Drouin, N. M.; Neau, D. B.; Snieckus, V.; Bolin, J. T.; Eltis, L. D. *Nat. Struct. Biol.* **2002,** *9*, 934-939.

50. Chen, J.; Li, W.; Wang, M. Z.; Zhu, G. Y.; Liu, D. Q.; Sun, F.; Hao , N.; Li, X. M.; Rao, Z. H.; Zhang, X. C. *Protein Sci.* **2008,** *17*, 1362-1373.

51. Titus, G. P.; Mueller, H. A.; Burgner, J.; Córdoba, S. R. D.; Penalva, M. A.; Timm, D. E. *Nat. Struct. Biol.* **2000,** *7*, 542-546.

52. Machonkin, T. E.; Doerner, A. E. *Biochemistry* **2011,** *50*, 8899-8913.

53. Xu, L.; Resing, K.; Lawson, S. L.; Babbitt, P. C.; Copley, S. D. *Biochemistry* **1999,** *38*, 7659-7669.

54. Ohtsubo, Y.; Miyauchi, K.; Kanda, K.; Hatta, T.; Kiyohara, H.; Senda, T.; Nagata, Y.; Mitsui, Y.; Takagi, M. *FEBS Lett.* **1999,** *459*, 395-398.

55. Nagata, Y.; Endo, R.; Ito, M.; Ohtsubo, Y.; Tsuda, M. *Appl. Microbiol. Biotechnol.* **2007,** *76*, 741-752.

56. Miyauchi, K.; Adachi, Y.; Nagata, Y.; Takagi, M. *J. Bacteriol.* **1999,** *181*, 6712-6719.

57. Yin, Y.; Zhou, N. Y. *Curr. Microbiol.* **2010,** *61*, 471-476.

58. Jeoung, J.-H.; Bommer, M.; Lin, T.-Y.; Dobbek, H. *Proc. Natl. Acad. Sci.* **2013,** *110*, 12625-12630.

59. Kovaleva, E. G.; Lipscomb, J. D. *Nat Chem Biol* **2008,** *4*, 186-193.

60. McCoy, J. G.; Bailey, L. J.; Bitto, E.; Bingman, C. A.; Aceti, D. J.; Fox, B. G.; Phillips, G. N. *Proc. Natl. Acad. Sci.* **2006,** *103*, 3084-3089.

61. Simmons, C. R.; Liu, Q.; Huang, Q. Q.; Hao, Q.; Begley, T. P.; Karplus, P. A.; Stipanuk, M. H. *J. Biol. Chem.* **2006,** *281*, 18723-18733.

62. Straganz, G. D.; Diebold, A. R.; Egger, S.; Nidetzky, B.; Solomon, E. I. *Biochem* **2010,** *49*, 996-1004.

63. Diebold, A. R.; Neidig, M. L.; Moran, G. R.; Straganz, G. D.; Solomon, E. I. *Biochemistry* **2010,** *49*, 6945-6952.

64. Adams, M. A.; Singh, V. K.; Keller, B. O.; Jia, Z. *Mol. Microbiol.* **2006,** *61*, 1469-1484.

65. Heistand II, R. H.; Roe, A. L.; Que, L., Jr. *Inorg. Chem* **1982,** *21*, 676-681.

66. Maroney, M. J.; Day, R. O.; Psyris, T.; Fleury, L. M.; Whitehead, J. P. *Inorg. Chem* **1989,** *28*, 173-175.

67. Rheingold, A. L.; Miller, J. Private Communication to Cambridge Structural Database. **2003**.

68. Rocks, S. S.; Brennessel, W. W.; Machonkin, T. E.; Holland, P. L. *Inorg. Chem* **2010,** *49,* 10914-10929.

69. Dei, A.; Gatteschi, D.; Pardi, L.; Russo, U. *Inorg. Chem* **1991,** *30*, 2589-2594.

70. Min, K. S.; DiPasquale, A. G.; Golen, J. A.; Rheingold, A. L.; Miller, J. S. *J. Am. Chem. Soc.* **2007,** *129*, 2360-2368.

71. Guo, D.; McCusker, J. K. *Inorg. Chem* **2007,** *46*, 3257-3274.

72. Jo, M.-H.; Grose, J. E.; Baheti, K.; Deshmukh, M. M.; Sokol, J. J.; Rumberger, E. M.; Hendrickson, D. N.; Long, J. R.; Park, H.; Ralph, D. C. *Nano Lett.* **2006,** *6*, 2014-2020.

73. Heersche, H. B.; de Groot, Z.; Folk, J. A.; van der Zant, H. S. J.; Romeike, C.; Wegewijs, M. R.; Zobbi, L.; Barreca, D.; Tondello, E.; Cornia, A. *Phys. Rev. Lett.* **2006,** *96*, 206801.

74. Mannini, M.; Pineider, F.; Sainctavit, P.; Danieli, C.; Otero, E.; Sciancalepore, C.; Talarico, A. M.; Arrio, M.-A.; Cornia, A.; Gatteschi, D.; Sessoli, R. *Nat. Mater.* **2009,** *8*.

75. Blundell, S. J.; Ardavan, A. *J. Mater. Chem.* **2009,** *19*, 1754-1760.

76. Sessoli, R.; Tsai, H. L.; Schake, A. R.; Wang, S.; Vincent, J. B.; Folting, K.; Gatteschi, D.; Christou, G.; Hendrickson, D. N. *J. Am. Chem. Soc.* **1993,** *115*, 1804-1816.

77. Rinehart, J. D.; Fang, M.; Evans, W. J.; Long, J. R. *Nat. Chem.* **2011,** *3*, 538-542.

78. Zhu, M.; Li, Y.-G.; Ma, Y.; Li, L.-C.; Liao, D.-Z. *Inorg. Chem* **2013,** *52*, 12326-12328.

79. Woods, T. J.; Ballesteros-Rivas, M. F.; Ostrovsky, S. M.; Palii, A. V.; Reu, O. S.; Klokishner, S. I.; Dunbar, K. R. *Chem. Eur. J.* **2015,** *21*, 10302-10305.

80. Gibson, D. T.; Parales, R. E. *Curr. Opin. Biotechnol.* **2000,** *11*, 236-243.

81. Parales, R.; Resnick, S. M., In *Biodegradation and Bioremediation*, Singh, A.; Ward, O. P., Eds. Springer: Heidelberg, 2004; pp 175-196.

82. Furukawa, K. *Curr. Opin. Biotechnol.* **2000,** *11*, 244-249.

83. Costas, M.; Mehn, M. P.; Jensen, M. P.; Que, L. J. *Chem. Rev.* **2004,** *104*, 939-986.

84. Straganz, G. D.; Nidetzky, B. *ChemBioChem* **2006,** *7*, 1536-1548.

85. Bruijnincx, P. C. A.; Van Koten, G.; Gebbink, R. J. M. K. *Chem. Soc. Rev.* **2008,** (37), 2716-2744.

86. Solomon, E. I.; Brunold, T. C.; Davis, M. I.; Kemsley, J. N.; Lee, S.-K.; Lehnert, N.; Neese, F.; Skulan, A. J.; Yang, Y.-S.; Zhou, J. *Chem. Rev.* **2000,** *100*, 235-349.

87. Borowski, T.; Georgiev, V.; Siegbahn, P. E. M. *J. Am. Chem. Soc.* **2005,** *127*, 17303-17314.

88. Machonkin, T. E.; Holland, P. L.; Smith, K. N.; Liberman, J. S.; Dinescu, A.; Cundari, T. R.; Rocks, S. S. *J. Biol. Inorg. Chem.* **2010,** *15*, 291-301.

89. Bugg, T. D. H.; Lin, G. *Chem. Commun.* **2001,** *11*, 941-953.

90. Becker, J. M.; Barker, J.; Clarkson, G. J.; van Gorkum, R.; Johal, G. K.; Walton, R. I.; Scott, P. *Dalton. Trans.* **2010,** *39*, 2309-2326.

91. Paria, S.; Que, L. J.; Paine, T. K. *Angew. Chem., Intl. Ed.* **2011,** *50*, 11129-11132.

92. Ogihara, T.; Hikichi, S.; Akita, M.; Moro-oka, Y. *Inorg. Chem* **1998,** *37*, 2614-2615.

93. Mehn, M. P.; Fujisawa, K.; Hegg, E. L.; Que, L. J. *J. Am. Chem. Soc.* **2003,** *125*, 7828-7842.

94. Park, H.; Baus, J. S.; Lindeman, S. V.; Fiedler, A. T. *Inorg. Chem* **2011,** *50*, 11978-11989.

95. Siewert, I.; Limberg, C. *Angew. Chem., Intl. Ed.* **2008,** *47*, 7953-7956.

96. Paria, S.; Halder, O.; Chakraborty, B.; Paine, T. K. *Indian J. Chem, Sect. A: Inorg., Bioinorg., Phys., Theor. Anal. Chem.* **2011,** *50*, 420-426.

97. Fujisawa, K.; Tada, N.; Nishida, Y.; Miyashita, Y.; Okamoto, K. *Inorg. Chem. Commun.* **2008,** *11*, 381-384.

98. Addison, A. W.; Rao, T. N.; Reedijk, J.; Vanrijn, J.; Verschoor, G. C. *J. Chem. Soc., Dalton Tans.* **1984**, 1349-1356.

99. Warren, J. J.; Tronic, T. A.; Mayer, J. M. *Chem. Rev.* **2010,** *110*, 6961-7001.

100. Ito, M.; Amagai, H.; Fukui, H.; Kitajima, N.; Moro-oka, Y. *Bull. Chem. Soc. Jpn.* **1996,** *69*, 1937-1945.

101. Pyrz, J. W.; Roe, A. L.; Stern, L. J.; Que, L. J. *J. Am. Chem. Soc.* **1985,** *107*, 614-620.

102. Davis, M. I.; Orville, A. M.; Neese, F.; Zaleski, J. M.; Lipscomb, J. D.; Solomon, E. I. *J. Am. Chem. Soc.* **2002,** *124*, 602-614.

103. Kitajima, N.; Fujisawa, K.; Fujimoto, C.; Moro-oka, Y.; Hashimoto, S.; Kitagawa, T.; Toriumi, K.; Tatsumi, K.; Nakamura, A. *J. Am. Chem. Soc.* **1992,** *114*, 1277-1291.

104. Hanss, D.; Walther, M. E.; Wenger, O. S. *Chem. Commun.* **2010,** *46*, 7034-7036.

105. Sheldrick, G. M. *Acta Crystallogr., Sect A: Fundam. Crystallogr.* **2008,** *64*, 112-122.

106. Dolomanov, O. V.; Bourhis, L. J.; Gildea, R. J.; Howard, J. A. K.; Puschmann, H. *J. Appl. Crystallogr.* **2009,** *42*, 339-341.

107. Burzlaff, N. *Angew. Chem. Intl. Ed.* **2009,** *48*, 5580-5582.

108. Beck, A.; Weibert, B.; Burzlaff, N. *Eur. J. Inorg. Chem* **2001**, 521-527.

109. Bruijnincx, P. C. A.; Lutz, M.; Spek, A. L.; Hagen, W. R.; Weckhuysen, B. M.; van Koten, G.; Gebbink, R. J. M. K. *J. Am. Chem. Soc.* **2007,** *129*, 2275-2286.

110. Harpel, M. R.; Lipscomb, J. D. *J. Biol. Chem.* **1990,** *265*, 6301-6311.

111. Buongiorno, D.; Straganz, G. D. *Coord. Chem. Rev.* **2013,** *257*, 541-563.

112. Baum, A. E.; Park, H.; Wang, D.; Lindeman, S. V.; Fiedler, A. T. *Dalton. Trans.* **2012,** *41*, 12244-12253.

113. Brown, R. S.; Huguet, J. *Can. J. Chem.* **1980,** *58*, 889-901.

114. Breslow, R.; Hunt, J. T.; Smiley, R.; Tarnowski, T. *J. Am. Chem. Soc.* **1983,** *105*, 5337-5342.

115. Slebockatilk, H.; Cocho, J. L.; Frakman, Z.; Brown, R. S. *J. Am. Chem. Soc.* **1984,** *106*, 2421-2431.

116. Allen, W. E.; Sorrell, T. N. *Inorg. Chem.* **1997,** *36*, 1732-1734.

117. Kimblin, C.; Allen, W. E.; Parkin, G. *J. Chem. Soc., Chem. Commun.* **1995**, 1813-1815.

118. Lynch, W. E.; Kurtz, D. M.; Wang, S. K.; Scott, R. A. *J. Am. Chem. Soc.* **1994,** *116*, 11030-11038.

119. Kunz, P. C.; Rieiss, G. J.; Frank, W.; Klaeui, W. *Eur. J. Inorg. Chem* **2003**, 3945-3951.

120. Kunz, P. C.; Klaeui, W. *Collect. Czech. Chem. Commun.* **2007,** *72*, 492-502.

121. Liu, S.; Su, T.; Zhang, C.; Zhang, W.-M.; Zhu, D.; Su, J.; Wei, T.; Wang, K.; Huang, Y.; Guo, L.; Xu, S.; Zhou, N.-Y.; Gu, L. *J. Biol. Chem.* **2015,** *290*, 24547-24560.

122. Bittner, M. M.; Baus, J. S.; Lindeman, S. V.; Fiedler, A. T. *Eur. J. Inorg. Chem* **2012**, 1848-1856.

123. Boyle, T. J.; Ottley, L. A. M.; Apblett, C. A.; Stewart, C. A.; Hoppe, S. M.; Hawthorne, K. L.; Rodriguez, M. A. *Inorg. Chem.* **2011,** *50*, 6174-6182.

124. Wiznycia, A. V.; Desper, J.; Levy, C. J. *Can. J. Chem.* **2009,** *87*, 224-231.

125. Tsou, C.-C.; Yang, W.-L.; Liaw, W.-F. *J. Am. Chem. Soc.* **2013,** *135*, 18758-18761.

126. Sun, W.-H.; Hao, P.; Zhang, S.; Shi, Q.; Zuo, W.; Tang, X.; Lu, X. *Organometallics* **2007,** *26*, 2720-2734.

127. Gong, D.; Jia, X.; Wang, B.; Zhang, X.; Jiang, L. *J. Organomet. Chem.* **2012,** *702*, 10-18.

128. Manner, V. W.; Markle, T. F.; Freudenthal, J. H.; Roth, J. P.; Mayer, J. M. *Chem. Commun.* **2008**, 256-258.

129. Izutsu, K., *Acid-Base Dissociation Constants in Dipolar Aprotic Solvents*. Blackwell Scientific Publications: Oxford, UK, 1990; Vol. 35.

130. Wang, P.; Yap, G. P. A.; Riordan, C. G. *Chem. Commun.* **2014,** *50*, 5871-5873.

131. Baum, A. E.; Park, H.; Lindeman, S. V.; Fiedler, A. T. *Inorg. Chem.* **2014,** *53*, 12240-12242.

132. Amada, I.; Yamaji, M.; Sase, M.; Shizuka, H. *J. Chem. Soc. Faraday Trans.* **1995,** *91*, 2751-2759.

133. Dohrmann, J. K.; Bergmann, B. *J. Phys. Chem.* **1995,** *99*, 1218-1227.

134. Hester, R. E.; Williams, K. P. J. *J. Chem. Soc. Faraday Trans.* **1982,** *78*, 573-584.

135. Verma, P.; Weir, J.; Mirica, L.; Stack, T. D. P. *Inorg. Chem.* **2011,** *50*, 9816-9825.

136. Vlcek, A. *Comments Inorg. Chem.* **1994,** *16*, 207-228.

137. Hartl, F.; Stufkens, D. J.; Vlcek, A. *Inorg. Chem* **1992,** *31*, 1687-1695.

138. Hartl, F.; Vlcek, A. J. *Inorg. Chem.* **1996,** *35*, 1257-1265.

139. Baum, A. E.; Lindeman, S. V.; Fiedler, A. T. *Chem. Commun.* **2013,** *49*, 6531-6533.

140. Dunn, T. J.; Chiang, L.; Ramogida, C. F.; Webb, M. I.; Savard, D.; Sakaguchi, M.; Ogura, T.; Shimazaki, Y.; Storr, T. *Dalton. Trans.* **2012,** *41*, 7905-7914.

141. Barreto, W. J.; Barreto, S. R. G.; Ando, R. A.; Santos, P. S.; DiMauro, E.; Jorge, T. *Spectrochim. Acta Part A* **2009,** *71*, 1419-1424.

142. Shimazaki, Y.; Kabe, R.; Huth, S.; Tani, F.; Naruta, Y.; Yamauchi, O. *Inorg. Chem.* **2007,** *46*, 6083-6090.

143. Puranik, M.; Chandrasekhar, J.; Snijders, J. G.; Umapathy, S. *J. Phys. Chem. A* **2001,** *105*, 10562-10569.

144. Bordwell, F. G.; Cheng, J. P. *J. Am. Chem. Soc.* **1991,** *113*, 1736-1743.

145. Drouza, C.; Keramidas, A. D. *Inorg. Chem.* **2008,** *47*, 7211-7224.

146. Lyaskovskyy, V.; de Bruin, B. *ACS Catal.* **2012,** *2*, 270-279.

147. Berben, L. A.; De Bruin, B.; Heyduk, A. F. *Chem* **2015,** *51*, 1553-1554.

148. Luca, O. R.; Crabtree, R. H. *Chem. Soc. Rev.* **2013,** *42*, 1440-1459.

149. Praneeth, V. K. K.; Ringenberg, M. R.; Ward, T. R. *Angew. Chem. Intl. Ed.* **2012,** *51*, 10228-10234.

150. Chaudhuri, P.; Wieghardt, K.; Weyhermuller, T.; Paine, T. K.; Mukherjee, S.; Mukherjee, C. *Biol. Chem.* **2005,** *386*, 1023-1033.

151. Chaudhuri, P.; Wieghardt, K. *Prog. Inorg. Chem.* **2001,** *50*, 151-216.

152. Weinberg, D. R.; Gagliardi, C. J.; Hull, J. F.; Murphy, C. F.; Kent, C. A.; Westlake, B. C.; Paul, A.; Ess, D. H.; McCafferty, D. G.; Meyer, T. J. *Chem. Rev.* **2012,** *112*, 4016-4093.

153. Smart, J. C.; Pinsky, B. L. *J. Am. Chem. Soc.* **1980,** *102*, 1009-1015.

154. Stoll, S.; Schweiger, A. *Journal of Magnetic Resonance* **2006,** *178*, 42-55.

155. Neese, F. *ORCA - An ab initio, Density Functional and Semi-empirical Program Package*, University of Bonn: Bonn, Germany, 2010.

156. Becke, A. D. *J. Chem. Phys.* **1993,** *98*, 5648-5652.

157. Lee, C. T.; Yang, W. T.; Parr, R. G. *Physical Review B* **1988,** *37*, 785-789.

158. Becke, A. D. *J. Chem. Phys.* **1986,** *84*, 4524-4529.

159. Perdew, J. P. *Phys. Rev. B* **1986,** *33*, 8822-8824.

160. Schafer, A.; Horn, H.; Ahlrichs, R. *J. Chem. Phys.* **1992,** *97*, 2571-2577.

161. Schafer, A.; Huber, C.; Ahlrichs, R. *J. Chem. Phys.* **1994,** *100*, 5829-5835.

162. Weigand, F.; Ahlrichs, R. *Phys. Chem. Chem. Phys.* **2005,** *7*, 3297-3305.

163. Stratmann, R. E.; Scuseria, G. E.; Frisch, M. J. *J. Chem. Phys.* **1998,** *109*, 8218-8224.

164. Bauernschmitt, R.; Ahlrichs, R. *Chem. Phys. Lett.* **1996,** *256*, 454-464.

165. Casida, M. E.; Jamorski, C.; Casida, K. C.; Salahub, D. R. *J. Chem. Phys.* **1998,** *108*, 4439-4449.

166. Hirata, S.; Head-Gordon, M. *Chem. Phys. Lett.* **1999,** *314*, 291-299.

167. Hirata, S.; Head-Gordon, M. *Chem. Phys. Lett.* **1999,** *302*, 375-382.

168. Laaksonen, L. *J. Mol. Graph.*, 1992.

169. Dei, A.; Gatteschi, D.; Pardi, L. *Inorg. Chem* **1993,** *32*, 1389-1395.

170. Sallmann, M.; Siewert, I.; Fohlmeister, L.; Limberg, C.; Knispel, C. *Angew. Chem. Intl. Ed.* **2012,** *51*, 2234-2237.

171. Chakraborty, B.; Paine, T. K. *Angew. Chem. Intl. Ed.* **2013,** *53*, 920-924.

172. Chakraborty, B.; Bhunya, S.; Paul, A.; Paine, T. K. *Inorg. Chem* **2014,** *53*, 4899-4912.

173. Chatterjee, S.; Paine, T. K. *Inorg. Chem* **2015,** *54*, 1720-1727.

174. Chiou, Y.-M.; Que, L. J. *Inorg. Chem* **1995,** *34*, 3577-3578.

175. Cox, D. D.; Que, L. J. *J. Am. Chem. Soc.* **1988,** *110*, 8085-8092.

176. Cox, D. D.; Benkovic, S. J.; Bloom, L. M.; Bradley, F. C.; Nelson, M. J.; Que, L. J. *J. Am. Chem. Soc.* **1988,** *110*, 2026-2032.

177. Jang, H. G.; Cox, D. D.; Que, L. J. *J. Am. Chem. Soc.* **1991,** *113*, 9200-9204.

178. Bittner, M. M.; Lindeman, S. V.; Popescu, C. V.; Fiedler, A. T. *Inorg. Chem* **2014,** *53*, 4047-4061.

179. Kitajima, N.; Tamura, N.; Amagai, H.; Fukui, H.; Moro-oka, Y.; Mizutani, Y.; Kitagawa, T.; Mathur, R.; Heerwegh, K.; Reed, C. A.; Randall, C. R.; Que, L. J.; Tatsumi, K. *J. Am. Chem. Soc.* **1994,** *116*, 9071-9085.

180. Mukherjee, A.; Cranswick, M. A.; Chakrabarti, M.; Paine, T. K.; Fujisawa, K.; Munck, E.; Que, L. J. *Inorg. Chem* **2010,** *49*, 3618-3628.

181. Chiang, C.-W.; Kleespies, S. T.; Stout, H. D.; Meier, K. K.; Li, P.-Y.; Bominaar, E. L.; Que, L. J.; Munck, E.; Lee, W.-Z. *J. Am. Chem. Soc.* **2014,** *136*, 10846-10849.

182. Shan, X.; Que, L. J. *Proc. Natl. Acad. Sci.* **2005,** *102*, 5340.

183. Park, H.; Bittner, M. M.; Baus, J. S.; Lindeman, S. V.; Fiedler, A. T. *Inorg. Chem* **2012,** *51*, 10279-10289.

184. Zhao, X.; Ogura, T.; Okamura, M.; Kitagawa, T. *J. Am. Chem. Soc.* **1997,** *119*, 5263-5264.

185. Cramer, W. A.; Hasan, S. S.; Yamashita, E. *BBA-Bioenergetics* **2011,** *1807* (7), 788-802.

186. Cape, J. L.; Bowman, M. K.; Kramer, D. M. *Proc. Natl. Acad. Sci. U.S.A.* **2007,** *104* (19), 7887-7892.

187. Ferreira, K. N.; Iverson, T. M.; Maghlaoui, K.; Barber, J.; Iwata, S. *Science* **2004,** *303*, 1831-1838.

188. Sasaki, K.; Kashimura, T.; Ohura, M.; Ohsaki, Y.; Ohta, N. *J. Electrochem. Soc.* **1990,** *137*, 2437-2443.

189. Connelly, N. G.; Geiger, W. E. *Chem. Rev.* **1996,** *96*, 877-910.

190. Brown, S. N. *Inorg. Chem* **2012,** *51*, 1251-1260.

191. Melesani, G.; Ferlin, M. G. *J. Heterocyclic Chem.* **1987,** *24*, 513-517.

192. Willstatter, R.; Wheeler, A. S. *Chem Ber.* **1914,** *47*, 2801.

193. Woo, C. M.; Lu, L.; Gholap, S. L.; Smith, D. R.; Herzon, S. B. *J. Am. Chem. Soc.* **2010,** *132*, 2540-2541.

194. Neese, F. *ORCA - An Ab Initio, DFT and Semiempirical Electronic Structure Package*, 2.9; Max Planck Institute for Bioinorganic Chemistry, Muelheim (Germany), 2012.

195. Noodleman, L. *J. Chem. Phys.* **1981,** *74*, 5737-5743.

196. Sinnecker, S.; Neese, F.; Noodleman, L.; Lubitz, W. *J. Am. Chem. Soc.* **2004,** *126*, 2613-2622.

197. Efremov, R. G.; Sazanov, L. A. *Biochim. Biophys. Acta, Bioenerg.* **2012,** *1817*, 1785-1795.

198. Huynh, M. H. V.; Meyer, T. J. *Chem. Rev.* **2007,** *107*, 5004-5064.

199. Muh, F.; Glockner, C.; Hellmich, J.; Zouni, A. *Biochim. Biophys. Acta, Bioenerg.* **2012,** *1817*, 44-65.

200. Sedoud, A.; Cox, N.; Sugiura, M.; Lubitz, W.; Boussac, A.; Rutherford, A. W. *Biochemistry* **2011,** *50*, 6012-6021.

201. Cox, N.; Lin, L.; Jaszewski, A.; Smith, P. J.; Krausz, E.; Rutherford, A. W.; Pace, R. *Biophys. J.* **2009,** *97*, 2024-2033.

202. Kaim, W. *Inorg. Chem* **2011,** *50*, 9752-9765.

203. Miller, J. S.; Min, K. S. *Angew. Chem., Intl. Ed.* **2009,** *48*, 262-272.

204. Min, K. S.; DiPasquale, A. G.; Rheingold, A. L.; White, H. S.; Miller, J. S. *J. Am. Chem. Soc.* **2009,** *131*, 6229-6236.

205. Yamaguchi, K.; Takahara, Y.; Fueno, T., In *Applied Quantum Chemistry*, Smith, V. H., Ed. Riedel: Dordrecht, 1986; p 155.

206. Attia, A. S.; Conklin, B. J.; Lange, C. W.; Pierpont, C. G. *Inorg. Chem* **1996,** *35*, 1033-1038.

207. Chaudhuri, P.; Verani, C. N.; E., B.; Bothe, E.; Weyhermuller, T.; Wieghardt, K. *J. Am. Chem. Soc.* **2001,** *123*, 2213-2223.

208. Hagen, W. R., In *Adv. Inorg. Chem.*, Cammack, R., Ed. Academic Press: San Diego, CA, 1992; Vol. 38, pp 165-222.

209. Allard, M. M.; Sonk, J. A.; Heeg, M. J.; McGarvey, B. R.; Schlegel, H. B.; Verani, C. N. *Angew. Chem., Intl. Ed.* **2012,** *51*, 3178-3182.

210. Holt, B. T. O.; Vance, M. A.; Mirica, L. M.; Heppner, D. E.; Stack, T. D. P.; Solomon, E. I. *J. Am. Chem. Soc.* **2009,** *131*, 6421-6438.

211. Friedman, J. R. *Annu. Rev. Condens. Matter Phys.* **2010,** *1*, 109-128.

212. Ritter, S. K., Single-Molecule Magnets Evolve. *C&EN: Science & Technology* December 13, 2004, 2004, pp 29-32.

213. Soler, M.; Wernsdorfer, W.; Folting, K.; Pink, M.; Christou, G. *J. Am. Chem. Soc.* **2004,** *126*, 2156-2165.

214. Layfield, R. A. *Organometallics* **2014,** *33*, 1084-1099.

215. Demir, S.; Jeon, I.-R.; Long, J. R.; Harris, T. D. *Coord. Chem. Rev.* **2015,** *289-290*, 149-176.

216. Jeon, I.-R.; Park, J. G.; Xiao, D. J.; Harris, T. D. *J. Am. Chem. Soc.* **2013,** *135*, 16845-16848.

217. Christou, G. *Polyhedron* **2005,** *24*, 2065-2075.

218. Powell, A. K.; Heath, S. L.; Gatteschi, D.; Pardi, L.; Sessoli, R.; Spina, G.; Del Giallo, F.; Pieralli, F. *J. Am. Chem. Soc.* **1995,** (117), 2491-2502.

219. Sokol, J. J.; Hee, A. G.; Long, J. R. *J. Am. Chem. Soc.* **2002,** *124*, 7656-7657.

220. Fortier, S.; Le Roy, J. J.; Chen, C.-H.; Vieru, V.; Murugesu, M.; Chibotaru, L. F.; Mindiola, D. J.; Caulton, K. G. *J. Am. Chem. Soc.* **2013,** *135*, 14670-14678.

221. Tanase, T.; Lippard, S. J. *Inorg. Chem* **1995,** *34*, 4682-4690.